2009

Nonlinear analysis of T-shaped concrete walls subjected to multi-directional displacements

Jonathan David Waugh
Iowa State University

Recommended Citation

Waugh, Jonathan David, "Nonlinear analysis of T-shaped concrete walls subjected to multi-directional displacements" (2009). *Graduate Theses and Dissertations*. 10525.
https://lib.dr.iastate.edu/etd/10525

Nonlinear analysis of T-shaped concrete walls subjected to multi-directional displacements

by

Jonathan David Waugh

A dissertation submitted to the graduate faculty
in partial fulfillment of the requirements for the degree of
DOCTOR OF PHILOSOPHY

Major: Civil Engineering (Structural Engineering)

Program of Study Committee:
Sri Sritharan, Major Professor
Fouad Fanous
Max Porter
Loren Zachary
Thomas Rudolphi

Iowa State University

Ames, Iowa

2009

Table of Contents

List of Figures

List of Tables

Acknowledgements

The study presented in this report is based upon the work supported by the National Science Foundation (NSF) under Grant No. CMS-0324559. The author gratefully acknowledges the support of Drs. Steven McCabe, Douglas Foutch, and M.P. Singh, who have served as NSF Program Directors on this grant. In addition, the author would like to acknowledge the contributions of some individuals without which this research would not have been successfully completed.

- My wife Sharon, who has been patient and understanding, even when things didn't go as planned, and required adjustments to get this research completed;
- my parents Dennis and Barb, who convinced me to join this project and provided insight, and understanding along the way;
- Dr. Sri Sritharan, for his guidance and mentoring provided as my major professor;
- Drs. Fanous, Porter, Zachary, and Rudolphi for serving on my committee and being available to answer questions about various subjects and help me work through challenges;
- Dr. Abendroth, who functioned as a member of my committee, even though it was not required;
- Dr. Silivia Mazzoni and Frank McKenna for their support of OpenSees;
- Dr. French for her guidance and opening her home to me while I was in MN;
- Suzanne Nakaki, for providing feedback about the seismic design community;
- Brenda Litka, for her aid in programming and good technique in C++ coding;
- Paul and Karly Hester, your contribution in terms of review and companionship goes beyond my ability to describe;
- the various staff of the CCEE department, including but not limited to Denise Wood, Doug Wood, Marva Banks, Kathy Petersen, Dan Ackerman, and Grant Stephenson for all your assistance in the daily life of a grad student;
- and finally the author would like to thank the numerous grad and undergrad students who provided their insight, friendship, and support to the author through

the whole process. I cannot list all the students to whom I owe my gratitude, but a partial listing is required: Travis Konda, Millan Jolley, Justin Doornink, Annie Fanous, Tyson Rupnow, John Kevern, Rob Haaland, Toni Tabbert, Sriram Aaleti, Beth Bruggen, John Harrington, Tony Post, David Connor, and many more. You have all been a blessing to me, and I am very grateful for your kindness.

Abstract

Structural walls are often used to resist lateral loads applied to buildings. Structural walls have historically been very successful at limiting damage to both structural and non-structural elements. Researchers at the University of Minnesota (UMN), Iowa State University (ISU), the University of Puerto Rico at Mayaguez, and a consulting engineer from the Nakaki Bashaw Group, Inc. in California tested and analyzed five cast-in-place concrete structural walls, three rectangular walls and two T-walls. All of the walls were analyzed using the open source finite element package OpenSees. Both pre- and post-test analysis of the walls was done to understand the simulation capabilities, and improvements that are required to improve the simulation and prediction of the response of the structural walls.

The OpenSees software was modified to include a new concrete model that improves the simulation of the response of concrete flexural members. The details of the concrete models are presented along with the modifications from a concrete model proposed by Chang and Mander in 1995.

The global force-displacement response of the structural walls are compared with the responses recorded during the testing at the University of Minnesota's Multi-Axial Subassemblage Testing Facility. The analysis was generally capable of capturing the measured response within 5-10%. The contribution of various displacement components were examined and compared with the contributions from the OpenSees analysis. The final T-wall response was successfully predicted using the modeling technique.

In addition to the global force-displacement, the local responses including the location of the neutral axis, curvature, and strain profiles are examined. The local response was well captured for the post-testing analysis and acceptably predicted for the pretesting analysis.

In general the fiber based modeling approach used in this investigation of the structural walls tested at the MAST facility was very successful at capturing both the global and local responses of both rectangular and non-rectangular walls under various applied loads. Recommendations for the simulation of concrete structural walls are given, and future research to further advance the simulation of concrete structural walls.

Chapter 1: Introduction

1.1 Structural Walls

Many concrete buildings in seismic regions use structural walls to limit lateral deformations of structures and minimize damage to nonstructural elements. Structural walls, which have been generally referred to as shear walls, are designed to resist lateral loads and control the lateral deformations due to their high in-plane stiffness along the length of the wall. These walls are often incorporated into features such as elevator shafts and stairwells so that these required building elements can also perform the primary structural functions. Structural walls can be used to resist gravity loads either alone or in combination with columns, depending on the needs of the owner.

In seismic design of buildings the life safety of the occupants is of paramount importance. For loads representative of wind or small, frequent earthquakes, structural walls are typically designed to respond in an elastic manner. However, during larger, less frequent earthquakes, the walls are designed to undergo inelastic deformations, but without experiencing significant strength degradation. This allows the walls to be smaller in cross-section and more economical than would be possible if the walls had to maintain elastic behavior without compromising the safety of the occupants. The American Concrete Institute [ACI, 2002] has adopted this concept in the building code, stating that "*the use of design forces representing earthquake effects … requires that the lateral-force resisting system retain a substantial portion of its strength into the inelastic range under displacement reversals.*" The ACI Building Code requires different levels of energy dissipation in the structure depending on the seismic region where the structure is located. This Code classifies these regions as having low, moderate, or high seismic risk, based on the maximum expected intensity of the ground motion.

Walls have been proven an effective means of maintaining structural strength under various strengths of ground motions [Fintel, 1995]. This researcher gives examples of the wide use of structural walls in numerous buildings in highly active seismic zones all over the world, including cities located in Chile, Macedonia, Venezuela, California, and Mexico. Based on the observed damage from past earthquakes in these locations, Fintel noted that buildings with structural walls experienced minimal damage, while ductile moment-resisting frame buildings experienced severe structural damage. For example, a 14-story Party Headquarters Building located in Macedonia had a structural wall-frame system and was subjected to a large earthquake in 1953. The earthquake measured 6.2 on the Richter scale, despite the building swaying considerably and throwing desks across the building, no structural or nonstructural damage occurred to this building, not even to the glass windows. Fintel [1995] concluded that because of over 30 years of the observed superior performance, no building in a seismic zone should be built without structural shear walls to resist lateral seismic loads.

Figure 1-1 shows the Plaza 1 Apartment Building that experienced the 1967 Caracas, Venezuela, earthquake. The building utilized structural walls and had no apparent damage to the structure. In contrast, Figure 1-2 shows the internal second story columns of the Macuto Sheraton Hotel, which had extensive damage to the columns and stairwells during the same Caracas earthquake. The structural walls on the upper stories, which were terminated at the top of the second story columns, were not damaged in the earthquake. Figure 1-3 shows the failure of a beam-column joint in the Cypress Gardens Building during the Caracas earthquake. As witnessed in the 1967 Caracas earthquake and documented by Fintel [1995], structural walls provide buildings with very good seismic performance.

In moderate to large earthquakes, inelastic flexural actions are designed to occur over the lower portion of the walls. In this region, especially at the endsstructural walls are expected to experience very high compressive and tensile flexural strains and thus, require special transverse reinforcement. These areas requiring special reinforcement consideration are known as the boundary elements. Dependable lateral load behavior of walls is thus dictated by the boundary elements being adequately reinforced to ensure the satisfactory design and acceptable performance. The transverse reinforcement required in boundary elements allows the concrete to achieve high compressive strains due to confinement effects and helps prevent buckling of the longitudinal reinforcement. If more transverse reinforcement is used than required, the wall will perform well under earthquake loads; however, the cost of the wall will increase and the constructibility will decrease. Insufficient reinforcement can cause premature failure of the structural wall due to crushing of the concrete or buckling of the longitudinal reinforcement, causing rapid strength degradation. Traditionally, the longitudinal reinforcement has been concentrated in the boundary elements in order to maximize the moment resistance and ductility. In this context, if the wall's behavior under lateral loads can be accurately predicted in the design process, the designer can develop efficient, cost-effective structural wall systems for buildings that will be adequate to resist large ductile deformations.

Figure 1-1: Plaza 1 Apartment Building that was undamaged during the Caracas Earthquake [1]

Figure 1-2: Damage to the 2nd Story Columns of the Macuto Sheraton due to the Caracas Earthquake [2]

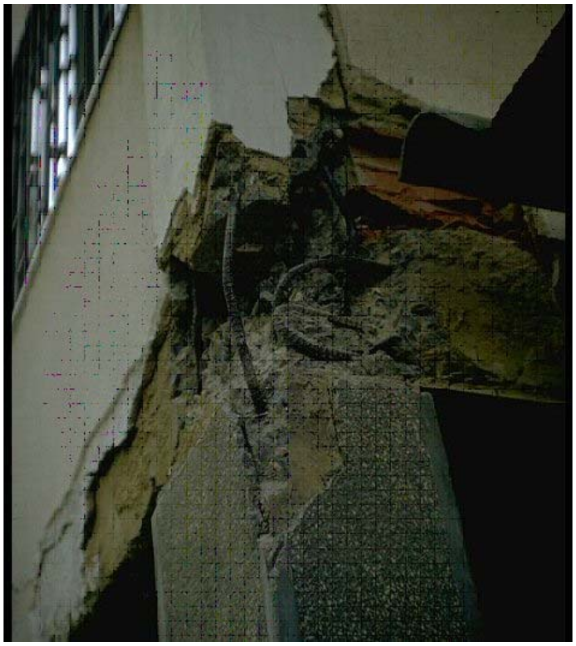

Figure 1-3: Joint Failure in the Cypress Gardens Building due to the Caracas Earthquake [3]

Structural walls can be symmetrical, such as rectangular or barbell walls, or asymmetrical, also known as nonrectangular, such as T-, L- or C-shaped walls, as shown in Figure 1-4. Symmetric walls have been extensively studied. Abrams [1991] lists numerous studies on symmetrical structural walls. However, nonrectangular walls have not been as thoroughly studied. Asymmetrical shapes for walls may occur because of irregular building geometry and/or due to specific space requirements from the owner or architect. When two or more walls in different directions are joined together, one acts as the flange and has a significant impact on the ductility, strength, and stiffness of the other wall(s) [Thomsen and Wallace, 1995]. The impact of the flange varies depending on the direction, in which the load is applied. This direction dependence must be accounted for in the analysis and design of the structural wall.

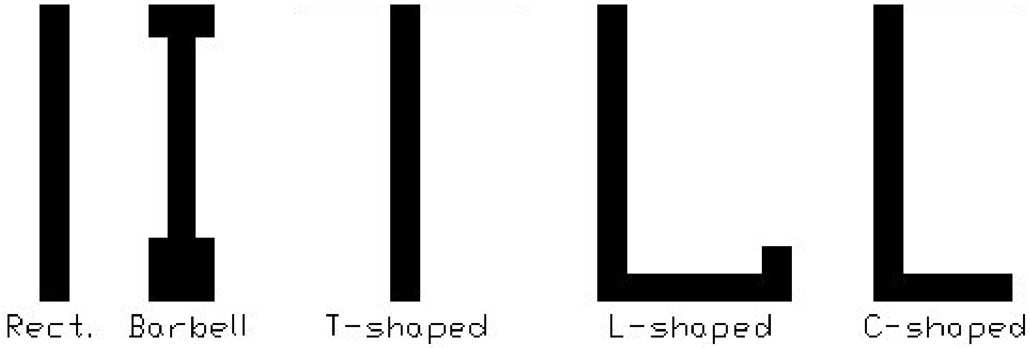

Figure 1-4: Common Wall Sections

Since the flange plays an important role in the behavior of a nonrectangular wall, it is essential that the design community understands how the flange affects the lateral load response of this wall type. Accurate prediction of the wall behavior is important in determining the reinforcement required for these structural elements in new buildings, as well as to evaluate retrofit techniques for existing structures containing this type of concrete wall. Given the complexity of wall behavior, models for predicting asymmetric wall behavior must be calibrated adequately against experimental data. Furthermore, since the direction of earthquake ground motions is random, the model representing these walls should be able to capture the wall response regardless of the direction of the earthquake attack.

1.2 Methods of Analysis

Various methods have been used to analyze structural walls and to predict their behavior under reversed cyclic loads. These methods have ranged from simple calculations based on moment-curvature relationships to general finite element analysis of the walls. For the current study, a fiber-based element analysis approach was chosen to model and analyze the structural walls was to model the structural walls using a fiber-based finite element analysis approach. The fiber concept represents a reinforced concrete section of a structural element with a group of uniaxial fibers and assigns the uniaxial concrete or steel behavior to these fibers. Three dimensional effects on material behavior are typically incorporated into the uniaxial behavior of the material in order to improve the accuracy of the analysis. Confinement of the concrete is handled this way in the analysis in this report, while the effects of buckling of the longitudinal reinforcement was not included in the analysis. Taucer *et al.* [1991] used this concept to develop a beam-column element for seismic response analysis of structural systems and demonstrated that it significantly improves the computation efficiency over the traditional finite element approaches. The main benefit of using this fiber-based element is that it allows the use of uniaxial stress-strain relationships that are well established, providing accurate force-displacement responses for structural members under lateral loads. An inherent assumption used in the fiber-based element is that plane sections remain plane after bending. When a section of a structural member does not satisfy this assumption such as a flanged wall, this assumption can lead to inaccurate strains and curvature at the critical sections. Consequently, the analysis would lead to an inaccurate estimate of damage and force-displacement responses as they are significantly dependent on local responses in the critical regions. Another drawback of the fiber-based analysis is that it typically ignores the effects of bond slip of longitudinal reinforcement resulting from strain penetration.

The open source finite element program OpenSees [Mazzoni *et al.*, 2006] was used for the study in this report because it was capable of using a fiber section in conjunction with beam-column elements. Access to the source code of the program allowed new section definitions and material models to be added to the program to overcome the challenges identified above and improve the simulation of the structural walls to lateral/multi-directional loads.

1.3 Project Description

In parallel with establishment of the George E. Brown, Jr. Network for Earthquake Engineering Simulation (NEES) (http://www.nees.org/) in October 2004, the National Science Foundation (NSF) funded an unsolicited collaborative research proposal to a team of researchers from the University of Minnesota (UMN), Iowa State University (ISU) and the University of Puerto Rico at Mayagüez. The focus of this research proposal was to experimentally and analytically study the behavior of nonrectangular structural walls subjected to the effects of multi-directional loading. In addition to addressing this fundamental problem, this project was aimed at verifying the capabilities of the Multi-Axial Subassemblage Testing (MAST) facility at UMN, which is one of 15 experimental facilities in the NSF's shared NEES network. This is one of three such projects to be awarded by NSF prior to establishing the NEES Research (NEESR) awards through a special solicitation for proposals that would utilize the unique capabilities of the NEES network. Consequently, these three projects funded through the unsolicited proposals were referred to as the PreNEESR projects.

As part of this PreNEESR research project on nonrectangular walls, two T-shaped large-scale concrete walls were tested at the MAST facility at UMN. Another motivation for using OpenSees for the analytical simulation of the concrete walls under prescribed sets of loading was that it was selected as the simulation component for NEES.

1.4 Research Objectives

In the context of the above described project, current state of knowledge and the shortcomings of OpenSees, the objectives of the study presented in this report are as follows:

- develop a model of T-walls that is computationally efficient, easy to build and understand. Model should be simple enough to be used by the design community when appropriate;
- implement a robust concrete model into OpenSees and verify its capabilities;
- accurately model the response of T-walls to multidirectional loading; including the force-displacement response, strain profile, and location of the neutral axis;
- model the contributions of the displacement components to the total displacement;
- calibrate the model technique against existing data, and predict the response of T-walls before testing using available material properties;
- investigate the distribution of base shear to a pair of T-walls in a building;
- determine the envelope that should be used for design to ensure proper behavior regardless of the loading direction.

1.5 Definition of Terms

Provided below is a list of the various terms used throughout the report that may not be familiar to all readers. The definition of the term is provided here to allow readers to refer back if a term is unclear. This is not an exhaustive list, but rather the key terms and concepts used in the report.

Aspect ratio: ratio of the wall height to the length of the wall that is used to determine if the wall behavior is shear or flexure dominated

Bond slip due to strain penetration: slip along a portion of adequately anchored longitudinal reinforcement of a flexural member into a footing (or an adjoining connecting member) due to localized crushing of concrete surrounding a portion of the anchored bar in the connecting element, which in turn introduces rotation to the flexural member at the connection interface.

Boundary elements: the ends of the wall that require special consideration including additional transverse reinforcement to ensure adequate seismic performance of concrete walls when high strains are expected in the concrete and reinforcement bars in these regions.

Fiber section analysis: a method for determining strains and stresses on a section of a structural member, thereby characterizing the member behavior by discretizing and analyzing the section as a group of uniaxial fibers.

Integration points: points along the length of beam-column element where strains and the corresponding stresses are calculated by satisfying compatibility and equilibrium conditions.

Neutral axis: location of zero strain on a section due to flexural bending.

Shear lag: refers to the phenomenon when the bending strain is unevenly distributed across a flange of a structural member subjected to moment in the direction perpendicular to the flange, limiting the effective flange participation in resisting the moment.

Plastic hinge length: the length over which all the plastic action maybe assumed to occur in lumped plasticity models, which is much shorter than the length of the actual plastic region

Plastic region – region in a flexural member where inelastic strains are expected to develop in concrete or steel fibers.

1.6 Report Layout

This report consists of seven chapters. The following chapter reviews the available literature on experimental tests of nonrectangular walls, the various analysis techniques that have been used to analyze structural walls, and investigations of the effects of shear lag in nonrectangular sections. Chapter 3 discusses a new concrete model that was implemented in OpenSees in order to improve the simulation of structural walls. Chapter 4 presents the analysis of the first T-wall, NTW1, tested at the MAST facility Both pre-test and post-test analysis of this wall subjected to multidirectional loading are presented. The various responses recorded during the test are compared to the OpenSees simulation results. Chapter 5 presents the pre-test analysis of NTW2. The global force-displacement responses are presented and compared to the force-displacement results from the OpenSees analysis; similarly, selected local responses are also compared. Chapter 6 presents the dynamic analysis of a pair of T-walls to determine the base shear distribution between the two walls under dynamic loading and the performance of a concrete building slice with structural T-walls at various earthquake intensities. Chapter 7 presents conclusions from the investigation and recommendations for future research on the analysis of T-walls. Appendix A presents a model used in the blind prediction contest conducted by the University of California – San Diego on the response of a 7-story building slice. This model is similar to the models used for the analysis of NTW1 and NTW2 and showed the modeling approach can be used for a dynamic analysis. This model also verifies the improvements of using the new concrete model introduced in OpenSees and described in Chapter 3.

Chapter 2: Literature Review

While rectangular structural walls have been extensively investigated, other wall shapes have not been as thoroughly tested an analyzed by the research community. This chapter outlines the existing research that has been conducted on non-rectangular structural walls, the nonlinear analysis of structural walls, and investigations of shear lag in non-rectangular walls.

2.1 Nonrectangular Structural Wall Tests

2.1.1 Goodsir [1985]

Goodsir tested a 1/3-scale, T-shaped reinforced concrete wall as part of AN experimental study. The wall had a 51 in. long web with a 27.5 in. wide flange and had a uniform thickness of 4 in. The wall specimen was constructed to give an aspect ratio of approximately 2.2 in the web direction, with a wall height of 112 inches.. When tested under cyclic loads, this wall achieved a displacement ductility of 6 and failed due to crushing of the unconfined concrete immediately adjacent to the confined concrete of the boundary element. Goodsir stated that the wall failure was due to the high ductility demand and eccentric loading arising from out-of-plane displacement. Goodsir concluded that the transverse reinforcement in the boundary element should be extended further into the section of the T-walls if large compressive zones were expected due to large displacements. The extent to which the boundary element should be extended was recommended for further study.

2.1.2 Sittipunt and Wood [1993]

Sittipunt and Wood conducted an analytical and experimental study of C-shaped structural walls. The objective of their research was to investigate a) the inelastic cyclic response and energy dissipation, b) the effective stiffness at various displacement levels, and c) the influence of web reinforcement on the response of C-walls. The wall section had a 60 in. long flange, with two parallel 36 in. long webs. The two walls, CLS and CMS, were 9 ft tall and 3 in. thick; a schematic of the wall is shown in Figure 2-1a. The researchers reported that the "60 in. flange width was chosen to be longer than the effective width defined for a T-beam with a 3 in. flange in Section 8.10.2 and 8.10.4 of the 1989 ACI Building Code" [Sittipunt and Wood, 1993].

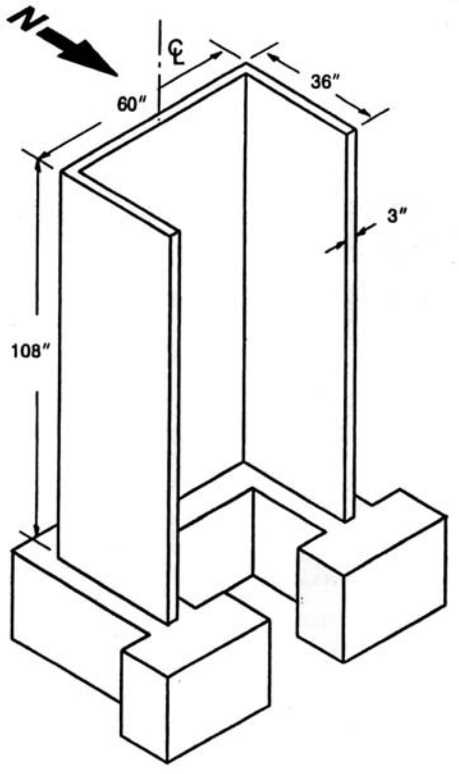

a) Overall Dimensions

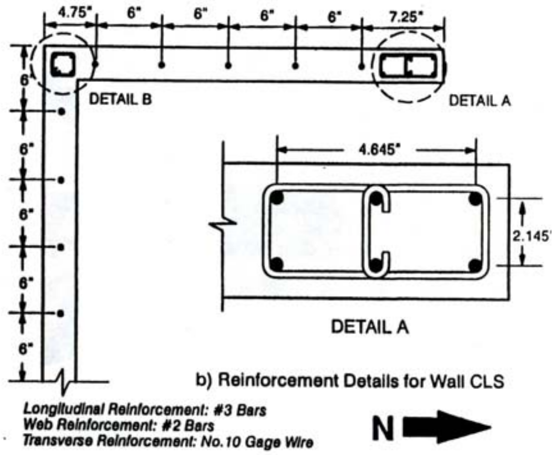

b) Reinforcement Details for Wall CLS

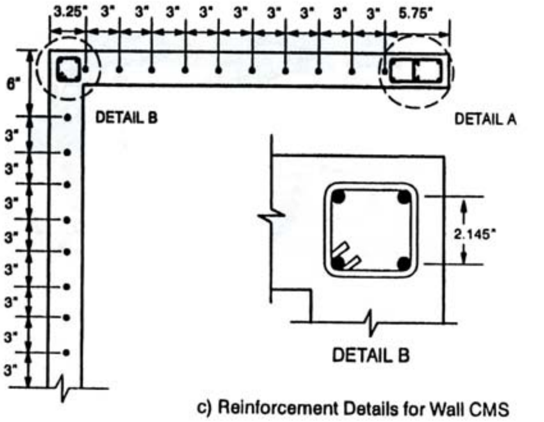

c) Reinforcement Details for Wall CMS

Figure 2-1: Overall Dimensions and reinforcement details of the C-Walls tested by Sittipunt and Wood [1993]

The reinforcement details for each C-wall, called CMS and CLS, is shown in Figure 2-1b and 2-1c. The same amount of flexural reinforcement was provided in the boundary of both walls, with 10 #3 bars in each web. Four of these bars were placed in the boundary element at the intersection between the flange and web, and the remaining six bars were placed in the web stem. The difference between the two C-shaped walls was the amount of distributed reinforcement in the web and flanges. One wall (CLS) had the minimum distributed reinforcement allowed in the 1989 ACI Building Code with a web reinforcement ratio of 0.0025, while the other wall (CMS) had twice as much reinforcement. The reinforcement ratios in the horizontal and vertical directions of each wall were equal. A single layer of #2 bars were used to provide the distributed reinforcement in both walls. Wall CLS used a nominal spacing of 6 in. whereas CMS used a 3 in. nominal spacing, doubling the reinforcement ratio of the wall, see Figure 2-1(b) and (c).

Transverse reinforcement consisted of square spirals made of No. 10 gauge wire around the four bar boundary element, while the same gauge wire rectangular spirals with cross ties were used for the six bar boundary element, see “Detail A” and “Detail B” in Figure 2-1. The spacing of the transverse reinforcement in both boundary elements was two inches. Both walls were designed such that their nominal flexural strength was less than the nominal shear strength; the shear capacity was calculated to be 22%-42% higher than the shear demand expected at full development of the full flexural capacity for CLS depending on if an elasto-plastic or strain hardening stress-strain relationship was used the reinforcement. The shear strength of CMS was 54%-87% higher than the flexural capacity, which allowed the walls to experience a ductile flexure dominated response rather than a brittle shear response.

Both walls were loaded at the top with quasi-static lateral load reversals in the web direction. An axial load of 100 k was applied to both test specimens through the centroid of the section, which induced a uniform stress of 265 psi to the walls. The walls were subjected to cycles of ±10 kips, ±1.0 in. of displacement, ±1.5 in. of displacement, and then cycles of greater than ±2.0 in. of displacement The force displacement responses measured for both CLS and CMS are shown in Figure 2-2.

Sittipunt and Wood used the test data to calibrate a general finite element model so that they could investigate the effects of various reinforcement details and the effective flange width on the response of C-walls. They developed a general two-dimensional model of concrete using the smeared crack model with fixed orthogonal directions for crack propagation. The reason for using this concrete model was largely based on the observations made during testing of the C-walls and the response of walls tested by Oesterle et al. [1979]. In the finite element model, they used a discrete steel model because it allowed them to more accurately model the specimens. Sittipunt and Wood used linear isoparametric 4-node elements with a 2x2 integration rule to represent the concrete and a 2-node bar element to represent the reinforcing. While the discrete steel model allows the use of linkage elements to include the effects of bond slip due to strain penetration, they did not use linkage elements in their finite element model. However, the possibility of using linkage elements to model the bond slip was suggested by Sittipunt and Wood.

Their model captured the global behavior of the wall adequately, with the calculated load versus deflection correlating acceptably with the recorded experimental response, as shown in Figure 2-2. Both the experimental data and analysis of the wall showed good energy dissipation and no strength degradation prior to crushing of concrete in the web tip boundary elements. However, no comparison of the strain and curvature simulations were presented. The local response paramters such as, strains, curvature, location of the neutral axis, etc. are important predictors of damage and their accurate prediction is required in performance-based seismic design.

Sittipunt and Wood concluded from their testing and analytical models that the effective flange width can be larger than that recommended by 1989 ACI Building Code for the effective flange width of T-beams. Furthermore, they suggested that using the 1989 ACI code recommendations for effective flange width is conservative when the flange is in compression; however, when the flange is placed in tension, using a too small effective flange width greatly underestimates the strength of the section, which can potentially lead to premature crushing of the concrete in the boundary elements in the web. This results from more tension reinforcing steel being mobilized and allowing the section to carry a larger moment than was implied by the 1989 ACI code recommendations. The extra moment places additional strain demand on the concrete in the web tips and can lead to crushing of the confined concrete at lower displacement levels than anticipated. However, they made no specific recommendation on how large and effective flange width should be used for C-walls; rather they recommended further research to determine the proper effective flange width.

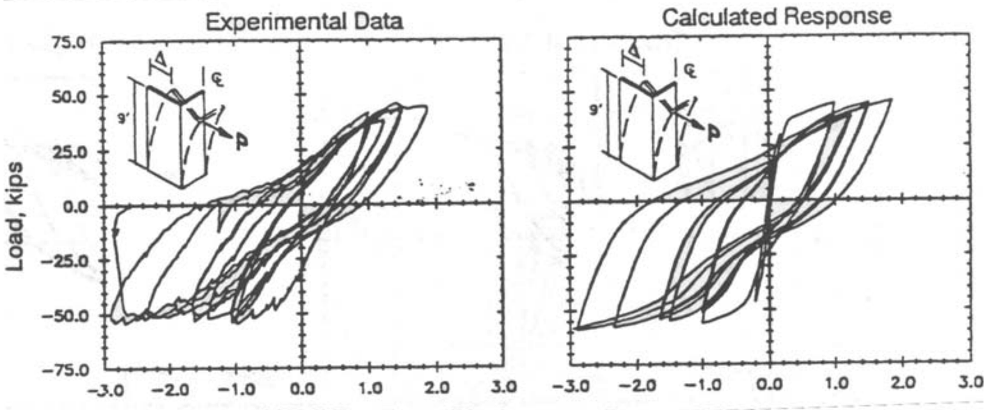

a) Wall Top Force-Displacement Response of CLS

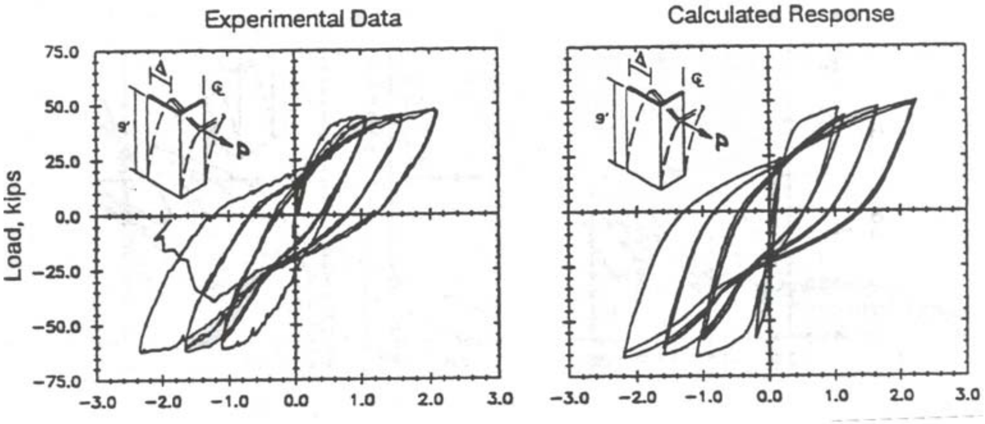

b) Wall Top Force-Displacement Response of CMS

Figure 2-2: Experimental and Analytical Force-Displacement Response of CLS and CMS [Sittipunt and Wood, 1993]

2.1.3 Thomsen and Wallace [1995]

Thomsen and Wallace conducted an investigation on the behavior of structural walls with rectangular and T-shaped cross-sections. The walls were selected based on a prototype building multi-story office building located in a high seismic region; see Figure 2-3 for the floor plan of the prototype building. The building was six stories tall, and incorporated both rectangular and T-shaped walls as well as moment resisting concrete frames to resist lateral and gravity loads.

Thomsen and Wallace used a displacement-based design procedure to determine estimates of the lateral roof displacement and story drifts of the prototype structure. In this procedure, individual walls are designed based on the required global deformations The section analysis program BIAX [Thomsen & Wallace, 1995] was used in the design procedure to determine the flexural strength of walls, transverse steel in the boundary elements, and the required shear strength of the wall. They wanted to show that their displacement-based design method effectively designed both rectangular and nonrectangular walls. The rectangular wall was designed considering the forces corresponding to the in-plane response, while the T-shaped wall was designed considering the forces in the plane of the flange and in the plane of the web.

The prototype rectangular wall was 192 in. long by 16 in. thick. The prototype T-wall was 192 in. wide at the flange and was 192 in. deep; both the flange and the web were 16 in. thick. The rectangular and T-walls were 864 in. tall in the prototype structure. Once the designs for the rectangular and T-shaped walls in the prototype structure were completed, four 1/4-scale test specimens were designed and constructed. They were identified as RW1, RW2, TW1, and TW2. Figures 2-4 and 2-5 show the dimensions and reinforcement details of Thomsen and Wallace’s rectangular specimens RW1 and RW2. RW2 differed from RW1 by using a closer spacing for the transverse reinforcing steel in the boundary elements to suppress buckling of the longitudinal reinforcement and allow the confined concrete to control the lateral load behavior of the wall. However, the diameter of the transverse reinforcement was not changed, increasing the volumetric ratio by 50% and thereby greatly increasing the confinement effects to the concrete.

Figure 2-6 shows the reinforcement details for the first T-wall, TW1. TW1 was designed by taking two rectangular walls and joining them together without considering the T-wall behavior. On the other hand, TW2 was designed considering the T-wall behavior and its reinforcement details were significantly different from those of TW1. Figure 2-7 shows the reinforcement details of TW2. The modified details of TW2 with respect to TW1 include: 1) the boundary element in the web tip was significantly longer to accommodate the high strains and location of the neutral axis expected when the flange is in tension, 2) the spacing of the transverse reinforcement in the web tip boundary element was reduced, and 3) the number of longitudinal bars in the web tip boundary element was increased by adding two #2 bars.

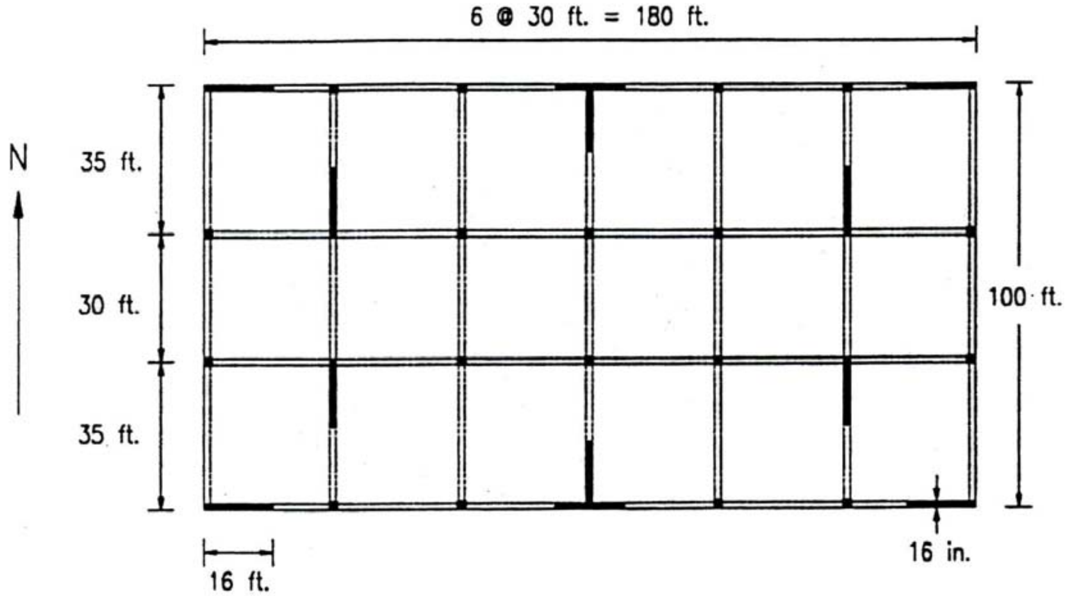

Figure 2-3: The Floor Plan of the Prototype Building chosen by Thomsen & Wallace [1995]

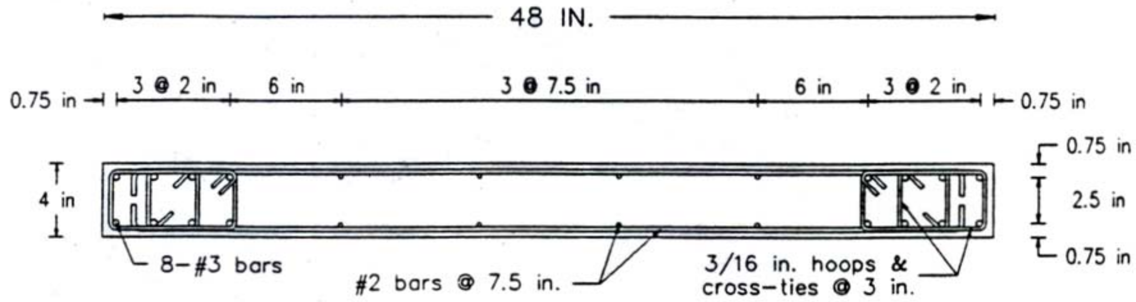

Figure 2-4: Section of Rectangular Wall RW1 Tested by Thomsen and Wallace [1995]

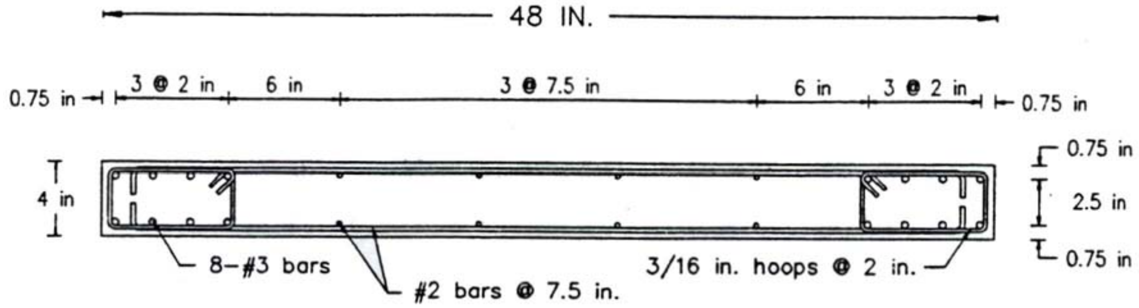

Figure 2-5: Section of Rectangular Wall RW2 Tested by Thomsen and Wallace [1995]

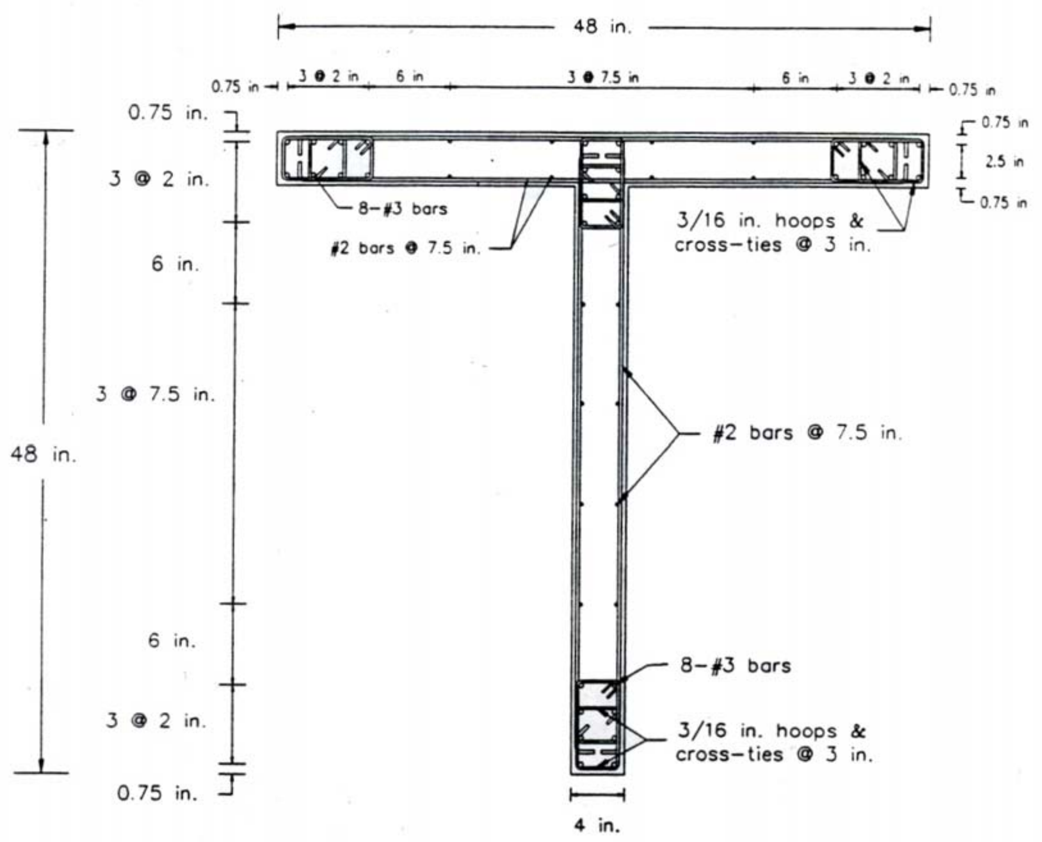

Figure 2-6: Wall Section TW1 Tested by Thomsen and Wallace [1995]

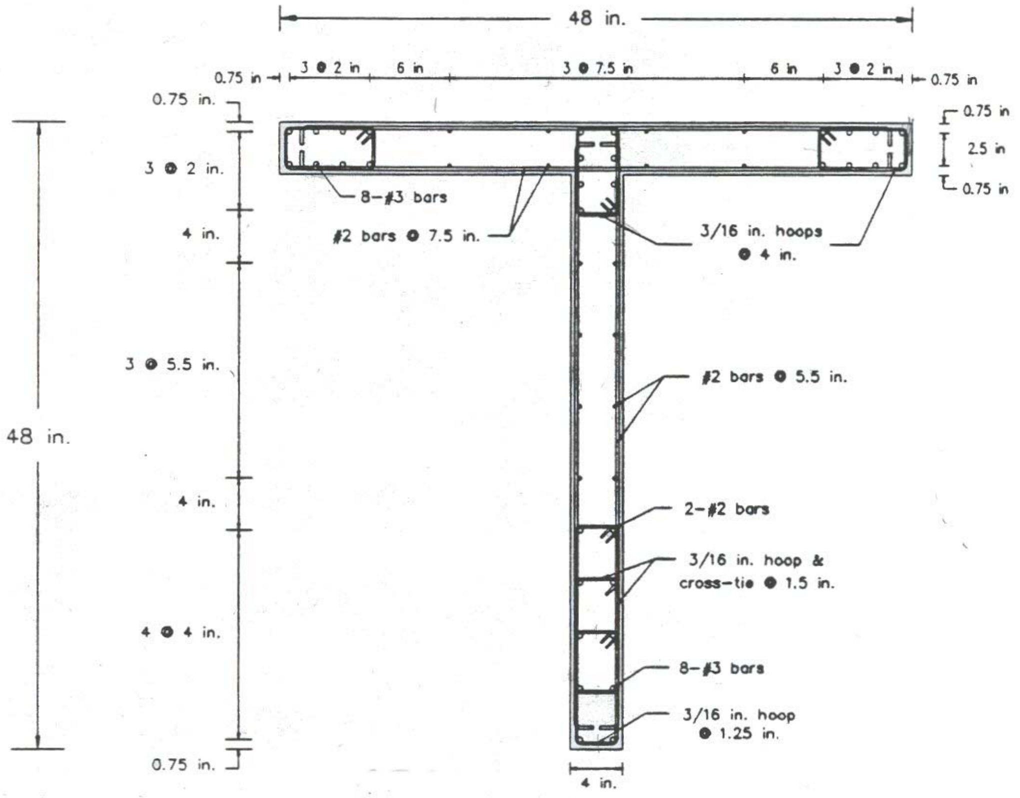

Figure 2-7: Wall Section TW2 Tested by Thomsen and Wallace [1995]

Prior to testing them lateral load, all walls were subjected to axial loads in the range of 0.07$A_g f'_c$ to 0.1$Agf'c$, where A_g is the gross cross-sectional area and f'_c is the measured concrete strength. The actual axial load ratio applied to each wall is noted in the force-displacement plots in Figures 2-8 to 2-11, where f'_c values were 4.58 ksi, 6.33 ksi, 4.92 ksi, 6.048 ksi for RW1, RW2, TW1, and TW2, respectively. The rectangular walls were loaded in the plane of the wall and cycled at least twice at each level of target story drift. The drift targets were 0.25%, 0.50%, 0.75%, 1.0%, 1.5%, 2.0%, and 2.5% drift. The T-walls were loaded in the plane of the web, causing compression or tension in the flange depending on the direction of the load.. With good detailing, specimen RW1, RW2, and TW2 were expected to provide adequate ductility with no strength degradation, TW1 was expected to perform poorly and was intended to show the effects of treating a T-wall as separate rectangular walls in each direction, thus ignoring the effects of the flange on the response. Figure 2-8 and 2-9 show the response of rectangular walls, which experienced a symmetric response in terms of strength and ductility when loaded alternatively in the positive and negative directions. RW1 failed by buckling of all eight longitudinal bars in the boundary element between the transverse reinforcement at 1.5% drift. RW2 also failed due to buckling of the longitudinal reinforcement between the transverse reinforcement; however, the reduced spacing of the transverse reinforcement delayed buckling until 2.5% lateral drift. However, the response of the T-walls, seen in Figure 2-10 and 2-11, was different depending on if the flange was in compression or tension. When the flange was in compression, the wall had a lower lateral force resistance; however, the ductility of the section was higher. The higher ductility results from the small neutral axis depth and low compressive strains in the flange. The tension steel is located far from the neutral axis and experiences very large strains allowing the steel to utilize its entire post-yield strain capacity. The lower lateral strength was due to the reduced amount of reinforcement area in the web tip when compared to the steel area in the flange. When the load was reversed and the flange was placed in tension, the lateral load resistance increased and the ductility of the wall was decreased. The increased load came from the large longitudinal steel area in the flange, allowing a higher flexural strength to be developed at the critical wall section. The neutral axis was located high in the web such that the compression and tension strains were approximately equal, leading to reduced strain demand in the steel and a lower ductility for the wall.

The flexural strength of the wall when the flange was in tension was almost twice as large as when the flange was in compression. This placed a larger shear demand on the wall. However, as seen in Figure 2-12, the shear deformation near the wall base was the largest when the flange was in compression, even though the corresponding shear demand was lower. Thomsen & Wallace [1995] offer the following explanation:

> “When the flange is in compression, the depth of the compression zone is extremely small (~3 in.), and large inelastic tensile strains are developed in the web, resulting in substantial flexural and shear cracking (diagonal shear cracks extend the entire length of the web). The inelastic shear

> distortions measured under this loading condition are relatively high, even though the measured shear force is comparatively low (half as large as the shear expected under reversed loading condition). When the flange is in tension, the wall stiffness increases and the depth of the compression zone is approximately half the wall length. Under this loading condition, less damage (diagonal cracking) was witnessed; therefore relatively small shear distortions were measured, even though the shear force was approximately twice as large."

TW1 failed due to global buckling of the entire web tip boundary element. The brittle buckling failure was expected due to the poor detailing, but was intended to show the brittle behavior that results from poor conceptual design and detailing. TW2 failed due to crushing of the confined concrete core at 2.5% lateral drift, the confined concrete was observed pushing out through the hoops and ties. The crushing of the confined core resulted in out-of-plane instability on subsequent cycles.

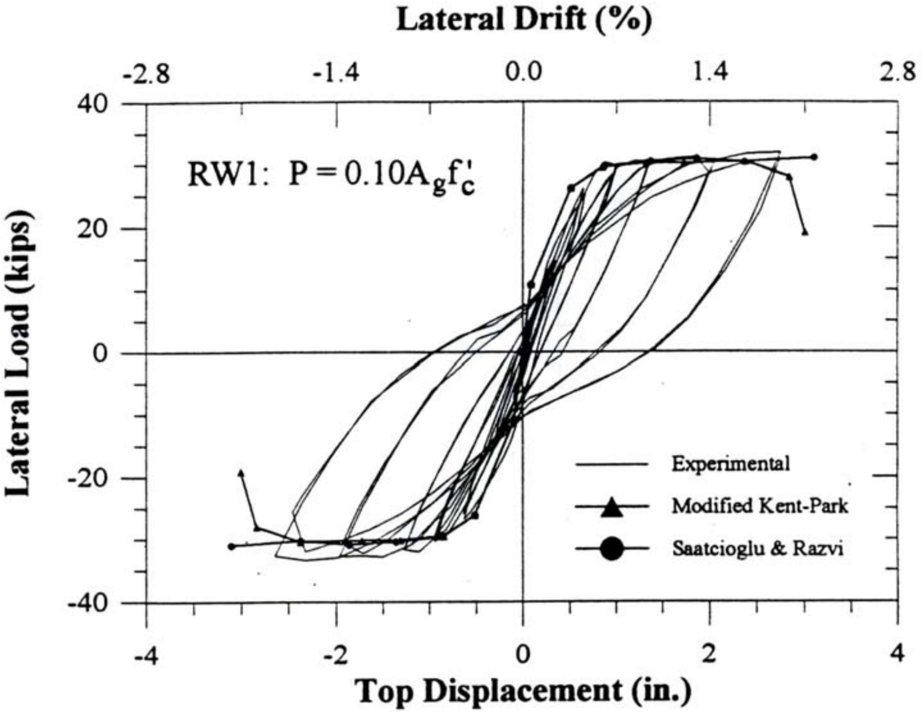

Figure 2-8: Measured and Analytical Response of RW1 [Thomsen & Wallace, 1995]

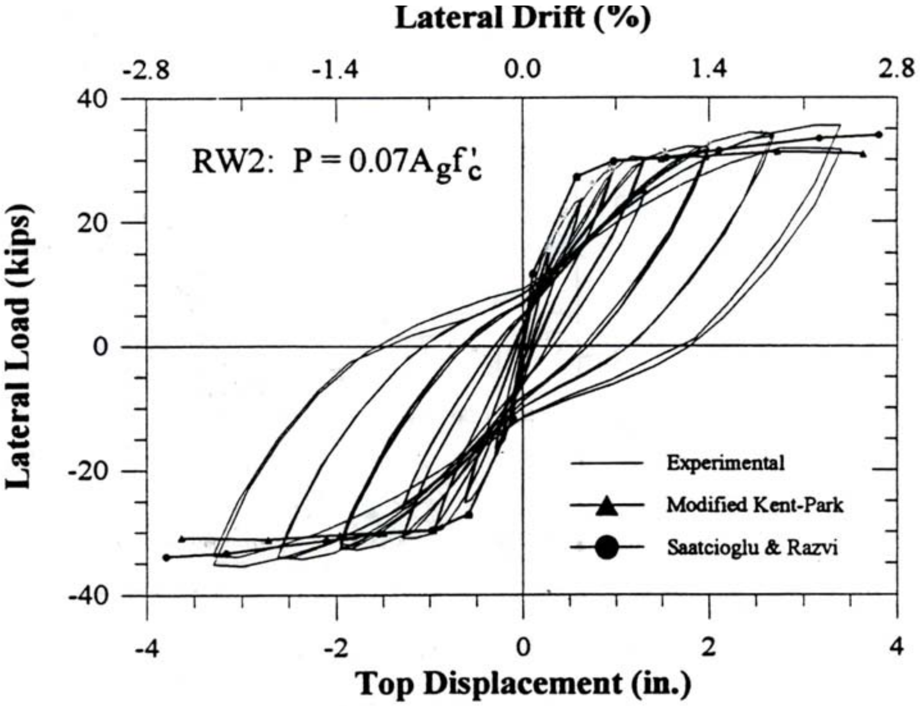

Figure 2-9: Measured and Analytical Response of RW2 [Thomsen & Wallace, 1995]

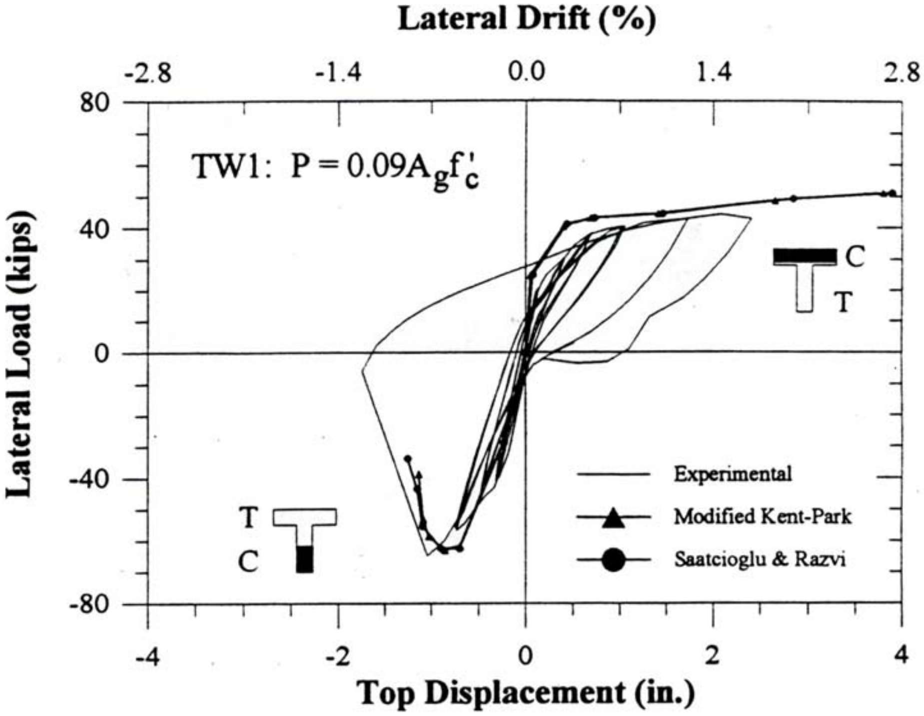

Figure 2-10: Measured and Analytical Response of TW1 [Thomsen & Wallace, 1995]

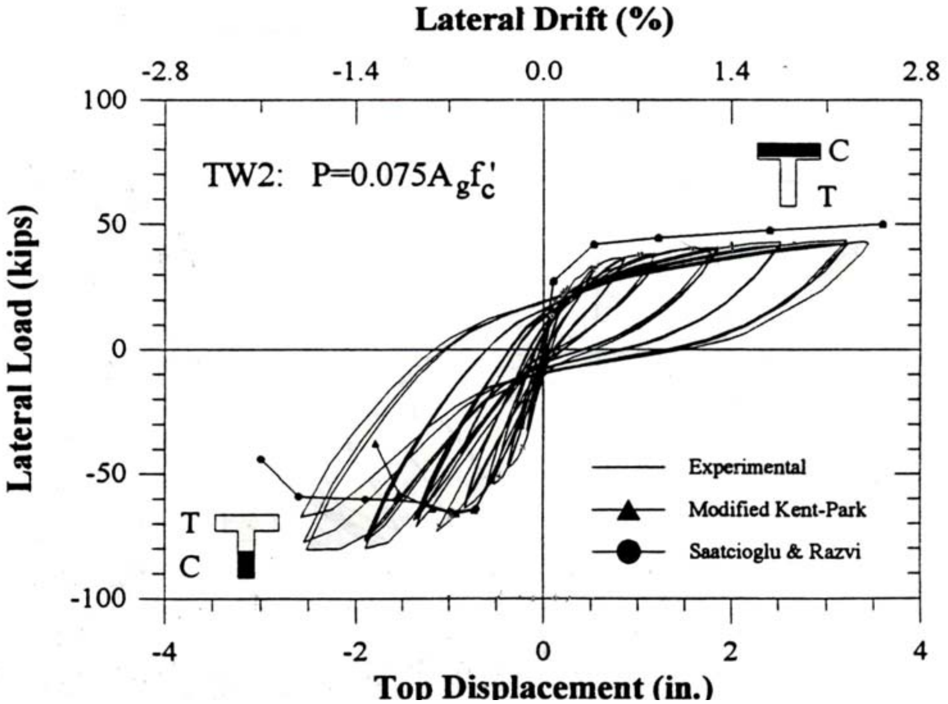

Figure 2-11: Measured and Analytical Response of TW2 [Thomsen & Wallace, 1995]

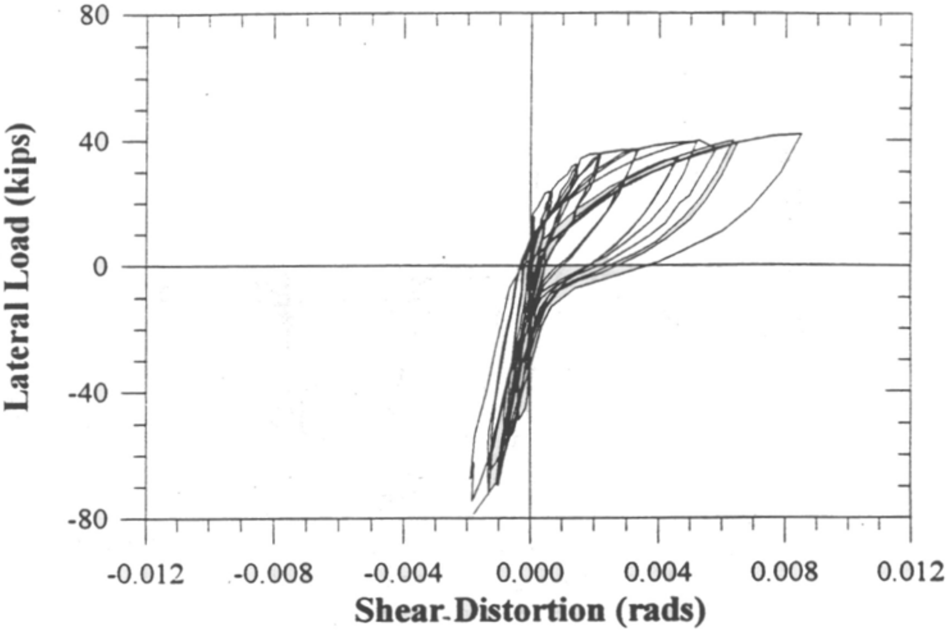

Figure 2-12: TW2 First Floor Shear Distortion [Thomsen & Wallace, 1995]

Thomsen and Wallace compared the predicted force-displacement response of the wall based on the moment-curvature results of the section analysis program BIAX [Wallace and Moehle, 1989] with the response recorded during the experiment. BIAX has different material models that can be used to simulate the behavior of the concrete. Thomsen and Wallace ran two separate analyses of each wall one using a Modified Kent-Park [Park, Priestley and Gill, 1982] concrete model and the other using the Sastcioglu & Razvu [1992] concrete model . Figure 2-8 shows that the BIAX results showed a slightly stiffer response predicted than that was observed in the elastic region; however, the lateral capacity of the wall was well predicted for RW1. Figure 2-9 compares similar results for RW2, and it appears that BIAX predicted the stiffness adequately, but somewhat under predicted the lateral strength of the wall. As shown in Figure 2-10, BIAX over predicted the strength and stiffness of TW1 when the flange was in compression, and greatly underestimated the stiffness for the flange-in-tension direction. The comparison of results for TW2 is shown in Figure 2-11. Similar to TW1, the strength and stiffness of the wall were over predicted for the flange-in-compression direction loading, while the stiffness in the flange-in-tension direction was under predicted. Additionally, the lateral capacity of the wall was significantly under predicted by the analysis, particularly at large displacement levels.

Based on a follow up analytical study, Orakcal and Wallace [2006] presented an improved analysis model for predicting lateral load behavior of reinforced concrete structural walls. Using the data recorded in the experiment, they concluded that shear-flexure interaction had a significant impact on the response of the wall. Consequently, they created a special type of element called the “Multi-Component-in-Parallel Model” (MCPM) to capture the flexure-shear interaction. The MCPM model is similar to the multiple-vertical-line-element models that will be discussed in the next section. The force-displacement response comparison between their analytical model and the experimental response shows an excellent match for RW2 seen in Figure 2-13. However, the data from RW2 was used to calibrate the parameters used in the MCPM model; a prediction of the response for a wall using the MCPM has not been presented.

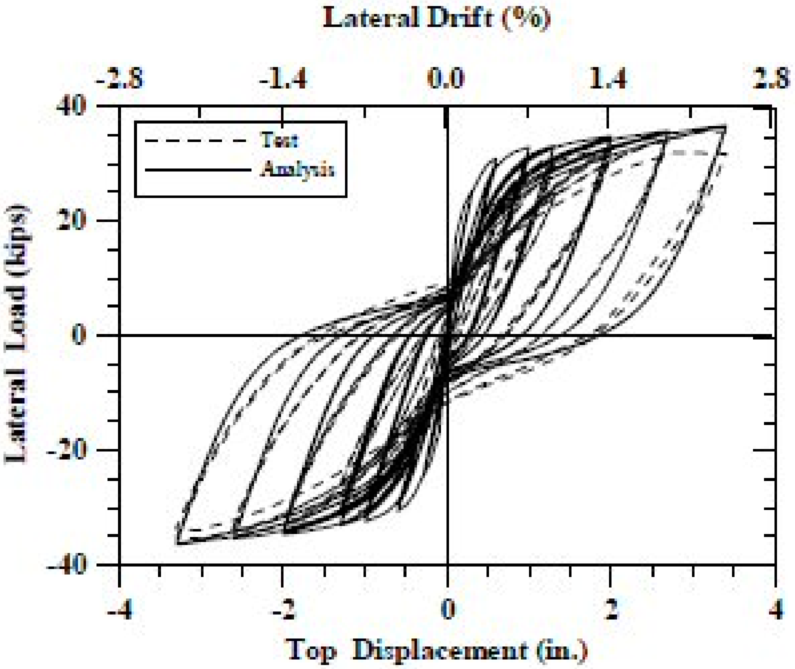

Figure 2-13: Comparison of results from the MCPM model of RW2 with the Measured Response [Orakcal and Wallace, 2006]

2.2 Analytical Studies

This section presents the various analytical approaches presented in literature for modeling the response of structural walls. Any of these techniques can be used for nonrectangular walls. Structural walls have been modeled and analyzed using a number of different approaches by researchers. Rather than making an extensive listing of all the analytical studies done on structural walls, a summary of various modeling approaches used for walls studies are presented, followed by a representative sample of analyses and commentary on the advantages and disadvantages of the different approaches.

2.2.1 Solid (Brick) Elements

The behavior of structural walls have been simulated using solid or brick elements. Solid elements have been used by a number of researchers [Deshmukh et al., 2006; Moaveni et al., 2006] to simulate the structural wall behavior under lateral loads. This modeling approach has the advantage of allowing the strain and corresponding stress to vary across the section without the user having to specify a particular distribution such as that based on the plane section remains plane assumption. Additionally the shear stiffness of the wall is determined for the individual elements. In this approach, the longitudinal and transverse reinforcement can be smeared across the solid element or modeled discretely using truss elements. The 3D nature of the model allows bi-directional lateral loads to be applied to the wall. However, solid elements have some significant disadvantages. These include incorporating an accurate 3D concrete material model that can accurately model the initiation, propagation, and orientation of cracks as they form in concrete elements as wells as the loading and unloading paths. A large number of solid elements may be required to model the concrete and reinforcement of a wall accurately, which may require significant computational time to run the analysis. Including the effects of strain penetration is challenging and typically ignored in the analysis [e.g., Moaveni et al, 2006; Deshmukh, 2006].

Deshmukh et al. [2006] modeled the 7-Story building slice tested at UCSD, which included gravity columns, floor slabs, a rectangular wall bending about its strong axis, and a rectangular wall bending about its weak axis. A complete description of the 7-story building slice is described in Appendix A. Deshmukh et al. modeled the 7-Story building slice in SAP 2000 using brick elements and the concrete material model available in SAP 2000. The steel reinforcement was modeled separately, and linked to the displacement of the nodes of the concrete solid elements through constraint equations. The SAP 2000 model used over 7000 solid elements to simulate the UCSD Building Slice.

2.2.2 Plane stress, Plane Strain, or Shell Elements

Plane stress, plane strain, and shell elements have also been used to simulate the response of structural walls in 2D. Studies conducted by Sittipunt and Wood [1993], Palermo and Vecchio [2004], and Kelly [2006, 2007] are good examples of this modeling approach. This approach has some of the same advantages and disadvantages as the solid element. A reliable 2D concrete model is required for the analysis that should include the effects of cracking and appropriate unloading/reloading rules. In addition to the concrete model, complexity and number of elements, these models are be limited to unidirectional loading only. Similar to solid elements, including the effects of strain penetration is difficult and commonly ignored [e.g. Sittipunt and Wood, 1993].

Kelly [2006] also modeled the 7-Story Building slice discussed in Appendix A. Kelly used nonlinear plane stress elements to model the web wall, flange wall, and post-tensioned column. The effects of strain penetration was modeled using pairs of nonlinear gap-truss elements to model the reinforcement at the base of each wall. The gap truss elements allowed for a large crack to form at the base of the wall, simulating the base rotation due to strain penetration. The model had 686 degrees-of-freedom which is relatively low. The comparison of the calculated and measured displacement profiles is shown in Figure 2-14, which that the model predicted the displacement response envelope for events EQ1 and EQ4. The relatively low number of DOFs make this modeling approach well suited for the analysis of a complete building in a design office.

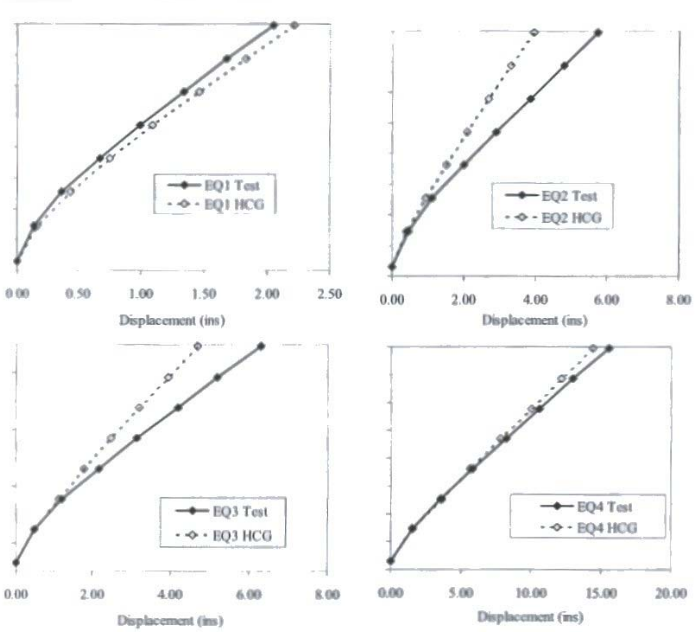

Figure 2-14: Displacement Profile Comparison [Kelly, 2006].

Hachem [2006] also used plane stress elements to model the response of 7-Story building slice. The web wall was modeled using 4-node, 8-degree-of-freedom plane stress elements with a nonlinear concrete material model that simulated both cracking and crushing of concrete. The reinforcement was modeled using truss elements connected to the nodes of plane stress elements. The effects of strain penetration were ignored in building the analytical model. The model consisted of a total of 3143 elements, of which 804 plane stress elements represented the web wall and 2322 truss elements represented the longitudinal reinforcement of the web wall. Figure 2-15 shows the displacement profile analytical and experimental profile for the 7-Story building slice.

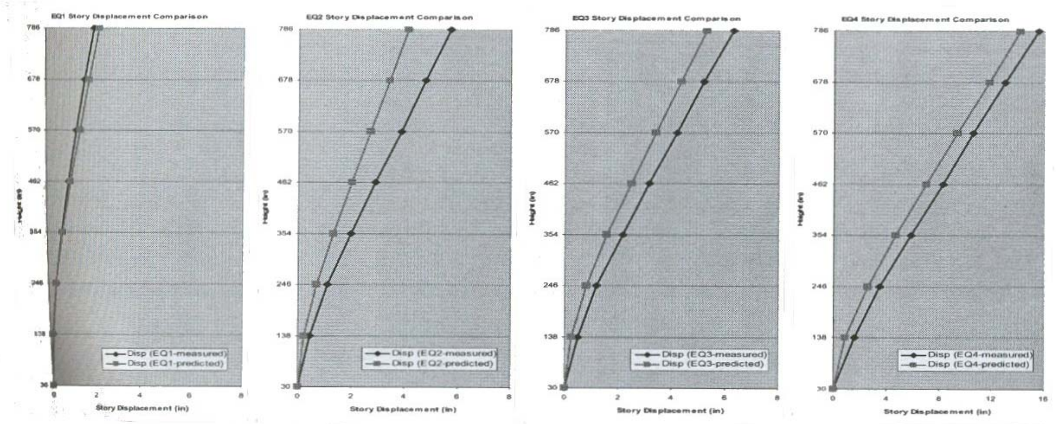

Figure 2-15: Calculated and Measured Displacement Profiles for UCSD Building Slice Analysis [Hachem, 2006].

2.2.3 Macro Model Elements

Macro model elements are a type of element that instead of specifying microscopic behaviors, such as stress-strain relationships, global response parameters are specified directly. Typically, macro models lump various behaviors into one element to simplify the analysis and increase the computational efficiency of the analysis. Macro model elements are used to capture regions of nonlinear behavior, while linear elements are used for regions that will remain elastic during the analysis.

One example of a macro model element is the multiple-vertical-line-element-models (MVLEM) that have been shown to capture the response of structural walls [Fischinger and Isakovic, 2006; Orakcal *et al.*, 2004]. This modeling approach simulates the behavior of rectangular walls using a series of vertical and shear springs connected by rigid beams at the top and bottom of the element. Figure 2-16 shows the MVLEM schematically. The force-displacement characteristics of the springs can be defined to incorporate the various response components of the structural walls.

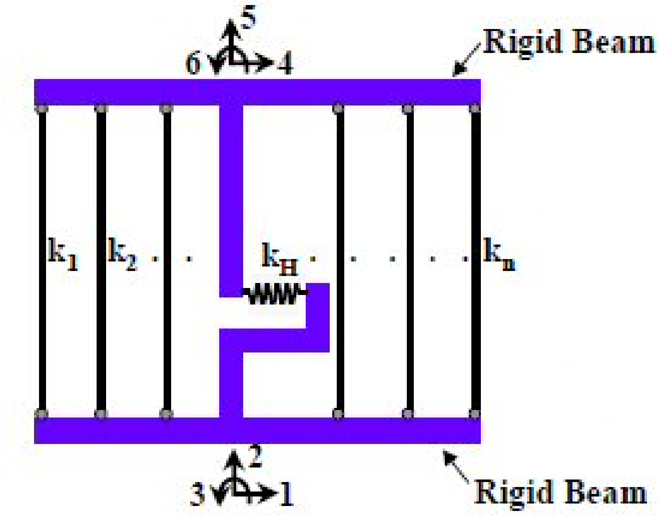

Figure 2-16: Multiple Vertical Line Element Model

A “beam with hinges” is another example of a macro model used to simulate structural walls [Bolander and Wright, 1991]. This model lumps all the nonlinear behavior at the ends through the use of axial and rotational springs. The spring behavior is then defined to give almost any type of response that is desired by the user.

The primary advantage of macro model elements is thatthey are very computationally efficient and provide good simulation of the global wall behavior. However, macro model elements require experience and knowledge to determine the force-displacement relationships for the springs, rather than stress-strain relationships of the material that are more familiar to most engineers. Additionally, strain penetration and other behaviors are lumped together in the spring behavior, potentially leading to inaccurate simulation at the local level.

Fischinger and Isakovic [2006] successfully modeled the UCSD 7-Story Building slice using the MVLEM approach. The web wall was modeled using a stack of MVL elements, of which four of them were used in the first story and one element in all the other stories. Five vertical springs were used to simulate the entire cross section of the wall and the compressive strength of the vertical spring was based on the compressive strength of the confined concrete, neglecting the steel reinforcement in compression. Empirically verified values were used to define the hysteretic relations in the vertical springs. The shear behavior was assumed to remain elastic. Figure 2-17 shows the predicted and measured maximum displacement profiles.

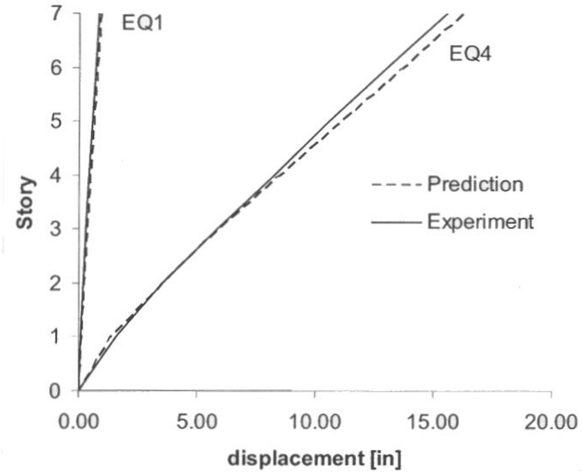

Figure 2-17: Predicted and Experimental Displacement Profiles

2.2.4 Beam-Column Elements

Beam-column elements with fiber sections have been used to simulate response of structural walls [e.g. Martinelli and Filippou, 2006; Grange et al., 2006; Dazio, 2006]. These models allow the user to specify uniaxial stress-strain behavior of longitudinal reinforcement as well as that of confined and unconfined concrete including the effects in the transverse direction. A large variety of models are available that can be used to characterize the behavior of different materials in order to capture the section and member responses accurately. Since the model is based on the uniaxial stress-strain behavior of groups of fibers, the models are easier to build and understand. The disadvantage of fiber beam-column elements is that the strain distribution at the section level is typically predefined. Additionally, some fiber based elements require the shear deformation to be handled separately. In this case, the beam-column element only considers the axial and bending deformations on the element, and no shear stiffness is included in the element stiffness. In order to include the effects of shear deformation, a separate material model must be used to define the global shear force-deformation relationship for the beam column element. The shear material model can be placed in parallel to the beam-column, thus including the shear stiffness in the global structural stiffness matrix.

2.3 Shear Lag Behavior

The Bernoulli-Euler assumption that plane sections before bending remain plane after bending is often used for the analysis of beams. This assumption states that the longitudinal strain is constant at all points in a flange section of a member located at the same distance from the neutral axis. However, this approximation fails to include the appropriate effects of shear flow on the section. The shear flow causes shear distortion in the flange causing the longitudinal strains at regions away from the flange-web junction to lag behind the strains at the flange-web junction [Kwan, 1996]. An example of shear lag effects is shown in Figure 2-18 which depicts the longitudinal bending stress distribution on a closed rectangular tube with and without shear lag. As shown, higher strains are observed at the flange-web junction than in the center of the flange. In a T-wall the strains would decrease along the flange towards the tips.

The effects of shear lag are due to distortion of the flange due to the shear flow in the cross-section. Thus increasing the shear stiffness of the flange will decrease the effects of shear lag; conversely, decreasing the shear stiffness of the flange will increase the shear lag effects. The shear stiffness of the flange is dependent on the length and thickness of the flange, a short, thick flange will have a much higher shear stiffness than a wide, thin flange. The distribution of both the longitudinal and transverse steel will affect the shear stiffness, well distributed longitudinal steel is better in shear than steel concentrated in the ends. The transverse reinforcement is generally designed as shear reinforcement, and a closer spacing of the transverse reinforcement increases the shear stiffness of the flange. Height of the wall will influence the shear stiffness, with shorter walls have a higher shear stiffness.

The shear lag reduces the effective width of the flange by changing the strain along the length of the flange and therefore stress distribution across the flange. The problems of shear lag has been studied by a number of researchers [Song and Scordelis, 1984a,b; Kwan, 1996; Haji-Kazemi and Company, 2002; Foutch and Chang, 1982]. However, most of the investigations have focused on “closed” section such as box girders [Foutch and Chang, 1982; Evans and Taherian, 1977, Chang, 2004] or tubular structures [Kwan, 1996; Haji-Kazemi and Company, 2002]. The studies have historically focused on the shear lag effect in bridge girders connected with concrete decks, rather than in structural walls.

Kwan [1996] examined shear lag in structural core walls and reviewed a number of techniques that are available to analyze the shear lag behavior. Kwan grouped the analytical methods into the following categories: 1) folded plate methods; 2) harmonic analysis methods; 3) finite stringer methods; 4) finite element methods; and 5) semiemperical methods.

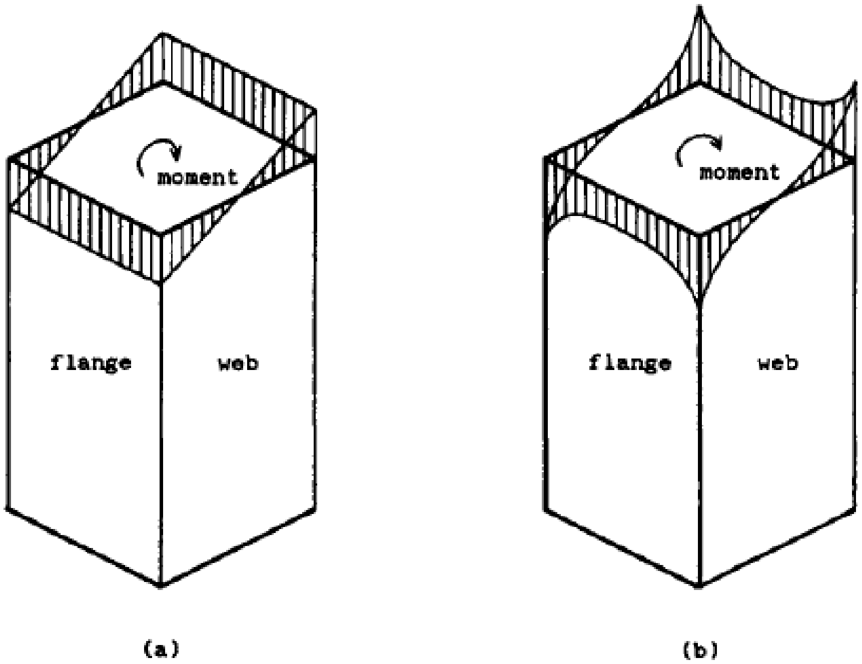

Figure 2-18: Longitudinal Stress Distribution a) without shear lag and b) with shear lag [Kwan, 1996].

The folded plate methods [Defries-Skene and Scordelis, 1964] treats the structure as a series of plates joined along their longitudinal edges. A Fourier series harmonic functions are used to express the forces and displacements along the joints. Each plate is analyzed considering bending and membrane forces. The joint displacements can then be placed in a stiffness matrix and the external loads are then represented as a Fourier series. The final results can then be expressed by summing the partial results from each term in the Fourier expansion.

Harmonic analysis methods [Song and Scordelis, 1984a,b] represents the externally applied load using a Fourier harmonic expansion. However, the analysis is simplified by disregarding any out-of-plane bending of the flange plates. In the model, the web plates are simplified by assuming bending only, thus allowing the analysis of the flange alone. The analysis of the flange is then carried out in a manner similar to the folded plate analysis. This analysis determines a stress function; however, strain is not a function of stress, i.e. More than one strain can correspond to a given stress. This makes this method of analysis in appropriate for concrete if post peak behavior is considered.

The finite stringer method also assumes that only bending occurs in the web plates; however, the flange is simplified as a series of stringers connected by plates. The plates carry only shear forces, while the stringers carry the axial forces. Separating the axial and shearing forces in the flange simplifies the governing equations and makes them simpler to solve. This methodology is only appropriate for linear behavior for converting the strains to stresses to determine the stress distribution.

Finite element has been used to investigate the effects of shear lag. Moffatt and Dowling [1975] carried out an extensive parametric study of shear lag in bridge decks. The web was modeled considering bending only, and the bridge deck was modeled using one layer of solid elements. However, fine meshes were required for the deck panels. The finite element results were used to create a set of design values to estimate the effect of shear lag in bridge decks. Finite element analysis could be used to investigate the shear lag phenomenon for concrete structural walls in the nonlinear range. It would be dependent on the accuracy of the concrete material model. The analysis would need to be conducted using either solid, shell, or plane stress/strain elements. A fine mesh would need to be used in order to capture the variation across the flange. Moffatt and Dowling [1975] noted that a fine mesh was needed over the length and width of the flange, particularly near supports or point loads.

Additionally, various researchers [Coull and Bose, 1975; Coull and Abu El Magd, 1980] have used semiempirical methods based on energy formulation to determine the effects of shear lag. These methods use simplifying assumptions about the longitudinal stress distribution in the web and the flange. Solutions are then reached by minimizing the strain energy or the total potential energy. While these methods are easier to use, they are not as accurate as the other more rigorous methods. Energy methods are more difficult for nonlinear systems, and the inaccuracy of the approach is undesirable.

As previously stated, most of these studies have focused on box or tubular sections; only two of these studies conducted by Song and Scordelis [1984a,b] and Coull and Abu El Magd [1980] examined T-shaped sections. While these two studies present equations for the stress distribution in T-walls, the equations are not useful in the current investigation. In both studies, the equations were developed in terms of the longitudinal stress assuming elastic behavior of the T-beam; a Twall is essentially a cantileverd T-beam. However, this investigation focuses on T-wall behavior in both the elastic and inelastic ranges. The equations developed by Song and Scordelis, and Coull and Abu El Magd, are complex and cannot be easily implemented in a framework like OpenSees. The equations are dependent on the location of the section of interest and the particular loading applied to the beam or wall. In OpenSees, shear lag would have to be handled at the section level because it is the section level that knows the particular details of the cross section and the location and type of each fiber; however, a section does not know its location in the global system, nor the particular external loading applied to it. In addition to the difficulty with implemention due to the constraints of a section in the OpenSees framework, the proposed shear lag equations would cause a significant increase in the computational time required for an analysis.

Chapter 3: Concrete Model

Analysis of walls tested by Thomsen and Wallace [1993] showed that the concrete model was limiting the accuracy of the simulation of the wall behavior, particularly the unloading and reloading behavior, as well as the residual displacements. The cross-section of the second of two rectangular walls tested by Thomsen and Wallace, referred to as RW2, is shown in Figure 3-1. RW2 was 144 in. tall, 48 in. long, and 4 in. thick. This wall was first modeled in OpenSees using beam-column elements with fiber sections. The confined and unconfined concreter fibers were modeled using the Kent and Park concrete model available in OpenSees [Mazzoni *et al.*, 2006]. Figure 3-2 shows the simple unloading and reloading rules for the hysteretic behavior of the concrete model. The confined concrete behavior was based on the model proposed by Mander et al. [1988] and the unconfined concrete properties were as recorded by Thomsen and Wallace. Figure 3-2 shows the force-displacement response of RW2 observed by Thomsen and Wallace and the response given by the OpenSees analysis.

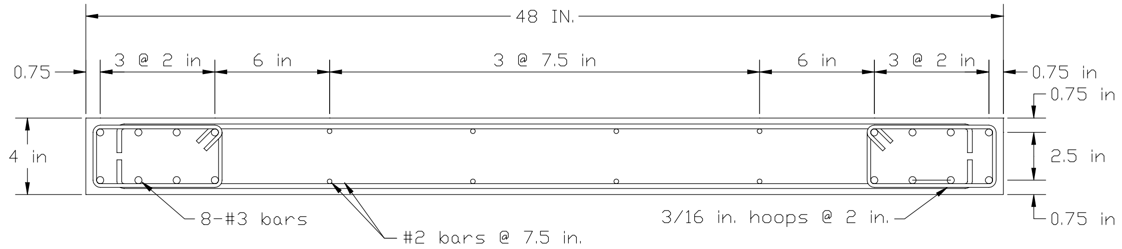

Figure 3-1: Cross-section Details of Thomsen and Wallace's Specimen RW2.

The reloading stiffness is not well captured by the analysis; particularly near zero displacement. Also, the OpenSees results show a significant change in stiffness and a kink in the response near zero displacement. This kink is due to how the concrete model handles crack closure. The Kent-Park concrete model does not allow compression stress to develop until after the tension strain is completely removed as shown in Figure 3-2. This is unrealilistic due to the presence of crushed concrete in open cracks. Additionally, the residual displacement is significantly underestimated by the analysis. Improving the concrete model will help address these issues.

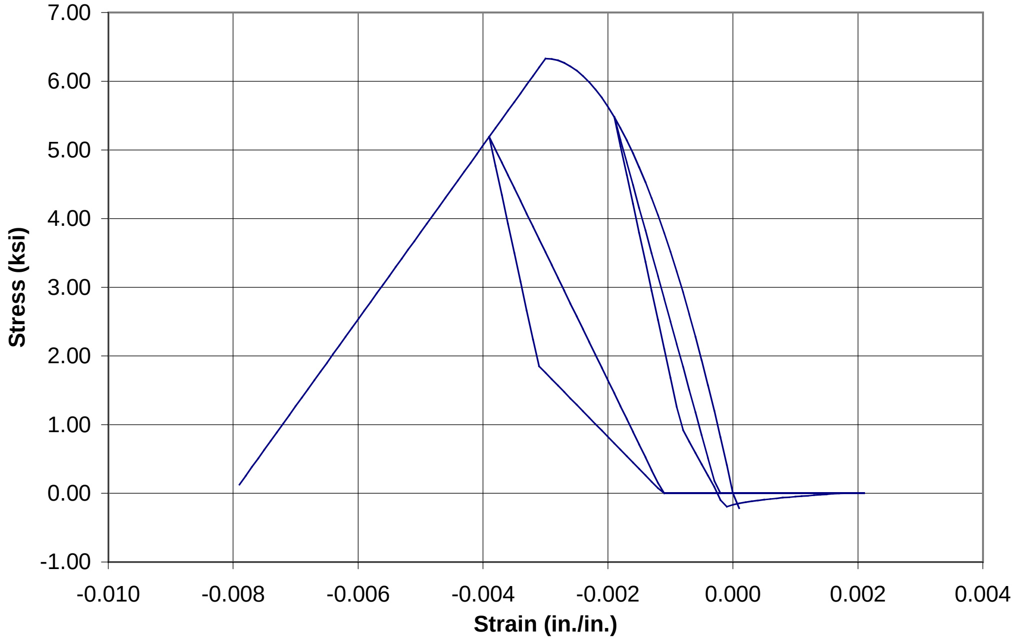

Figure 3-2: Response OpenSees Concrete03 Based on Kent and Park Model

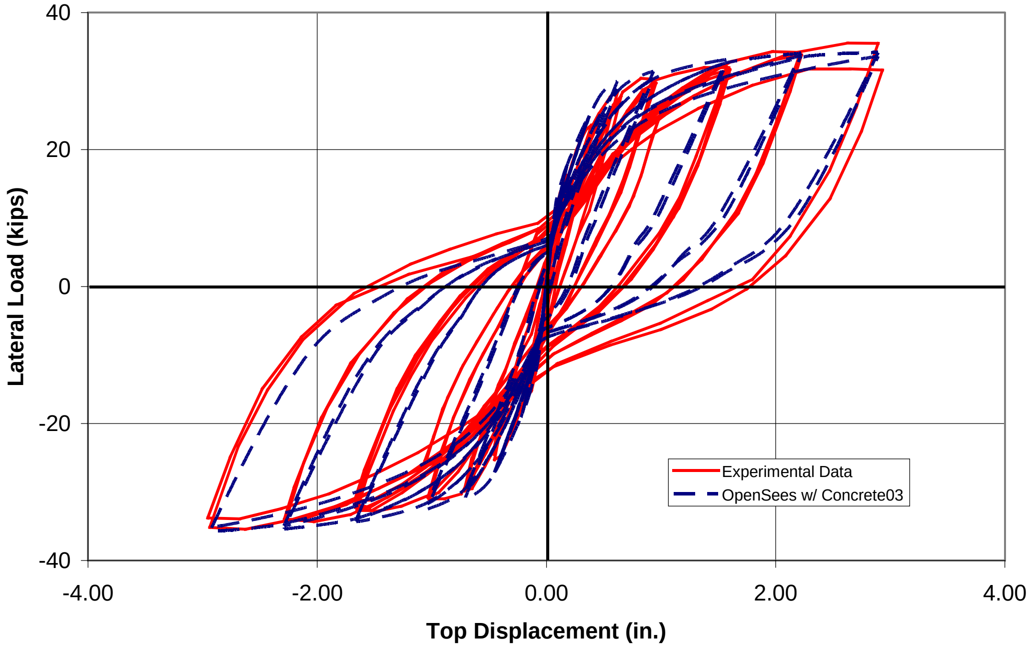

Figure 3-3: Force-Displacement Response of RW2

To overcome the aforementioned challenges, the concrete model proposed by Chang and Mander [1994] was selected for implementation in OpenSees for a number of reasons. First, this model assumes that wedging action occurs in the cracks causing compression stress to develop prior to crack closure. Second, the model has different behavior depending on when the strain reversal occurs, providing a more robust hysteretic behavior. Third, the confined concrete model proposed by Mander et al. [1988] has become widely used to determine the confined concrete properties, and the Chang and Mander model extends the 1988 model to include the behavior of unconfined and high strength concrete. Fourth, Chang and Mander used a large number of cyclic concrete tests to validate the model behavior.

The implementation of the Chang and Mander [1994] concrete model is presented in the chapter. First the original model as described by Chang and Mander is presented; next, the challenges associated with the original model and steps taken to overcome these challenges are presented. Then, a simplified version of the Chang and Mander model is introduced. Finally, the improvement of the simulation of RW2 due to the use of new concrete model is then shown.

3.1 Model Description:

Chang and Mander [1994] proposed a hysteretic material model for the simulation of cyclic behavior of both confined and unconfined concrete. The proposed model was an advanced rule-based model in comparison to other concrete models and the ability to simulate the hysteretic behavior of both ordinary (<6 ksi) and high strength (6-12 ksi) concrete in both cyclic compression and tension. The model incorporates the degradation that occurs due to incomplete unloading cycles in addition to that due to completed unloading cycles. A complete cycle is unloading from the monotonic envelope in one direction to the envelope in the other direction. The effects of both partial and complete reloading to the monotonic envelope is also incorporated. The model pays particular attention to effects of opening and closing of cracks. Chang and Mander noted that most models assumed sudden crack closure with a rapid change in the section modulus, but this assumption is not supported by experimental results obtained on lightly loaded columns.

The general shape of the concrete stress-strain curve of their model is shown in Figure 3-4 and has certain characteristics: (1) the initial slope of the curve at the origin is the elastic modulus (E_c), (2) it reaches a maximum value at the peak stress and corresponding strain (ε_c, f'_c), and (3) it has both an ascending and descending branch. Controlling the slope of the ascending and descending branches of the model is important because they are different for confined and unconfined concrete. For unconfined concrete, the slope of the ascending and descending curves becomes steeper. In confined concrete, the slope of the descending branch is dependent on both the level of confinement and strength of the concrete. Chang and Mander investigated a number of different curves to use for describing the envelope response, and selected Tsai's (1988) equation. The equation has the following form:

$$x=\frac{\varepsilon_c}{\varepsilon'_c} \tag{3.1}$$

$$y=\frac{f_c}{f'_c} \tag{3.2}$$

$$y=\frac{nx}{1+\left(n-\frac{r}{r-1}\right)x+\frac{x^r}{r-1}} \tag{3.3}$$

where x, y, n, and r are parameters to control the shape of the curve.

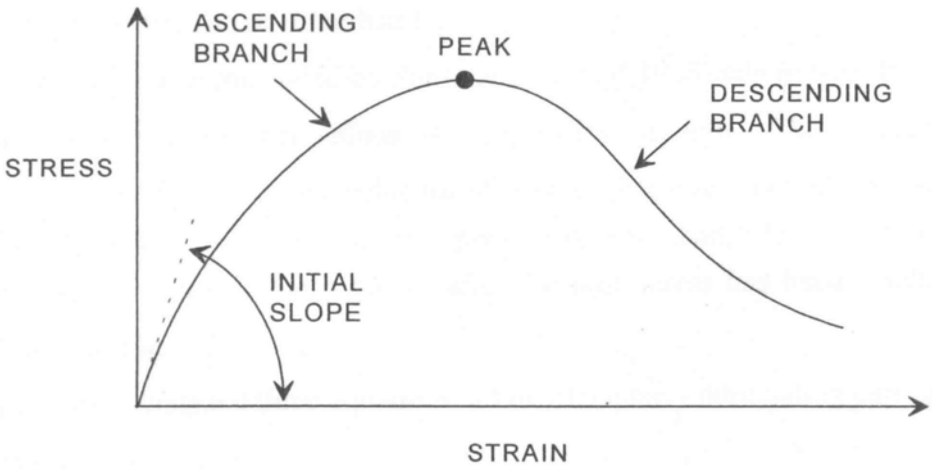

Figure 3-4: General Characteristics of a Concrete Material Model

3.2 Recommended Stress-Strain Parameters

3.2.1 Unconfined Concrete Behavior

Chang and Mander proposed suitable values to be used in Tsai's equation to represent the stress-strain response of concrete. They proposed the following equations for determining the modulus of elasticity for both normal and high strength concrete:

$$E_c = 185{,}000\,(f'_c)^{3/8}\ psi \quad \text{or} \tag{3.4a}$$

$$E_c = 8{,}200\,(f'_c)^{3/8}\ MPa \tag{3.4b}$$

The strain at which the peak compression stress occurs for both ordinary and high strength concrete can be obtained using the following equations:

$$\varepsilon'_c = \frac{(f'_c)^{1/4}}{4{,}000}\ psi \quad \text{or} \tag{3.5a}$$

$$\varepsilon'_c = \frac{(f'_c)^{1/4}}{28}\ MPa \tag{3.5b}$$

To control the descending branch, Tsai's equation uses parameter *r*; the value of this parameter is determined by the following formulas:

$$r = \frac{f'_c}{750} - 1.9\,psi \quad \text{or} \tag{3.6a}$$

$$r = \frac{f'_c}{5.2} - 1.9\,MPa \tag{3.6b}$$

$$f_{l2} \geq f_{l1}$$

The other parameter, *n,* that controls the ascending branch of the curve is defined as:

$$n = \frac{E_c \varepsilon'_c}{f'_c} \tag{3.7}$$

which, if Eqs. 3.1 and 3.2 for E_c and ε'_c are substituted in and simplified, reduces to:

$$n = \frac{46}{(fi_c)^{3/8}}\,psi \quad \text{or} \tag{3.8a}$$

$$n = \frac{7.2}{(f'_c)^{3/8}}\,MPa \tag{3.8b}$$

3.2.2 Confined Concrete Behavior

When axial load is applied to concrete, the section will attempt to dilate in the transverse direction due to thePoisson's effect. Restraining this dilation leads to an increase in strength, peak strain, and ductility of the concrete section. Chang and Mander proposed the following equation to calculate the increase in peak strength of the concrete.

$$f'_{cc} = f'_{c0} * (1 + k_1 * x') \tag{3.9}$$

where,

f'_{cc} = peak concrete strength of confined concrete

f'_{c0} = unconfined peak concrete strength

$$k_1 = A * \left(0.1 + \frac{0.9}{1 + B * x'}\right) \tag{3.10}$$

$$x' = \frac{f_{l1} + f_{l2}}{2\mathrm{f}'_{c0}} \tag{3.11}$$

$$A = 6.886 - (0.6069 + 17.275\text{r})\, e^{-4.989\gamma} \tag{3.12}$$

$$B = \frac{4.5}{\frac{5}{A}(0.9849 - 0.6306\, e^{-3.8939\gamma}) - 0.01} \tag{3.13}$$

where A and B are factors that determine the increased strength from lateral confinement.

$$\gamma = \frac{f_{l1}}{f_{l2}} \tag{3.14}$$

$$\varepsilon_{cc} = \varepsilon_{c0}(1 + k_2 * x') \tag{3.15}$$

$k_2 = 5\text{k}_1$ Normal strength transverse reinforcement ($F_y \leq 60$ ksi)

$k_2 = 3\text{k}_1$ High strength transverse reinforcement ($F_y > 60$ ksi)

$$E_c = 185{,}000 * (f_c^{'})^{\frac{3}{8}} \tag{3.16}$$

The model description by Chang and Mander does not give directions on determining the decending branch parameter for confined concrete. However, the confined concrete model proposed by Mander *et al.* (1988) uses Popovics' (1973) equation for the shape of the concrete stress-strain diagram. Popovics' equation can be shown to be a constrained version of Tsai's equation [Chang and Mander, 1994]. Using the relationship between Popovics' and Tsai's equations and the concrete model of Mander *et al.* [1988], the descending branch parameter, *r*, of the confined concrete model was determined according to the following:

$$n = \frac{E_c * \varepsilon_{cc}}{f_{cc}^{'}} \tag{3.17}$$

$$r = \frac{n}{n-1} \tag{3.18}$$

3.3 Cyclic Behavior of Confined and Unconfined Concrete

3.3.1 Compression Envelope Curves

The compression envelope shown in Figure 3-5 is defined by the initial slope (E_c), the coordinate of the peak stress (ε'_{cc}, f'_{cc}), Tsai's equation parameters (r and n), and a nondimensional critical strain (x^-_{cr}) to define the spalling strain of the concrete.

Chang and Mander used Tsai's equation in for both the tension and compression envelope curves and can be written in nondimensional form by using the following equations:

$$y(x)=\frac{n\,x}{D(x)} \tag{3.19}$$

$$z(x)=\frac{(1-x^r)}{[D(x)]^2} \tag{3.20}$$

where,

$$D(x)=1+\left(n-\frac{r}{r-1}\right)x+\frac{x^r}{r-1} \text{ when r}\neq 1 \tag{3.21}$$

$$D(x)=1+(n-1+\ln x)x \text{ when r=1} \tag{3.22}$$

Let n and x be defined as:

$$n^-=\frac{E_c\varepsilon'_{cc}}{f'_{cc}} \tag{3.23}$$

The spalling nondimensional strain can be calculated using:

$$x_{sp}=x^-_{cr}-\frac{y(x^-_{cr})}{n^- z(x^-_{cr})} \tag{3.24}$$

Where n^- is the n value for the compressions curve, f'_{cc} is the peak compressive strength of the concrete, E_c is the initial Young's Modulus for concrete, ε'_{cc} is the strain at peak stress, x^-_{cr} is the nondimensional critical strain in compression used to determine the tangent line up to spalling strain, x^-_{sp} is the nondimensional spalling strain, ε_c is the concrete strain, $y(x)$ is the nondimensional stress function, and $z(x)$ is the nondimensional tangent modulus function. The stress and tangent Young's Modulus at any strain on the envelope is then given by:

a) For $x^- < x^-_{cr}$ (Tsai's equation) **(Rule 1)**

$$f_c^- = f'_{cc}\, y(x^-) \tag{3.25}$$

$$E_t^- = E_c\, z(x_{cr}^-) \tag{3.26}$$

b) For $x^-_{cr} < x^- < x^-_{cr}$ (Straight Line) **(Rule 1)**

$$f_c^- = f'_{cc}\left[y(x_{cr}^-) + n^- z(x_{cr}^-)(x^- - x_{cr}^-) \right] \tag{3.27}$$

$$E_t^- = E_c\, z(x_{cr}^-) \tag{3.28}$$

c) For $x^- > x^-_{sp}$ (Spalled) **(Rule 5)**

$$f_c^- = E_t^- = 0 \tag{3.29}$$

Where E^-_t is the tangent modulus and f'_{cc} is the concrete stress. After the concrete has spalled, it has zero stress and stiffness from that moment onwards. For confined concrete, a large value of x^-_{cr} should be chosen since confined concrete does not spall. The minus signs in Eqs. 3.20-3.26 refer to the compression side of the stress-strain behavior.

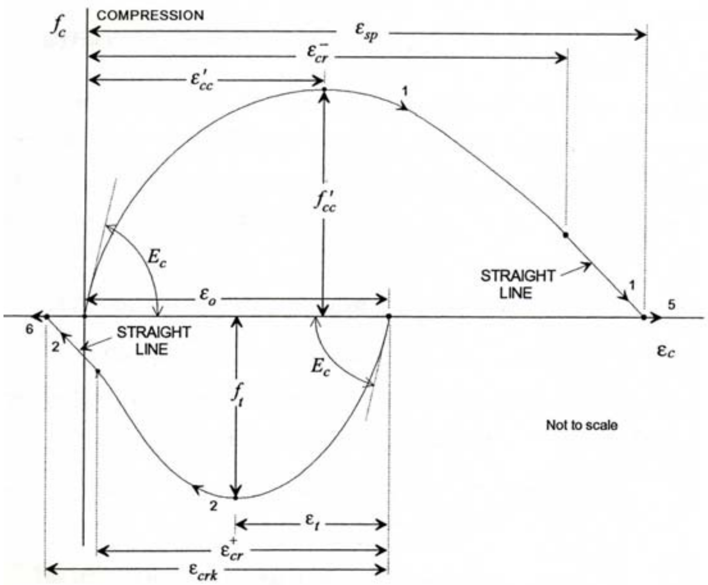

Figure 3-5: Compression and Tension Envelope Curves from Chang and Mander [1994]. (Numerals shown on the figure identify the rule number)

3.3.2 Tension Envelope Curves

Chang and Mander uses the same shape for the tension side of the envelope as for the compression side. Chang and Mander shifts the origin of the tension side by a parameter ε_0; however, this was left out of the implementation in OpenSees because the reason for the shift was not explained. Consequently, the nondimensional parameters are as follows:

$$x^{+}=\left|\frac{\varepsilon_c-\varepsilon_0}{\varepsilon_t}\right| \tag{3.30}$$

$$n^{+}=\frac{E_c\varepsilon_t}{f_t} \tag{3.31}$$

The cracking nondimensional strain is calculated from the positive critical nondimensional strain by:

$$x_{sp}=x_{cr}^{+}-\frac{y(x_{cr}^{+})}{n^{+}z(x_{cr}^{+})} \tag{3.32}$$

The stress and tangent modulus for any strain on the tension envelope are given by:

a) For $x^{+} < x^{+}_{cr}$ (Tsai's equation) **(Rule 2)**

$$f_c^{+}=f_t\,y(x^{+}) \tag{3.33}$$

$$E_t^{-}=E_c\,z(x^{+}) \tag{3.34}$$

b) For $x^{+}_{cr} < x^{+} < x^{+}_{cr}$ (Straight Line) **(Rule 2)**

$$f_c^{+}=f_t[y(x_{cr}^{+})+n^{+}z(x_{cr}^{+})(x^{+}-x_{cr}^{+})] \tag{3.35}$$

$$E_t^{+}=E_c\,z(x_{cr}^{+}) \tag{3.36}$$

c) For $x^{-} > x^{-}_{sp}$ (Spalled) **(Rule 6)**

$$f_c^{+}=E_t^{+}=0 \tag{3.37}$$

Where *y* and *z* are the same as defined previously for the compression envelope. Once the concrete has cracked it is assumed to have zero tension carrying capacity due to the crack opening. However, gradual crack closure is considered to occur by allowing compression stress to develop immediately upon strain reversal. The gradual crack closure behavior will be discussed later in Section 3.3.4

3.3.3 Pre-Cracking Unloading and Reloading Curves

The basic elements of the unloading and reloading curves are addressed in this section. Every rule has a smooth curve that starts at a starting point with an initial slope and ends at a second point with a final slope. The curve for the transition in terms of the stresses and strains is as follows:

$$f_c = f_I + (\varepsilon_c - \varepsilon_I)\left[E_I + A\left|(\varepsilon_c - \varepsilon_I)^R\right|\right] \tag{3.38}$$

$$E_t = E_I + A(R+1)\left|\varepsilon_c - \varepsilon_I\right|^R \tag{3.39}$$

$$R = \frac{E_F - E_{SEC}}{E_{SEC} - E_I} \tag{3.40}$$

$$A = \frac{E_{SEC} - E_I}{\left|\varepsilon_F - \varepsilon_I\right|^R} \tag{3.41}$$

$$E_{SEC} = \frac{f_F - f_I}{\varepsilon_F - \varepsilon_I} \tag{3.42}$$

Where *I* is the initial value, *F* is the final value, E_{SEC} is the secant modulus of elasticity, and *R* and *A* are equation parameters.

In order to define the cyclic properties of concrete, a number of statistical regressions were carried out on the tests conducted by Sinha, Gerstle and Tulin [1964], Karsan and Jirsa [1969], Spooner and Dougill [1975], Okamoto [1976], and Tanigawa [1979]. The model parameters obtained by Chang and Mander are shown in Figure 3-6, and the results of the regression analysis are as follows:

$$E^{-}_{SEC} = E_c\left(\frac{\left|\dfrac{f^{-}_{un}}{E_c\,\varepsilon'_{cc}}\right| + 0.57}{\left|\dfrac{\varepsilon^{-}_{un}}{\varepsilon'_{cc}}\right| + 0.57}\right) \tag{3.43}$$

$$E^{-}_{pl} = 0.1\,E_c\,e^{-2\left|\frac{\varepsilon^{-}_{un}}{\varepsilon'_{cc}}\right|} \tag{3.44}$$

$$\Delta f^{-} = 0.09 f^{-}_{un} \sqrt{\left|\frac{\varepsilon^{-}_{un}}{\varepsilon'_{cc}}\right|} \tag{3.45}$$

$$\Delta\varepsilon^{-} = \frac{\varepsilon^{-}_{un}}{1.15 + 2.75\left|\frac{\varepsilon^{-}_{un}}{\varepsilon'_{cc}}\right|} \tag{3.46}$$

The derived variables are:

$$\varepsilon^{-}_{pl} = \varepsilon^{-}_{un} - \frac{f^{-}_{un}}{E^{-}_{SEC}} \tag{3.47}$$

$$f^{-}_{new} = f^{-}_{un} - \Delta f^{-} \tag{3.48}$$

$$E^{-}_{new} = \frac{f^{-}_{new}}{\varepsilon^{-}_{un} - \varepsilon^{-}_{pl}} \tag{3.49}$$

$$\varepsilon^{-}_{\mathrm{re}} = \varepsilon^{-}_{un} + \Delta\varepsilon^{-} \tag{3.50}$$

$$f^{-}_{\mathrm{re}} = f^{-}\left(\left|\frac{\varepsilon^{-}_{\mathrm{re}}}{\varepsilon'_{cc}}\right|\right) \tag{3.51}$$

$$E^{-}_{\mathrm{re}} = E^{-}\left(\left|\frac{\varepsilon^{-}_{\mathrm{re}}}{\varepsilon'_{cc}}\right|\right) \tag{3.52}$$

For cyclic behavior in tension, the statistical regression showed that slightly different values should be used for the parameters. Hence, the parameters for the hysteretic response of concrete in tension are given by:

$$E^{+}_{SEC} = E_c\left(\frac{\left|\frac{f^{+}_{un}}{E_c\,\varepsilon_t}\right| + 0.67}{\left|\frac{\varepsilon^{+}_{un} - \varepsilon_0}{\varepsilon_t}\right| + 0.67}\right) \tag{3.53}$$

$$E^{-}_{pl} = \frac{E_c}{\left|\frac{\varepsilon^{-}_{un} - \varepsilon_0}{\varepsilon_t}\right|^{1.1} + 1} \tag{3.54}$$

$$\Delta f^{-} = 0.15 f^{+}_{un} \tag{3.55}$$

$$\Delta\varepsilon^{-} = 0.22\varepsilon_{un}^{+} \tag{3.56}$$

Similarly:

$$\varepsilon_{pl}^{+} = \varepsilon_{un}^{+} - \frac{f_{un}^{+}}{E_{SEC}^{+}} \tag{3.57}$$

$$f_{new}^{+} = f_{un}^{+} - \Delta f^{+} \tag{3.58}$$

$$E_{new}^{+} = \frac{f_{new}^{+}}{\varepsilon_{un}^{+} - \varepsilon_{pl}^{+}} \tag{3.59}$$

$$\varepsilon_{\mathrm{re}}^{+} = \varepsilon_{un}^{+} + \Delta\varepsilon^{+} \tag{3.60}$$

$$f_{\mathrm{re}}^{+} = f^{+}\left(\left|\frac{\varepsilon_{\mathrm{re}}^{+}}{\varepsilon_{t}}\right|\right) \tag{3.61}$$

$$E_{\mathrm{re}}^{+} = E^{+}\left(\left|\frac{\varepsilon_{\mathrm{re}}^{+}}{\varepsilon_{t}}\right|\right) \tag{3.62}$$

Where ε_{un} is the unloading strain from the envelope curve, f_{un} is the unloading stress, ε_{pl} is the plastic strain, E_{pl} is the tangent modulus at the plastic strain, f_{new} is the new stress at the unloading strain, E_{new} is the tangent modulus at the unloading strain, and ε_{re}, f_{re}, and E_{re} are respectively the strain, stress, and tangent modulus at the point where the envelope response is rejoined.

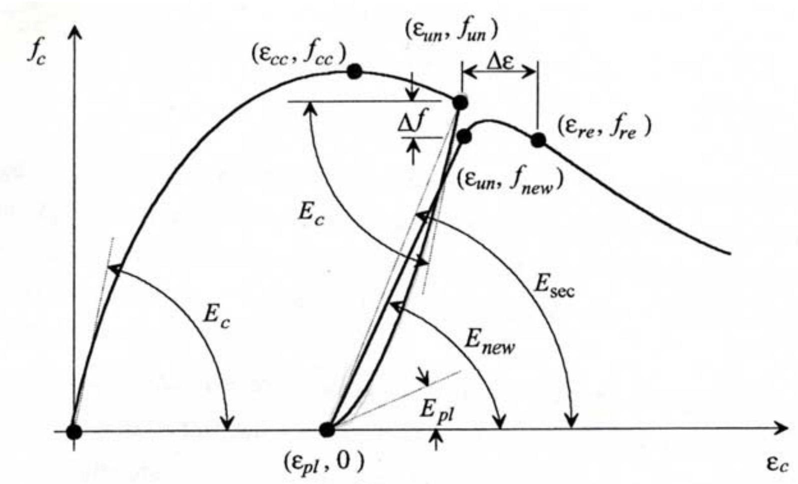

Figure 3-6: Cyclic Properties for Concrete in Compression as per Chang and Mander [1994].

The rules and parameters for the connecting curves for the reversal from compression envelope curve shown in Figure 3-7 are defined as:

$$\begin{aligned} \varepsilon_I &= \varepsilon_{un}^- \\ f_I &= f_{un}^- \\ E_I &= E_c \\ \varepsilon_F &= \varepsilon_{pl}^- \\ f_F &= 0 \\ E_F &= E_{pl}^- \end{aligned} \qquad \textbf{Rule 3} \qquad (3.63)$$

$$\begin{aligned} \varepsilon_I &= \varepsilon_{pl}^- \\ f_I &= 0 \\ E_I &= E_{pl}^- \\ \varepsilon_F &= \varepsilon_{un}^+ \\ f_F &= f_{new}^+ \\ E_F &= E_{new}^+ \end{aligned} \qquad \textbf{Rule 9} \qquad (3.64)$$

$$\begin{aligned} E_I &= E_{new}^+ \\ \varepsilon_F &= \varepsilon_{\mathrm{re}}^+ \\ f_F &= f_{\mathrm{re}}^+ \\ \varepsilon_I &= \varepsilon_{un}^+ \\ f_I &= f_{new}^+ \\ E_F &= E_{\mathrm{re}}^+ \end{aligned} \qquad \textbf{Rule 8} \qquad (3.65)$$

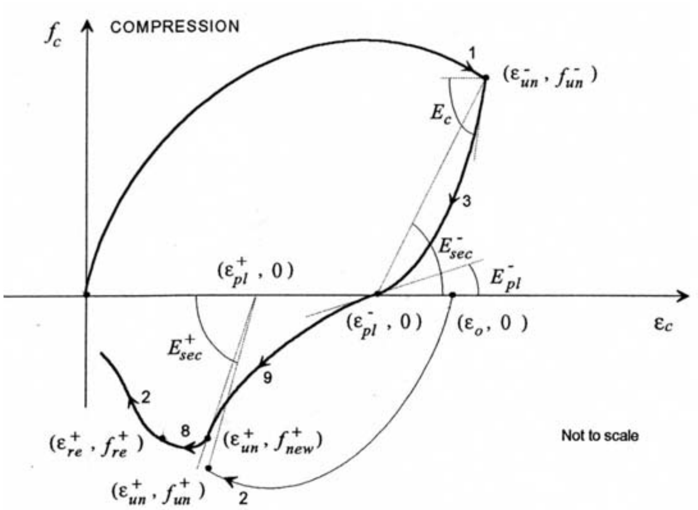

Figure 3-7: Complete Unloading Branch from the Compression Envelope per Chang and Mander [1994]. (Numerals shown on the figure identify the rule number)

Similarly, a reversal from the tension envelope curve, shown in Figure 3-8, is defined by:

$$\begin{aligned}\varepsilon_I &= \varepsilon_{un}^{+}\\ f_I &= f_{un}^{+}\\ E_I &= E_c\\ \varepsilon_F &= \varepsilon_{pl}^{=}\\ f_F &= 0\\ E_F &= E_{pl}^{+}\end{aligned} \qquad \textbf{Rule 4} \qquad (3.66)$$

$$\begin{aligned}\varepsilon_I &= \varepsilon_{pl}^{+}\\ f_I &= 0\\ E_I &= E_{pl}^{+}\\ \varepsilon_F &= \varepsilon_{un}^{-}\\ f_F &= f_{new}^{-}\\ E_F &= E_{new}^{-}\end{aligned} \qquad \textbf{Rule 10} \qquad (3.67)$$

$$\begin{aligned} \varepsilon_I &= \varepsilon^-_{un} \\ f_I &= f^-_{new} \\ E_I &= E^-_{new} \\ \varepsilon_F &= \varepsilon^-_{\mathrm{re}} \\ f_F &= f^-_{\mathrm{re}} \\ E_F &= E^-_{\mathrm{re}} \end{aligned} \qquad \textbf{Rule 7} \tag{3.68}$$

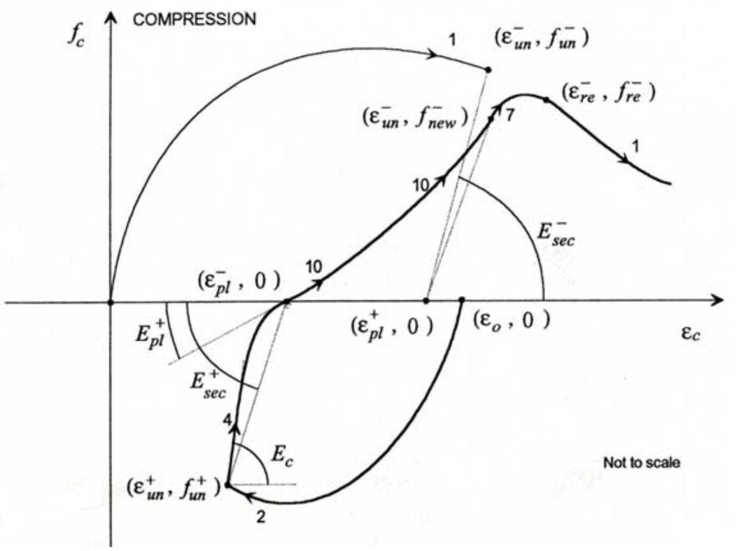

Figure 3-8: Complete Loading Branch Reversed from Tension Envelope per Change and Mander [1994]. (Numerals shown on the figure identify the rule number)

3.3.4 Post-Cracking Unloading and Reloading Curves

After cracking of the concrete is considered to have occurred, the tension capacity is assumed to be zero. Therefore, the tension side of the hysteresis behavior will not exist. Figure 3-9 shows after unloading to the plastic strain (Rule 3), the crack opens (Rule 6), and when the strain reverses and gradual crack closure occurs (Rule 13).

$$\begin{aligned} \varepsilon_I &= \varepsilon_r \\ f_I &= 0 \\ E_I &= 0 \\ \varepsilon_F &= \varepsilon^-_{un} \\ f_F &= f^-_{new} \\ E_F &= E^-_{new} \end{aligned} \qquad \textbf{Rule 13} \tag{3.69}$$

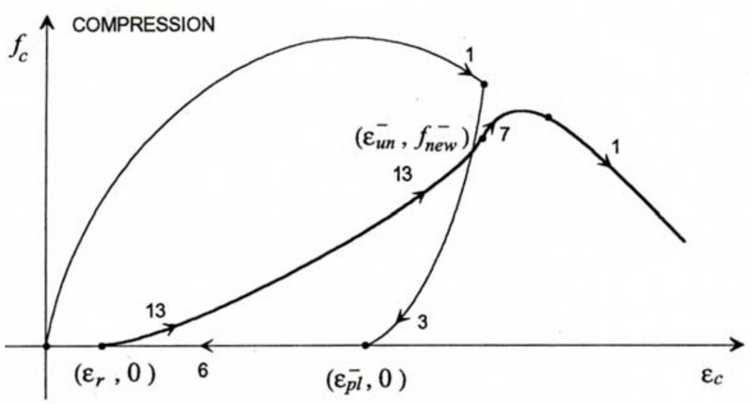

Figure 3-9: Unloading and Reloading Curve in the Post Cracking region per Chang and Mander [1994]. (Numerals shown on the figure identify the rule number)

3.3.5 Pre-Cracking Transition Curves

When a partial loading or unloading from one of the connecting curves occurs, a transition curve is used to move back to another connecting curve. Rules 3, 4, 9, and 10 are all connecting curves, and thus partial loading and unloading on each curve must be considered separately. Figure 3-10 shows how reversals from Rules 3 and 4 are addressed. When a partial unloading from the compression envelope occurs, a reversal from Rule 3, then f_{new} needs to be changed, and a new stress f_{new*} is calculated, and the point where the envelope is rejoined $(\varepsilon^-_{re}, f_{re})$ is changed to $(\varepsilon^-_{re*}, f_{re*})$. The equations for these modified expressions given by Chang and Mander are:

$$f^-_{\text{new}*} = f^-_{un} - \Delta f^- \frac{\varepsilon^-_{un} - \varepsilon^-_{ro}}{\varepsilon^-_{un} - \varepsilon^-_{pl}} \tag{3.70}$$

$$E^-_{\text{new}*} = \frac{f^-_{\text{new}*} - f^-_{ro}}{\varepsilon^-_{un} - \varepsilon^-_{ro}} \tag{3.71}$$

$$\varepsilon^-_{\text{re}*} = \varepsilon^-_{un} - \Delta\varepsilon^- \frac{\varepsilon^-_{un} - \varepsilon^-_{ro}}{\varepsilon^-_{un} - \varepsilon^-_{pl}} \tag{3.72}$$

$$f^-_{\text{re}*} = f^-\left(\left|\frac{\varepsilon^-_{\text{re}*}}{\varepsilon'_{cc}}\right|\right) \tag{3.73}$$

$$E^-_{\text{re}*} = E^-\left(\left|\frac{\varepsilon^-_{\text{re}*}}{\varepsilon'_{cc}}\right|\right) \tag{3.74}$$

The curve for the modified Rule 7 is then given by:

$$\begin{aligned} \varepsilon_I &= \varepsilon^-_{ro} \\ f_I &= f^-_{ro} \\ E_I &= E_c \\ \varepsilon_F &= \varepsilon^-_{un} \\ f_F &= f^-_{\text{new*}} \\ E_F &= E^-_{\text{new*}} \end{aligned} \qquad \textbf{Rule 7.1} \quad \left|\varepsilon^-_{ro}\right| \le \left|\varepsilon_c\right| \le \left|\varepsilon^-_{un}\right| \tag{3.75}$$

$$\begin{aligned} \varepsilon_I &= \varepsilon^-_{un} \\ f_I &= f^-_{\text{new*}} \\ E_I &= E^-_{\text{new*}} \\ \varepsilon_F &= \varepsilon^-_{\text{re*}} \\ f_F &= f^-_{\text{re*}} \\ E_F &= E^-_{\text{re*}} \end{aligned} \qquad \textbf{Rule 7.2} \quad \left|\varepsilon^-_{un}\right| < \left|\varepsilon_c\right| < \left|\varepsilon^-_{\text{re*}}\right| \tag{3.76}$$

Similarly, when a reversal from a partial unloading from the tension envelope occurs, reversal from Rule 4, then the $f^+_{\text{new*}}$ must be determined, and the point at which the tension envelope is regained $(\varepsilon^+_{\text{re*}}, f^+_{\text{re*}})$ must be calculated. The equations to determine these new values are as follows:

$$f^-_{\text{new*}} = f^+_{un} - \Delta f^+ \frac{\varepsilon^+_{un} - \varepsilon^+_{ro}}{\varepsilon^+_{un} - \varepsilon^+_{pl}} \tag{3.77}$$

$$E^+_{\text{new*}} = \frac{f^+_{\text{new*}} - f^+_{ro}}{\varepsilon^+_{un} - \varepsilon^+_{ro}} \tag{3.78}$$

$$\varepsilon^+_{\text{re*}} = \varepsilon^+_{un} - \Delta\varepsilon^+ \frac{\varepsilon^+_{un} - \varepsilon^+_{ro}}{\varepsilon^+_{un} - \varepsilon^+_{pl}} \tag{3.79}$$

$$f^+_{\text{re*}} = f^+\left(\left|\frac{\varepsilon^+_{\text{re*}} - \varepsilon_0}{\varepsilon'_{cc}}\right|\right) \tag{3.80}$$

$$E^+_{\text{re*}} = E^+\left(\left|\frac{\varepsilon^+_{\text{re*}} - \varepsilon_0}{\varepsilon_t}\right|\right) \tag{3.81}$$

Rule 8 is modified as follows:

$\varepsilon_I = \varepsilon_{ro}^{+}$
$f_I = f_{ro}^{+}$
$E_I = E_c$
$\varepsilon_F = \varepsilon_{un}^{+}$
$f_F = f_{\text{new*}}^{+}$
$E_F = E_{\text{new*}}^{+}$

Rule 8.1 $\left|\varepsilon_{ro}^{+} - \varepsilon_0\right| \leq \left|\varepsilon_c - \varepsilon_0\right| \leq \left|\varepsilon_{un}^{+} - \varepsilon_0\right|$ (3.82)

$\varepsilon_I = \varepsilon_{un}^{+}$
$f_I = f_{\text{new*}}^{+}$
$E_I = E_{\text{new*}}^{+}$
$\varepsilon_F = \varepsilon_{\text{re*}}^{+}$
$f_F = f_{\text{re*}}^{+}$
$E_F = E_{\text{re*}}^{+}$

Rule 8.2 $\left|\varepsilon_{un}^{+} - \varepsilon_0\right| < \left|\varepsilon_c - \varepsilon_0\right| < \left|\varepsilon_{\text{re*}}^{+} - \varepsilon_0\right|$ (3.83)

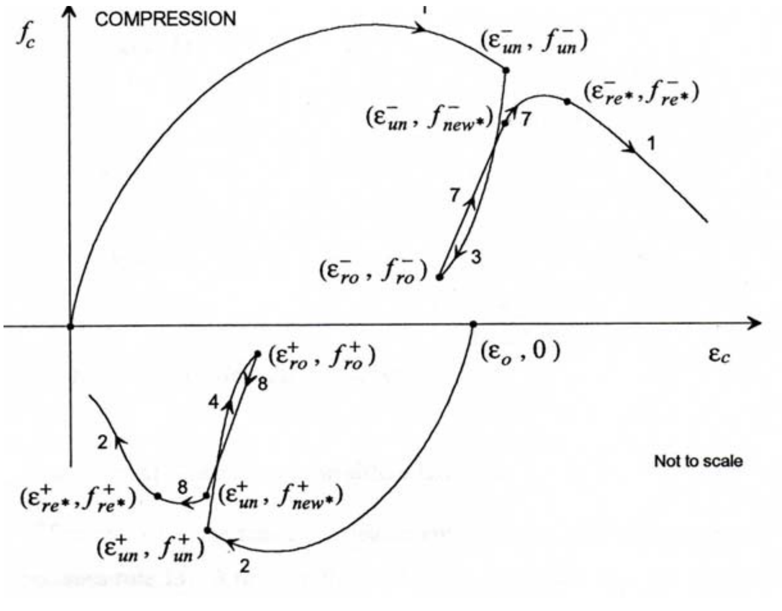

Figure 3-10: Partial Unloading and Reloading from the Tension and Compression Envelope as per Chang & Mander [1994]. (Numerals shown on the figure identify the rule number)

Figure 3-11 shows that reversal from Rule 9 at point A (ε_a, f_a) will target point B (ε_b, f_b) on Rule 10 through Rule 11; incomplete loading on Rule 11 will target point A again through Rule 12. Similarly, reversal from Rule 10 at Point B (ε_b, f_b) will target point A (ε_{a}, f_a) on rule 9 through Rule 12. The relationship between the target points A and B is expressed by the following:

$$\frac{\varepsilon_a - \varepsilon_{pl}^-}{\varepsilon_{un}^+ - \varepsilon_{pl}^-} = \frac{\varepsilon_{un}^- - \varepsilon_b}{\varepsilon_{un}^- - \varepsilon_{pl}^+} \tag{3.84}$$

$$\left.\begin{aligned} \varepsilon_I &= \varepsilon_r \\ f_I &= f_r \\ E_I &= E_c \\ \varepsilon_F &= \varepsilon_b \\ f_F &= f_b \\ E_F &= E_t(\varepsilon_b) \end{aligned}\right\} \quad \textbf{Rule 11} \tag{3.85}$$

$$\left.\begin{aligned} \varepsilon_I &= \varepsilon_r \\ f_I &= f_r \\ E_I &= E_c \\ \varepsilon_F &= \varepsilon_a \\ f_F &= f_a \\ E_F &= E_t(\varepsilon_a) \end{aligned}\right\} \quad \textbf{Rule 12} \tag{3.86}$$

where (ε_r, f_r) is the coordinate of the last reversal.

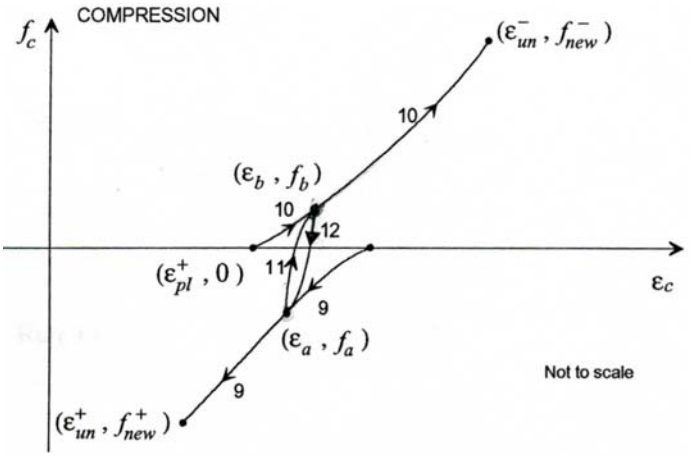

Figure 3-11: Pre-Cracking Transition Curves as per Chang & Mander [1994]. (Numerals shown on the figure identify the rule number)

3.3.6 Post-Cracking Transition Curves

After cracking, the tension envelope follows the x-axis, and the connecting compression curve was Rule 13. Figure 3-12 shows that reversal from Rule 13 at ($\varepsilon_{a,}, f_a$) will target ε_b on the ordinate axis. The target strain, ε_b, is calculated by the following:

$$\varepsilon_b = \varepsilon_a - \frac{f_a}{E_{SEC}^{-}} \tag{3.87}$$

$$\begin{aligned} \varepsilon_I &= \varepsilon_r \\ f_I &= f_r \\ E_I &= E_c \\ \varepsilon_F &= \varepsilon_b \\ f_F &= 0 \\ E_F &= 0 \\ \varepsilon_I &= \varepsilon_r \end{aligned} \qquad \textbf{Rule 14} \tag{3.88}$$

$$\begin{aligned} f_I &= f_r \\ E_I &= E_c \\ \varepsilon_F &= \varepsilon_a \\ f_F &= f_a \\ E_F &= E_t(\varepsilon_a) \end{aligned} \qquad \textbf{Rule 15} \tag{3.89}$$

Where (ε_r, f_r) is the coordinate of the last reversal.

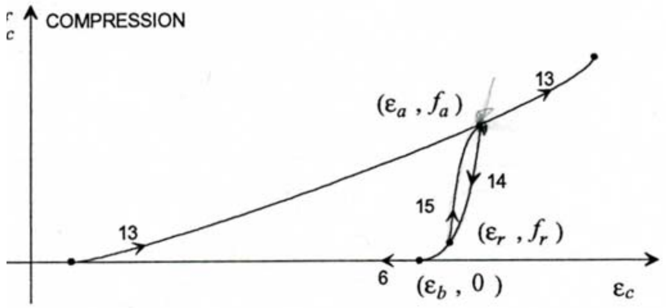

Figure 3-12: Post-Cracking Transition Curves as per Chang & Mander [1994]. (Numerals shown on the figure identify the rule number)

Figure 3-13 summarizes how the rules presented in this section are related. The tension side of the curve has been enlarged for clarity. Figure 3-13 shows all the rules that are defined by Chang and Mander. However, all of these rules are not available at any one time. Rules 2, 4, 6, 8, 8.1, 8.2, 9, 10, 11, 12 are only occur prior to cracking, and Rules 13, 14, 15 only occur after cracking of the model has occurred.

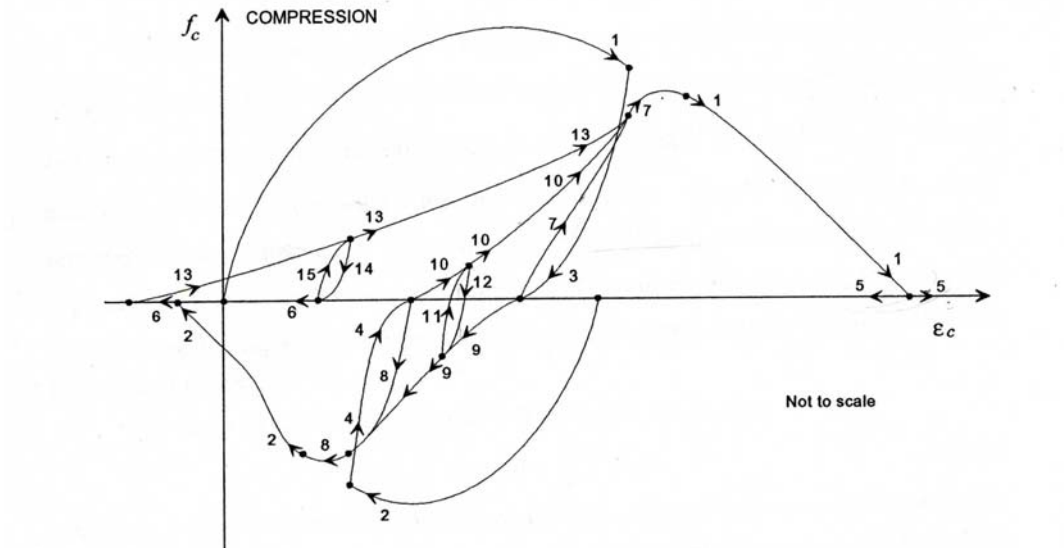

Figure 3-13: Behavior of concrete Model Proposed by Chang & Mander [1994]. (Numerals shown on the figure identify the rule number)

3.4 Challenges with Implementing Chang and Mander's Concrete Model.

Implementing Chang and Mander's concrete model in OpenSees as presented in the previous section exhibited some challenges in the model. This section summarizes the challenges encountered, how they were addressed, and the modifications that were made to the rules presented in the previous sections.

3.4.1 Numerical Stability of the Unloading and Reloading Function

The curve that was used in the original model for the shape of the connecting and transition curves was chosen so that it starts from an initial point (x_0,y_0) with an initial slope (E_0) and ends at a point (x_f,y_f) with a final slope (E_f). The algebraic equation that was selected for the connecting and transition curves had the following general form:

$$y = y_0 + E_0(x - x_0) + A(x - x_0)^B \tag{3.90}$$

Applying the conditions that at $x = x_0$, $y = y_f$ and $E = E_f$, Eq. 3.90 can be rewritten into the following form:

$$y = y_0 + (x - x_0)[E_0 + A|x - x_0|^R] \tag{3.91}$$

$$y' = E_0 + A(R-1)|x - x_0|^R \tag{3.92}$$

where,

$$R = \frac{E_f - E_{SEC}}{E_{SEC} - E_0} \tag{3.93}$$

$$A = \frac{E_{SEC} - E_0}{|x_f - x_0|^R} \tag{3.94}$$

$$E_{SEC} = \frac{y_f - y_0}{x_f - x_0} \tag{3.95}$$

If E_{SEC} is very close to the value of E_0, then the denominator of the Eq. 3.93 becomes a very small number and the value of R becomes very large. Parameter A becomes impossible to calculate because the difference between the x values is less than one and when raised to a large power, it becomes nearly zero. This problem only occurs when E_{SEC} is approximately equal to E_0; if this is the case, then the curve should be represented as a straight line. A straight line occurs when R takes a value of zero.

In order to address this problem, a number of “if” statements were added prior to parameter A being calculated. The “if” statement set R = 0 when any of the following conditions are true.

i) $0.985 \leq E_{SEC}/E_0 \leq 1.015$

ii) $0.9999 \leq x_f/x_0 \leq 1.0001$

iii) $R > 50$

The second statement noted above covers the case of a small strain increment that causes E_{SEC} to become a large number due to a small denominator. The last condition on R greater than 50 was selected based on the values of parameter A during testing of the code. With this change, the stability of the unloading and reloading curves were improved, which was confirmed by performing the analysis of RW2 to ensure the performance of the concrete model.

3.4.2 Strain Reversals Not Considered in Original Description

In a general program, the strain can reverse direction at any time; however, a reversal from Rules 7, 7.1, 7.2, 8, 8.1, and 8.2 was not discussed by Chang and Mander. To ensure convergence and that the program will not stall, rules for these reversals must be defined.

Reversals from Rules 7, 7.2, 8, and 8.2 are handled as if the reversal occurred from the envelope. Rule 3 is followed for reversals from Rules 7 and 7.2 and Rule 4 for reversals from Rules 8 and 8.2. Since Rules 7, 7.2, 8, and 8.2 handle rejoining the envelope response, the rules for unloading from the envelope were felt to be the most appropriate behavior.

A reversal occurring after a partial unloading and reloading cycle was also not considered by the original model. If the model follows Rule 7.1 or 8.1 and a strain reversal occurs, no guidance is given for the unloading path. These reversals are handled by returning on a straight line to the point on Rule 3 where Rule 7.1 started if the reversal occurs from Rule 7.1. Similarly, Rule 4 was used if the reversal occurs from Rule 8.1. Once the unloading reaches Rule 3 or 4, Rule 3 or 4 is followed as defined in Section 3.3.3.

3.5 Model Verification

To provide further verification to the models, four types of confined concrete blocks were constructed and tested in cyclical compression. Although, this attempt was generally unsuccessful, a brief documentation of this effort is included to provide useful information for others interested in similar tests.

The test blocks measured 6 in. wide by 10 in. long, and three of the four types of blocks were 10 in. tall, while one was 5 in. tall. The volumetric ratio of the transverse reinforcement was varied among the blocks. Three of four types had #2 deformed bars spaced at 2.5 in. o.c., while the other type of block had a lower level of transverse reinforcement with #2 hoops at 3.25 in. o.c. The details of the four block types are shown in Figure 3-14. Types 1, 2, and 4 had the same transverse reinforcement ratio; while type 3 had a lower amount of transverse reinforcement. Type 1 blocks had #2 vertical bars in the four corners of the hoops. These vertical bars were greased to prevent them from bonding to the concrete and adding to the axial strength of the block allowing them to only participate in providing confinement to the concrete. Strain gages were placed on the vertical bars to determine if they were participating in the axial resistance. Type 2 blocks were the same size as Type 1; however, the longitudinal reinforcement was removed. Type 4 blocks were half the height of the Type 1 and 2 blocks to investigate the influence of the size of the specimen on the results. The Type 1 and 2 blocks were intended to determine the influence of the longitudinal reinforcement on the confinement of the section. Type 4 was expected to provide the influence of size of the specimen to be investigated, while Type 3 intended to examine the confined effects for two levels of transverse reinforcement. The blocks were tested in strain control to verify the loading and unloading characteristics of the model. Figures 3-15 and 3-16 show the load frame setup used for testing the concrete blocks. The actuator and load cell were offset from the test specimen because neither the load cell nor the actuator had the expected capacity of the confined concrete blocks. Each block was instrumented by mounting a DCDT on each face of the specimen. The movement of two rods embedded in the concrete block was measured to determine the approximate strain on each side. The gauge length for the strain measurements was approximately 2.5 in.

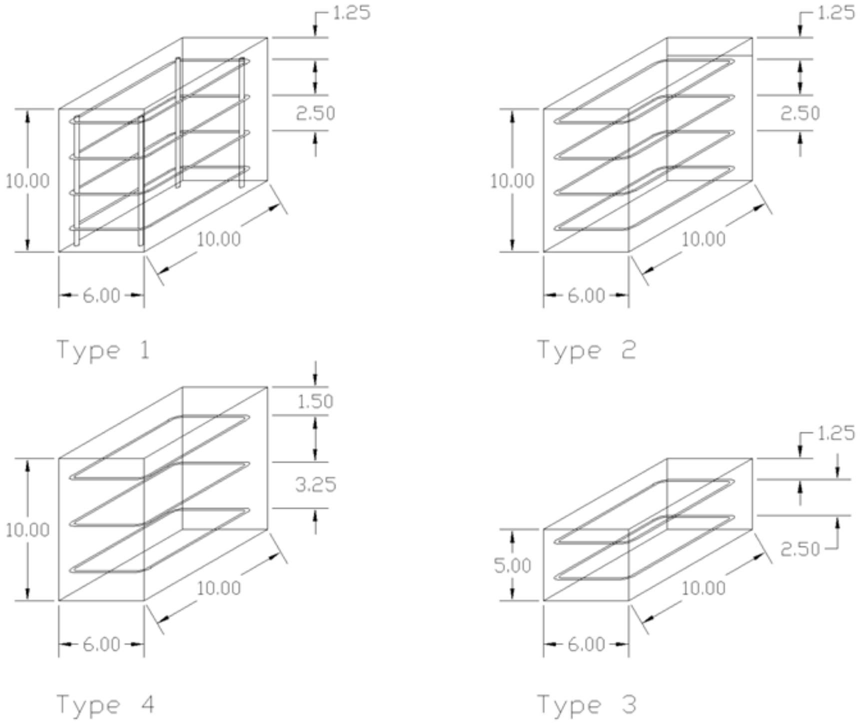

Figure 3-14: Reinforcement Details of Concrete Blocks

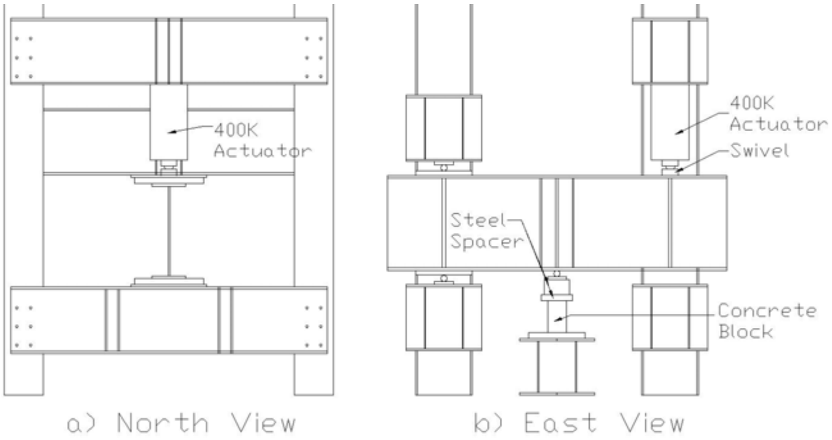

Figure 3-15: Testing Frame Setup

In the test setup shown in Figures 3-15, the load on the specimen was twice the load registered by the load cell. However, the test setup caused problems due to curvature of the load beam as well as the inability to ensure uniform stress on the block once cracking occurred as a result of concrete dilation. At the start of the test, the strains measured on each face were approximately equal; however, once cracking occurred in the specimen, the strains were not equal on each face. The four strains measured on one specimen after cracking were -0.0025, 0.0007, -0.006, and -0.005. The unequal strains were due to eccentric loading on the specimen, causing it to experience axial and flexural actions about both axises. However, because of the bending moment the specimens during testing, the data could not provide confirmation of the cyclic behavior of the confined concrete model beyond the validation conducted by Chang and Mander in their original 1994. Additionally, the peak strength was significantly below the expected value from the confined model. The average stress-strain data did show that the envelope, unloading, and reloading curves follow the shape given by Chang and Mander, see Figure 3-16. Further validation of the concrete model cannot be provided beyond that shown by Chang and Mander.

3.6 Simplified Concrete Model

The concrete model described previously was shown to be an adequate by Chang and Mander [1994]. However, the nonlinear nature of the loading and unloading curves can require a number of iterations to converge to solution at the section level. In a large, complex model, the extra iterations can add significantly to the computation time required for the analysis. After implementing the original concrete model of Chang and Mander in OpenSees and experiencing significant time required for convergence of the solution due to the use of this model, a simplified model was created from the original model that would reduce the number of iterations required to achieve the converged state.

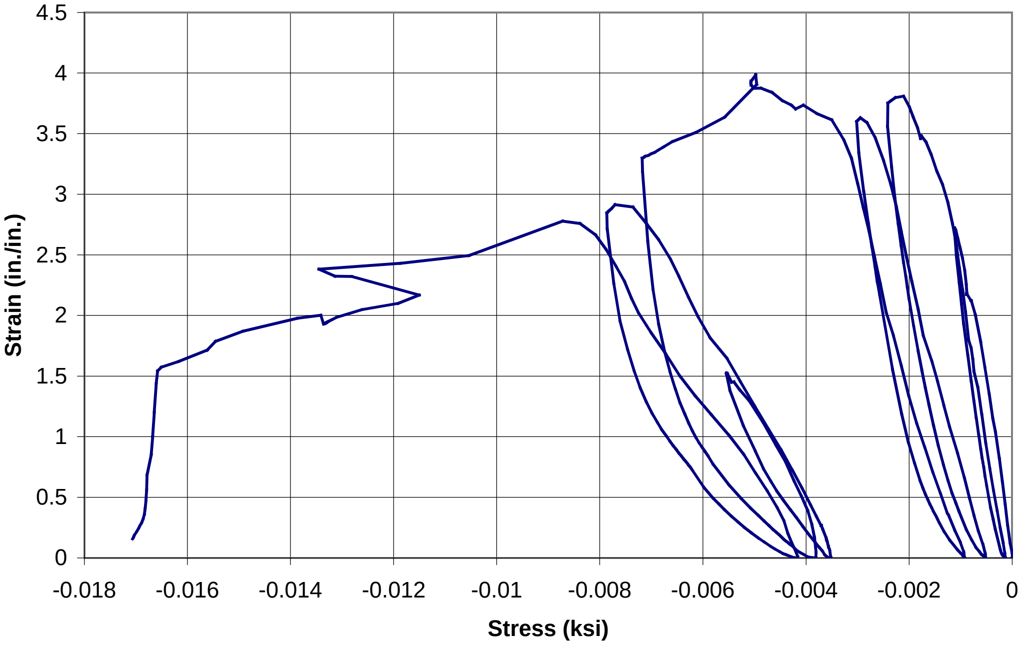

Figure 3-16: Cyclic Behavior of Confined Concrete Blocks

The simplified model uses a trilinear approximation to represent the smooth curve used for the loading and unloading portions. The model is assumed to return to the compression or tension envelope at the point where it left. Figure 3-17 shows the trilinear approximation used for the connecting curves. The critical strain for the trilinear relationship is defined in Eq. 3.96, using the following terms: stress, strain, and slope terms used in the original Chang and Mander model

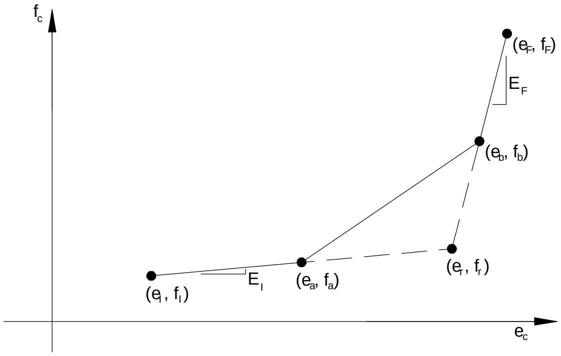

Figure 3-17: Trilinear Approximation used for Loading and Unloading in the Simplified Model

$$\varepsilon_r = \frac{(E_I * \varepsilon_I - E_F * \varepsilon_F - f_I + f_F)}{E_I - E_F} \tag{3.96}$$

If the strain is less than the average of ε_r and ε_I, see Figure 3-18, then the stress is calculated from the initial stress, strain, and slope. If the strain is greater than the average of ε_r and ε_F, then the stress is calculated from the final stress, strain, and slope. The third line section connects the endpoints of the the initial and final line sections.

The initial and final strain, stress, and slopes for the rules in the simplified model are the same as those defined in Section 3.3 However, Rules 7, 7.2, 8, and 8.2 were removed in the simplified model, allowing the model to rejoin the envelope at the same strain where it had previously unloaded from. Removing Rules 7, 7.2, 8, and 8.2 requires modifications to Rules 9, 10, and 13 in order to change their endpoint to a point on the tension or compression envelope. Accordingly,

$$\begin{aligned} \varepsilon_I &= \varepsilon_{pl}^{-} \\ f_I &= 0 \\ E_I &= E_{pl}^{-} \\ \varepsilon_F &= \varepsilon_{un}^{+} \\ f_F &= f_{un}^{+} \\ E_F &= E_{new}^{+*} \end{aligned} \qquad \textbf{Rule 9} \tag{3.97}$$

$$\begin{aligned} \varepsilon_I &= \varepsilon_{pl}^{+} \\ f_I &= 0 \\ E_I &= E_{pl}^{+} \\ \varepsilon_F &= \varepsilon_{un}^{-} \\ f_F &= f_{un}^{-} \\ E_F &= E_{new}^{-*} \end{aligned} \qquad \textbf{Rule 10} \tag{3.98}$$

where,

$$E_{new}^{-*} = \frac{f_{un}^{-}}{\varepsilon_{un}^{-} - \varepsilon_{pl}^{-}} \tag{3.99}$$

$$E_{new}^{+*} = \frac{f_{un}^{+}}{\varepsilon_{un}^{+} - \varepsilon_{pl}^{+}} \tag{3.100}$$

Rule 13 uses the power curve proposed by Chang and Mander with the following rules to prevent the numerical instability discussed previously in Section 3.4.1.

i) $0.985 \leq E_{SEC}/E_0 \leq 1.015$

ii) $0.9999 \leq x_f/x_0 \leq 1.0001$

iii) $R > 80$

If any of the above conditions is found to be true, then the trilinear connecting curve is used in place of the power function suggested by Chang and Mander. With the trilinear approximation, Rule 13 was:

$$\begin{aligned} &\varepsilon_I = \varepsilon_r \\ &f_I = 0 \\ &E_I = 0.25 * E_{SEC} \\ &\varepsilon_F = \varepsilon_{un}^{-} \qquad \textbf{Rule 13} \\ &f_F = f_{un}^{-} \\ &E_F = E_{new}^{-*} \end{aligned} \tag{3.101}$$

where E_{SEC} is as defined in Eq. 3.31. The $0.25E_{SEC}$ for E_I was based on the observed response when the numerical instability occurred. Otherwise if numerical the above conditions are false, Rule 13 is defined with the following parameters:

$$\begin{aligned} &\varepsilon_I = \varepsilon_r \\ &f_I = 0 \\ &E_I = 0.0 \\ &\varepsilon_F = \varepsilon_{un}^{-} \qquad \textbf{Rule 13} \\ &f_F = f_{un}^{-} \\ &E_F = E_{new}^{-*} \end{aligned} \tag{3.102}$$

Rules 7.1, 8.1, 11, 12, 14, and 15 are all replaced with straight lines. are defined below:

$$\begin{aligned} E &= \frac{f^-_{un} - f^-_{ro}}{\varepsilon^-_{un} - \varepsilon^-_{ro}} \\ f &= E * (\varepsilon - \varepsilon^-_{ro}) + f^-_{ro} \end{aligned} \qquad \textbf{Rule 7.1} \tag{3.103}$$

$$\begin{aligned} E &= \frac{f^+_{un} - f^+_{ro}}{\varepsilon^+_{un} - \varepsilon^+_{ro}} \\ f &= E * (\varepsilon - \varepsilon^+_{ro}) + f^+_{ro} \end{aligned} \qquad \textbf{Rule 8.1} \tag{3.104}$$

$$\begin{aligned} E &= \frac{f_b - f_r}{\varepsilon_b - \varepsilon_r} \\ f &= E * (\varepsilon - \varepsilon_r) + f_r \end{aligned} \qquad \textbf{Rule 11} \tag{3.105}$$

$$\begin{aligned} E &= \frac{f_a - f_r}{\varepsilon_a - \varepsilon_r} \\ f &= E * (\varepsilon - \varepsilon_r) + f_r \end{aligned} \qquad \textbf{Rule 12} \tag{3.106}$$

where ε_b and ε_a are calculated using Eq. 3.84.

$$\begin{aligned} E &= \frac{0.0 - f_r}{\varepsilon_b - \varepsilon_r} \\ f &= E * (\varepsilon - \varepsilon_r) + f_r \end{aligned} \qquad \textbf{Rule 14} \tag{3.107}$$

$$\begin{aligned} E &= \frac{f_a - f_r}{\varepsilon_a - \varepsilon_r} \\ f &= E * (\varepsilon - \varepsilon_r) + f_r \end{aligned} \qquad \textbf{Rule 15} \tag{3.108}$$

where

$$\varepsilon_b = \varepsilon_r - \frac{f_r}{E^-_{SEC}} \tag{3.109}$$

where ε_a and E^-_{SEC} are as defined in Eq. 3.84 and 3.43. Figure 3-18 shows the loading and unloading rules for the simplified concrete model. This Figure is equivalent to Figure 3-13.

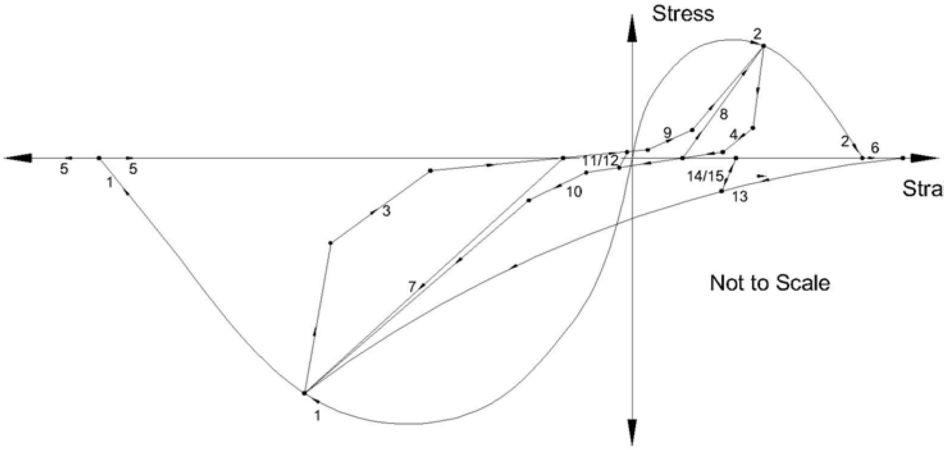

Figure 3-18: Cyclic Behavior of Simplified Chang and Mander Concrete Model. (Numerals shown on the figure identify the rule number)

3.7 Verification of the Simplified Model

The effect of the simplified Chang and Mander model on the overall structureal response needs to be examined. The structure chosen for this comparison was the second of the two rectangular walls, RW2 tested by Thomsen and Wallace (1993) shown earlier in Figure 3-1. The cyclic response of RW2 from OpenSees using the simplified concrete model is shown in Figure 3-19. The deficiencies seen in Figure 3-3 are not present in Figure 3-19. The residual displacement and reloading stiffness are well simulated. The kinking seen near zero displacement that was observed in Figure 3-3 is not present due to the gradual crack included in the simplified Chang and Mander concrete model.

The difference in the stiffness of the response at low displacement levels is due to shear deformation not being included in the analytical model. Fiber-based elements in OpenSees do not account for shear deformation, and in order to better observe the effect of the concrete model, the shear deformation was left out. If shear deformation effects are included in the model, the monotonic envelope is well simulated. This is shown in Figure 3-20 that confirms inclusion of shear deformation accurately simulates the force-displacement response of RW2 at all displacement levels. Cyclic simulation of RW2 including shear deformation was not conducted because there was not a good material model available to simulate the cyclic shear-distortion of the wall.

Both the simplified model and the original Chang and Mander model were used to model RW2 to determine the effect the simplifications had on the overall response of a structure. Figure 3-21 showed that the simplified model simulates the response as well as the original Chang and Mander models for the loading and unloading stiffnesses, and lateral force resistance. The two models show slightly difference responses near zero lateral force due to how the numerical instability of Rule 13 are handled in the two models. Overall, the simplifications had little effect of the simulation, but significantly increased the computational efficiency.

Due to the improved simulation of wall behavior seen in the simulation of RW2, the simplified concrete material model was submitted to the OpenSees community and was included in version 1.7.4 as Concrete07. The model has already been used by researchers at several universities, who are engaged in analytical simulation of the nonlinear behavior of concrete structures using OpenSees.

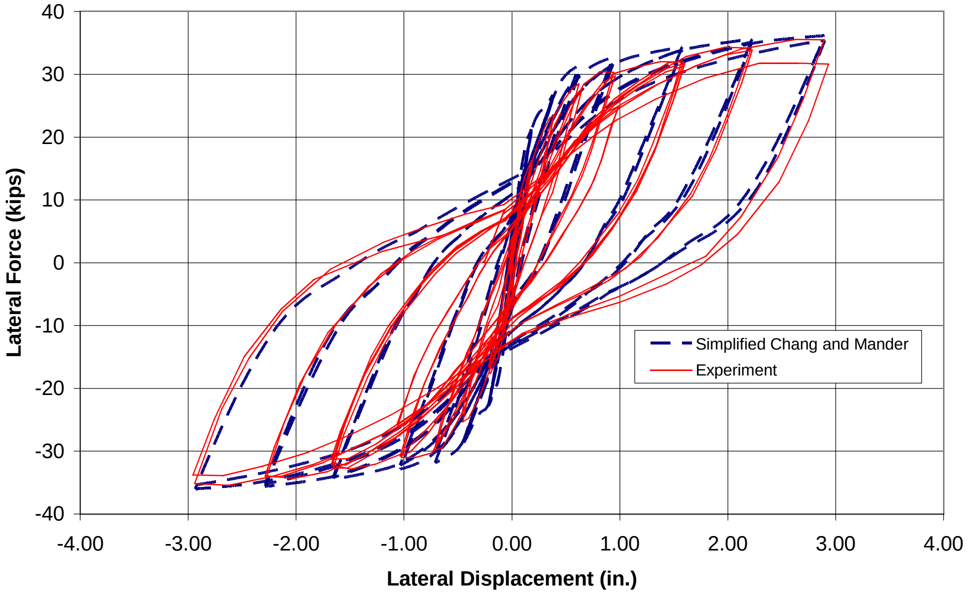

Figure 3-19: RW2 Cyclic Response Comparison using Simplified Chang and Mander Concrete Material Model.

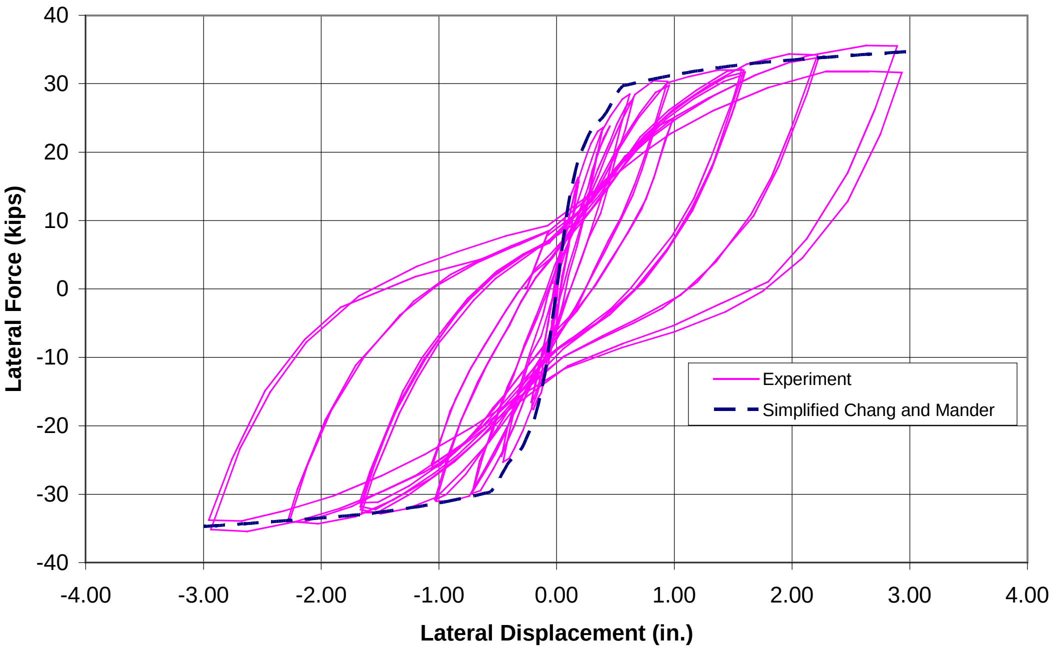

Figure 3-20: Monotonic Envelope Including Shear Deformations

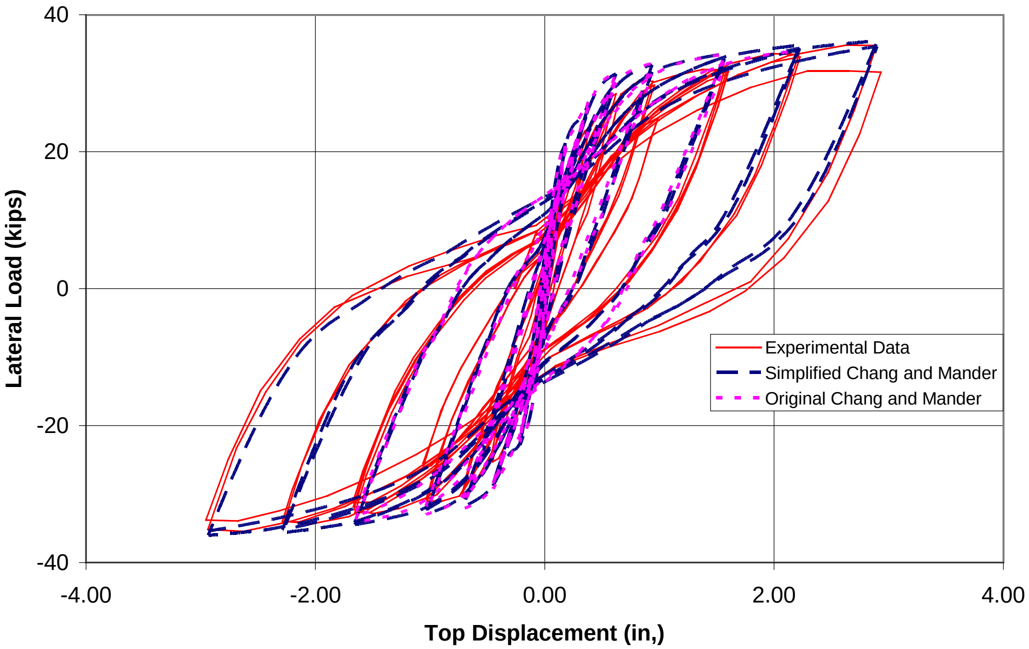

Figure 3-21: Cyclic Response Comparison using Original and Simplified Chang and Mander Concrete Models.

Chapter 4: Analysis of NTW1

As previously stated, in this PreNEESR project, two T-walls were constructed at 50 percent scale and tested to multi-directional loading at the NEES-MAST Facility in Minnesota. This chapter discusses the analysis of the first T-wall, NTW1, and the compares to the analysis results recorded during the test.

4.1 Prototype Wall

The prototype T-wall used in this study was a T-wall designed for a six-story prototype building located in Los Angeles, California. The floor plan of the prototype building is shown in Figure 4-1, and it had a 22,500 square foot (SF) floor plan with story heights of 12 feet at all levels. The gravity and lateral loads of the building were resisted by two separate systems. The gravity load system consisted of a 7 in. cast-in-place (CIP) concrete floor slab spanning between CIP or precast beams. The beams were supported on gravity columns located in a 20 ft by 45 ft grid. The lateral load was resisted by CIP concrete structural walls. A total of 10 T-walls resisted all the lateral force in the transverse direction, while additional rectangular walls were required in the building core to resist lateral load in the longitudinal direction.

The T-walls in the prototype building were designed using the IBC [2003] to resist a total building base shear of 351 kips and a base overturning moment of 183,887 kip-ft. These forces resulted in each T-wall having a 15 ft web, 12 ft flange, and a uniform thickness of 12 in. as shown in Figure 4-2, which shows details of a full-size T-wall with a design concrete strength of 5000 psi; the web and flange of the wall were detailed with boundary elements. The longitudinal reinforcement in the boundary element was 12 #11 bars in the flange and web tips. In addition, distributed vertical steel consisted of #5 bars at 18 in. on center (o.c.) was provided on each face of the wall in the regions outside of the boundary elements. The confinement ties were required for the bottom 13 ft 6 in. of the flange reinforcement and 15 ft of the web reinforcement. The confined region extended 30 in. into the flanges and web. In order to prevent shear failure occurring prior to developing full flexural capacity, the required horizontal shear reinforcement was #5 at 12 in. o.c. on each face of the web and #5 at 18 in. o.c. on each face of the the flange. More description of the protype T-wall design may be found in Brueggen *et al*. (2009).

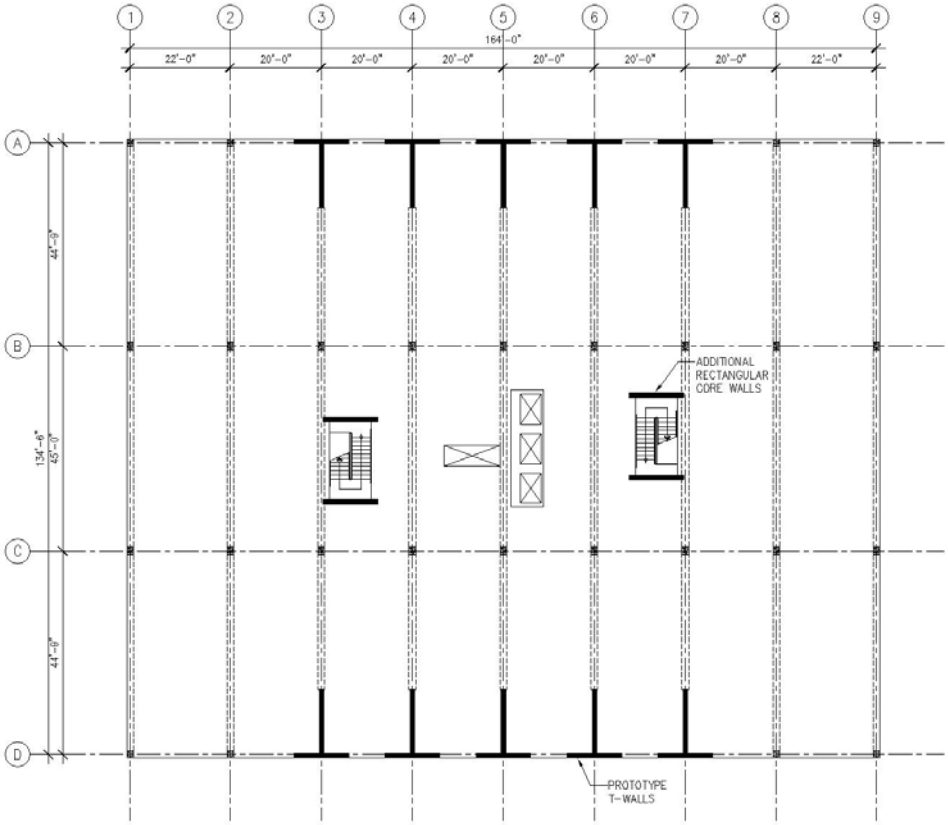

Figure 4-1: Floor Plan of the Six-Story Prototype Building

4.2 Description of NTW1

The first T-wall specimen tested at UMN, referred to as NTW1, was a 50% scale wall of the prototype T-wall as shown in Figure 4-3. While the T-walls in the prototype building were six stories high, NTW1 only had four stories but the effect of the missing two stories was included by applying a moment at the top of the wall in addition to the lateral force to simulate the moment gradient along the wall height as accurately as that expected for the prototype wall. NTW1 had a 6 ft long flange and 7 ft 6 in. long web, with a uniform thickness of 6 in. With a concrete design strength of 4,000 psi, NTW1 was designed with eight #6 bars and two #5 bars in the boundary elements in the flange tips. The web tip boundary element was extended by adding two #3 bars to the eight #6 and two #5 bars. This extension was required to meet the length of boundary element required by ACI 318-02 [2002]. The distributed steel in the web of the T-wall outside the boundary element was #3 at 12.5 in. o.c. on each face; while six #3 bars were used in the flange at a spacing of 6.5 in. The shear reinforcement was #3 bars at 7 in. o.c. on each face of the flange and web. The wall was 288 in. tall with 21 in. thick base and top blocks, totaling a specimen height of 330 in.

4.3 Description of Analysis Model

Modeling of NTW1 in OpenSees posed a number of new challenges in comparison to the modeling of the response of rectangular walls. The T-wal model needed to be capable of a) being loaded in a number of load paths in multiple directions, b) accounting for shear lag, and c) accurately simulate the moment and lateral force. The analytical model developed is described in this section, along with how these challenges were overcome.

The base block of NTW1 was connected to the strong floor with ten three-in. diameter threaded Dywidag bars. The height of the base block provide adequate anchorage for the wall longitudinal reinforcement. Consequently, the base block was not represented with a node in the analysis model, the degrees-of-freedom of this node was fixed in all directions. The base block did not move during the test, satisfying the assumed boundary condition in the model.

The interface between the T-wall and the base block was modeled using a zero-length interface element to account for the strain penetration effects. The interface element had a fiber section with the same cross section as NTW1 except that the steel reinforcement was replaced with the strain penetration material model developed by Zhao and Sritharan [2007]. This material model relates the stress in the reinforcement to the total bar slip at the interface, which contributes to lateral displacement at the top of the wall due to rotation at the wall-base block interface.

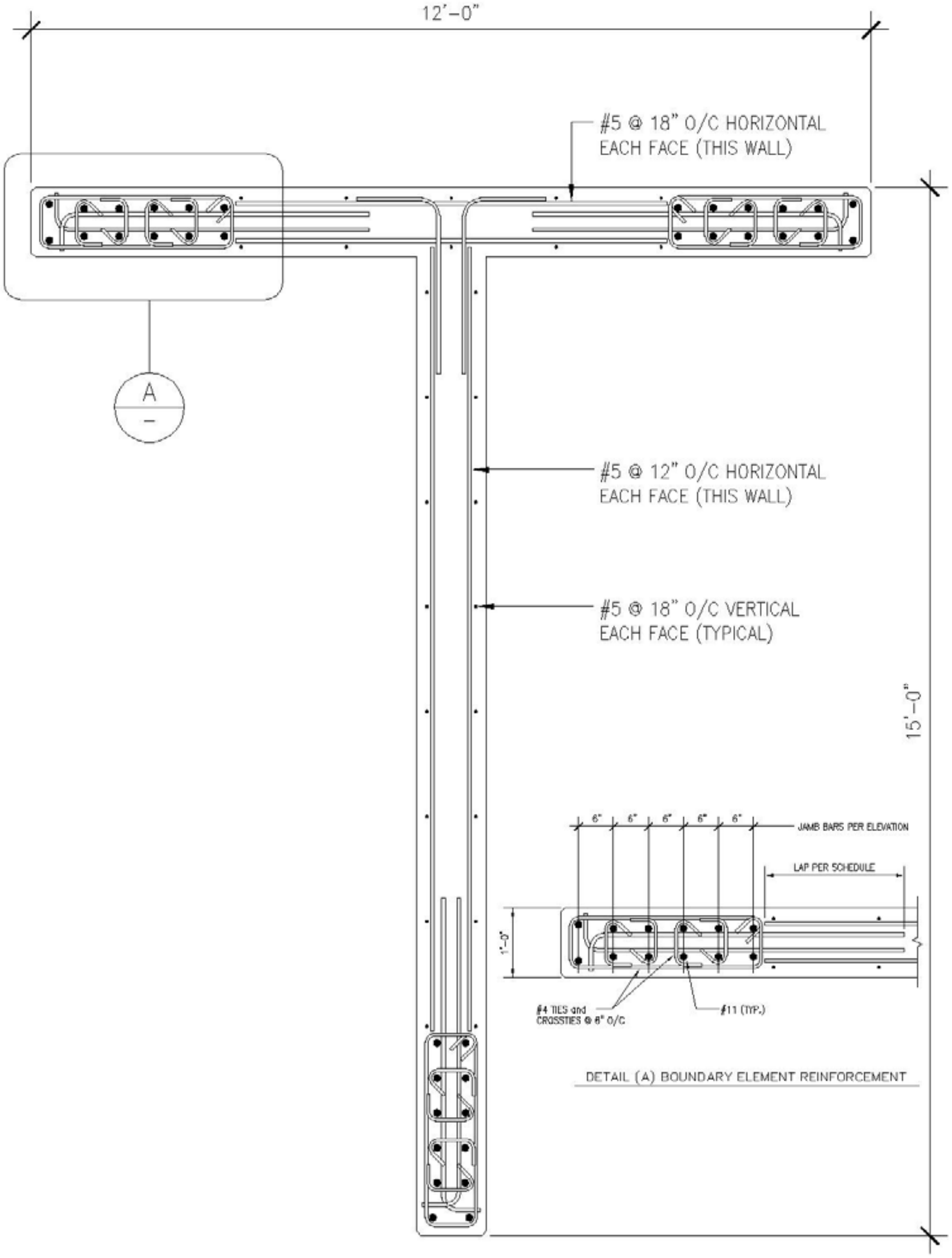

Figure 4-2: Details of a T-wall in the Prototype Building

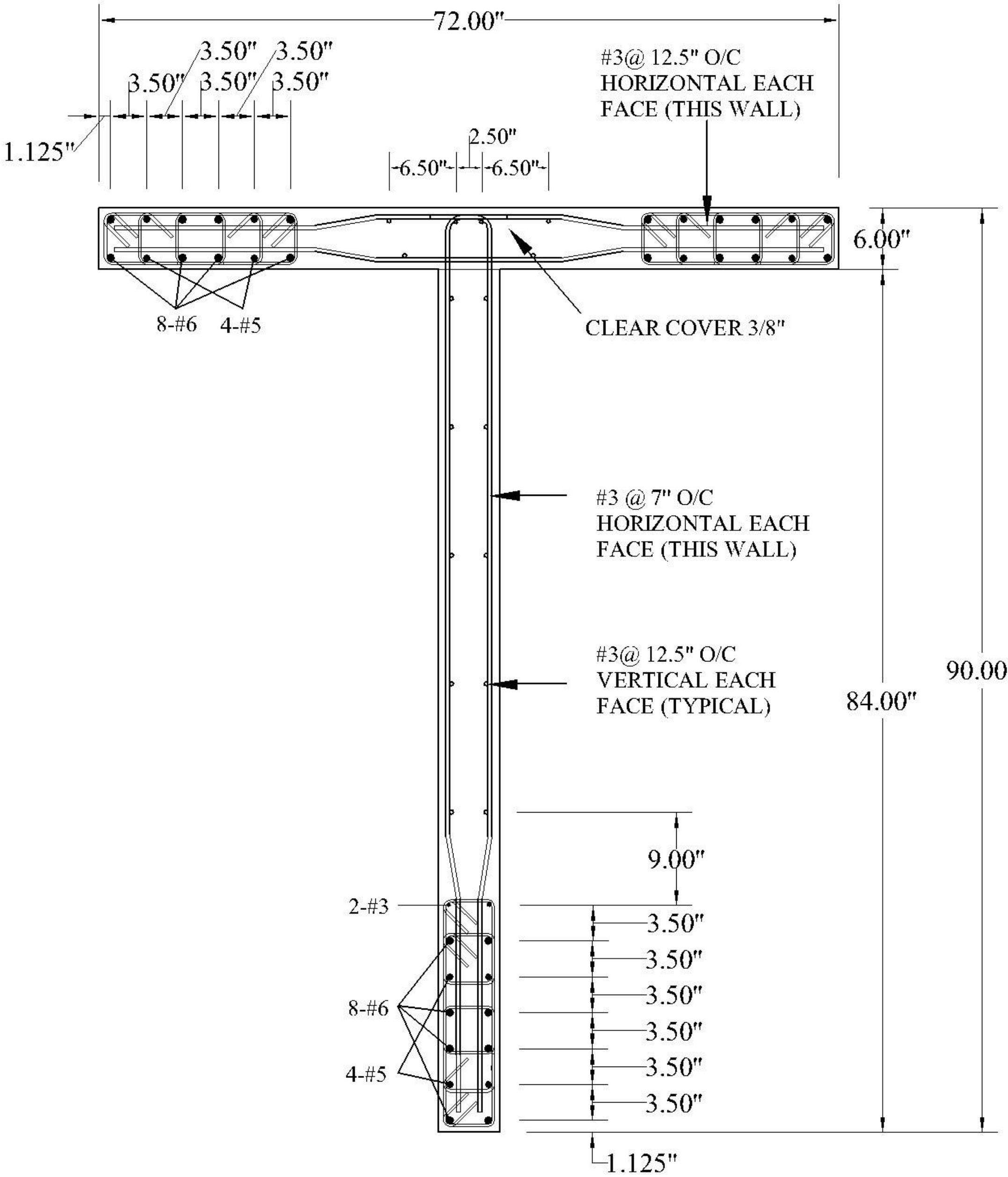

Figure 4-3: Cross-Sectional Details of Test Specimen NTW1

The wall was modeled using a force-based beam-column element developed by Taucer *et al.* [1991]. Neuenhofer and Filippou [1997] have shown that force-based beam-column elements have a number of advantages over the commonly used displacement-based beam-column elements. The primary advantage is that force-based beam-column elements can more accurately simulate the behavior of the plastic hinge and spread of plasticity along a member. A single force-based beam-column was used to model the entire height of the wall, with five integration points located at 0 in., 99.46 in, 144 in., 238.27 in, and 288 in above the base of the wall. A fiber section was used to model the cross section of the wall. And it was discretized using fibers approximately 0.25 in. by 0.25 in. for the confined and unconfined concrete regions. The confined and unconfined concrete were modeled using a Kent & Park model with nonlinear tension softening which was available in OpenSees as “Concrete03”. Implementation of Concrete07 was not completed prior to testing of NTW1. The peak tension stress of the concrete was assumed to be $7.5*\sqrt{f_c'(psi)}$ with the post peak behavior similar to the University of Houston model recommended by Belarbi and Hsu [1991] and Pang and Hsu [1992]. The unconfined concrete was based on 130% of the design concrete strength of 4000 psi with the assumption of peak compressive strain occurring at 0.002. The confined concrete properties were calculated using the confined concrete model proposed by Mander *et al.* [1998] based on the details of the transverse reinforcement and assumed unconfined concrete. The longitudinal reinforcement was modeled by matching the modified Menegotto-Pinto model available in OpenSees (i.e., Steel02) using the average results obtained from testing three tension for the #3, #5, and #6 bars. The reinforcement properties used for the OpenSees model are shown in Table 4-1.

Table 4-1: Analytical Reinforcement Properties Used in the NTW1 Model

Bar Size	Yield Stress (ksi)	Elastic Modulus (ksi)	Strain Hardening Ratio
#3	76	29000*	0.02
#5	63	29000*	0.02
#6	60	29000*	0.02

* Assumed value

The top block of NTW1 was modeled using a rigid beam-column element, as shown in Figure 4-4. This element allowed the deformations of NTW1 model at the height of the bottom of the crosshead to be monitored during analysis. This information was critical as the force and displacements were applied to the test specimen at the MAST facility at this location. Additionally, another rigid element was included in the NTW1 model (See Figure 4-4) to allow load to be applied at 24 in. above the top of the wall because this application point best simulated the moment gradient through the first floor when an inverse triangular load as typically used in design for the original 6 story wall was imposed. Consequently, this point became the control point in the analysis model; Figure 4-5 shows the moment diagram for the inverse triangular load pattern and the moment diagram for the applied loading. The difference in displacement between the bottom of the crosshead and the control point was less than 0.00001 in.

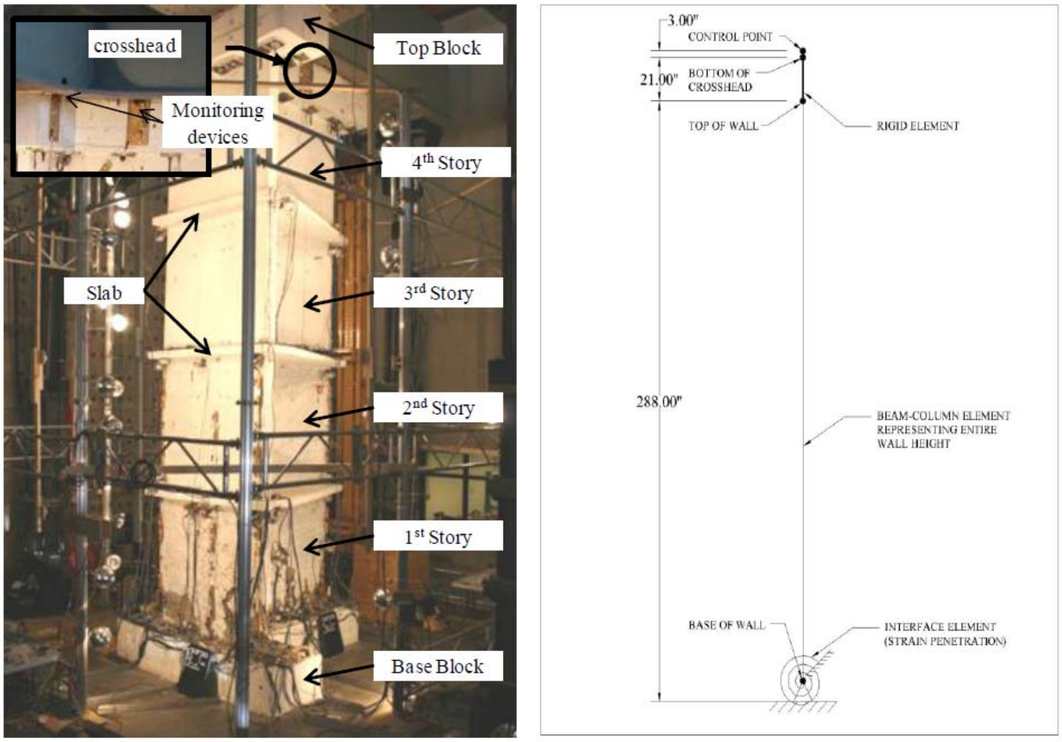

a) Full view of NTW1 specimen

b) Schematic of the analytical model of NTW1

Figure 4-4: Full View of NTW1 Test Setup and Schematic of the Analysis Model of NTW1

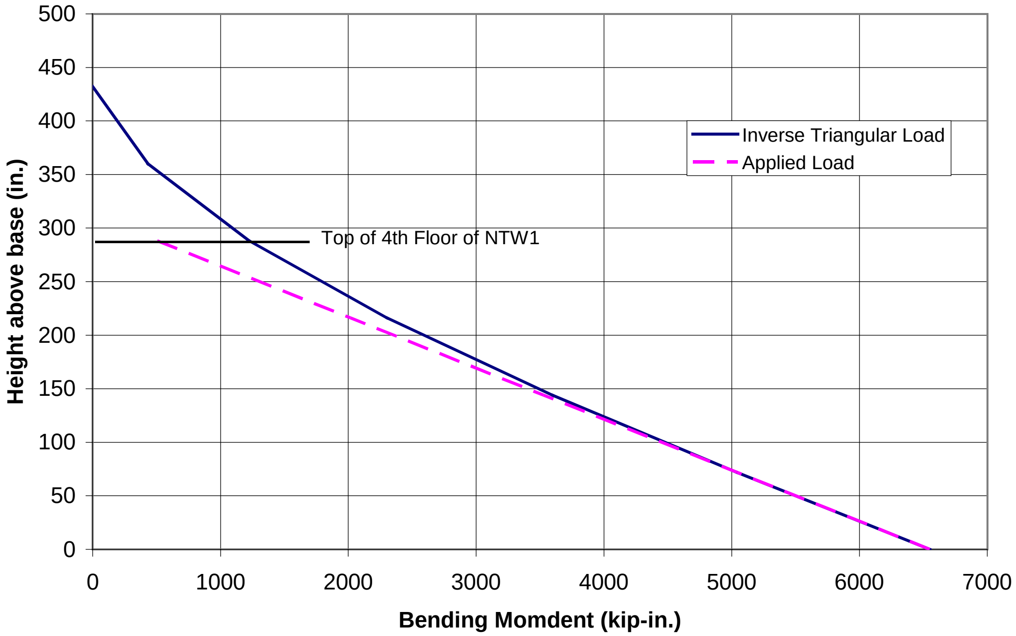

Figure 4-5: Bending Moment Profiles

An axial load of 186.5 kips was applied to NTW1 at the top of the wall. This value was determined based on the prototype building to reflect the axial load effect that would be typical of a T-wall in the prototype structure. In order to apply the displacement in the directions parallel to the web and the flange, boundary constraints were applied to the control point, located 24 in. above the top of the test wall. During analysis, the values of the two lateral displacement degrees-of-freedom (DOF) at the control point were specified at every time step, allowing the wall to be displaced in any desired direction or path.

4.4 Multidirectional Load Path

In order to develop a load path suitable for testing of NTW1, the envelope responses were needed to be defined. In a unidirectional test, the monotonic force-displacement response will define this envelope. In the two dimensional lateral loading used for the the T-wall test, the envelope had to be defined by a surface. The two critical points on a monotonic envelope in a one dimensional space are the “first yield” and “ultimate” points. For the first T-wall test, the “first yield” point in any direction of loading was defined as the displacement when the first bar in the cross section reaches the yield strain of the reinforcement. The “ultimate” point was defined by the strain in the confined concrete at the critical region achieving the compressive strain capacity or the tension strain in the critical longitudinal bar reaching 0.06 to account for bar fracture due to low cycle fatigue. The compressive strain capacity for the confined concrete was calculated based on the model proposed by Mander *et al.* (1988). However, since the ultimate strain is significantly underpredicted by this model, the strain capacity was increased by 30% over the theoretical value.

It was intended that NTW1 would be displaced in directions parallel to the web, parallel to the flange, and with components parallel to the web and flange. Therefore, the wall model was analyzed in several different directions, and the first yield displacement and the ultimate displacement capacity were defined for each loading direction. These displacement could then be plotted with respect to the direction to develop the yield and failure surface for NTW1. Figures 4-6 and 4-7 show the surfaces in terms of displacement and force, respectively. In the figures throughout this chapter, positive displacements parallel to the web place the flange in compression, while negative displacements in the web direction loading place the flange in tension. The idealized yield displacement is shown in Figure 4-6 as the “ductility 1” surface. The “ductility 1” displacement was calculated by multiplying the first yield displacement in any given direction by the force corresponding to either a strain in the concrete of 0.004 or a tension strain in the reinforcement of 0.015, whichever occurred first and dividing by the first yield lateral force in that direction. These strain limits chosen for the ideal strength of walls followed the recommendation of Priestley *et al.* (1996). Failure points defined by both concrete and steel strain limits are included in Figures 4-6 and 4-7 to show what controlled the failure surface as a function of loading direction. These figures do not include the effect of shear lag across the flange for the flange-in-tension loading direction. From the results of these analyses, the load path for the test specimen was determined.

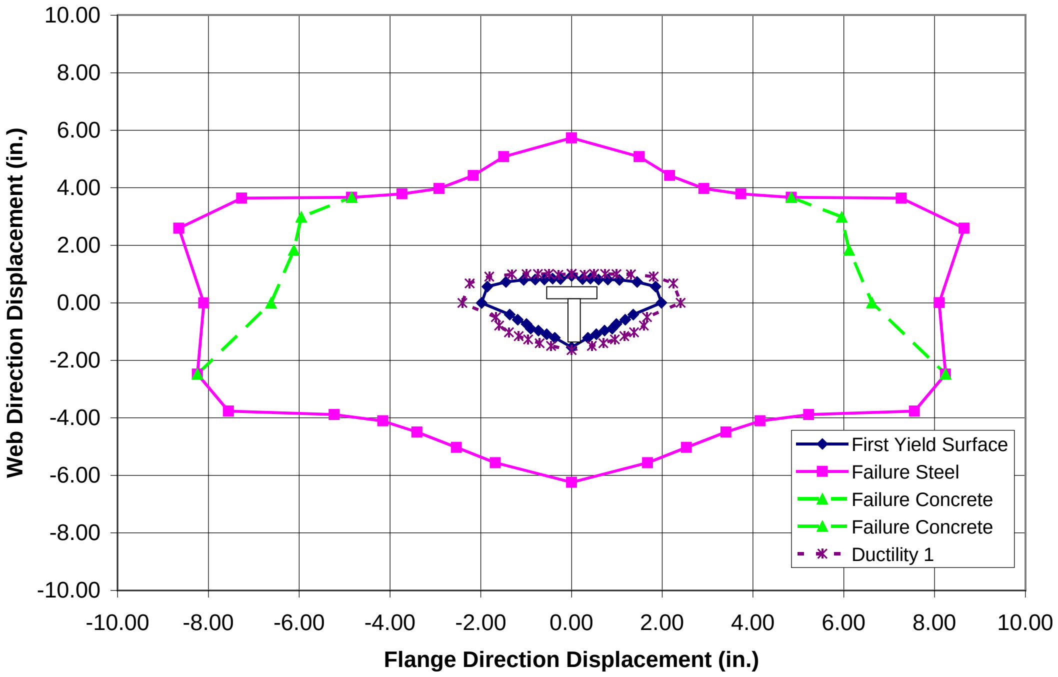

Figure 4-6: Theoretical First Yield and Ultimate Displacement Surfaces Established for NTW1

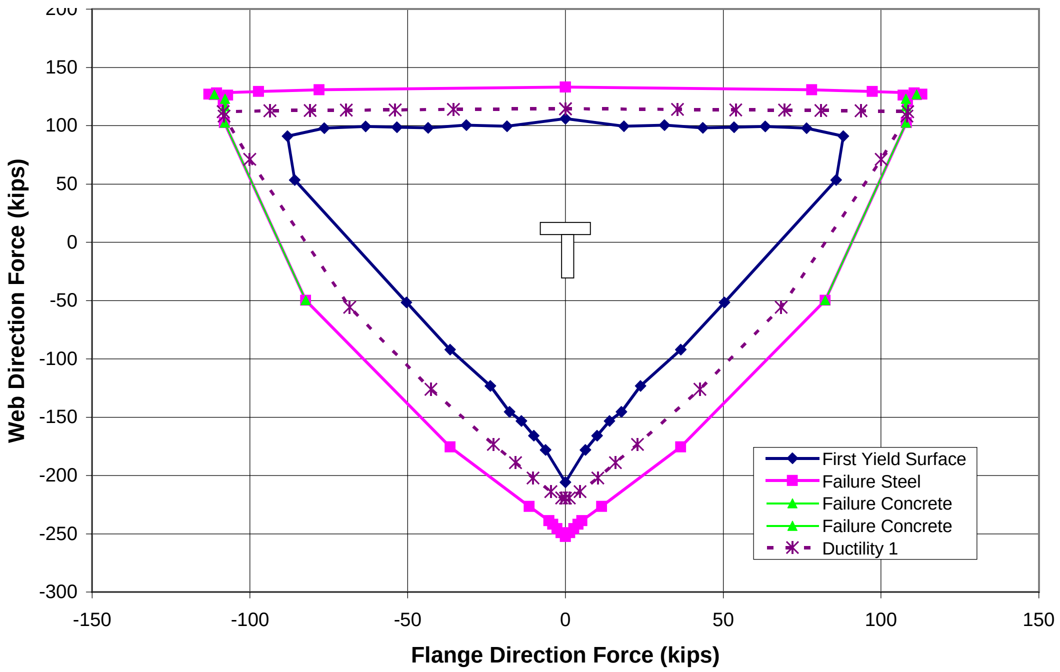

Figure 4-7: Theoretical First Yield and Ultimate Force Surfaces Established for NTW1

For all test cycles, the displacements of the translational degrees-of-freedom (DOF) at the control point, located 24 in. above the top of the top block of NTw1, were specified. The rotational DOF were unconstrained, and thus could take any value required by the analysis. The values of the translational DOF were specified at each time step to allow the wall to be displaced along predicted displacement paths. Although,this approach was initially used for establishing the load paths for the test, the lateral displacements applied by the crosshead were eventually used for the analysis to ensure the analytical model was subjected to the same displacement path as NTW1 for comparing the results. The displacement targets at the bottom of the crosshead were recorded during the tests, these targets were applied at the control point. The 3 in. difference in location resulted in a difference of less than 0.00001 in.

All analyzes were executed using the Krylov-Newton algorithm to minimize the computation time. This algorithm does not update the stiffness matrix at each iteration, saving computational time but may require additional iterations to reach a converged solution. The Krylov-Newton algorithm uses subspace acceleration in order to reduce the number of iterations required to find the converged solution. The convergence was determined based on the displacement increment, and the analysis was allowed up to 200 iterations to find a converged solution. Two hundred iterations allowed the analysis to find a solution, few steps required more than 10 iterations to find a converged solution. If the iteration limit was reached, it was because of an error in the analysis model, or the step was too large and was reduced.

The load path suitable for testing NTW1 was developed in terms of the first yield displacement for any given direction. This resulted in different displacement values in each direction; however, this approach was intended to allow the maximum strains and, therefore, damage in each direction to a similar level prior to moving to the next level of displacement. The selected load path for testing NTW1 are prescribed in Figures 4-8 through 4-19. These load paths were motivated to gain as much experimental information as possible on the following behavior of walls:

- Shear lag for flange-in-tension direction loading;
- Bond slip due to strain penetration;
- Largest strain demand on the concrete/reinforcement;
- Simulation capability of OpenSees; and
- Effect of 2D lateral load path on T-wall response.

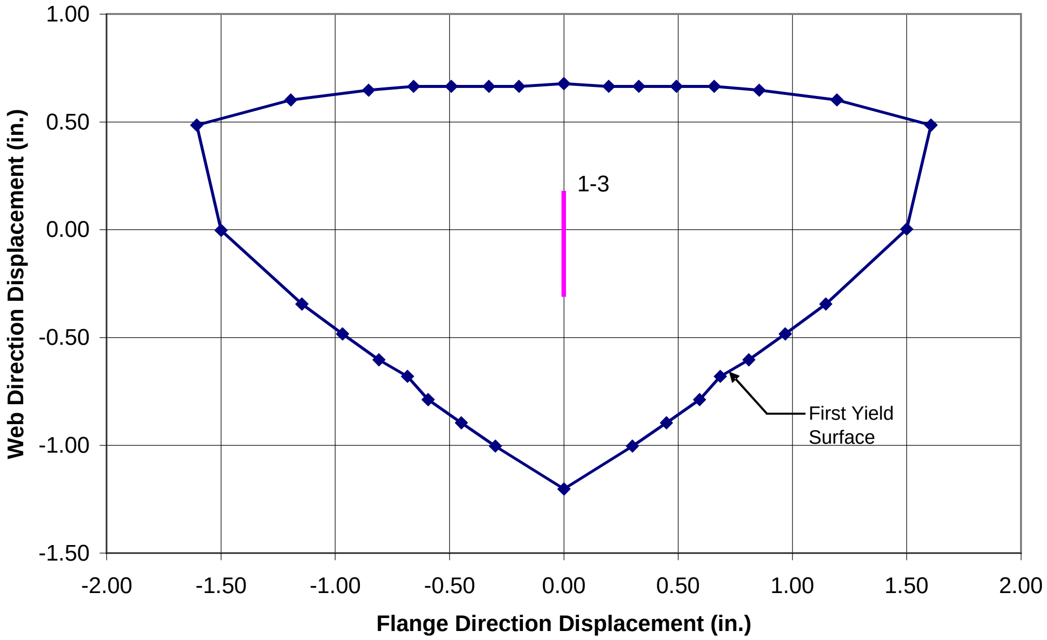

Figure 4-8: Load Steps 1 to 3 to Test in the Web Direction at 25% of the First Yield Displacement.

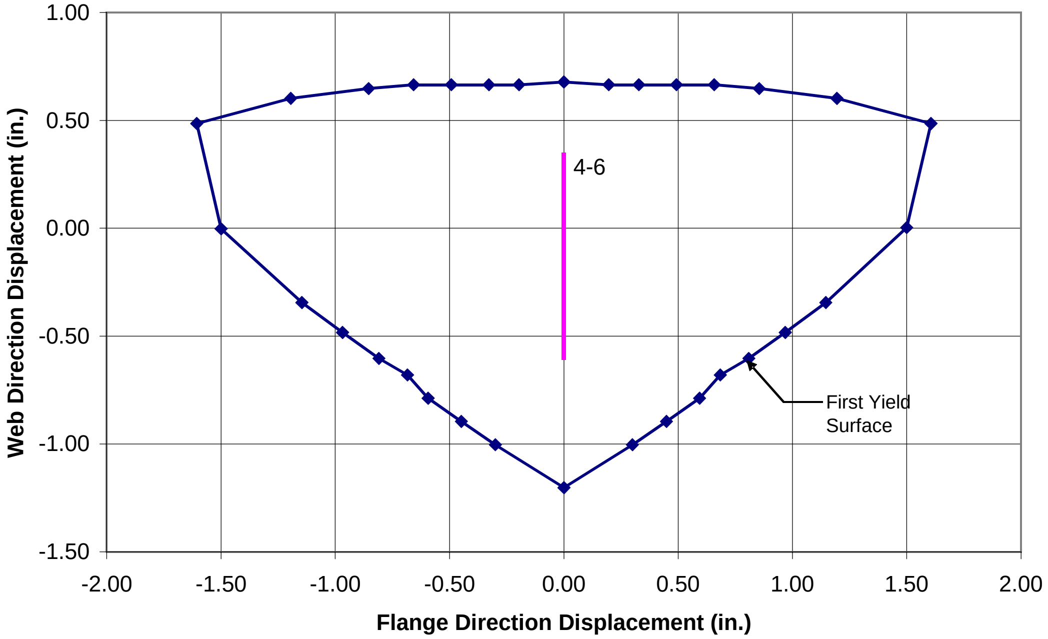

Figure 4-9: Load Steps 4-6 to Test in the Web Direction at 50% of the First Yield Displacement

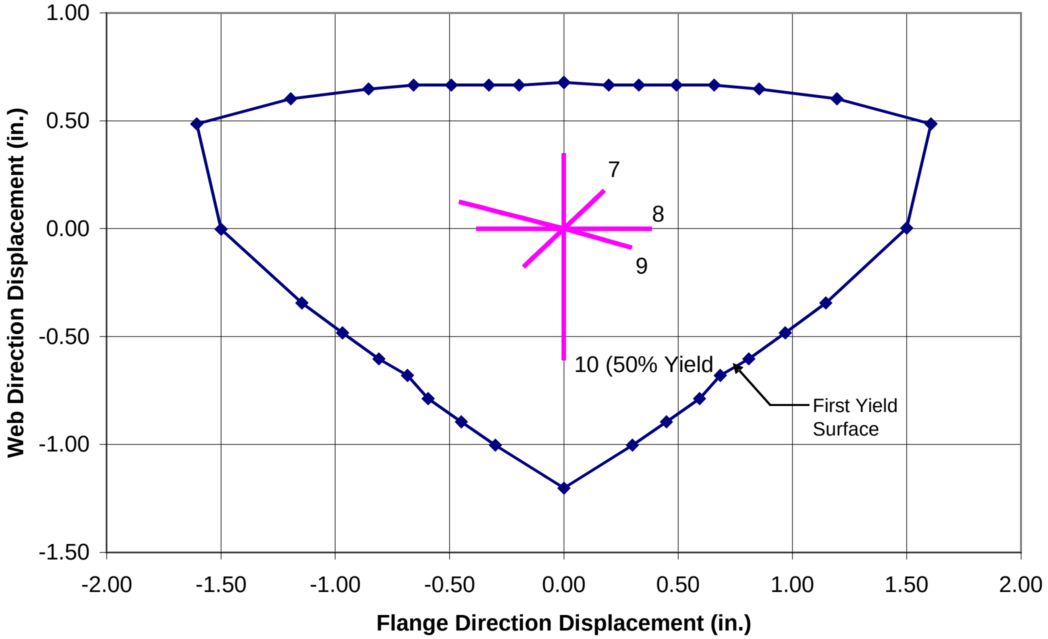

Figure 4-10: Load Steps 7 to 10 to NTW1 at Test 45º, Parallel to the Web, and 100+30 Directions at 25% of First Yield Displacement, and Repeat 50% of the First Yield in the Web Direction

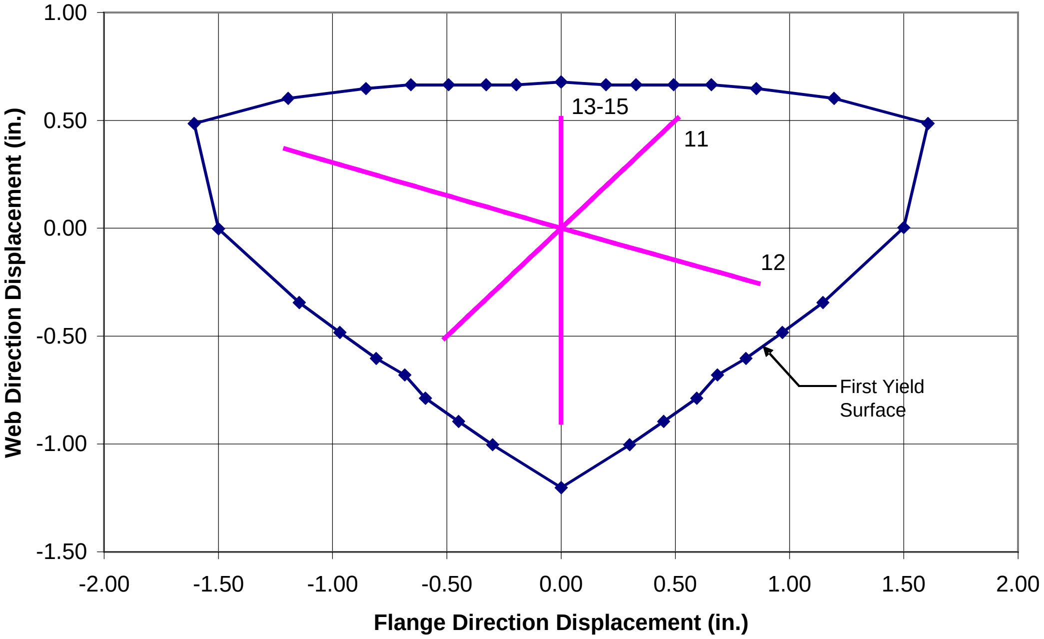

Figure 4-11: Load Steps 11 to 15 to Test NTW1 at 45º, 100+30, and the Web Direction at 75% of the First Yield Displacement

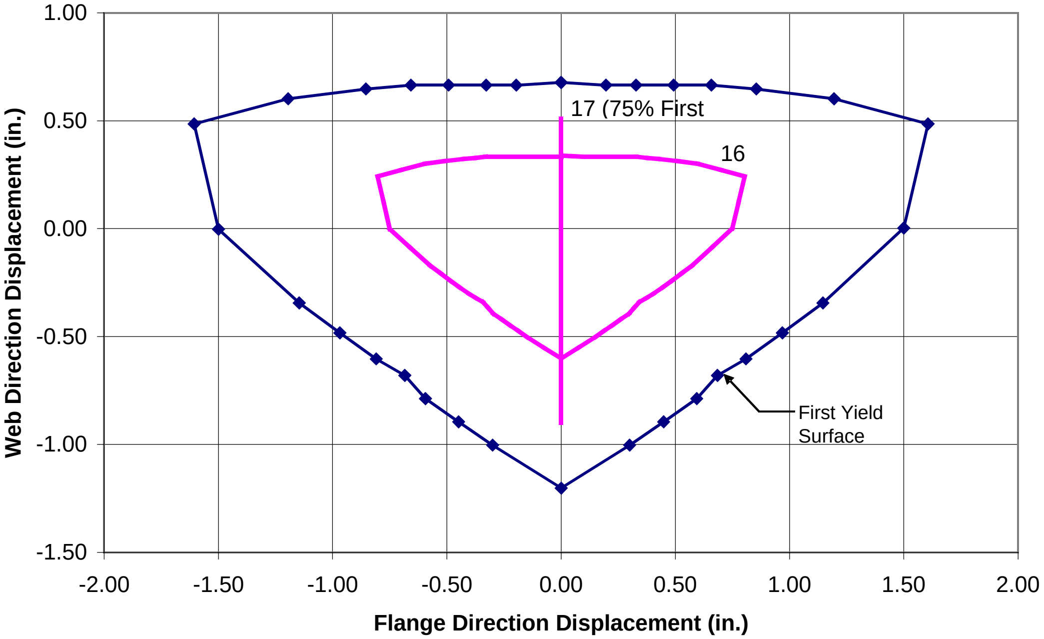

Figure 4-12: Load Steps 16 and 17, to Test NTW1 at 50% First Yield Surface Path and the Web Direction to 75% of the First Yield Displacement

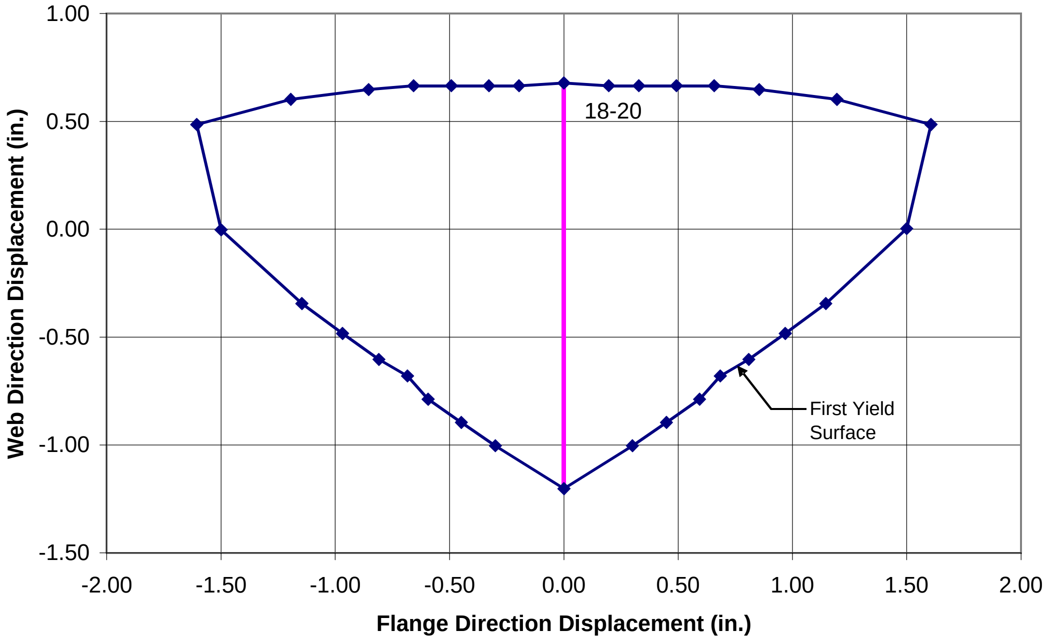

Figure 4-13: Load Steps 18 to 20 to Test NTW1 in the Web Direction at 100% of the First Yield Displacement

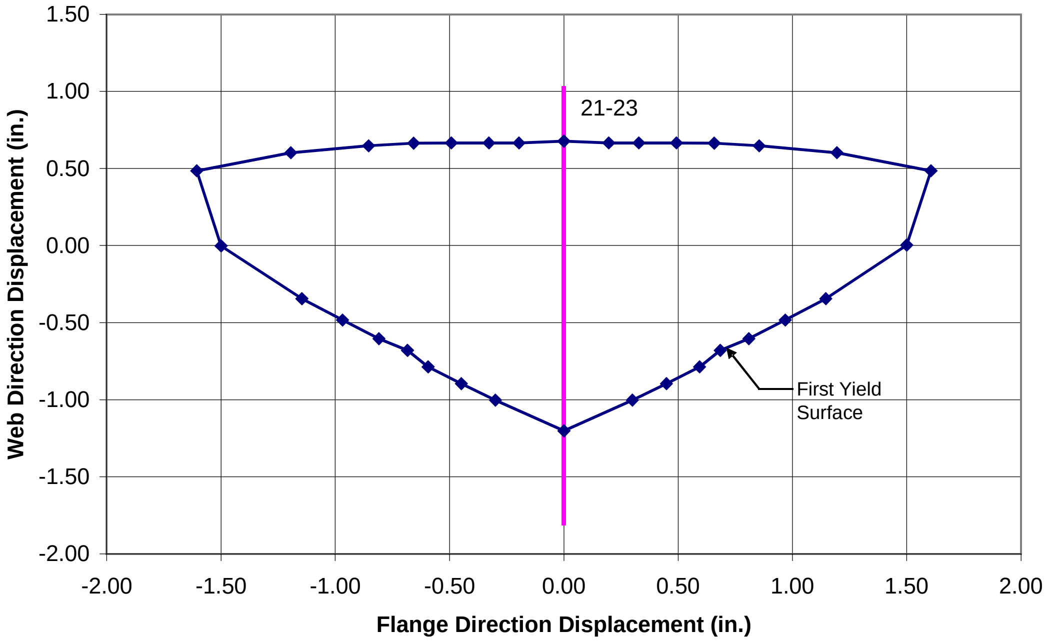

Figure 4-14: Load Steps 21 to 23, to Test NTW1 in the Web Direction at 150% of the First Yield Displacement

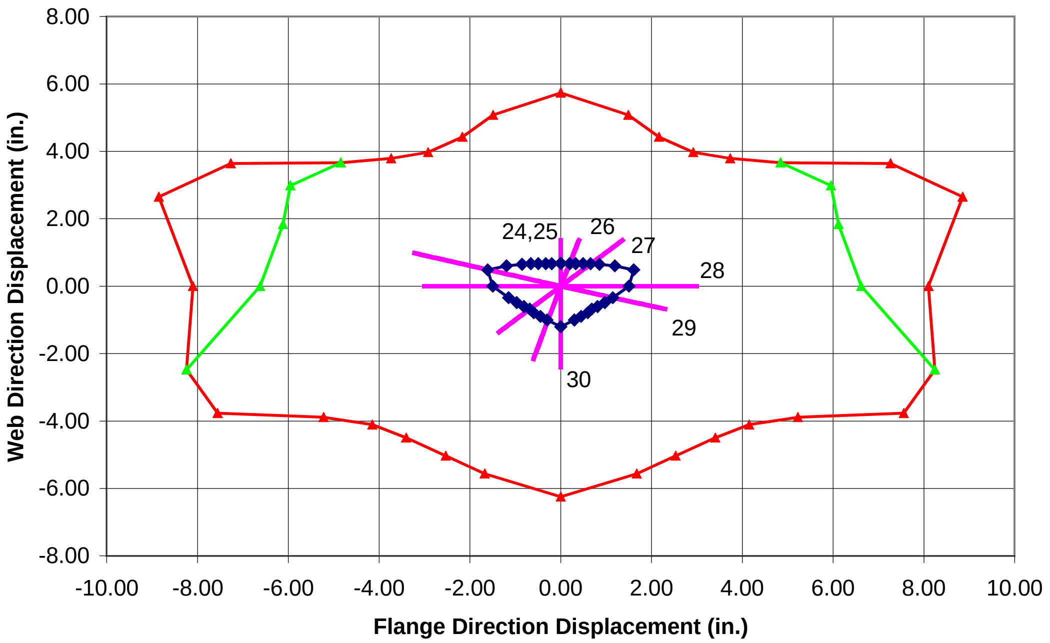

Figure 4-15: Load Steps 24 to 30 to Test NTW1 in Multidirectional Direction at 200% of the First Yield Displacement

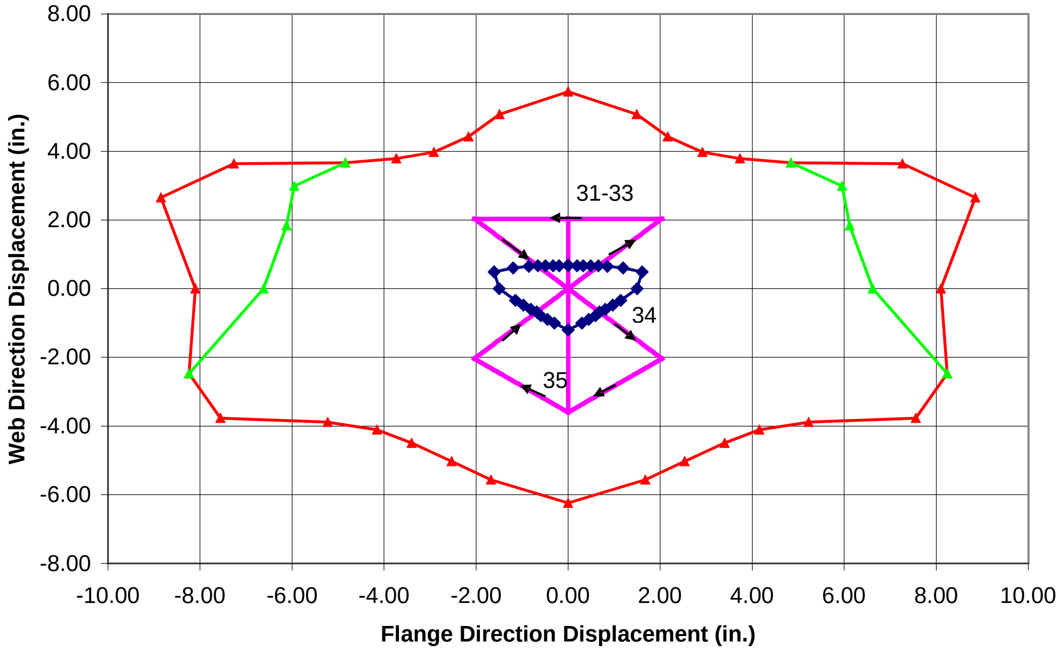

Figure 4-16: Load Steps 31 to 33 and 35 to Test NTW1 in the Web Direction and Load Step 34 to Test NTW1 to Hourglass Path at 300% of the First Yield Displacement

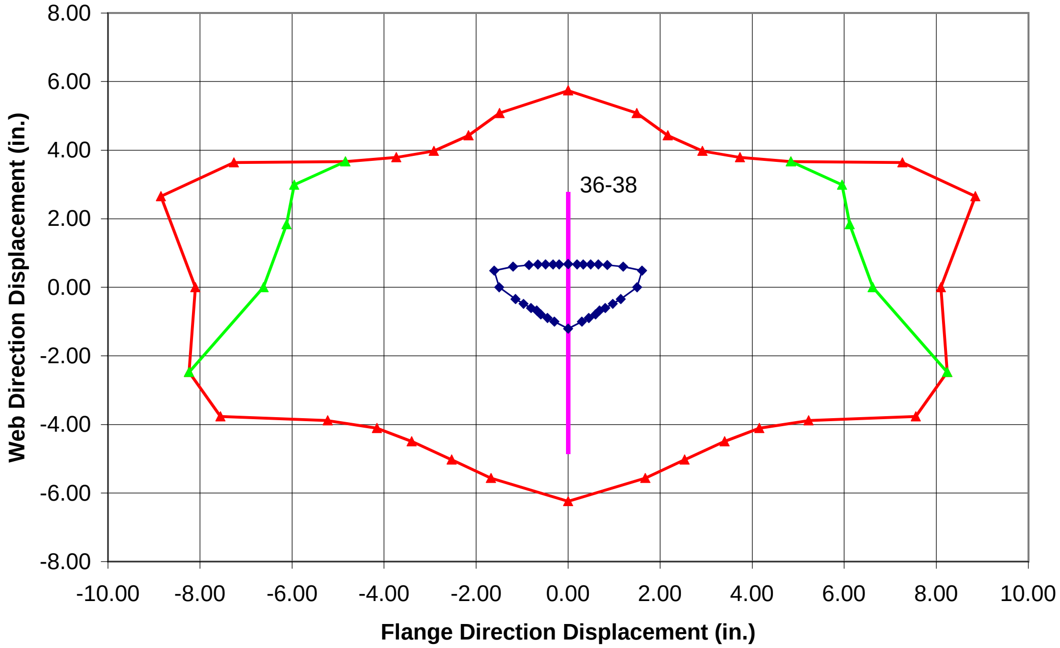

Figure 4-17: Load Steps 36 to 38 to Test NTW1 in the Web Direction at 400% of the First Yield Displacement

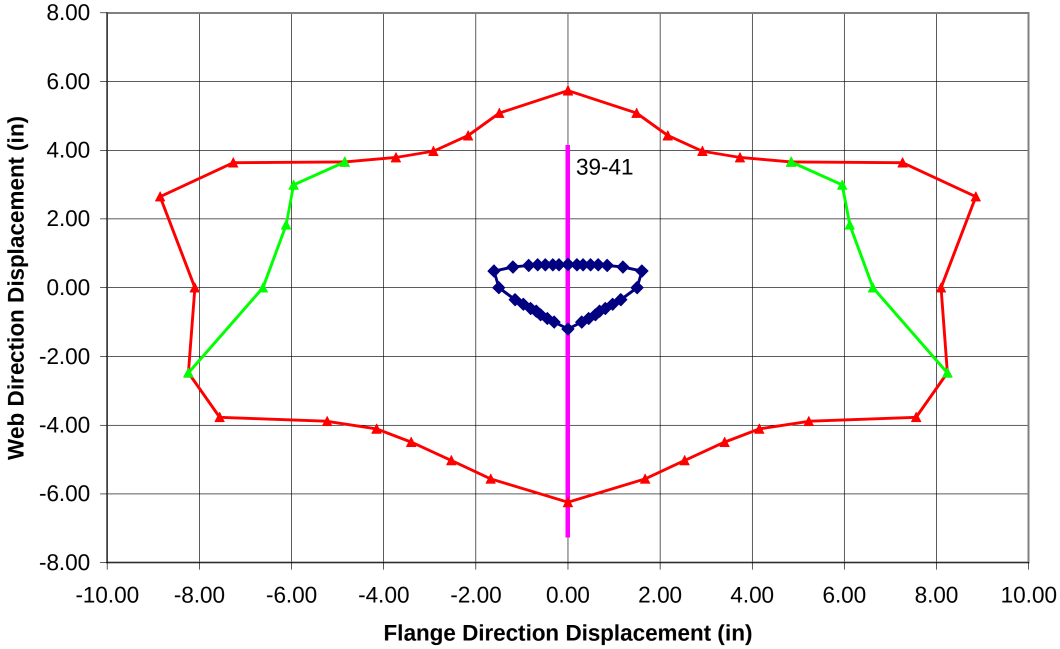

Figure 4-18: Load Steps 39 to 41 to Test NTW1 in the Web Direction at 600% of the First Yield Displacement

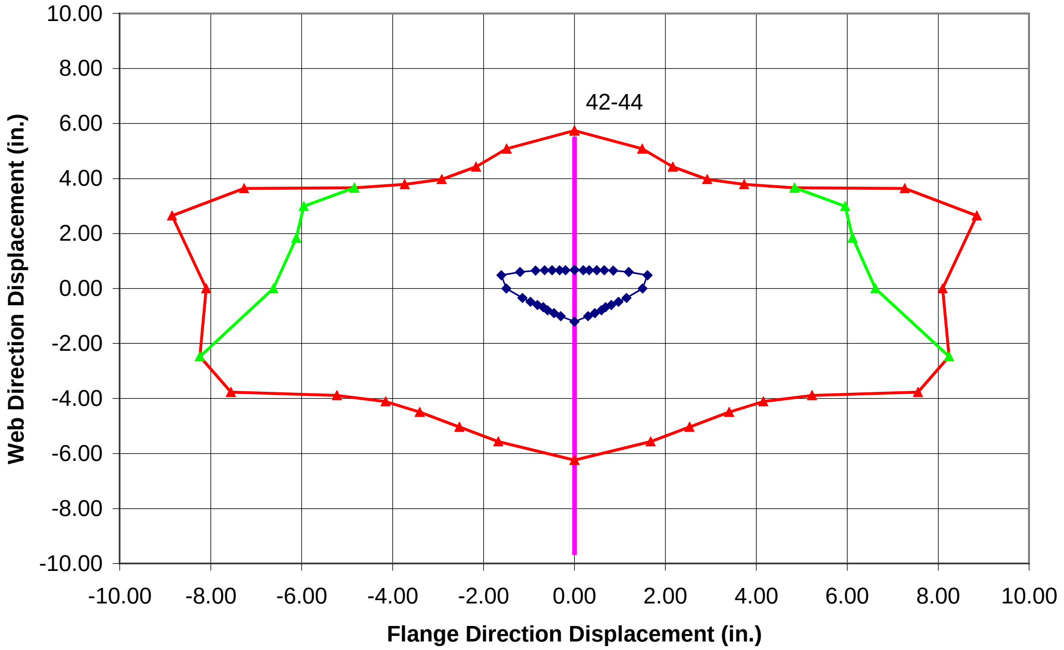

Figure 4-19: Load Steps 42-44 to Test NTW1 in the Web Direction at 800% of the First Yield Displacement

The web direction load cycles were targeted to obtain information on the shear lag and strain penetration behavior. For this reason, the web direction cycles were typically completed first at each new displacement level. The selected inclined load paths subjected the web and flange direction displacements at a constant ratio (e.g., Load Steps 11 and 12 in Fig. 4-11) because they placed high demands on the flange and web tip confined regions.

The load paths described above was the one that was developed prior to the testing of the specimen. However, during testing a number of events that led to modifications to the planned loading protocol. These events included:

- Larger shear deformation than those obtained from the OpenSees analysis.
- Premature buckling of the longitudinal reinforcement in the web tip.

The planned directions of the load path was generally followed up to approximately 2% drift during testing of NTW2. However, the target displacements correspond to the different load cycles were increased because of the increased contribution of the shear deformations in an attempt to reach the desired strain levels. After imposing the 150% of first yield displacement during the test, the target displacements were replaced with target drifts instead of relating targets to the first yield displacements. During the hourglass shaped load path at 2% drift level, buckling of the longitudinal reinforcement in the web tip was observed. In order to maximize the data gained from the test, the loading protocol at this point was changed and the specimen was loaded parallel to the flange to reach target lateral drifts of ±1%, ±1.5%, ±2%, ±3%, and ±4%. Table 4-2 summarizes the actual load protocol used during the test. Figures 4-20 and 4-21 shows the displacement components parallel to the web and flange, respectively, versus the the load step, defined as a movement from one target point to the next target point. For example, a cycle 0 in the web direction includes two load steps, one moving to 0.08 in. and a second moving to -0.12 in.

Table 4-2: Applied Displacement Targets

Cycle No.	Displacement Level	Flange Direction (in.)	Web Direction (in.)
0	10% of First Yield Displacement	0.0	0.08
	Web Direction	0.0	-0.12
1-3	25% of First Yield Displacement	0.0	0.3
	Web Direction	0.0	-0.4
4-6	50% of First Yield Displacement	0.0	0.6
	Web Direction	0.0	-1.1
7	25% of First Yield Displacement	0.86	0.0
	Flange Direction	-0.86	0.0
8	25% of First Yield Displacement	0.29	0.29
	45° Direction	-0.30	-0.30
9	25% First Yield Displacement	0.66	-0.2
	100% Flange + 30% Web	-0.88	0.27
10	50% of First Yield Displacement	0.0	0.6
	Web Direction	0.0	-1.1

Table 4-2 (continued)

Cycle No.	Displacement Level	Flange Direction (in.)	Web Direction (in.)
11	75% of Yield Displacement 45º Direction	0.9	0.9
		-0.71	-0.71
12	75% Yield Displacement 100% Flange + 30% Web	2.0	-0.6
		-2.7	0.8
13-15	75% of Yield Displacement Web Direction	0.0	1.2
		0.0	-1.7
16	Mimic the 50% Yield Surface	0.0	0.8
		0.8	0.8
		1.5	0.55
		1.4	0
		0	1.1
		-1.4	0
		-1.5	0.55
		-0.8	0.8
		0.0	0.9
17	75% of Yield Displacement Web Direction	0.0	1.2
		0.0	-1.6
18-20	100% Yield Displacement Web Direction	0.0	1.56
		0.0	-2.1
21-23	150% Yield Displacement Web Direction	0.0	2.35
		0.0	-3.25
24	1% & 1.5% Drift Web Direction	0.0	3.1
		0.0	-4.7
25	1% & 1.5% Drift 100% Web + 30% Flange	1.0	3.0
		-1.5	-4.5
26	1% Drift Flange Direction	3.2	0.0
		-3.2	0

Table 4-2 (continued)

Cycle No.	Displacement Level	Flange Direction (in.)	Web Direction (in.)
27	1.5% Drift 45º Direction	3.4	3.4
		-3.4	-3.4
28	1.5% Drift Flange Direction	4.8	0.0
		-4.8	0.0
29	1.5% Drift 100% Flange + 30% Web Direction	-4.6	1.4
		4.6	-1.4
30-31	1% & 1.5% Drift Web Direction	0.0	3.1
		0.0	-4.7
32-34	1.5% & 2% Drift Web Direction	0.0	4.8
		0.0	-6.4
35	2.0% Drift Hourglass Displacement Path	4.5	4.5
		-4.5	4.5
		4.5	-4.5
		0	-6.4
		-4.5	-4.6
		0	0
36	1.5% Drift Flange Direction	4.8	0.0
		-4.8	0.0
37-39	2% Drift Flange Direction	6.4	0.0
		-6.4	0.0
40-42	2.5% Drift Flange Direction	8.0	0.0
		-8.0	0.0
43-45	3% Drift Flange Direction	9.6	0.0
		-9.6	0.0

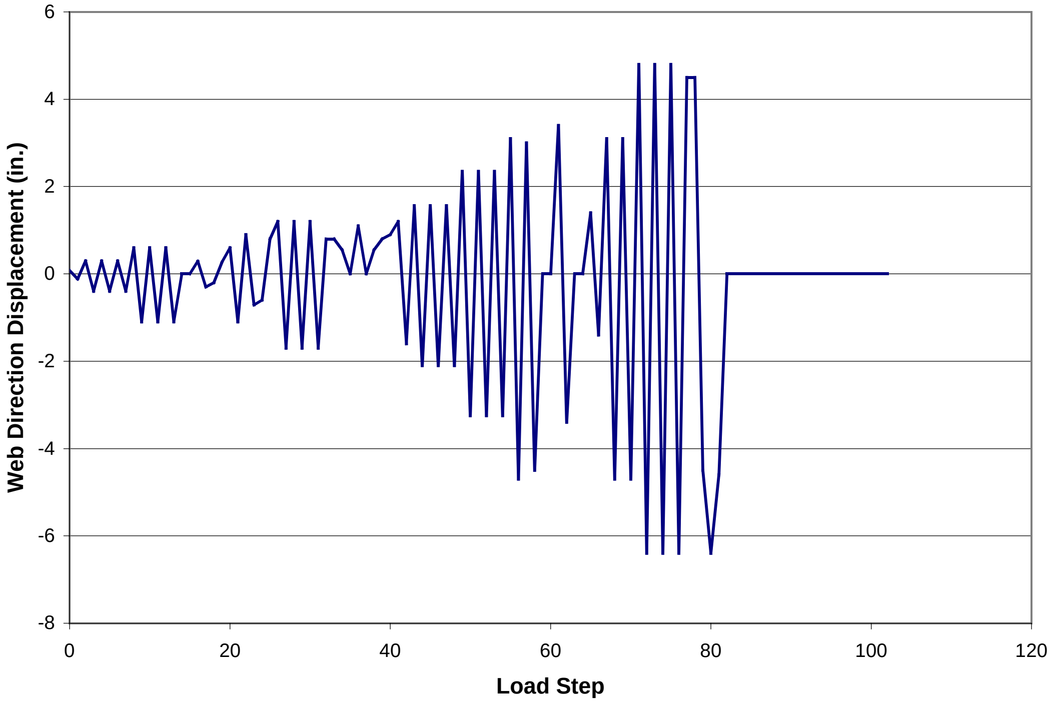

Figure 4-20: Displacement Component of the Load Protocol used for NTW1 Parallel to the Web Direction

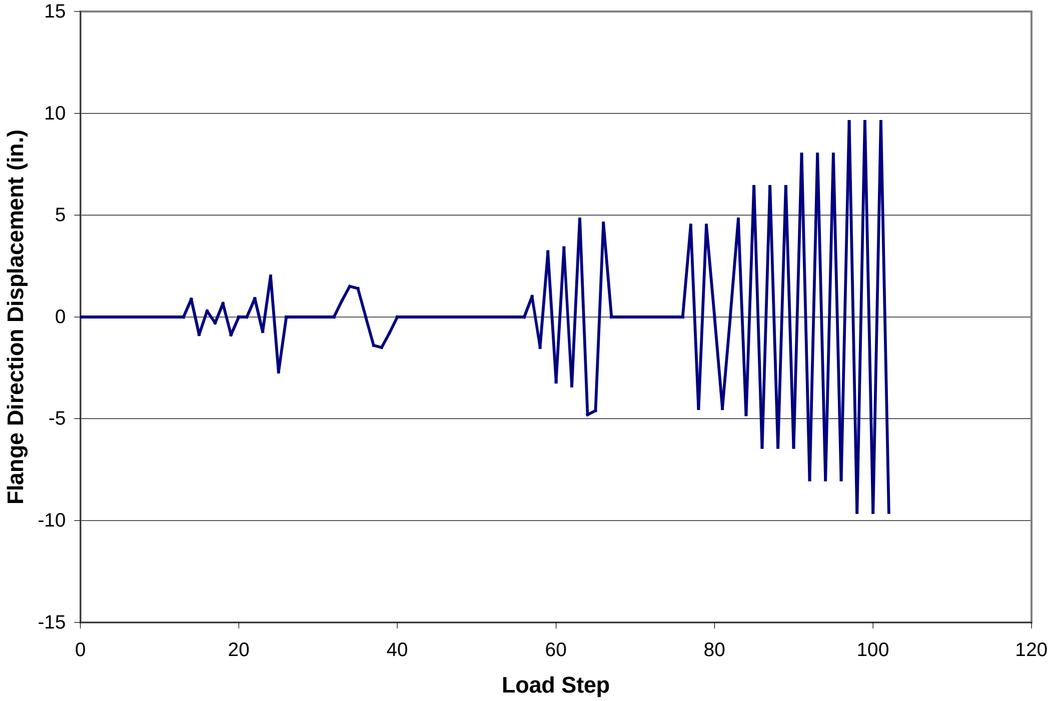

Figure 4-21: Displacement Component of the Load Protocol used for NTW1 Parallel to the Flange Direction

4.5 Summary of Response

NTW1 was subjected to the load protocol summarized in Table 4-2 beginning on June 15, 2006 and was completed on June 28, 2006. The test took 7 days to complete. The observed cracking of the wall followed a specific pattern; cracks were small and well distributed in the boundary elements and then became significantly wider and spaced further apart outside of the boundary elements. The reduced spacing of the longitudinal reinforcement in the boundary elements led to better crack distribution; whereas the large spacing of the longitudinal reinforcement outside of the boundary elements led to large concentrated cracks. This crack pattern is seen in Figure 4-22 for the web, a similar pattern was observed in the flange. The response was very stable in all the loading directions, repeated cycles showed a small drop in the second cycle at a displacement level; however, no drop was observed between the second and third cycle.

Failure was first observed in the web tip during the hourglass shaped load path. As NTW1 approached the -6.4 in. of web direction displacement target buckling of the longitudinal reinforcement in the boundary element was observed. This failure ceased loading in the web direction. The specimen was then cycled to return the specimen as close to zero displacement, zero force in both the web and flange directions.

NTW1 was then cycled parallel the flange in order to maximize the information from the test. The specimen showed a stable response in this direction even after failure in the orthogonal direction. The specimen showed a stable response until failure due to bucking of the longitudinal reinforcement in the boundary element at 3% lateral drift. Upon reversal the bars that had buckled fractured. Figure 4-23 shows NTW1 following failure of the flange boundary element.

NTW1 performed very well overall, with the exception of the large cracks that formed outside the boundary elements in both the flange and the web. For additional information about the testing see Brueggen (2009) where a complete description of NTW1's response can be found.

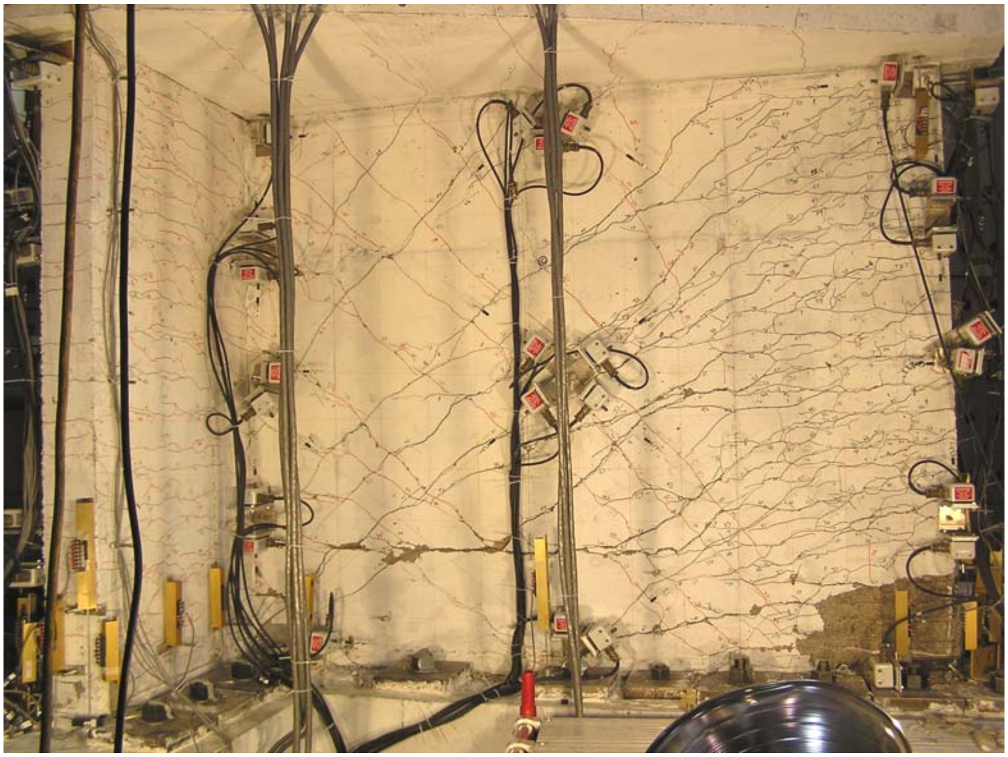

Figure 4-22: Observed Cracking of NTW1 in the Web

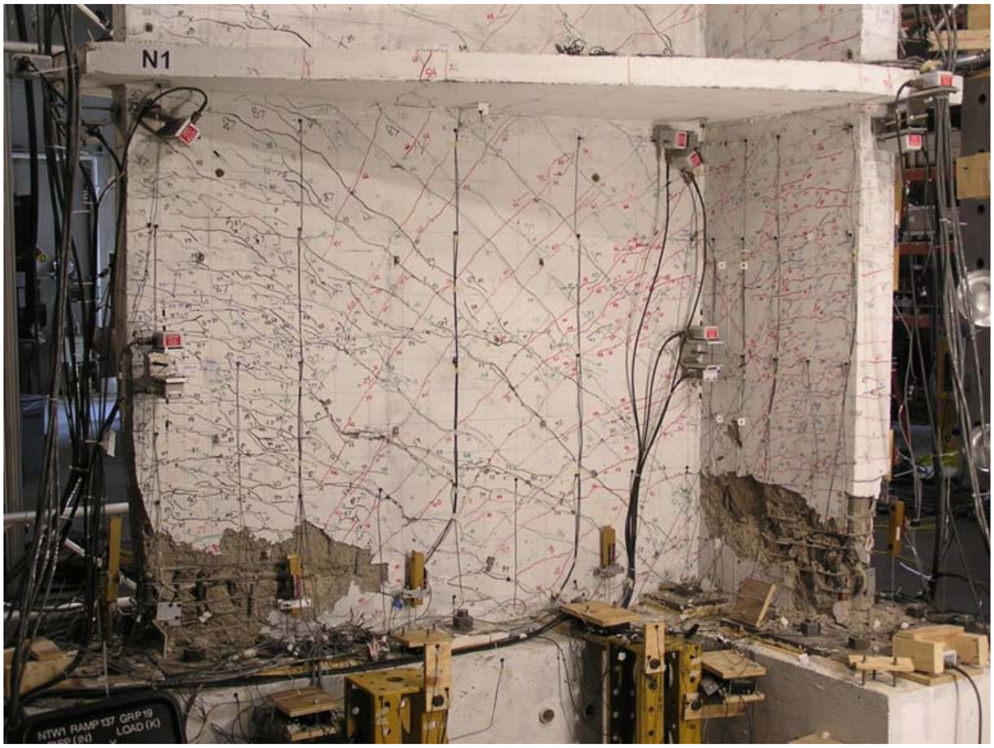

Figure 4-23: NTW1 Following Completion of the Load Protocol

4.6 Pretest Analysis Results

The concrete material properties were updated from the estimated properties based on three uniaxial compressive tests of six-inch diameter concrete cylinders tested on the day before testing NTW1 began. The average measured unconfined concrete compressive strength was 7260 psi, the average tensile strength was taken as 880 psi based on split cylinder tests. The confined concrete properties were updated using the average measured concrete strengths and the Mander *et. al.* (1988) confined concrete model. However, he model used for the prediction of the behavior of NTW1 was generally unsatisfactory and can be seen in the comparison between the analytical monotonic response envelope and experimental response shown in Figure 4-24 for the direction parallel to the web and in Figure 4-25 for the direction parallel to the flange. As can be seen, the OpenSees model failed to capture the elastic stiffness of the wall in both loading directions and overpredicted the envelope for the flange direction loading.

The prediction of the cyclic response was generally not satisfactory. The stiffness of the wall was overpredicted similar to the monotonic prediction. Additionally, the residual displacement was underpredicted by the analysis, due to the use of Kent-Park concrete model (i.e. Concrete03 in OpenSees. The cyclic prediction is not presented because of the poor comparison, as expected based on the monotonic prediction.

4.7 Details of Improved Model

Following completion of testing of NTW1, the causes of the discrepancies in Figure 4-24 and 4-25 were investigated. The cause for the discrepancies was largely attributed to neglecting the effects of shear deformation and inaccurate simulation of the shear lag in the flange. The large discrepancies seen in the flange direction response is due to the load protocol emphasizing loading NTW1 in virgin territory in the direction parallel to the web. This caused some damage to the specimen in the flange tips prior to loading the wall in the flange direction, leading to the significant decrease in the lateral force resistance seen in Figure 4-25, demonstrated in the next section through the cyclic analysis of NTW1. In addition to using test day material properties, in the post-test analysis of NTW1, the concrete model for the fibers was also changed from the Kent-Park model to the the modified Chang and Mander model described in Chapter 3.

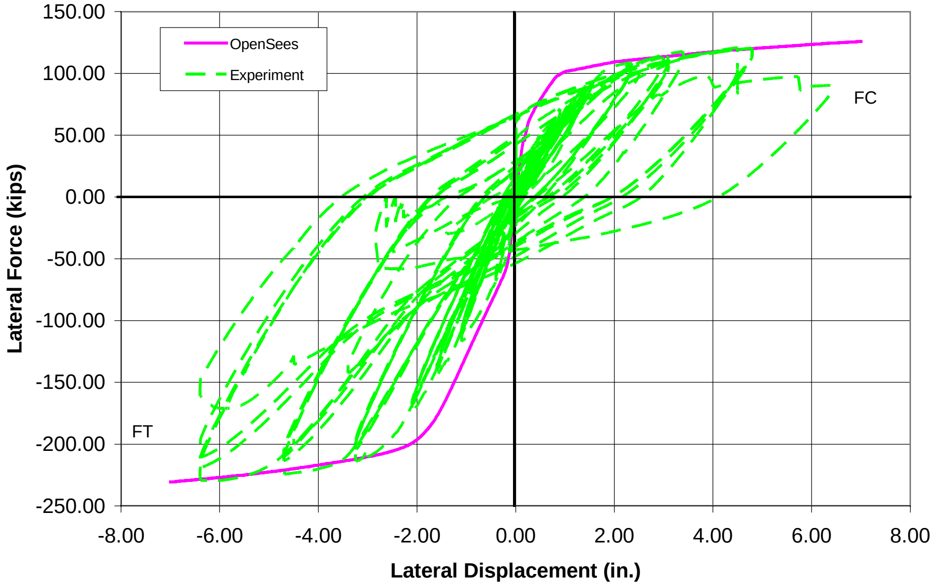

Figure 4-24: Comparison of Predicted Monotonic Envelope of NTW1 in the Web Direction with Experimental Data (shear deformation was not included)

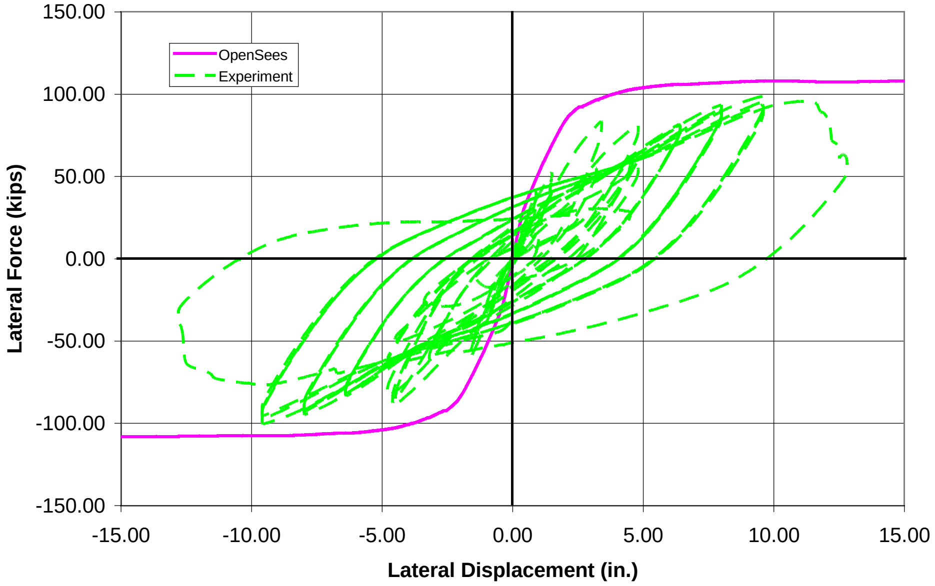

Figure 4-25: Comparison of Predicted Monotonic Envelope of NTW1 in the Flange Direction with Experimental Data (shear deformation was not included)

The reason for ignoring the effects of shear deformation in the original analysis was that the aspect ratio of the wall was greater than three, suggesting flexurally dominant response of the wall. However, the experimental data clearly showed that shear deformations contributed to the overall wall response significantly. The fiber sections used in OpenSees did not account for the shear deformation of the specimen and had to be addressed separately. The method chosen to address this issue was to use a uniaxial material model to simulate the force-distortion relationship using Pinching4 available in OpenSees. The envelope of the Pinghing4 material model suitable for NTW1 was determined by selecting four points in the experimental force-distortion graph in both the positive and negative quadrants. The parameters for reloading/unloading were selected by comparing the cyclic behavior of the material model to the recorded shear distortion in NTW1. The Pinching4 model as included to capture the shear deformation for the first floor of NTW1 is compared with the experimental data in Figure 4-26, which shows that the analytical model simulated the envelope and the reloading stiffness satisfactorily. However, the unloading stiffness and residual distortion were not generally well simulated. This discrepancy was due to the limitations of the chosen material model but the Pinching4 model was the best material model available in OpenSees for this application.

Figure 4-27 shows the Origin-Centered Hysteretic model chosen for the simulation of the shear deformation in the second and third floors of NTW1. The Origin-Centered Hysteretic model was considered to be adequate to capture the shear deformation in the upper floors due to the limited inelastic shear deformations expected at these floor levels. Figure 4-25 compares the Pinching4 material model used for the shear-distortion behavior in the direction parallel to the flange for the first floor of NTW1. The shear deformation above the third floor parallel to the web direction and above the first floor parallel to the flange direction was modeled using elastic material models, with stiffness of 448,074 k/rad and 40,508 k/rad for parallel to the web and flange directions, respectively. The decision to use elastic properties was based on observing no inelastic shear deformation in the second floor level in the flange direction, and observing no inelastic shear distortion of the fourth floor prior to failure in the web direction. The stiffness was chosen to match the average shear stiffness of the experimental response determined from the web and flange panel data.

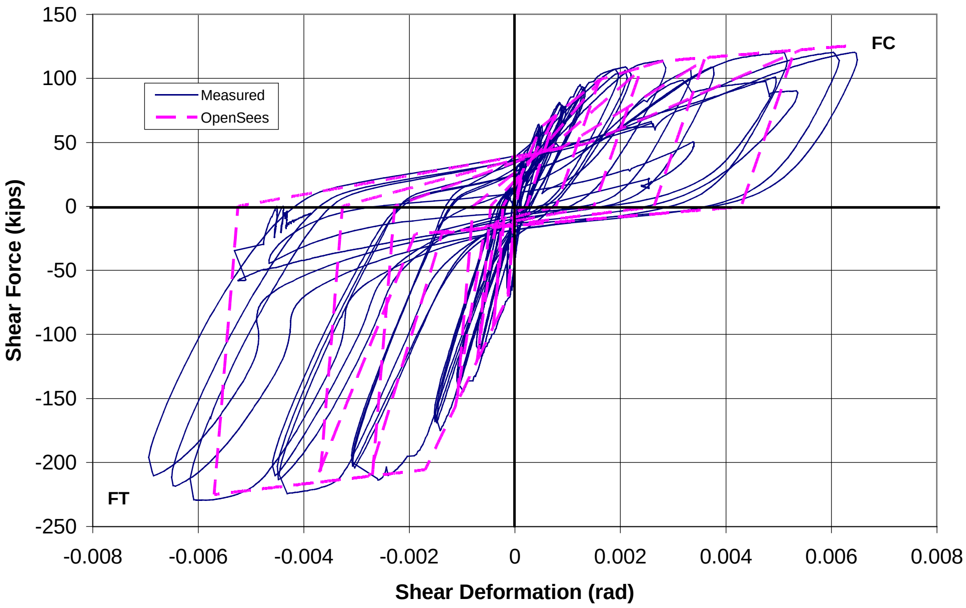

Figure 4-26: Comparison of Measured Shear Response for the First Floor of NTW1 in the Web Direction with the Response of Selected OpenSees Material Model

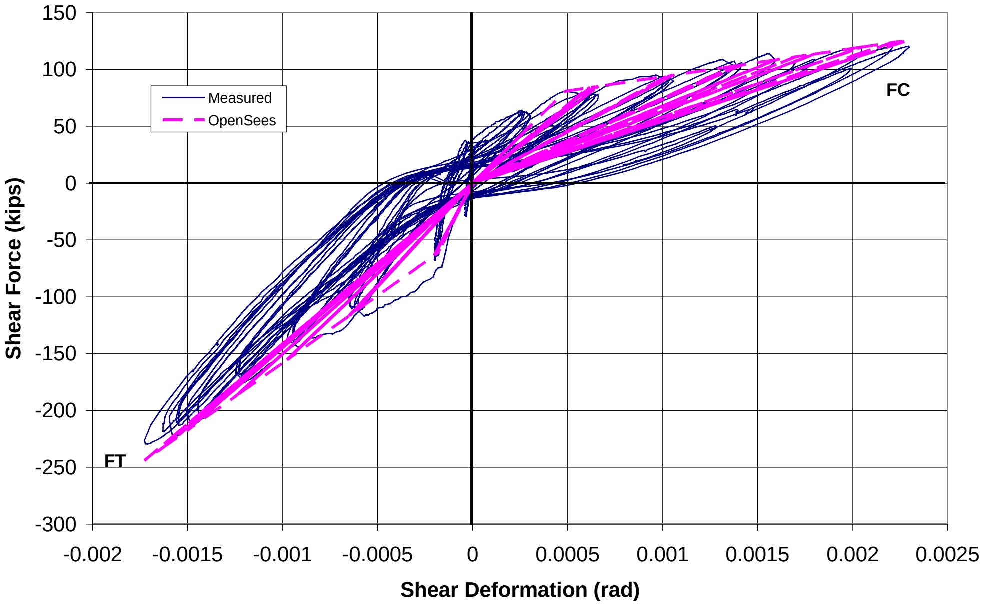

Figure 4-27: Comparison of Measured Shear Response for the Second Floor of NTW1 in Web Direction with the Response of Selected OpenSees Material Model

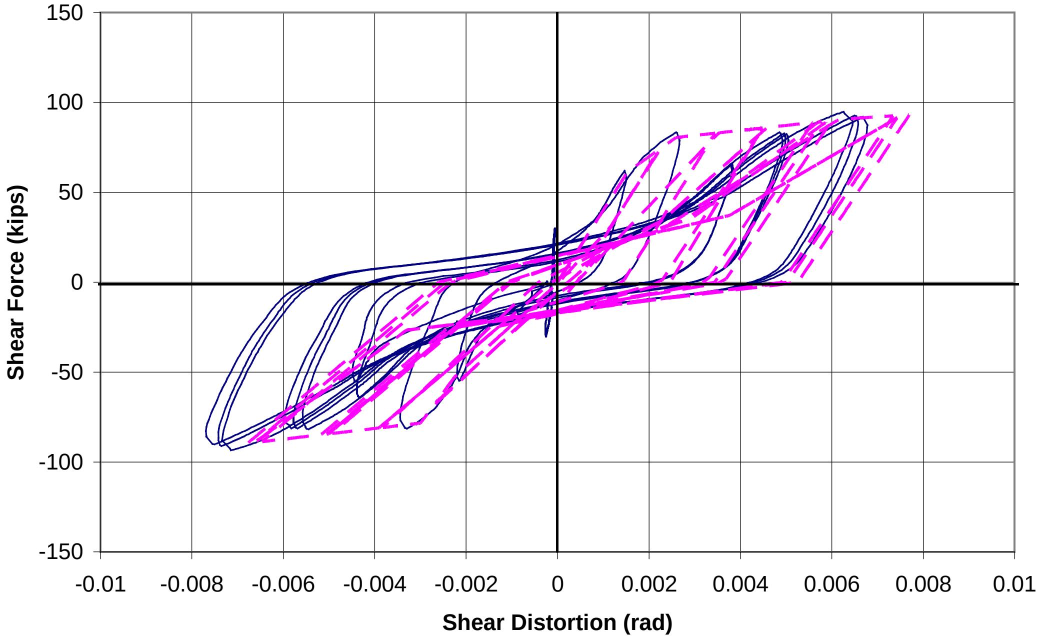

Figure 4-28: Comparison of Measured Shear Response for the First Floor of NTW1 in the Flange Direction with the Response of Selected OpenSees Material Model

Because different material models were used to simulate the shear behavior at each floor level, the OpenSees model had to be modified appropriately. The model used for the post-testing analysis consisted of one force-based beam-column element at each floor level. The shear response is a member level response; however, it is specified with the section definition in OpenSees. Even though the shear material is connected to the section, the shear does not modify the response of the fiber section. The shear material model was then aggregated onto the section used for the beam-column at each floor level. Thus the section uses the fiber discretization to determine the axial and flexural responses, and provides the shear force to the shear material to determine the shear distortion response. Aggregating the material model onto the section is conceptually similar to placing a shear spring in parallel with the beam-column element. This increased the number of elements and run time of the analysis.

Two issues related to the approach described above for including the shear deformation in the analysis are worthy of discussion. The shear deformation in each direction was calibrated against the test data from that direction only. Therefore, the shear deformation in the web direction loading only included the shear behavior of the web, while the flange direction loading was created based only on the shear deformation of the flange. While this includes the major source of the shear deformation, the effect of the flange on the shear-distortion for the direction parallel to the web loading was not included. However, the data on the shear-distortion data from the flange during web direction loading did not show a clear pattern of response and was limited to 0.08 rad, and thus ignoring this component was not of a significant concern. A similar observation was made with regard to the effect of the shear deformation of the web on the flange direction response. Additionally, because the shear response is aggregated onto the section response in the two primary directions, the shear deformation in any arbitrary direction is simply the summation of the shear deformations obtained for the two directions separately. How accurately this reflects the real behavior of the T-wall needs to be examined. If this is not an accurate reflection of the behavior of the T-wall, this topic would deserve further research and appropriate modification to the fiber analysis in OpenSees.

4.7.1 Modeling of Shear Lag

Based on the results of an analysis of the second of two T-walls tested by Thomsen and Wallace [1993], a new fiber section was implemented in OpenSees by modifying the existing fiber section to include the effects of shear lag. The results from the Thomsen and Wallace T-wall indicated that significant shear lag should occur across the width of the flange, as illustrated in Figure 4-29. In order to understand the effect of shear lag, the new fiber section varied the strain passed down to the material models in the flange when the flange is placed in tension. The shape of the strain distribution was based on the average strain obtained from the LVDTs mounted at the base of the wall. The equation used for determining the strain across the flange width was:

$$\varepsilon = \varepsilon_0 + \Phi_y * z * (-0.1140527 * \left(\frac{B}{t}\right) * \left(\frac{2\mathrm{y}}{B}\right)^2 + 1) + \Phi_z * y \qquad \text{(Eqn. 4-1)}$$

where ε is the total uniaxial strain in the fiber, ε_0 is the strain due to axial load, Φ_y is the curvature about the local y-axis, Φ_z is the curvature about the local z-axis, B is the flange overhang length, t is the flange thickness, and z and y are respectively, the coordinates of the fiber of interest relative to the centroid. Figure 4-30 illustrates the physical interpretation of the variables

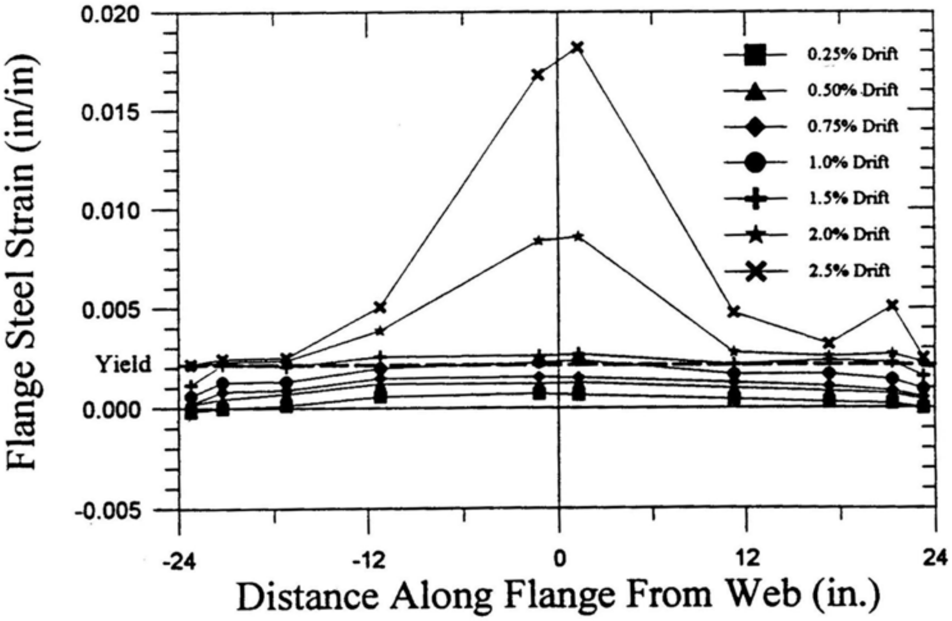

Figure 4-29: Strain Distribution Across Flange Near Base of T-wall from Thomsen and Wallace Specimen TW2 [Thomsen & Wallace, 1993].

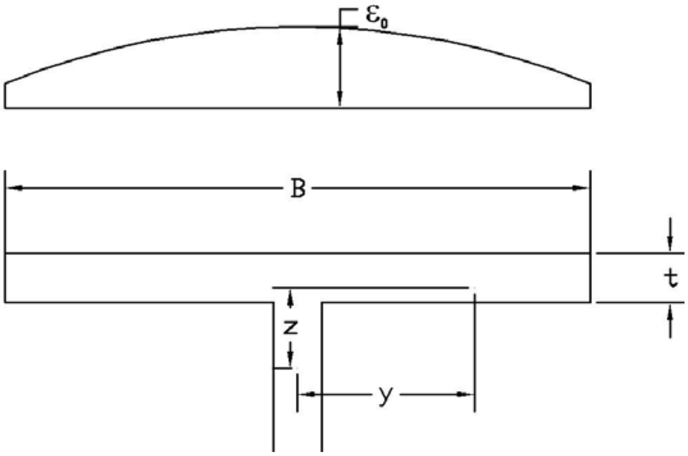

Figure 4-30: Variables used to Define Shear Lag Behavior

4.8 Results of Improved Analytical Model

Figures 4-31 and 4-32 show the monotonic response envelope after including the effects of shear and shear lag. The monotonic envelope is well captured in the two orthogonal directions. The discrepancy seen in the flange direction after yielding is caused by the damage that occurred during loading in the web direction prior to loading in the flange direction. The experimental response would be closer to the the monotonic envelope if the load path had focused on the flange direction rather than the web direction. This is confirmed by the cyclic comparison presented in the next section as well as the study presented in Appendix A.

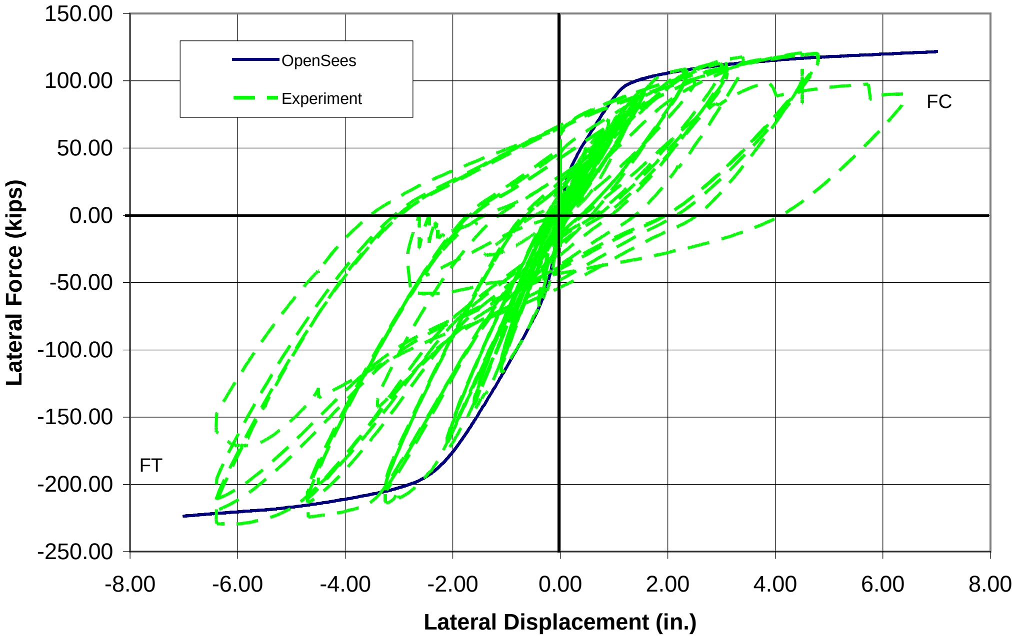

Figure 4-31: Comparison of Monotonic Envelope of NTW1 in the Web Direction Including the Effects of Shear and Shear Lag with Experimental Response

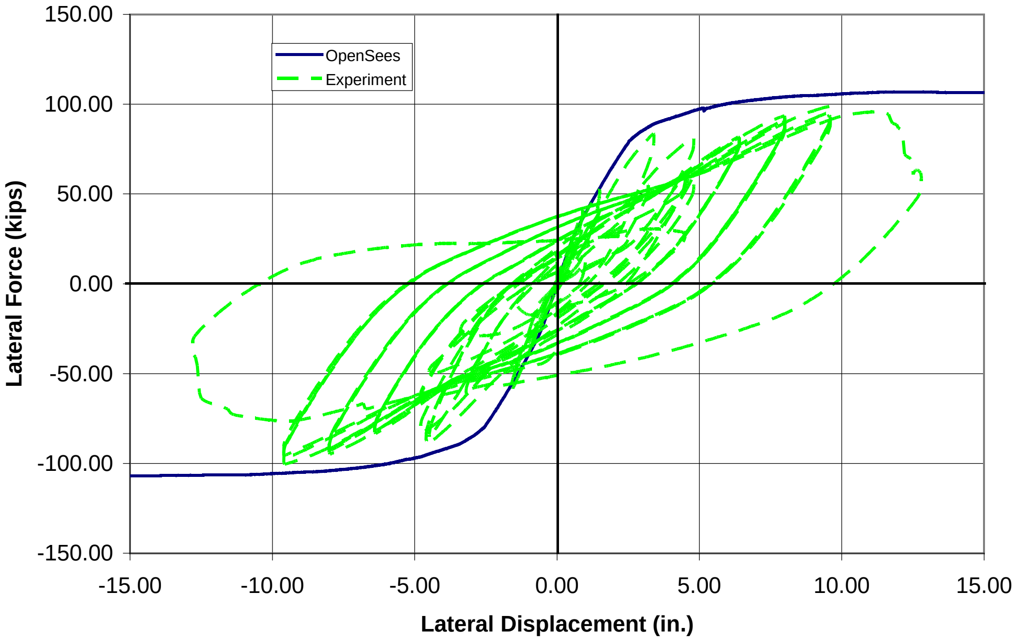

Figure 4-32: Comparison of Monotonic Envelope of NTW1 in the Flange Direction Including the Effects of Shear and Shear Lag with Experimental Response

4.8.1 Cyclic Response Comparison

The measured and calculated cyclic responses of NTW1 to the load path defined in Figures 4-19 and 4-20 are shown in Figures 4-33 and 4-34 for the flange and web directions, respectively. For the post-testing analysis, the concrete was modeled using the modified Chang and Mander concrete model and the test day concrete properties. As shown, the OpenSees simulation accurately captured the force-displacement response of NTW1 in the flange direction. The unloading, reloading, and residual displacement were well simulated by the analysis model. However, in the web direction although the simulated response is satisfactory, the OpenSees model did not capture the response as accurately as it did in the flange direction. This can be seen in Figures 4-35 and 4-36 that show the lateral force versus cumulative displacement for the web and flange direction responses, respectively. These figures give a different view of the comparison between the OpenSees model and measured responses. In addition, Figures 4-37 and 4-38 show the same force versus cumulative displacement responses, but they present close-up views of the initial region in order to examine the responses in the elastic region. Overall, Figures 4-35 to 4-38 more clearly show many of the observations made in the force-displacement responses in Figures 4-33 and 4-34. Furthermore, they show how accurately the OpenSees model simulated the behavior of NTW1 in both elastic and inelastic regions despite subjecting NTW1 to a complex load path. There were some differences in the flange-in-tension direction response after developing flexural cracks at a drift of 0.15% and prior to yielding of the longitudinal reinforcement in the flange. In the flange direction, the measured and OpenSees responses were almost identical, supporting the conclusion that the plane section remain plane assumption for bending parallel to the flange is an acceptable assumption of the section behavior in that direction.

In neither the flange nor the web direction response is any pinching of the response near the origin evident either in the analytical nor measured response. The walls were designed to code requirements and was detailed with adequate shear reinforcement to prevent shear failure. Thus it is not surprising that pinching of the global for displacement response. Repeat cycles at a particular displacement level did not show continuing degradation, also as expected. Pinching of the response, rather than the large, open hysteretic loops seen in the response of NTW1 would be expected if the specimen were experiencing significant damage at each cycle, such as during failure. Pinching of the force-displacement response would be indicative of poor detailing and adequate shear reinforcement. However, the code requirements were adequate to to prevent any pinching of the observed response.

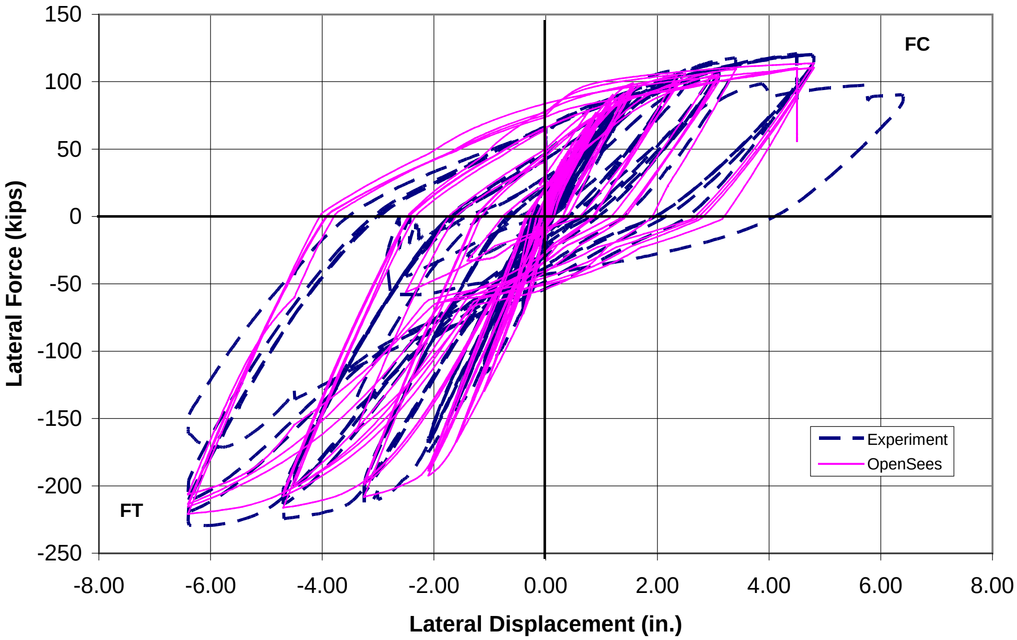

Figure 4-33: Measured and Calculated Force-Lateral Displacement Responses of NTW1 in the Web Direction

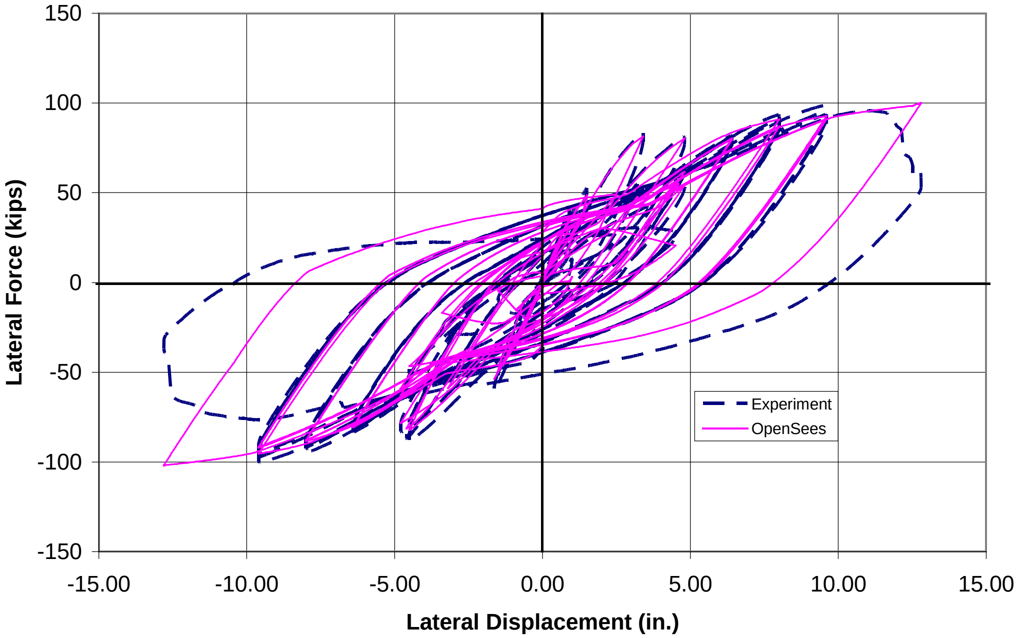

Figure 4-34: Measured and Calculated Force-Lateral Displacement Response of NTW1 in the Flange Direction

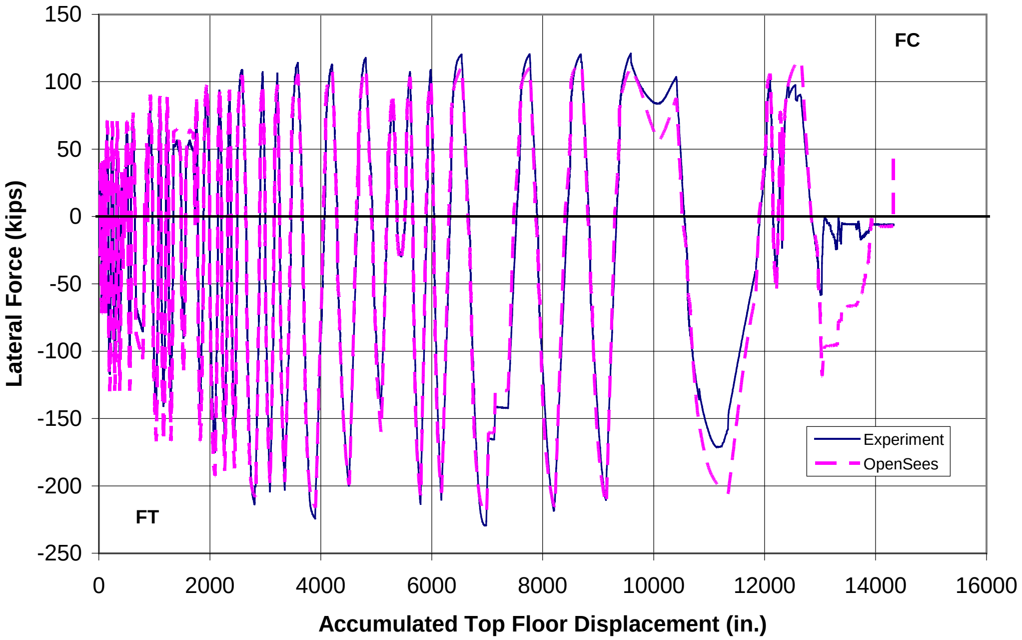

Figure 4-35: Comparison of Responses of NTW1 in the Web Direction as a Function of Cumulative Displacement

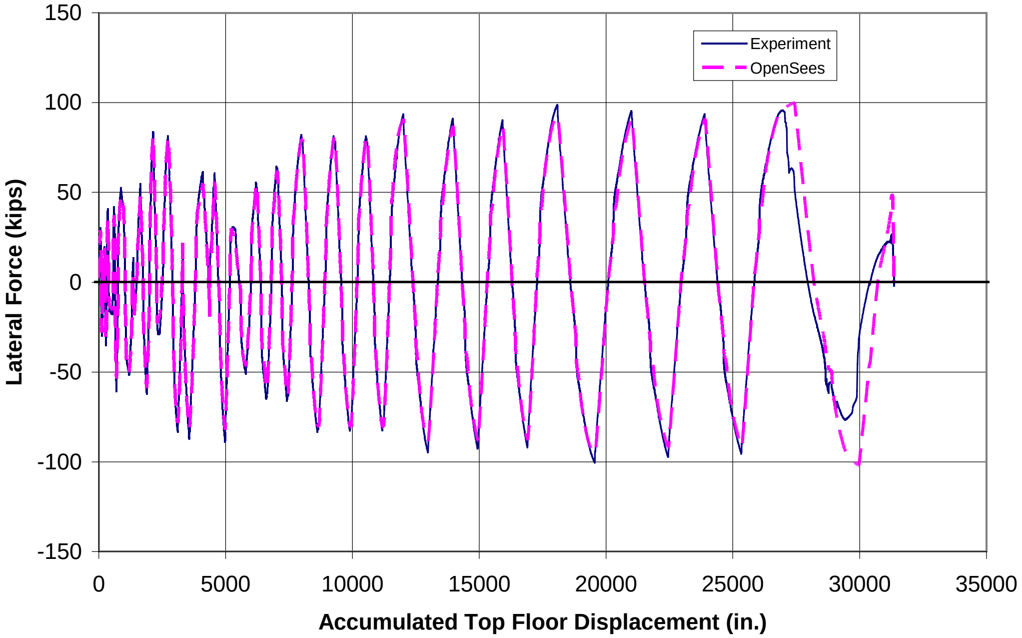

Figure 4-36: Comparison of Responses of NTW1 in the Flange Direction as a Function of Cumulative Displacement

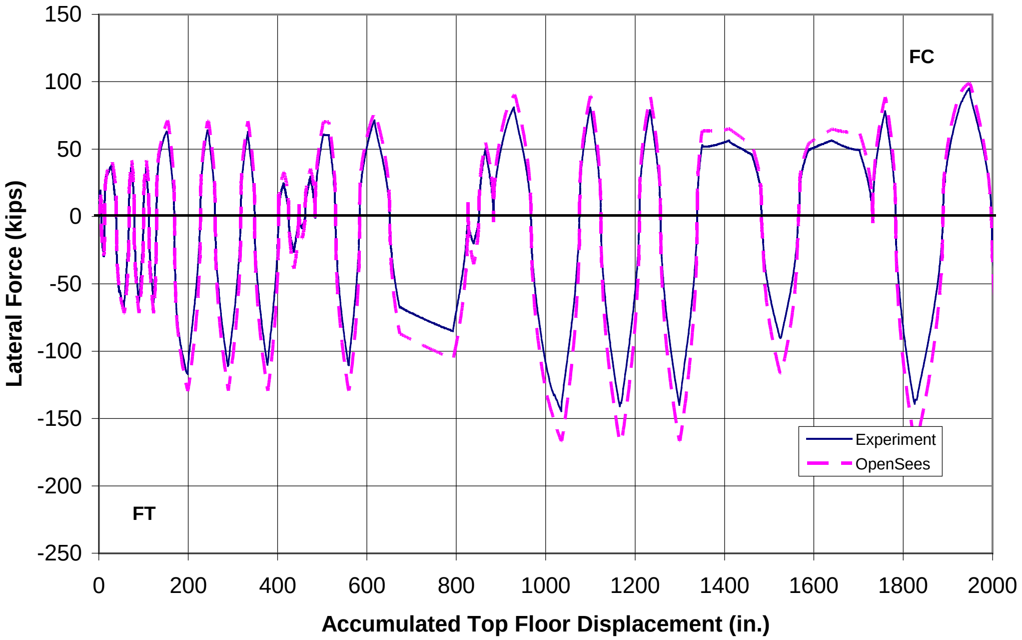

Figure 4-37: Comparison of Responses of NTW1 in the Web Direction as a Function of Cumulative Displacement in the Elastic Region

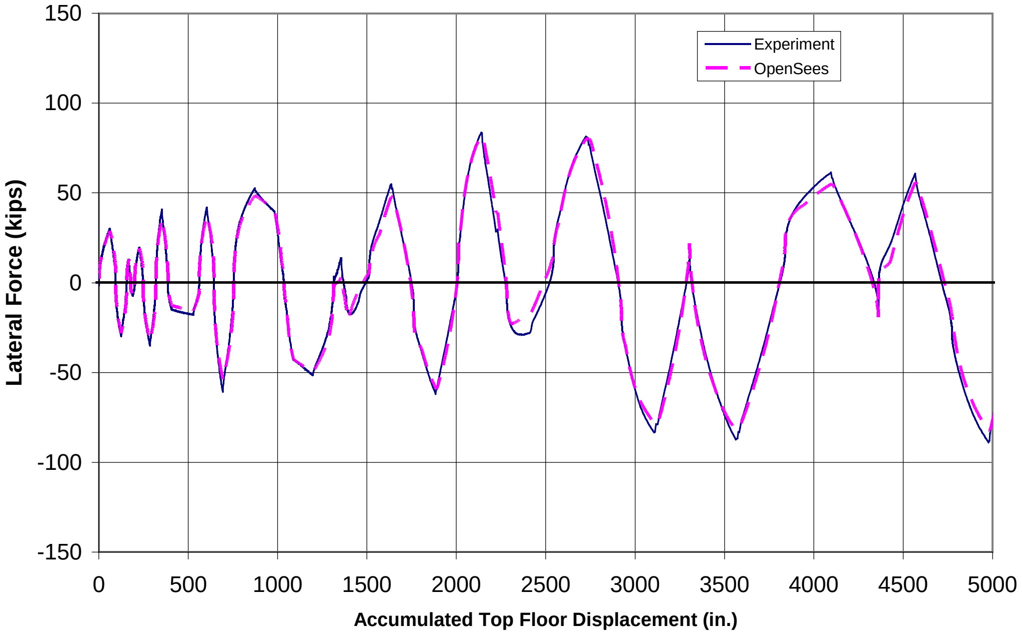

Figure 4-38: Comparison of Responses of NTW1 in the Flange Direction as a Function of Cumulative Displacement in the Elastic Region

4.8.2 First Floor Response

To ensure that the OpenSees model adequately captured the different deformation components accurately, the responses of NTW1 at the floor levels were also examined. It was expected that the first floor response would be more heavily influenced by the contribution of shear deformation. This provides an opportunity to more clearly examine the accuracy of the shear deformation component. The calculated and measured force-displacement responses of the first floor is shown in Figures 4-39 and 4-40 for the web and flange directions, respectively. The reported measured lateral displacement was the average of the displacements recorded by string potentiometers mounted to the flange and web tips. The OpenSees model did not capture the first floor response in both directions as good as it did for the top floor responses. Figure 4-39 and 4-40 show the first floor peak and residual displacements were overestimated by the analysis. However, as seen in Figure 4-39, the web direction response was captured within a reasonable degree of accuracy. Figure 4-41 and 4-42 show the first floor displacement as a function of the measurement number for the web and flange directions, respectively. In this perspective, it is easier to see that the analysis simulates the lateral displacement within 5 to 10% for the web direction, with a few exceptions where the difference being significantly larger. The measurement number is the number of times a measurement was taken In the flange direction. This approach for defining he x-axis was performedbecause the displacement from OpenSees at the first floor level was significantly larger than the measured displacement, The peak displacements are off by 40% in some places; however, at regions between the peaks the displacement is simulated within 15%. The cause of the discrepancy at the peaks was due to the shear distortion overestimating the shear deformation at higher levels in the positive direction, see Figure 4-28. This would have led to the oversimulation of the lateral displacement. The faster unloading of the Pinching4 material allowed the shear distortion to quickly return to the proper level, cause the response between peaks to be more better captured.

As noted, significant damage to NTW1 occurred in the plastic hinge region at drifts above 2%. The wall was heavily cracked with some spalling of the cover concrete near the toes, seen in Figure 4-42 and 4-44. Figure 4-43 shows the boundary element located at the flange tip, while Figure 4-44 shows the web tip. Large diagonal cracks formed between the boundary elements along the length of the flange and web. Additionally, truss action can develop in the plastic hinge after the diagonal cracks form in the web. The truss action, which can potentially carry a significant portion of the lateral load [Park and Priestley, 1998], facilitates the interaction between the shear and flexural actions. Due to this interaction, the strain in the longitudinal reinforcement increases as it participates in both flexural and shear actions. Similarly, the concrete strain will be different than that calculated from the plane sections remain plane assumption. This interaction was not explicitly modeled in the OpenSees analysis. It is possible that lack of explicit modeling of the shear-flexure contributed to the differences seen between the measured and calculated response at the first floor, particularly in the direction parallel to the flange.

In NTW1, the strain data from the longitudinal reinforcement showed that the strain obtained at 18 in. above the wall-foundation interface was higher than strains recorded at the interface. Figure 4-45 shows the strain profile for a bar located in the flange tip boundary element at 1% drift. The difference in strain could be due to the confinement effect of the foundation. This effect of the foundation was not included in the OpenSees model. The OpenSees model did not include the foundation because it was not thought to significantly influence the wall behavior, nor could this behavior be included easily in the OpenSees model due to the choice of using beam-column elements to model the wall.

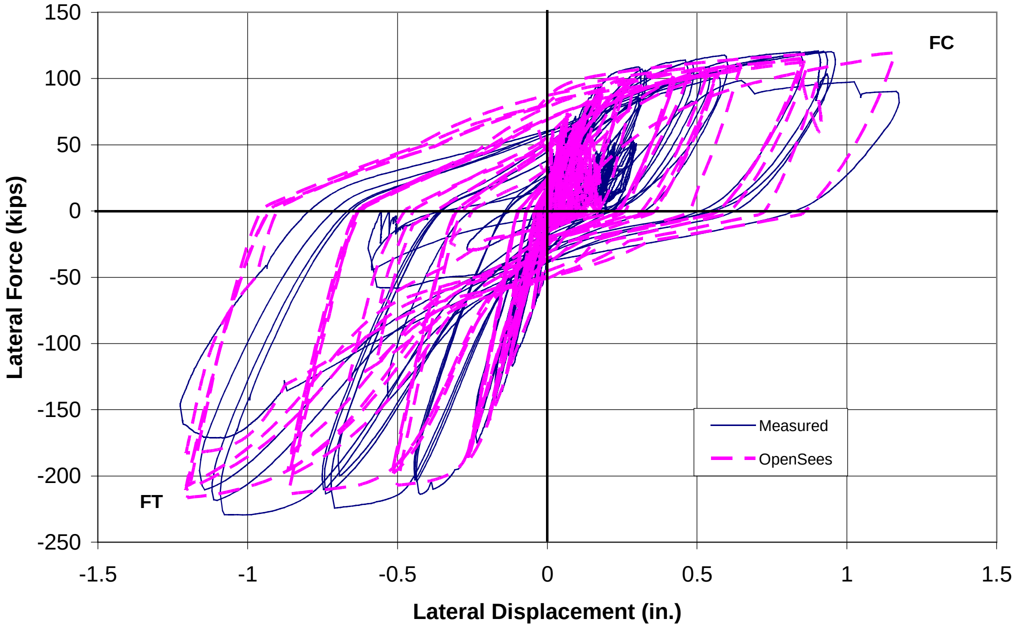

Figure 4-39: Measured and Calculated First Floor Force-Lateral Displacement Responses of NTW1 in the Web Direction

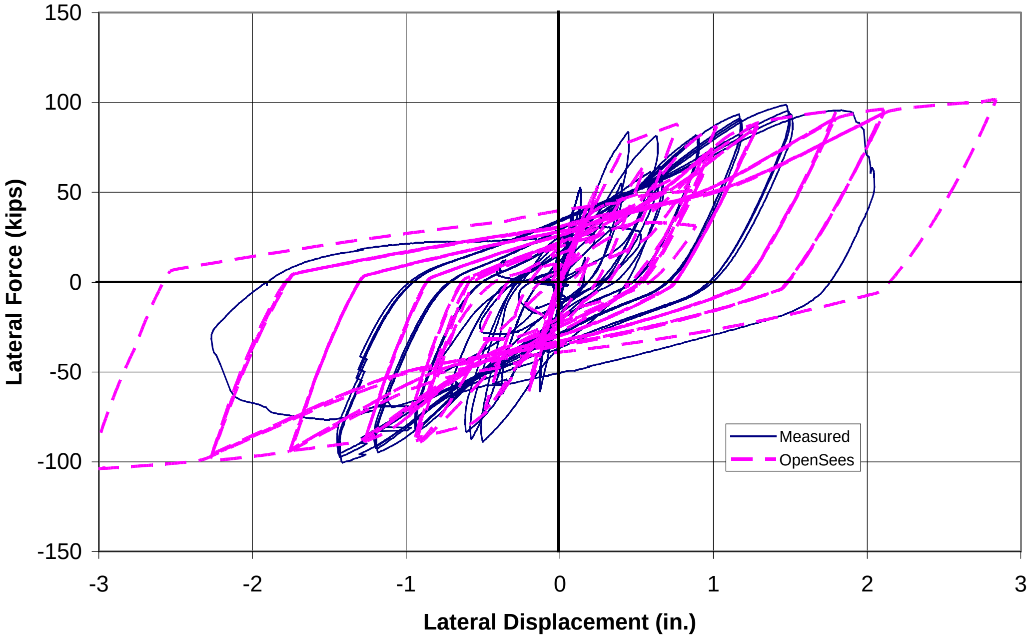

Figure 4-40: Measured and Calculated First Floor Force-Lateral Displacement Responses of NTW1 in the Flange Direction

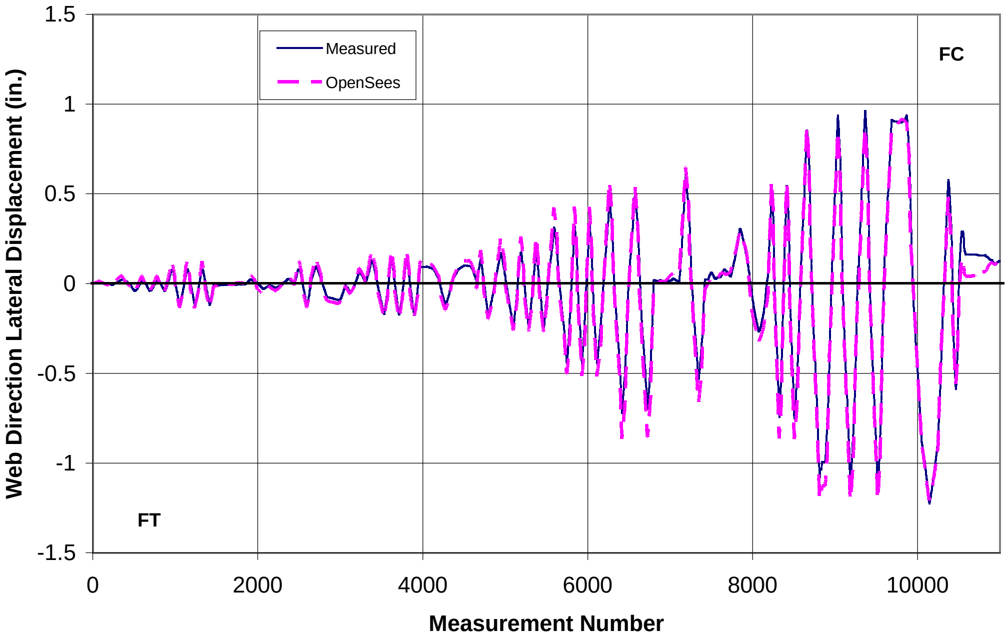

Figure 4-41: Comparison of First Floor Displacement of NTW1 in the Web Direction as a Function of Measurement Number

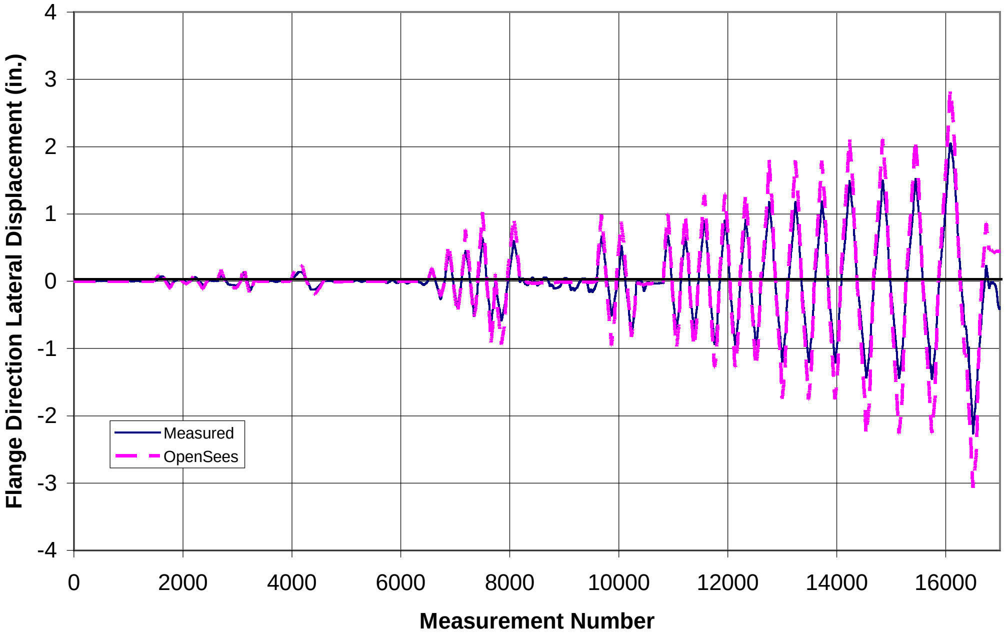

Figure 4-42: Comparison of First Floor Displacement of NTW1 in the Flange Direction as a Function of Measurement Number

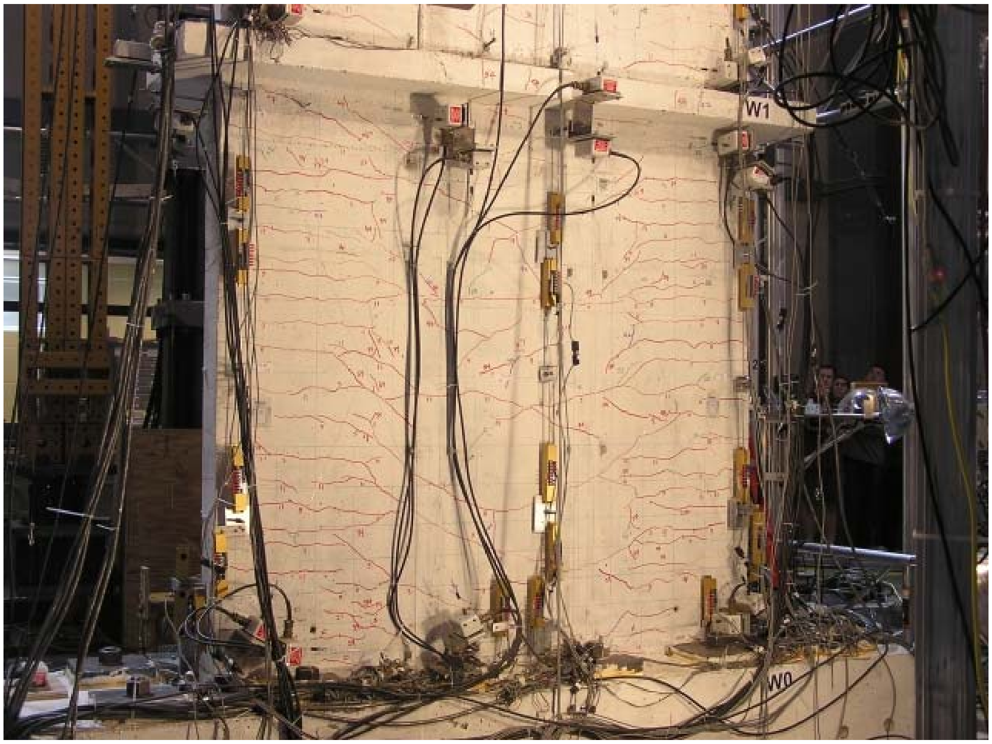

Figure 4-43: Condition of Flange at First Floor After Subjected to 1% Drift Cycles

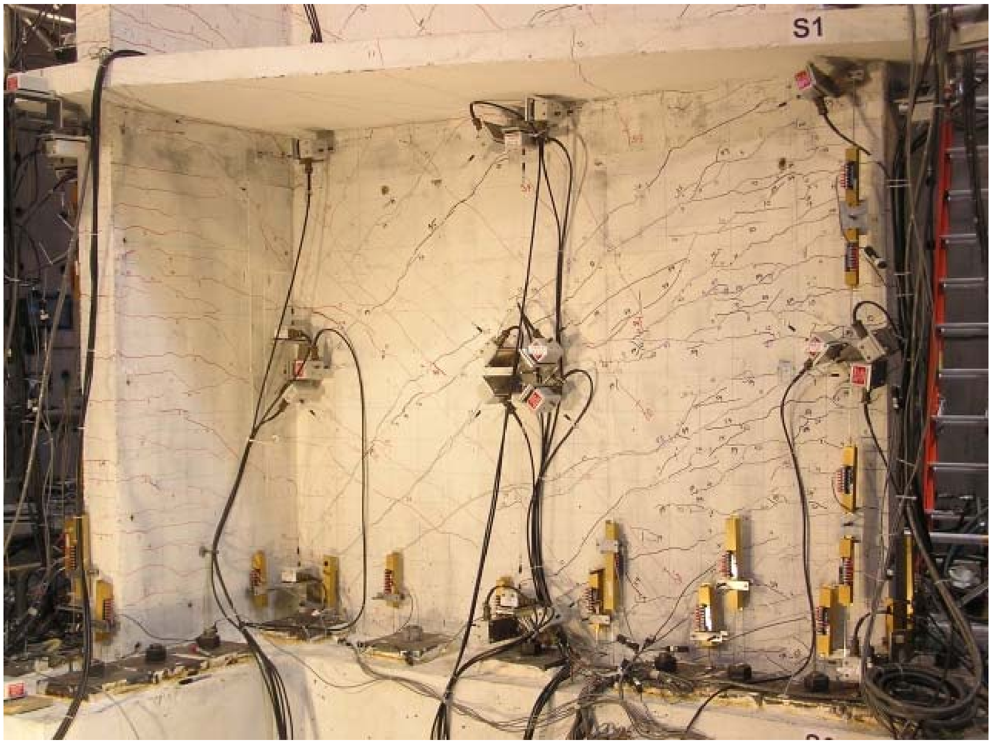

Figure 4-44: Condition of Web at First Floor After Subjected to 1% Drift Cycles

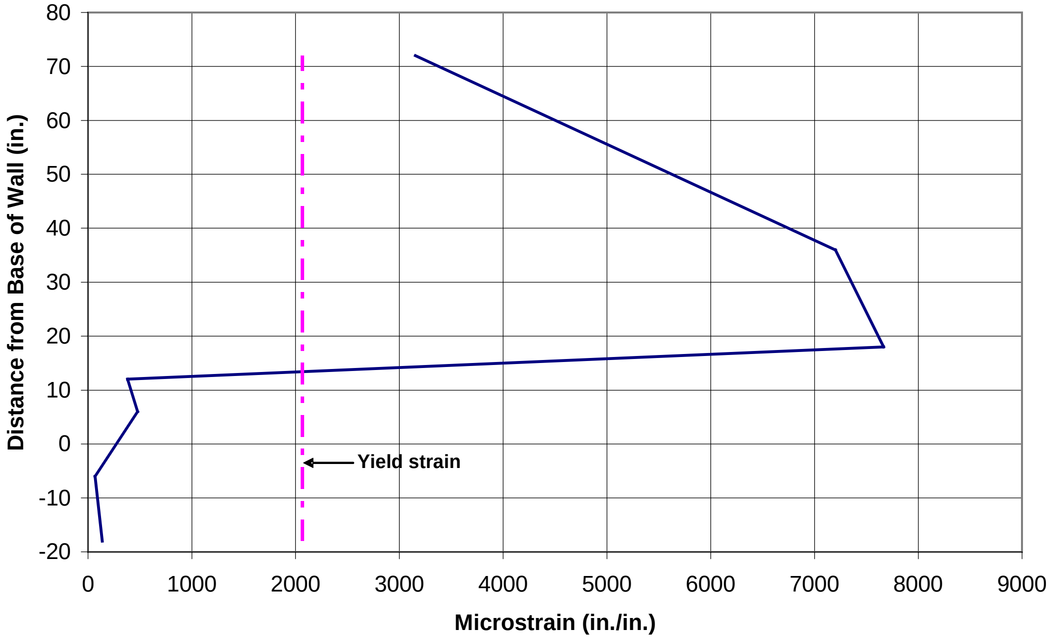

Figure 4-45: Measured Strain in a Longitudinal Tension Reinforcement Bar in the Flange Boundary Element at 1% Drift.

Another source for the discrepancies between the measured and calculated responses of NTW1 could be due to the simple material model used to simulate the shear response. Figures 4-26 and 4-28 show that the Pinching4 model did not perfectly simulate the shear response at the first floor level. The lower floor level displacements are influenced more by the shear response than lateral displacement at the top of the wall. As noted previously, the inaccurate simulation of the unloading stiffness was due to the simple unloading rules of Pinching4 dominating the unloading response of the model. However, the Pinching4 model was found to be the best one available at the time of modeling NTW1 to simulate the shear response of the first floor level.

4.8.3 Second Floor Response

The calculated lateral displacement response of NTW1 at the second floor was also compared to the measured experimental data. The lateral movements of both flange tips and the web tip were measured using string potentiometers during the test. The responses from each of the three instruments were averaged to determine the experimental response. As seen in Figures 4-46 and 4-47, the second floor response was better simulated by the OpenSees model than the first floor response. The improved simulation was likely caused by the increased contribution of flexure to the total deformation and decreased influence of any foundation effects, along with other reasons discussed in Section 4.4.3.

Figures 4-48 and 4-49 compare the measured lateral displacement of NTW1 and that from the OpenSees analysis as a function of the measurement number for the web and flange direction, respectively. As noted previously, this perspective allows the accuracy of the analysis to be seen more clearly. In Figures 4-48 and 4-49, the OpenSees analysis typically overestimated the lateral displacement by approximately 10% in the web direction and 15% in the flange direction at the peak displacements. Displacements between the peaks are simulated within 5-10% of the measured displacements. There are isolated peaks where the OpenSees analysis overpredicted the lateral displacement by as much as 15% in the web direction and 20% in the flange direction. While not as well simulated as the global response, the second floor response shows that the model is simulating the behavior of the wall better outside of the first floor. The adequate simulation seen for the second floor response confirms that improving the model performance in the critical region of the first floor level will improve the response of the analytical model at the second floor as well. Similar to the global force-displacement responses, the residual displacements were somewhat poorly captured by the model.

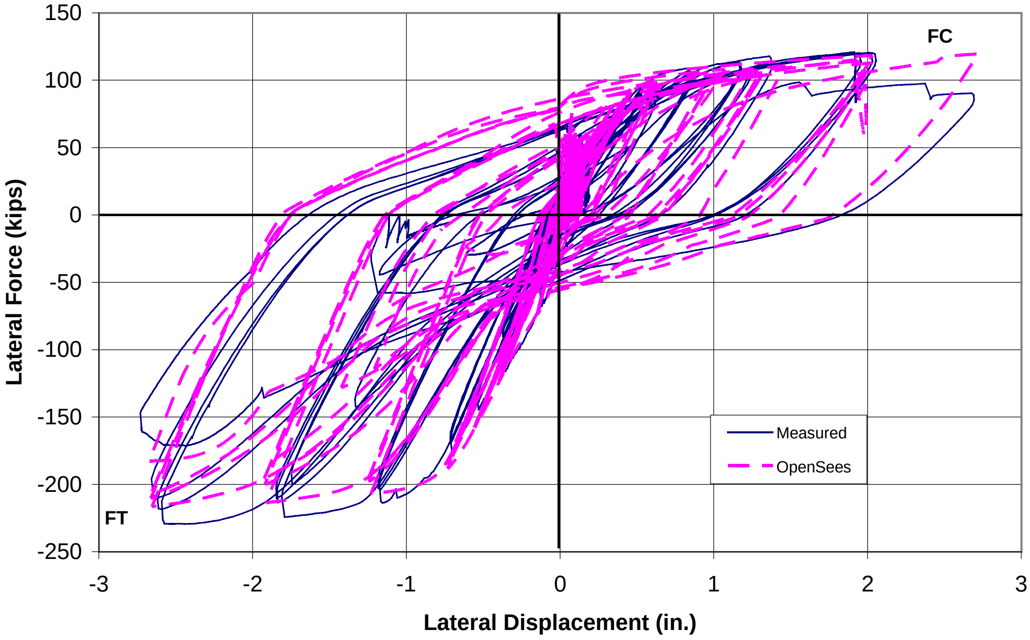

Figure 4-46: Measured and Calculated Second Floor Force-Lateral Displacement Responses of NTW1 in the Web Direction

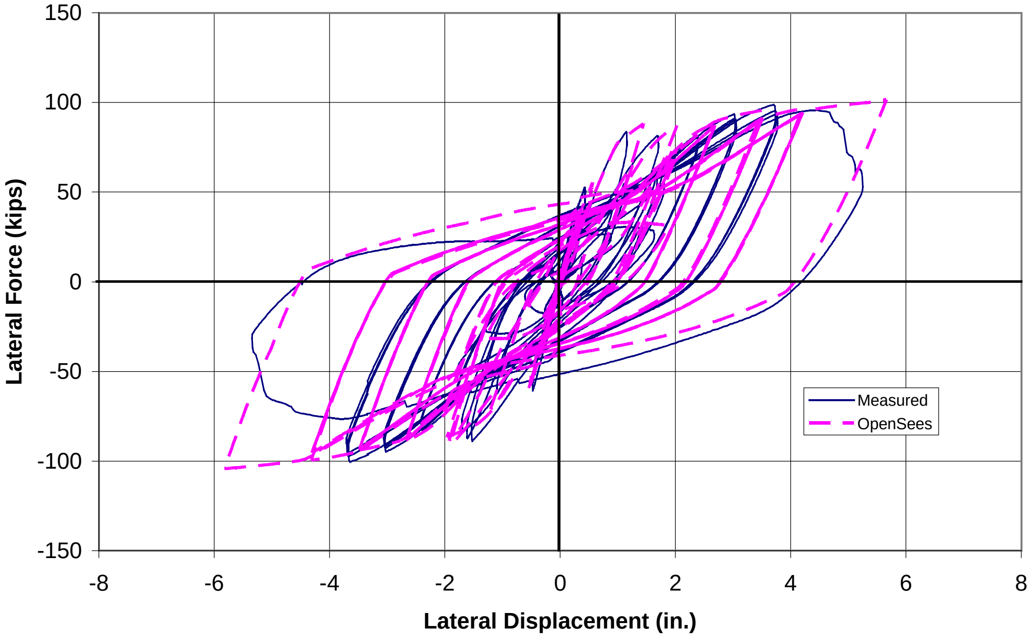

Figure 4-47: Measured and Calculated Second Floor Force-Lateral Displacement Responses of NTW1 in the Flange Direction

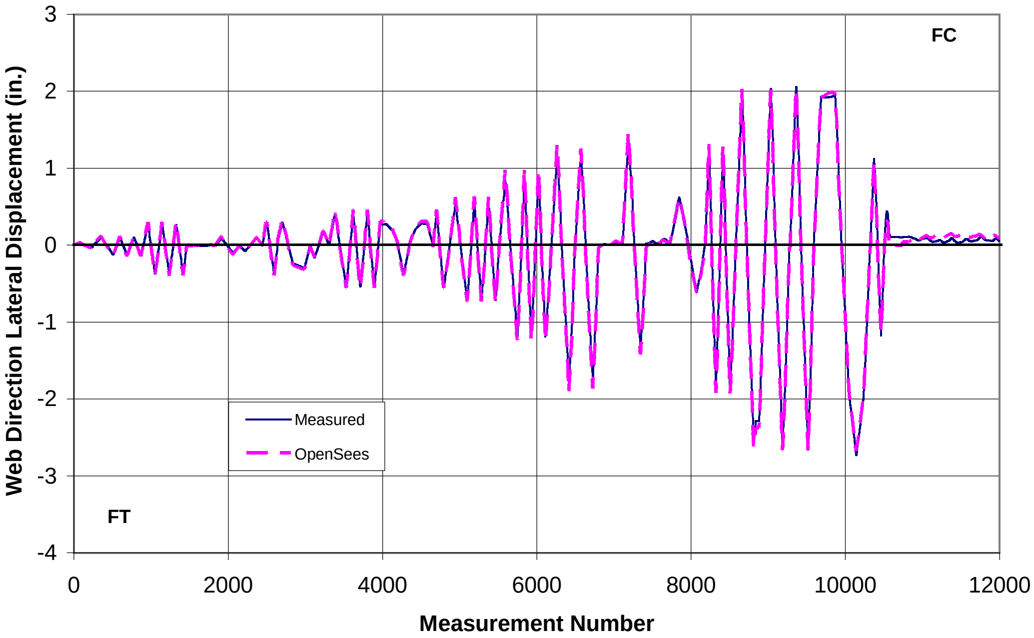

Figure 4-48: Comparison of Second Floor Displacement of NTW1 in the Web Direction as a Function of Measurement Number

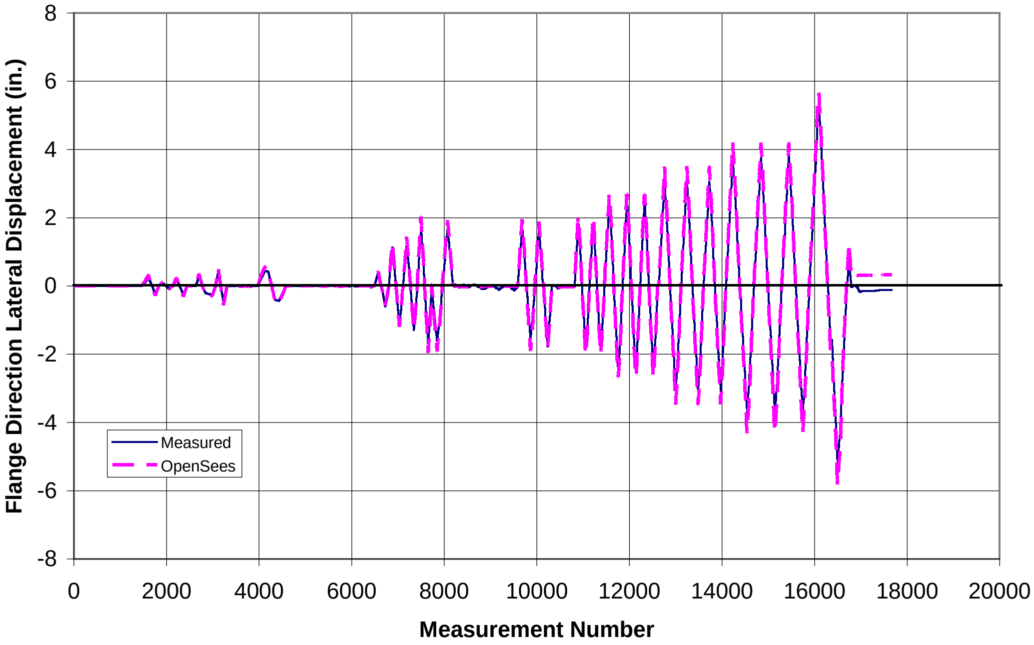

Figure 4-49: Comparison of Second Floor Displacement of NTW1 in the Flange Direction as a Function of Measurement Number

4.8.4 Components of Lateral Deformation

The lateral displacement measured in the test of NTW1 was decomposed into the various components, including the flexural component, shear component, and strain penetration component. A method used for doing the same for bridge joints by Sritharan and Priestley [Sritharan *et al.*, 1996] was followed to decompose the lateral displacement into various components based on the measurements recorded by LVDTs and string potentiometers. Figures 4-50 and 4-51 compare the calculated and analytical contribution of the flexural, shear, and strain penetration displacement components as a fraction of the total first floor displacement for the web and flange directions, respectively. Each line represents the displacement of the component alone. Figure 4-50 shows that the OpenSees analysis is capturing the contribution of the shear and flexure with a reasonable degree of accuracy in the the flange-in-tension direction. However, in the flange-in-compression direction the shear and flexure contribution are almost equal, and the flexural contribution is overestimated and the shear contribution underestimated. The large increase in shear distortion and thus higher shear contribution in the flange-in-compression direction compared to the flange-in-tension direction was also observed by Thomsen and Wallace in their test of specimen TW2 as discussed in Chapter 2. This behavior was attributed to inelastic shear deformation resulting from inelastic flexural response [Orakcal and Wallace, 2006]. The contribution of strain penetration was well captured by the analysis. Slightly lower contribution was recorded in the flange-in-compression direction compared to the analysis. The components were determined from the data for positive displacement in the parallel to the flange direction. Since the response was symmetrical the displacement components were not determined for the negative direction. In the flange direction the flexural component is adequately captured, but the shear contribution is underestimated. The measured strain penetration contribution is poorly captured; however, the decomposition shows strain penetration contribution was equal to shear deformation. This is not possible and is attributed to instrument malfunction.

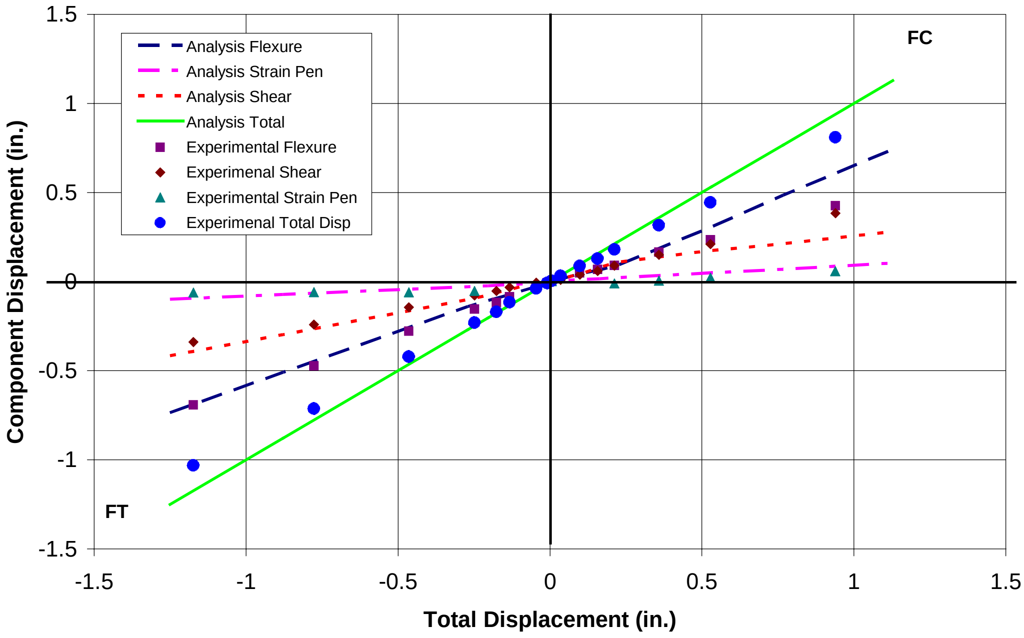

Figure 4-50: Comparison of the First Floor Lateral Displacement Components in the Web Direction

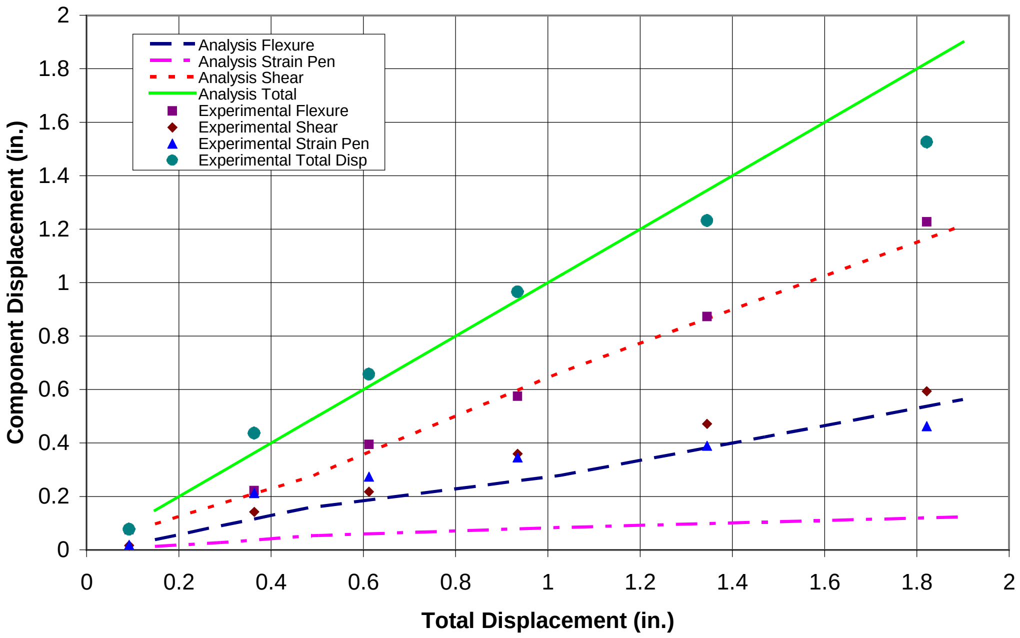

Figure 4-51: Comparison of the First Floor Lateral Displacement Components in the Flange Direction

The contribution of each component to the total top displacement is presented in Figure 4-52. The analysis accurately captures all the components of the lateral displacement at the top of the wall. The strain penetration contribution is shown for the top of the wall displacement, which indicates that the model is capturing the the strain penetration up to a displacement of 1.36 in. Beyond this displacement the contribution of strain penetration decreases, which is contrary to the fact that the strain penetration should increase for increasing displacements, particularly in the nonlinear range. The flexural contribution is is very well captured by the analysis at all displacement levels. Overall the shear contribution at the top of the wall is adequately simulated. Due to the instrumentation, the top of the wall displacement cannot be decomposed in the flange direction. The shear distortion was not measured in the web direction above the second floor for the flange direction. Thus it is impossible to separate the lateral displacement that is due to flexural deformation and that due to shear distortion of the wall. Thus comparison of the displacement components cannot be presented. However, Figure 4-53 shows the theoretical displacement components from the OpenSees analysis.

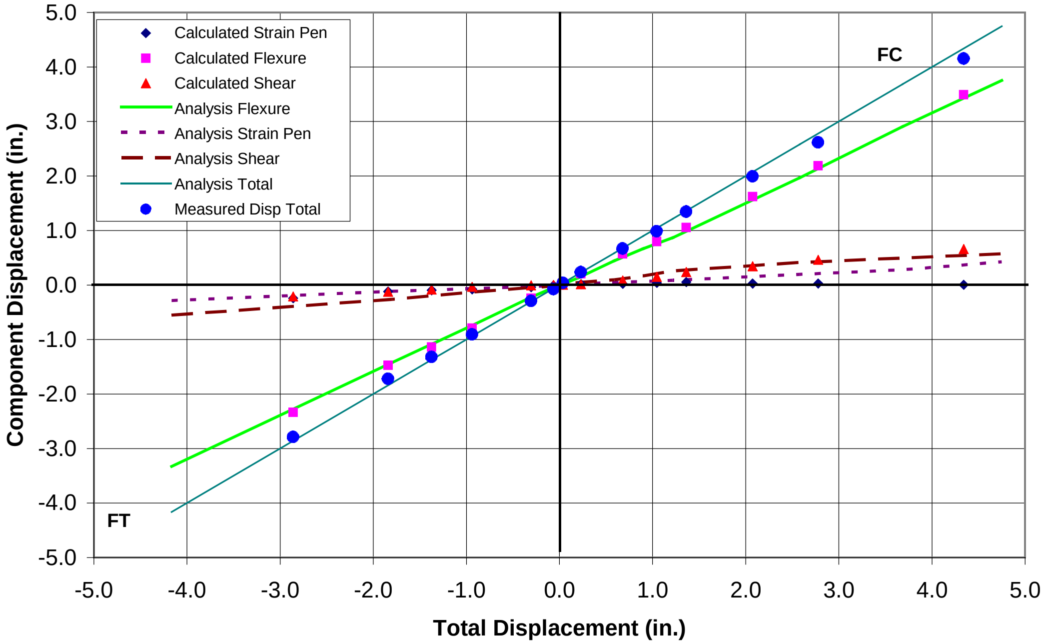

Figure 4-52: Comparison of the Wall Top Lateral Displacement Components in the Web Direction

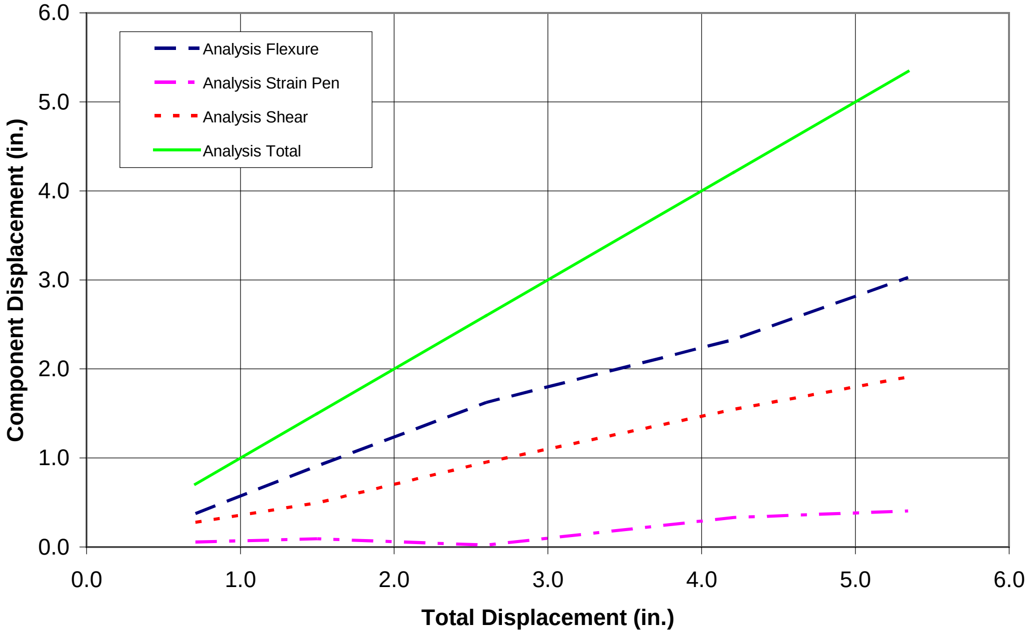

Figure 4-53: Comparison of the Wall Top Lateral Displacement Components in the Flange Direction

4.8.5 Multidirectional Load Path

As detailed in the load path in Section 4.3 (see Figures 4-12 and 4-16 and in Table 4-2), NTW1 was subjected to complex load paths, which had a pentagon shape and an "hourglass" shape. These paths were chosen to examine the ability of the analysis model to predict the behavior of NTW1 under complex bi-directional load. The pentagon shape was targeted at approximately 50% of the yield displacement at any given direction, which was achieved by making the load path to approximate the expected shape of the yield surface of NTW1. Due to the effects of shear lag and shear-flexure interaction, the strain in the critical reinforcement at the base of the wall in any given direction of loading was not expected to be at a constant value. However, the load path did allow the accuracy of the analysis model under complex loading in the elastic region to be evaluated. The hourglass shape was conducted at approximately 2% drift level. This path allowed the analysis in the nonlinear range to be evaluated.

Figure 4-54 to 4-57 show the comparison of experimental and analysis results from the pentagon shape loading in the elastic region, which shows that the analysis model of NTW1 satisfactorily captured the response in both the flange and web directions. Figure 4-54 shows the displacement at the top of the wall from the analytical model and the average experimental value obtained from potentiometer readings. It is seen that the OpenSees model experienced slightly larger displacements at the top of the wall in comparison to the average measured lateral displacement at the top of the wall. The overestimation of the wall top displacement in the model was due to the difference between the actual stiffness of the top block and that was modeled in OpenSees by applying the displacements at an artificial control point above the wall. Figure 4-55 shows the comparison between the measured force resistance at the top of the wall and that determined by the OpenSees analysis. Figures 4-56 and 4-57 show the force-displacement comparison in the web and flange directions, respectively, for the pentagon load path. Given the complexity of the load path, OpenSees model captured the response well under this multidirectional displacement path. The flange direction force-displacement was better simulated than the web direction response. One possible source for the somewhat large discrepancy in the web direction response is that shear lag that occurs in this direction of response is expected to be dominant in the elastic range and this could have influenced the analysis result. The other possible source of the discrepancy is the post-peak behavior of concrete in tension. Although the post-peak behavior of concrete would affect both directions, it would be more prominent in the flange-in-tension direction due to the larger area of concrete in tension in the flange. However, the response of the wall in the nonlinear range will be less sensitive to these effects.

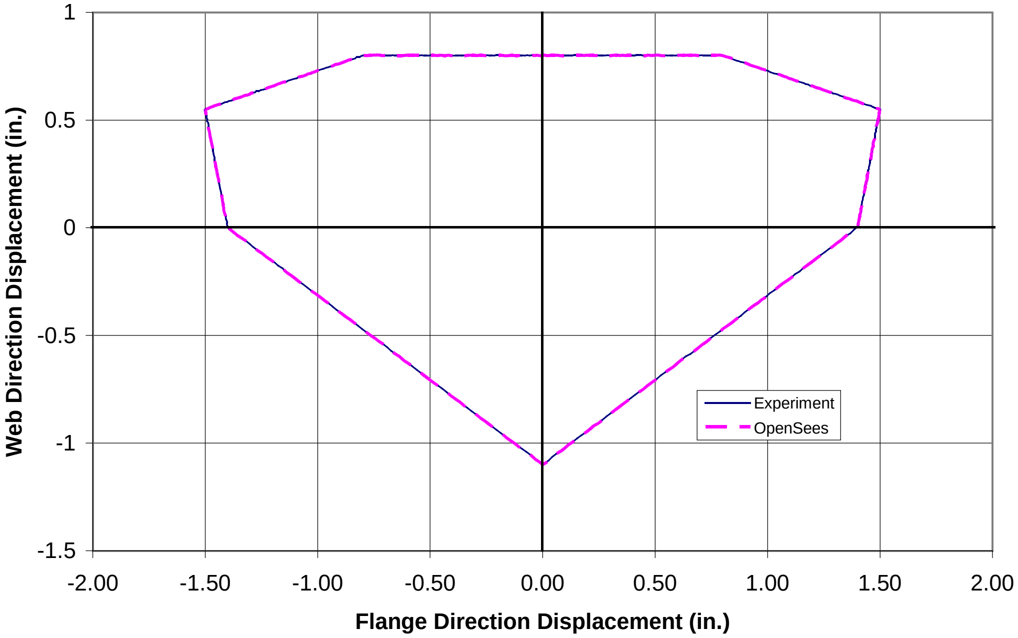

Figure 4-54: Comparison of Displacements at the Top of NTW1 for the Pentagon Shape Load Path at 50% of Yield

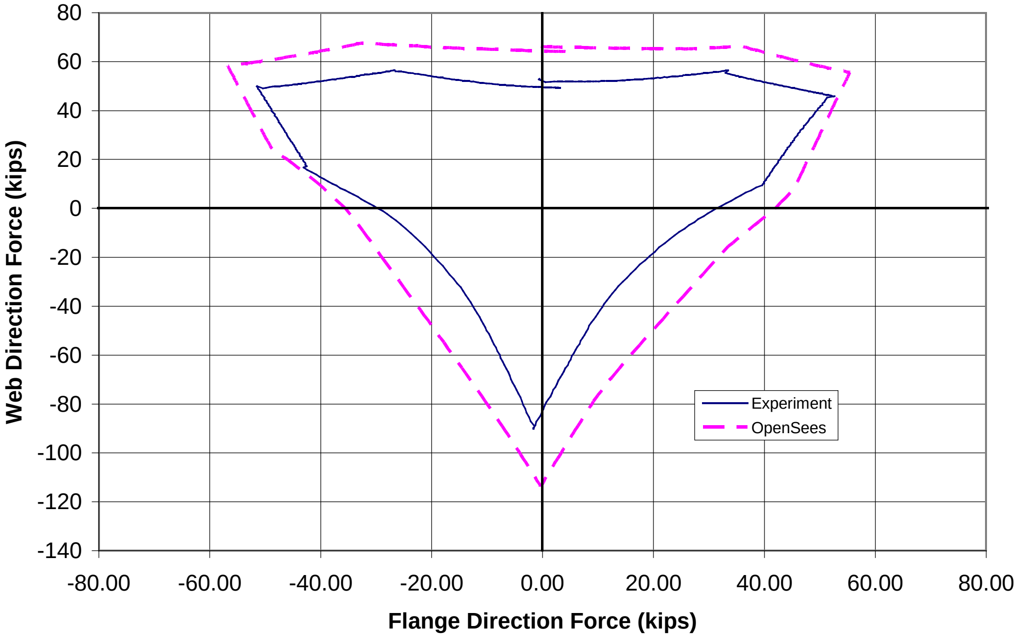

Figure 4-55: Comparison of Forces at the Top of NTW1 for the Pentagon Shape Load Path at 50% of Yield

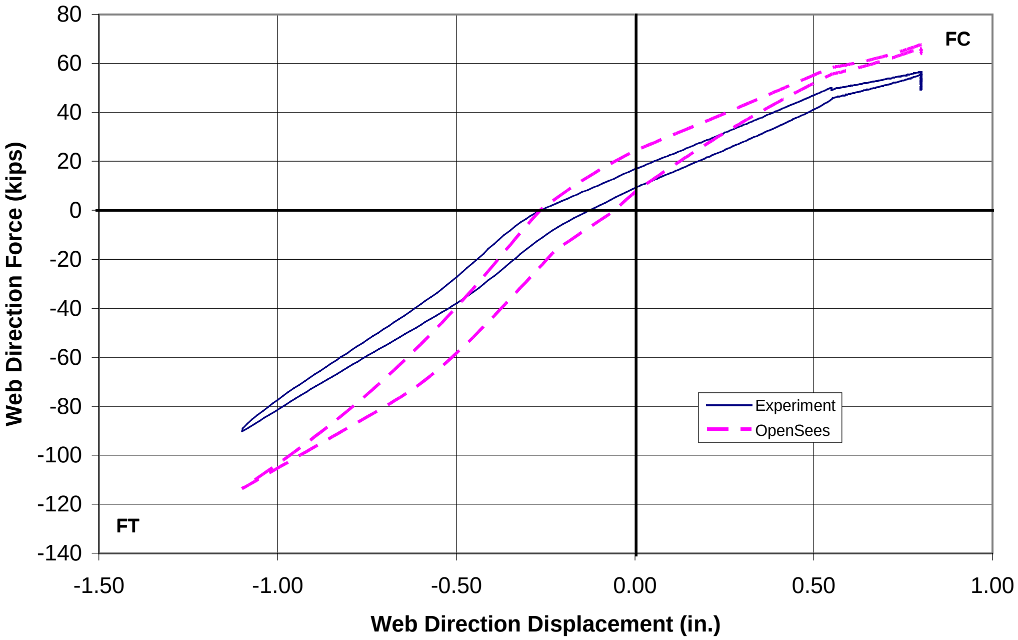

Figure 4-56: Comparison of Force-Displacement Response of NTW1 for the Pentagon Shape Load Path at 50% Yield in the Web Direction

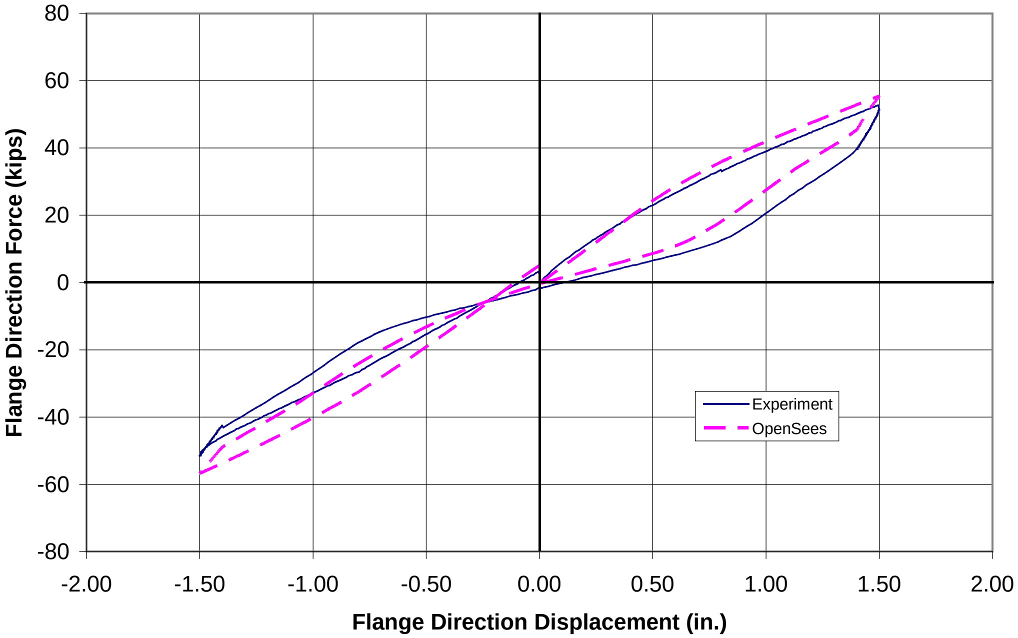

Figure 4-57: Comparison of Force-Displacement Response of NTW1 for the Pentagon Shape Load Path at 50% Yield in the Flange Direction

The results of hourglass shape load path conducted at 2.0% drift level are shown in Figure 4-58 to 4-61. At this displacement level, all longitudinal reinforcement in the critical regions of the web and flange was taken well into the inelastic range, and the wall was fully cracked under the influence of both flexure and shear actions, see Figure 4-62. Figure 4-58 shows the target displacement comparison at the top of the wall; the OpenSees analysis simulated the displacement targets at the top of the wall in comparison to the measured values. Figure 4-59 presents the comparison between the measured lateral force resistance and the results from the OpenSees analysis. The force-displacement response comparison for the web and flange directions for the hourglass load path are shown in Figures 4-60 and 4-61, respectively. The force-displacement responses compared in these figures confirm that they were well captured by the OpenSees model. A slight overprediction seen for the flange-in-tension direction in Figure 4-60 was due to the fact that crushing of concrete began to occur in the web tip of NTW1. The lateral force-displacement response in the flange directions are compared in Figure 4-58. Again a good comparison is seen between the measured and analytical responses except for the first half cycle which led to some overprediction of the force resistance. This discrepancy may also be attributed to the fact that the flange had experienced some damage due to testing in the web direction, which may not have been adequately captured by the analytical model, Figure 4-62 shows significant cracking and damage prior to starting the hourglass load path. Figure 4-60 shows that the longitudinal reinforcement in the web tip had buckled during the hourglass load path, which occurred as the peak displacement, -6.38 in., was reached in the flange-in-tension direction. Upon deconstruction of the wall following testing, three bars in the web tip were found to have buckled over a number of the transverse stirrups, see Figure 4-63. This failure mode, however, was not included by the OpenSees model. The material models used in the OpenSees model of NTW1 did not have the ability to capture the buckling of the longitudinal reinforcement. During testing, crushing of concrete outside the confined region of the web boundary element was also observed in the web tip, which was accounted for in the analytical model through appropriate definition of concrete fibers.

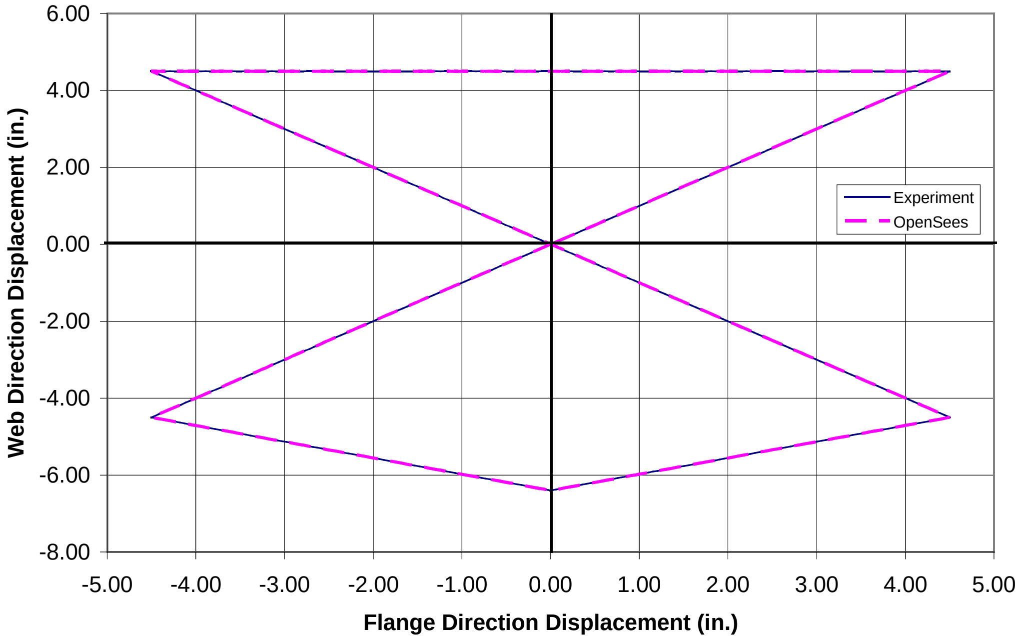

Figure 4-58: Comparison of Displacements at the Top of NTW1 for the Hourglass Shape Load Path at 2% Drift

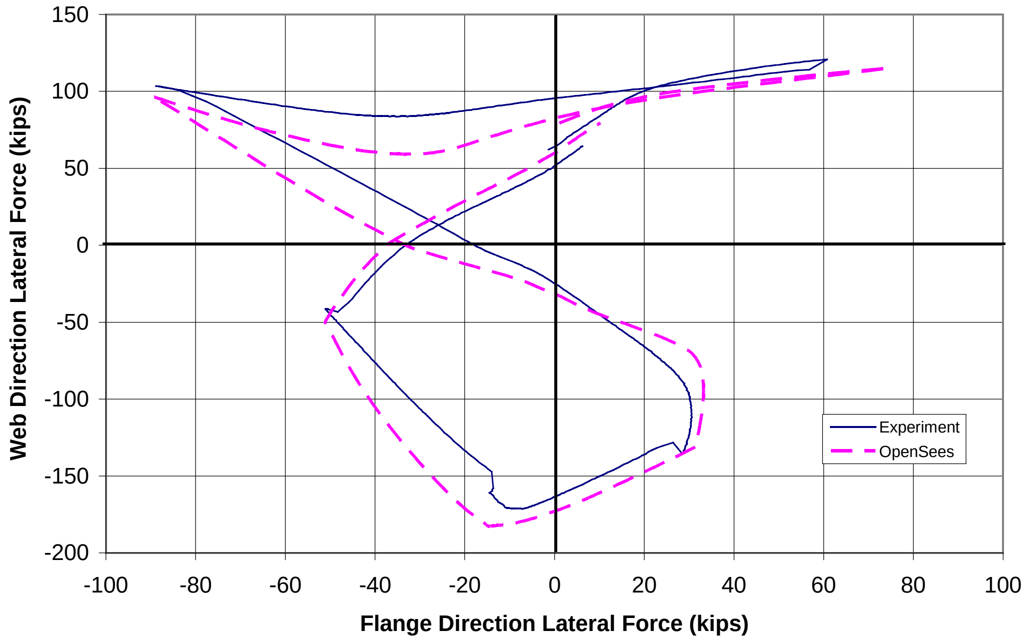

Figure 4-59: Comparison of Forces at the Top of NTW1 for the Hourglass Shape Load Path at 2% Drift

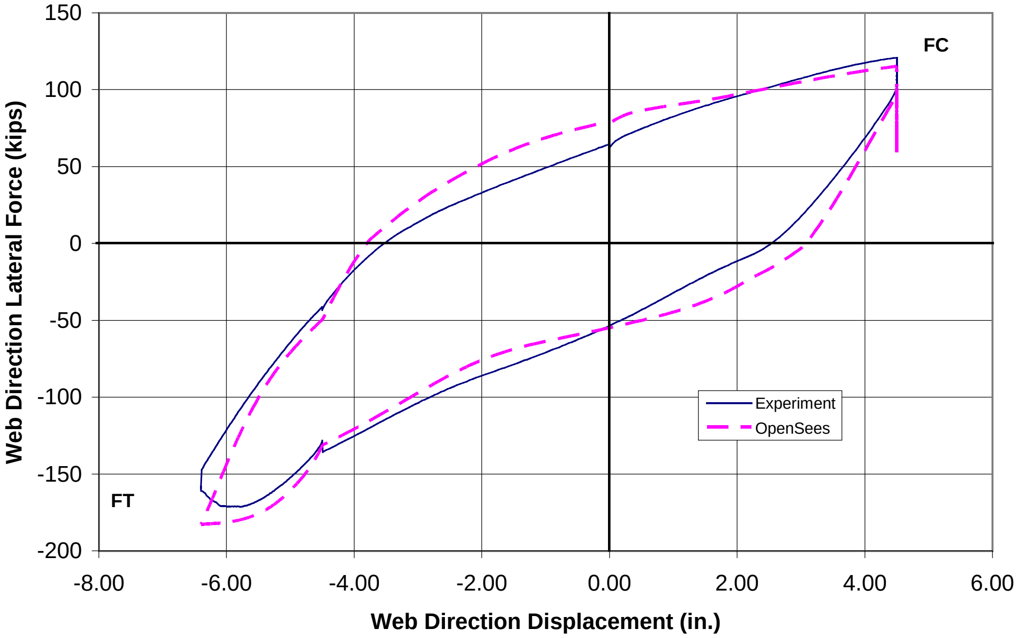

Figure 4-60: Comparison of Force-Displacement Response of NTW1 for the Hourglass Shape Load Path at 2 % Lateral Drift in the Web Direction

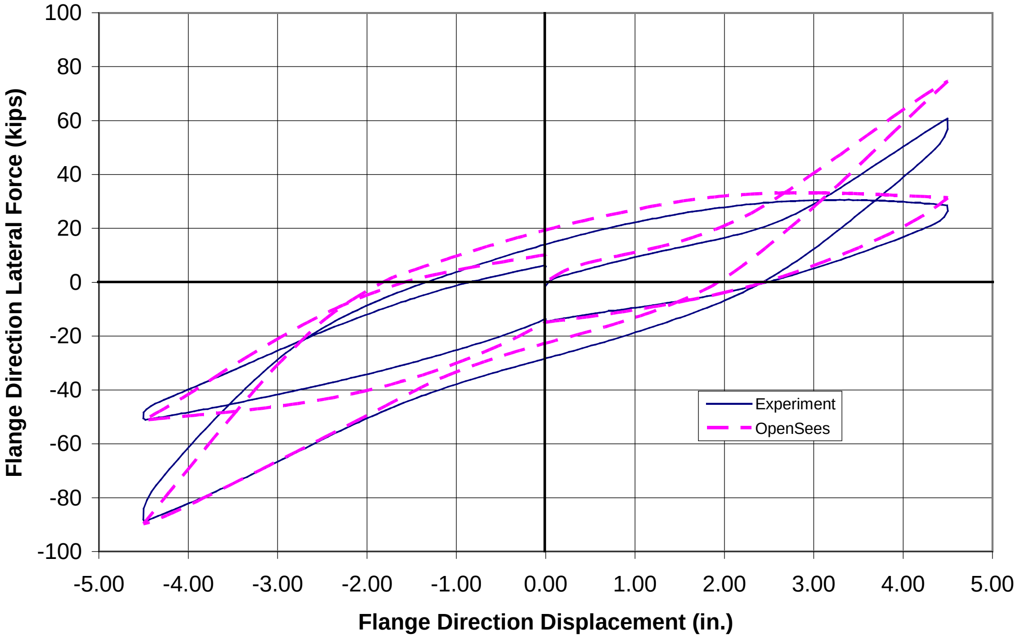

Figure 4-61: Comparison of Force-Displacement Response of NTW1 for the Hourglass Shape Load Path at 2% Lateral Drift in the Flange Direction

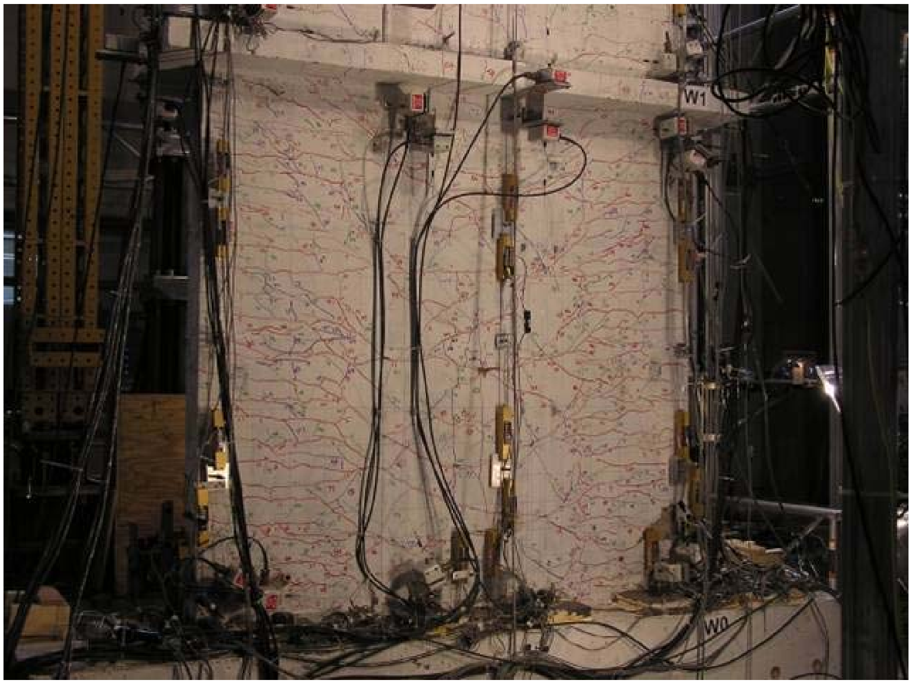

Figure 4-62: Base of the First Floor Flange of NTW1 Prior to Beginning of the Hourglass Shape Load Path

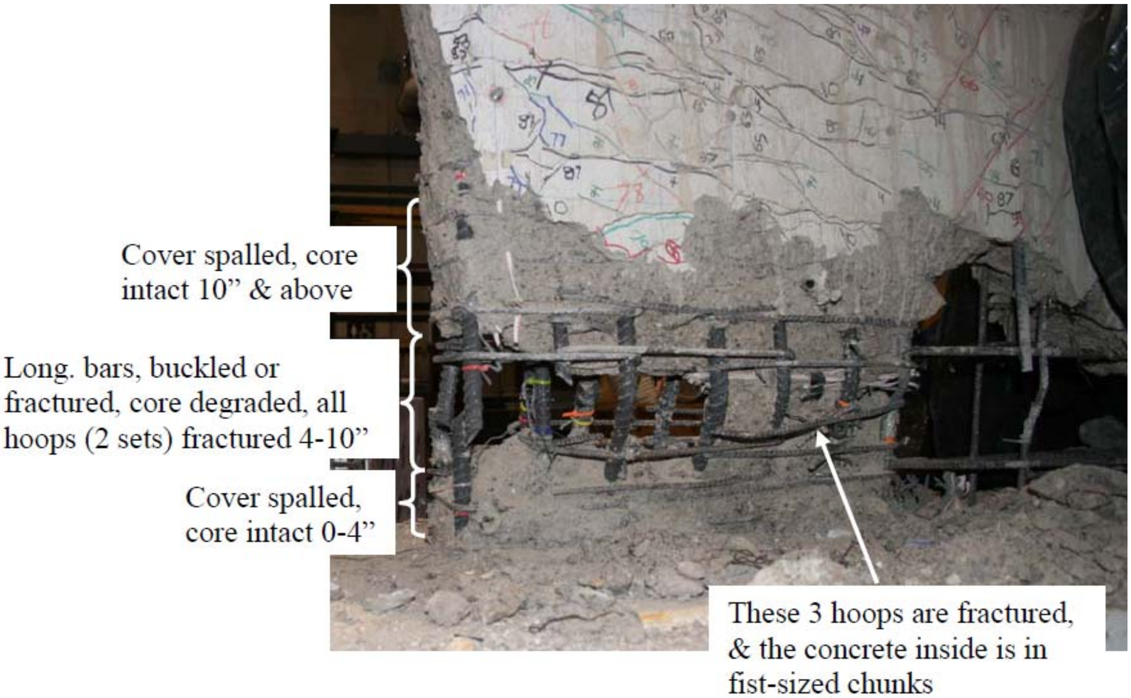

Cover spalled, core intact 10” & above

Long. bars, buckled or fractured, core degraded, all hoops (2 sets) fractured 4-10”

Cover spalled, core intact 0-4”

These 3 hoops are fractured, & the concrete inside is in fist-sized chunks

Figure 4-63: Buckling of the Longitudinal Reinforcement in the Web Tip Boundary Element of NTW1 at 2% drift

4.8.6 Strain Profile Comparison

Adequate simulation of the local response, including strains and neutral axis depths at the critical region, is important from a design perspective. Also, strain is a better predictor of damage to the structure at a particular location than a global parameter such as lateral displacement. Therefore, adequate simulation of local strains should be considered as an important feature when evaluating the adequacy of a particular modeling approach. The strains recorded nominally at six inches above the base were used for the comparison purposes since this location had the most complete set of gages, giving the most complete strain profiles.

Figures 4-64 and 4-65 show the strain profiles established at the first peak various displacements parallel to the length of the web for the flange-in-compression and flange-in-tension direction. The analysis satisfactorily captured the location of the neutral axis depth in both the flange-in-compression and flange-in-tension directions of loading. Figure 4-64 also shows the analysis captured the curvature up to the yield cycles. The strain and curvature of cycles below yield are particularly well captured by the analysis. The strain profile for the flange-in-tension direction was only plotted up to the yielding condition. Above yield, some gages in the flange malfunctioned, not providing adequate data to develop the strain profiles.

Under the flange direction of loading, a sufficient number of data was not obtained that was adequate to establish the strain profiles. Several strain gages in the flange failed prior to the majority of the flange direction testing began. Since this direction was not tested heavily until after the web tip experienced buckling of the longitudinal bars, the bars in the flange had been subjected to large strains in previous load cycles. As shown in Figure 4-66, a strain profile for the flange direction loading was established at 0.25% of the yield displacement, which shows a good agreement between the experimental and analytical OpenSees model.

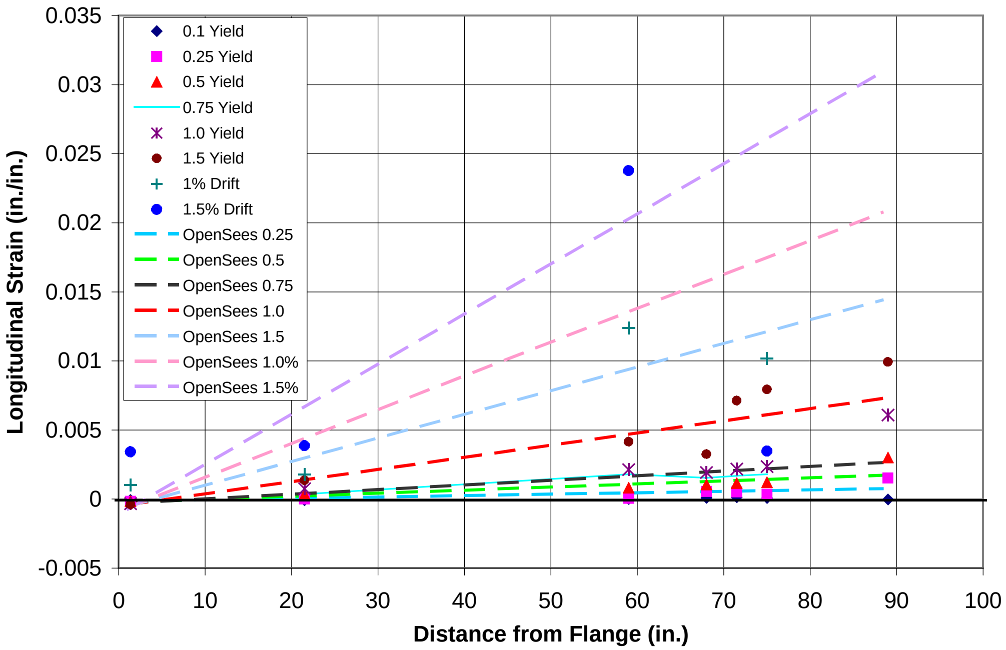

Figure 4-61: Comparison of Strain Profiles for the Flange-in-Compression Direction Response of NTW1

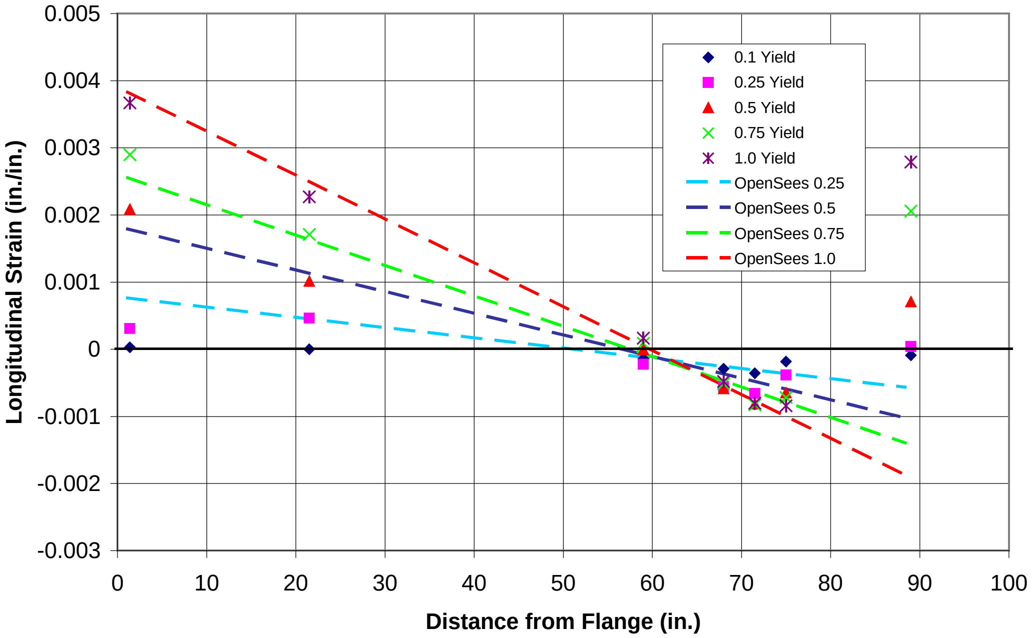

Figure 4-62: Comparison of Strain Profiles for the Flange-in-Tension Direction Response of NTW1

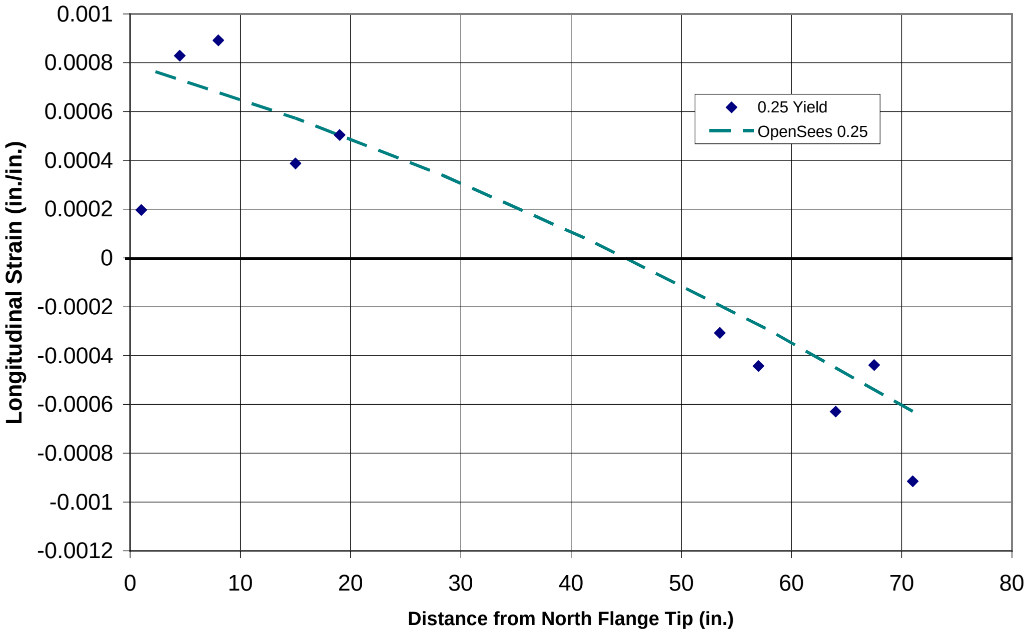

Figure 4-63: Comparison of Strain Profiles for the Flange Direction Response of NTW1

Chapter 5: Analysis of NTW2

This chapter presents the analysis conducted prior to the testing of the second T-wall unit, NTW2. Post-testing analysis is not presented in this chapter, and was not conducted as part of this investigation. The analysis of NTW1 in Chapter 4 showed that a fiber-based model can adequately capture the experimental response of a T-wall subjected to multi-directional loading. The goal of the second T-wall analysis was to predict the response of NTW2 using the measured material properties and the experience gained from post-testing analysis of NTW1 and compare results with experimental data. Furthermore, post-testing analysis similar to that was conducted for NTW1 was not expected to provide significantly further information on the simulation of T-walls beyond what was learned in NTW1. The local response was not significantly examined because of discrepancies observed in the global response due to differences between NTW2 and other T-walls analyzed.

5.1 Description of NTW2

The second T-wall specimen, referred to as NTW2, was designed based on the observed response of NTW1 to the multidirectional loading. The reinforcement details were modified to improve the performance of the wall when subjected to multi-directional loading similar to that was used for testing NTW1. The reinforcement details used for NTW2 are shown in Figure 5-1. The same gross dimensions of NTW2 were identical to those of NTW1 since both walls, represented the same prototype wall at 50% scale. The total amount of longitudinal steel in the flange was similar to that in NTW1. A perfect match of the total reinforcement area was not possible as the number, size, and distribution of the longitudinal bars were altered; thus, NTW2 had approximately 0.88 sq in. or 9.4% less steel area in the flange than NTW1. A critical change in the detailing was that the amount of steel in the boundary elements of the NTW2 flange was reduced, and more steel was distributed along the length of the flange. Contrary to the current design practice, the researchers felt that having more distributed steel would provide better crack control and allow for smaller, more distributed diagonal cracks to form, rather than allowing large concentrated cracks to develop as observed in NTW1, see Figure 4-22. A complete discussion of crack distribution and the effects of reinforcement can be found in Waugh *et al.* [2008]. The distributed steel in the web was not modified from that used in NTW1. However, the boundary element in the web tip was extended deeper into the web by increasing the confined concrete region because crushing of concrete just outside of the boundary element in NTW1 (see Section 4.4). Additionally, the arrangement of the confinement reinforcement in the web tip was modified from that used in NTW1. A number of the transverse reinforcement hoops with 135° hooks opened up during testing of NTW1 , which led to loss of confinement to concrete [Brueggen, 2009]. The loss of transverse reinforcement would also lead to premature buckling of the longitudinal reinforcement as seen in the web tip of NTW1. The hoops were rearranged such that the 135° hooks were positioned away from the web tip as much as possible, as seen in Figure 5-1. In NTW1, continuous longitudinal reinforcement without any splices was used over the entire wall height. In NTW2, the longitudinal reinforcement was spliced at the first floor level. Tests of rectangular walls conducted as part of the PreNEESR project showed that splicing the longitudinal reinforcement at the foundation interface led to undesirable behavior of the wall and premature failure when compared to equivalent walls designed with continuous reinforcement without splices or mechanical couplers located at the foundation interface. For more information on the rectangular walls, readers are directed to the Johnson [2007] and Waugh *et al.* [2008]. Relocating the splice to the first floor level was investigated to determine if this would be an acceptable location for a construction splice.

In addition to investigating the effects of the improved reinforcement details, NTW2 was used to further investigate the ability of the MAST facility to simulate the critical behavior of the prototype T-wall using shorter specimens. Instead of constructing four of the six stories of the prototype wall like in NTW1, only the bottom two stories of NTW2 were constructed and tested. The MAST control capabilities were then used to apply the same shear-to-moment ratio along the height of the test wall. While the axial load was not added for two additional missing floors, this issues was addressed partway through the test. The increase in axial load is shown in Section 5.3 as part of the load path applied to both NTW2 and the OpenSees simulation.

The connection details of the base block to the strong floor nor the base block reinforcement details were not modified from NTW1. Since the actuators could only be placed at certain heights, the reduced height of NTW2 required the base block height to be increased. Additionally, the base block was constructed in two pieces to allow the wall to be constructed in the staging area at the MAST facility. Figure 5-2 shows the two-part construction of the base block used for NTW2.

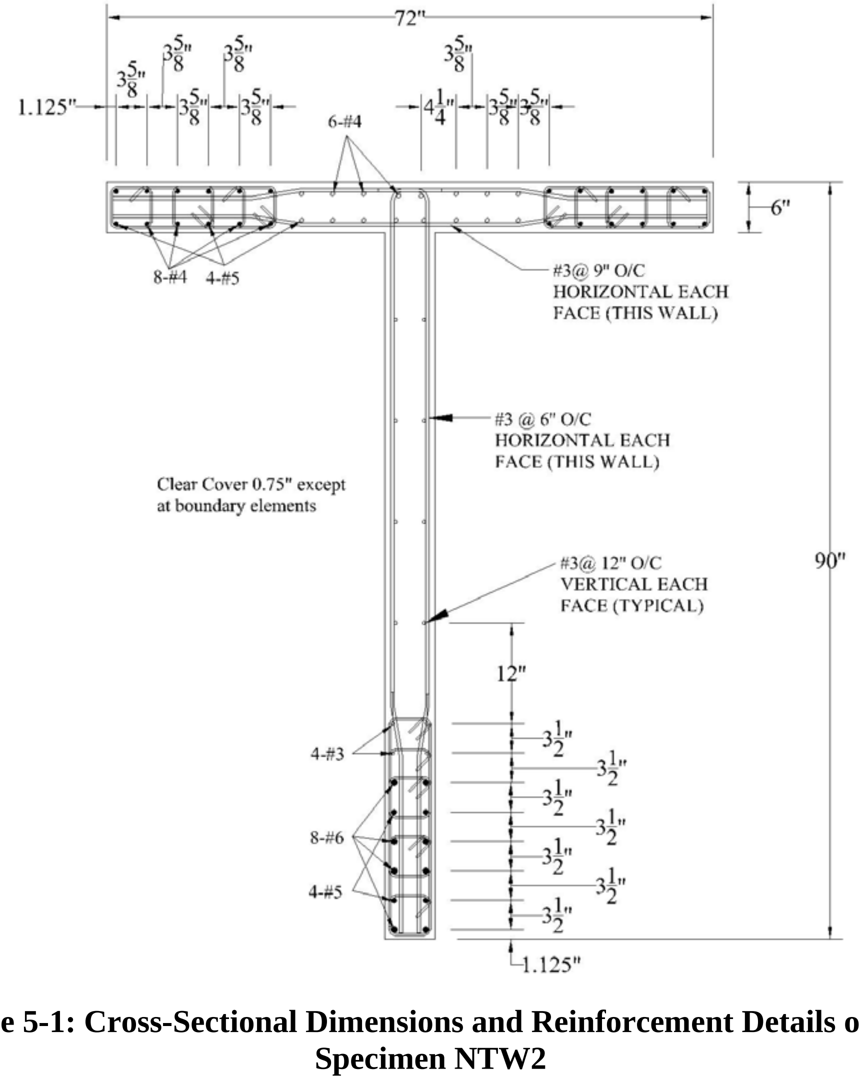

Figure 5-1: Cross-Sectional Dimensions and Reinforcement Details of Test Specimen NTW2

Figure 5-2: Two-part Base Block used for NTW2 to Expedite Construction

5.2 Description of Analysis Model

An OpenSees model for NTW2 was developed in a similar manner to the NTW1 analysis model used for the post-test analysis. The post-test model of NTW1 was established to accurately simulate the behavior of the T-wall by including the effects of shear lag, shear deformation, and strain penetration as shown in Figures 4- 33 and 4-34. The test wall NTW2 provided an opportunity to evaluate the predictive capabilities of the modeling approach proposed for flanged walls based on experimental data and analysis results of NTW1 as well as TW2 tested by Thomsen and Wallace [1993].

As with NTW1, a single force-based nonlinear beam-column was used to model the first floor level. However, since the longitudinal reinforcement was spliced at the second floor level, three beam-column elements were used to model the second floor of NTW2. One beam-column element modeled the splice region and was assigned a section that had twice the area of steel as the section used for regions outside of the splice. The length of the splice region was determined to be 25.5 in. which extended upwards from 5 in. above the first floor level. The length of the splice region was determined based on the equations for bond stress given by Priestley *et al.* [1996]. NTW2 had a story height of 72 in., leading to the wall model being 144 in. tall for the two stories that were constructed and tested. For an accurate shear-to-moment ratio to be applied to the critical region of the wall in the model, the displacements were applied at a control point located 312 in. above the base of the wall. The top of the wall and the control point were connected using a rigid element, see Figure 5-3.

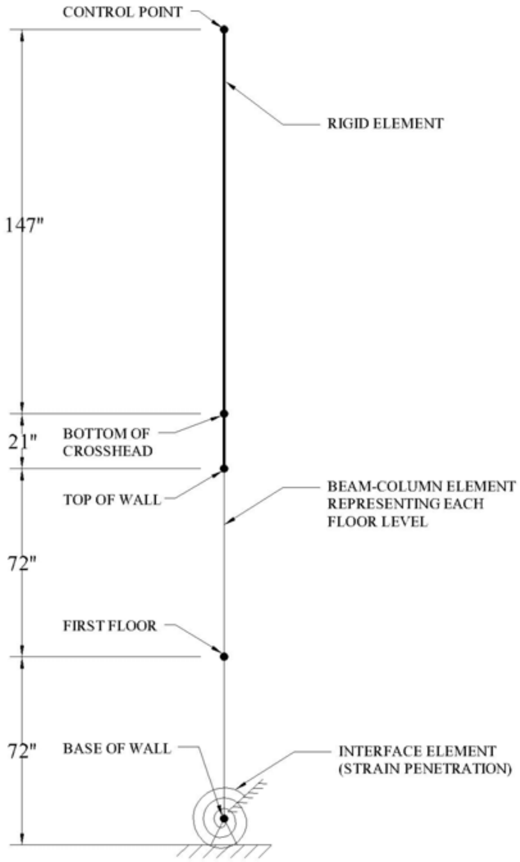

Figure 5-3: Schematic View of NTW2 Model

The fiber section that included the effects of shear lag described in Section 4.5.1 was used for all the beam-column elements modeling NTW2. The cross section of NTW2 was discretized using fibers to simulate the confined and unconfined concrete and the longitudinal steel similar to the procedure used for modeling of NTW1. A fiber size of 0.25 in. by 0.25 in. was used to discretize the wall cross section of NTW2. Further details on the discretization used for NTW1 and NTW2 may be found in Section 4.3. The confined and unconfined concrete behavior was modeled using the modified Chang and Mander model discussed in Chapter 3. The confined concrete properties were defined based on the measured unconfined concrete and steel strengths as well as the details of the confinement reinforcement. The peak tensile strength of concrete was based on split cylinder tests conducted on the day before testing of NTW2 started. The longitudinal reinforcement was again modeled using the modified Menegotto-Pinto steel model that is available in OpenSees. The parameters for the longitudinal reinforcement material model were taken from monotonic tension tests on the reinforcement conducted at UMN. The material properties for the the unconfined concrete and steel fibers are summarized in Tables 5-1 and 5-2, respectively. The concrete behavior was the same in the sections modeling both the non-spliced wall reinforcement and the spliced reinforcement.

As with NTW1, the effects of shear deformation were included by aggregating a uniaxial material model simulating the shear deformation response onto the previously defined fiber sections. Because the horizontal shear reinforcement of NTW2 was similar to NTW1, the shear deformation model defined for NTW1 was used for the shear-deformation model of NTW2. The distribution of the longitudinal steel in the flange would reduce the shear deformation of the flange in NTW2. Due to the lack of information, no adjustment to the shear model was made. As discussed in Section 4.4, although the shear deformation is handled as an element level response, the shear-deformation behavior was defined and connected to a particular section, rather than an element. This required that the shear deformation behavior be aggregated onto the NTW2 fiber sections defined for the spliced and non-spliced regions.

The effects of strain penetration at the interface between the wall and the base block were handled in the same manner as in NTW1. A zero-length element was used with a section similar to the section of the wall without any splices for the longitudinal reinforcement. The steel material model was replaced with the strain penetration model developed and implemented in OpenSees by Zhao and Sritharan [2007].

Table 5-1: Concrete Properties used for the Analysis of NTW2

f'_c (ksi)	ε_c (in./in.)	E_c (ksi)	f'_t (ksi)	ε_t (in./in.)
5.80*	0.00218	4769.33	0.571*	0.0002395

*Average results obtained from three test cylinders; all other values assumed based on concrete model presented in Chapter 3

Table 5-2: Reinforcement Properties for the Analysis of NTW2

Bar Size	Yield Stress (ksi)	Elastic Modulus (ksi)	Strain Hardening Ratio
#3	63.8*	29000	0.02
#4	72.1*	29000	0.02
#5	70.7*	29000	0.02
#6	70.7*	29000	0.02

*Average results from monotonic tension tests of three coupons; all other values were assumed based on typical reinforcement steel behavior

The difference between the cross head location 21 in. above the wall, where displacements were actually applied to the test specimen, and the control point where displacements were applied to the analytical model posed a challenge for defining the load path targets for NTW2. This is because the same load path that the NTW1floors experienced was selected for NTW2 to simplify comparisons between the performance of the two walls, thereby removing any path-dependent effects on the wall responses. This required that the displacement targets for both the crosshead location and control point had to be developed for NTW2 such that they matched the recorded second floor displacements of NTW1.

Two methods were investigated to determine how the recorded peak displacements at the second floor of NTW1 could be scaled up to the crosshead and control point locations for the testing and analysis of NTW2. The first method was based on the assumption that both the top block and the rigid element connecting the top block to the control point would remain elastic during all stages of loading. The additional displacement was calculated as a function of the recorded lateral force applied to NTW1. The second method was to determine the displacement at the control point and crosshead locations as functions of the analytical displacements at the second floor and fourth floor levels. The ratio of the displacement at the control point to the displacement at the second floor level and the ratio of the displacement at the crosshead to the displacement to the at fourth floor level were determined from the analysis. The two ratios could then be used to scale up the recorded peak second floor displacements to the control point and crosshead locations. The second method was found to give more consistent values for the determining the displacements at the crosshead and control point for all loading ranges of NTW1, and thus this method was selected to determine the displacement targets at the cross head and control point for NTW2. Consequently, the recorded peak displacements from NTW1 was multiplied by the appropriate ratio shown in Table 5-3 to determine the displacement targets for the crosshead and the control point location of NTW2. The second floor displacements were monitored and compared with the recorded NTW1 displacements at the same location. The displacement of the second floor level of NTW2 was within 0.1 in. of the displacements recorded for NTW1.

Table 5-3: Displacement Ratio Used to Scale NTW1 Second Floor Displacements

Direction	Control Point Location	Crosshead Location
Flange-in-Tension	1.153	2.229
Flange-in-Compression	1.141	2.133
Flange	1.125	2.003

The base block of NTW2 was connected to the strong floor with ten three-in. diameter threaded Dywidag bars. The height of the base block provide adequate anchorage for the wall longitudinal reinforcement. Consequently, the base block was not represented with a node in the analysis model, the degrees-of-freedom of this node was fixed in all directions. The base block was instrumented with LVDTs and string potentiometers in order to monitor the base block during testing, because there was some concern that the increased height of the base block and its two-piece construction would cause it to distort during testing. No movement or rotation of the base block or relative movement between the two pieces was recorded during testing, validating the assumed fixed boundary condition used for the base block..

An axial load of 186.5 kips was applied to NTW2 initially; however, as stated earlier in Section 5.1, the axial load was later increased to 201.4 kips to account for the weight of the missing third and fourth floors. This required the analysis of NTW2 to be conducted in several different loading stages. The first stage modeled the 186.5 kips of axial load when it was applied to the wall, then lateral displacements were applied to the model in the next stage. In the third stage, the axial load was increased to 201.2 kips, and the remaining displacement history was applied to the model in the fourth and final stage.

5.3 Multidirectional Load Path

As previously noted in Section 5.1, the load path for NTW2 was selected primarily to match the displacements measured at the second floor level of NTW1. The improved reinforcement details were expected to allow NTW2 to be displaced further in both the flange and web directions than those experienced by NTW1. As in NTW1, positive displacement in the web direction places the flange in compression, while negative displacement places the flange in tension. Incorporating the factors from Table 5-3, Table 5-4 presents the displacements targets established for the crosshead. Graphical representations of the applied displacement path is shown in Figure 5-4 through 5-18.

Table 5-4: Applied Displacement Targets For NTW2 at the crosshead

Load Step	Load Description	Parallel Flange (in.)	Parallel Web (in.)
0	Apply Axial Load of 186.5 kips	0.0	0.0
1-3	25% First Yield Displacement in Web Direction	0.0	0.062
		0.0	-0.073
4-6	50% First Yield Displacement in Web Direction	0.0	0.127
		0.0	-0.166

Table 5-4 Cont'd

Load Step	Load Description	Parallel Flange (in.)	Parallel Web (in.)
7	25% First Yield Displacement in Flange Direction	0.16	0.0
		-0.155	0.0
8	25% First Yield Displacement in 45º Direction	0.044	0.046
		-0.04	-0.061
9	25% First Yield Displacement in (100% Flange + 30% Web) Direction	0.118	-0.03
		-0.159	0.06
10	50% First Yield Displacement in Web Direction	0.0	0.127
		0.0	-0.168
11	75% First Yield Displacement in 45º Direction	0.269	0.296
		-0.245	-0.263
12	75% First Yield Displacement in (100% Flange + 30% Web) Direction	0.435	-0.124
		-0.592	0.225
13-15	75% First of Yield Displacement in Web Direction	0.0	0.40
		0.0	-0.51
	Increase Axial Load on Specimen to 201.2 k	0.0	0.0
16	75% First Yield Displacement in Web Direction	0.0	0.40
		0.0	-0.51
17	50% First Yield Pentagram Shaped Load Path	0.0	0.127
		0.116	0.127
		0.417	0.0
		0.0	-0.168
		-0.417	0.0
		-0.116	0.127
		0.0	0.127
18	75% First Yield Displacement in Web Direction	0.0	0.4
		0.0	-0.51
19-21	100% First Yield Displacement in Web Direction	0.0	0.616
		0.0	-0.733

Table 5-4 Cont'd

Load Step	Load Description	Parallel Flange (in.)	Parallel Web (in.)
22-24	150% First Yield Displacement in Web Direction	0.0	0.924
		0.0	-1.1
25-27	1% & 1.5% Drift in Web Direction	0.0	1.62
		0.0	-2.403
28	1% & 1.5% Drift in 100% Web + 30% Flange	0.43	1.330
		-0.68	-2.010
29	1% Drift in Flange Direction	1.25	0.0
		-1.25	0.0
30	1.5% Drift in 45° Direction	1.3	1.56
		-1.45	-1.53
31	1.5% Drift in Flange Direction	1.91	0.0
		-1.91	0.0
32	1.5% Drift in 100% Flange + 30% Web Direction	-1.81	0.7
		1.85	-0.69
33-34	1% & 1.5% Drift in Web Direction	0.0	1.616
		0.0	-2.403
35-37	1.5% & 2% Drift in Web Direction	0.0	2.46
		0.0	-3.15
38	2.0% Drift Hourglass Displacement Path	1.81	2.21
		-1.81	2.21
		0.0	0.0
		1.90	-2.26
		0.0	-3.15
		-1.90	-2.26
39	2% & 2.5% Drift in Web Direction	0.0	2.78
		0.0	-3.89
41	1.5% Drift in Flange Direction	1.91	0.0
		-1.91	0.0

Table 5-4 Cont'd

Load Step	Load Description	Parallel Flange (in.)	Parallel Web (in.)
42-44	2% Drift in Flange Direction	2.69	0.0
		-2.69	0.0
45-47	2.5% Drift in Flange Direction	3.41	0.0
		-3.41	0.0
48-50	3% Drift in Flange Direction	4.15	0.0
		-4.15	0.0
51-52	4% Drift in Flange Direction	5.95	0.0
		-5.95	0.0

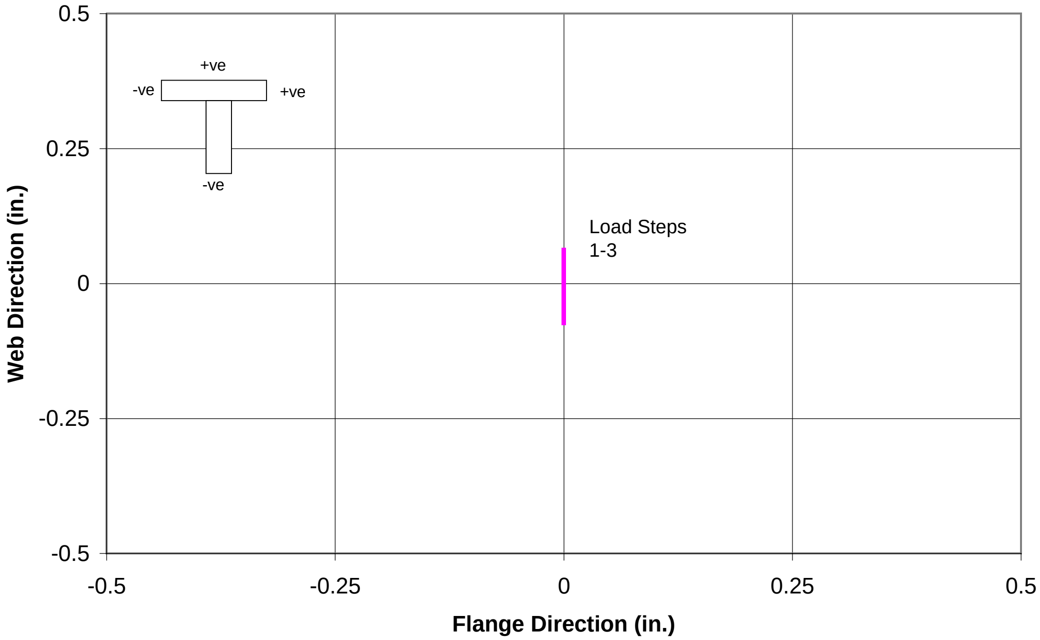

Figure 5-4: Load Steps 1 to 3 to Test NTW2 in the Web Direction at 25% of First Yield Displacement.

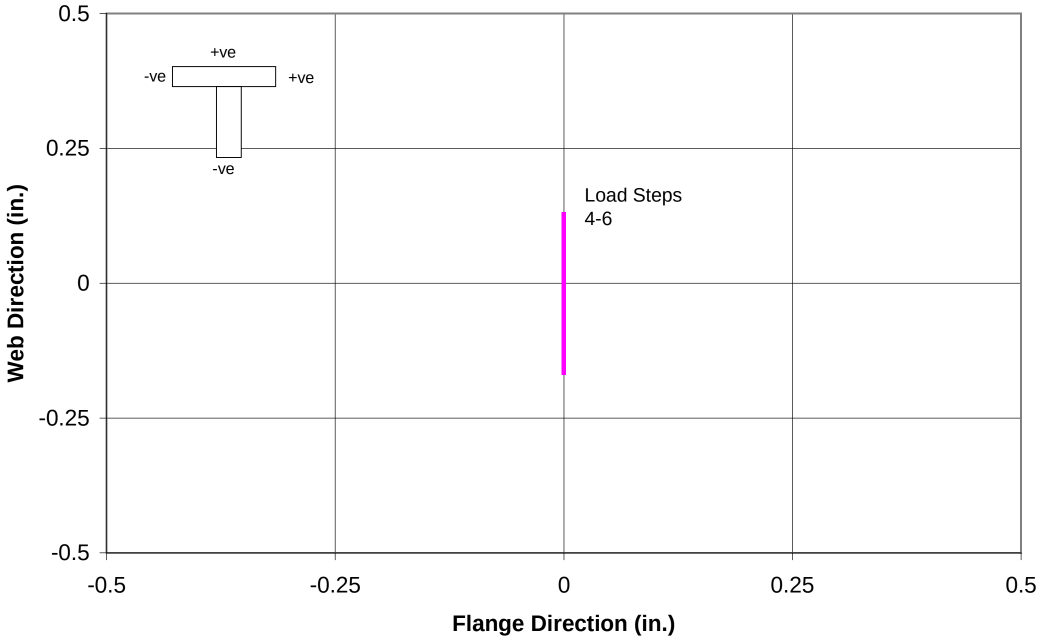

Figure 5-5: Load Steps 4-6 to Test NTW2 in the Web Direction at 50% of First Yield Displacement

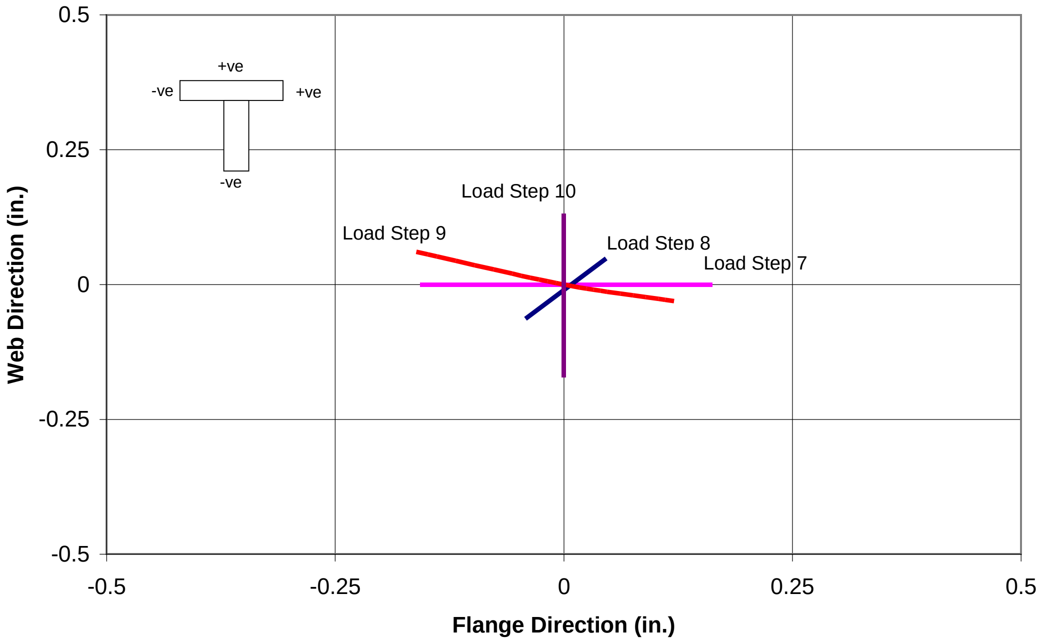

Figure 5-6: Load Steps 7 to 10 to Test NTW2 at 45°, Parallel to the Web, and 100+30 Directions at 25% of First Yield Displacement, and Repeat of 50% of First Yield in Web Direction

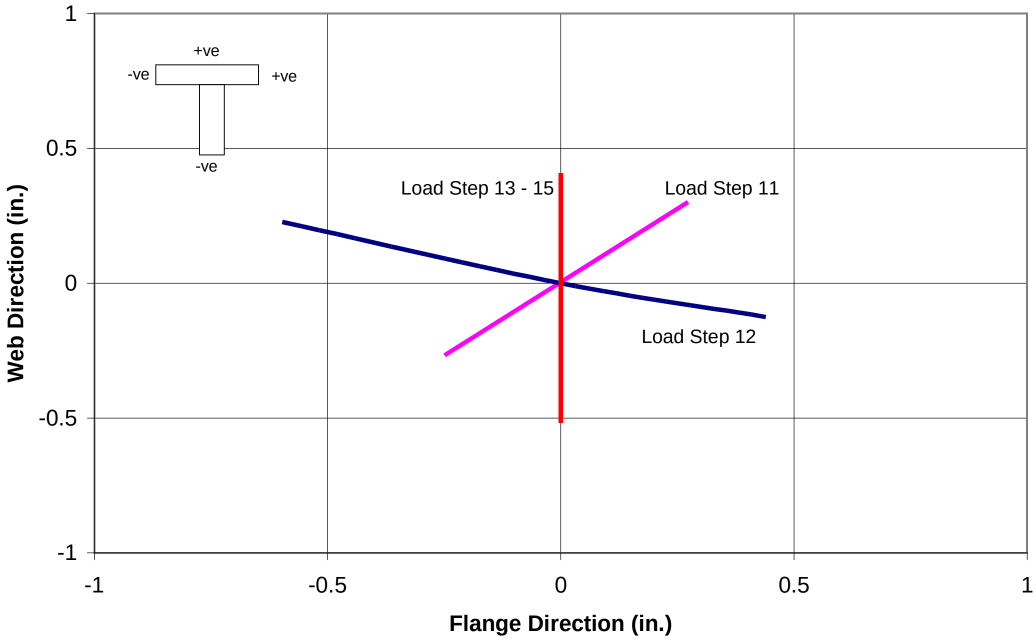

Figure 5-7: Load Steps 11 to 15 to Test NTW2 at 45º, 100+30, and Web Direction at 75% of First Yield Displacement

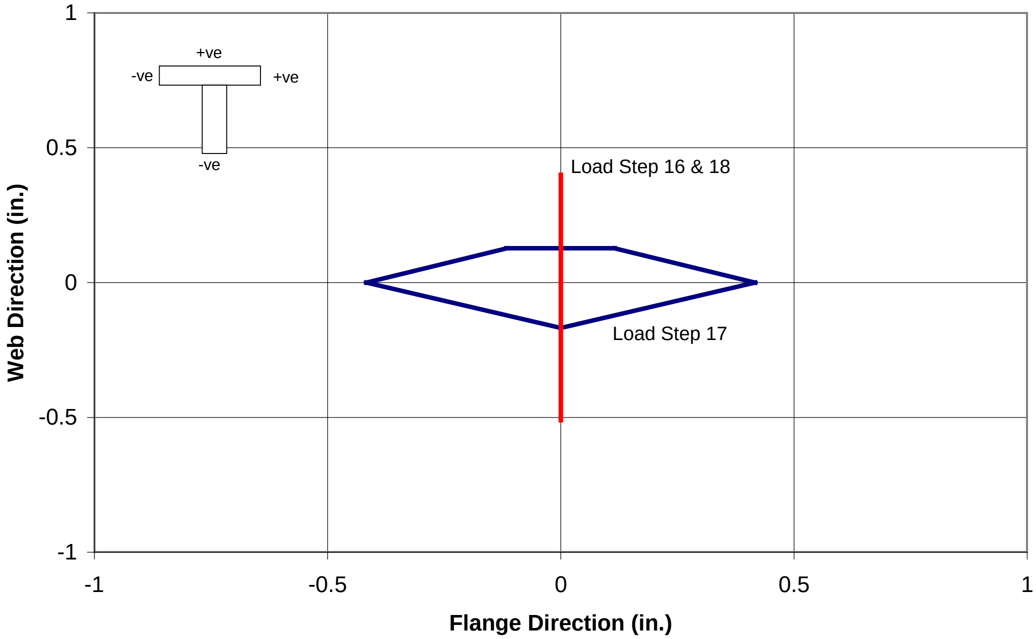

Figure 5-8: Load Step 16 to Test NTW2 Web Direction at 75% First Yield Displacement, Load Step 17 to Test 50% First Yield Pentagon Load Path, and Load Step 18 Repeat Web Direction at 75% First Yield Displacement

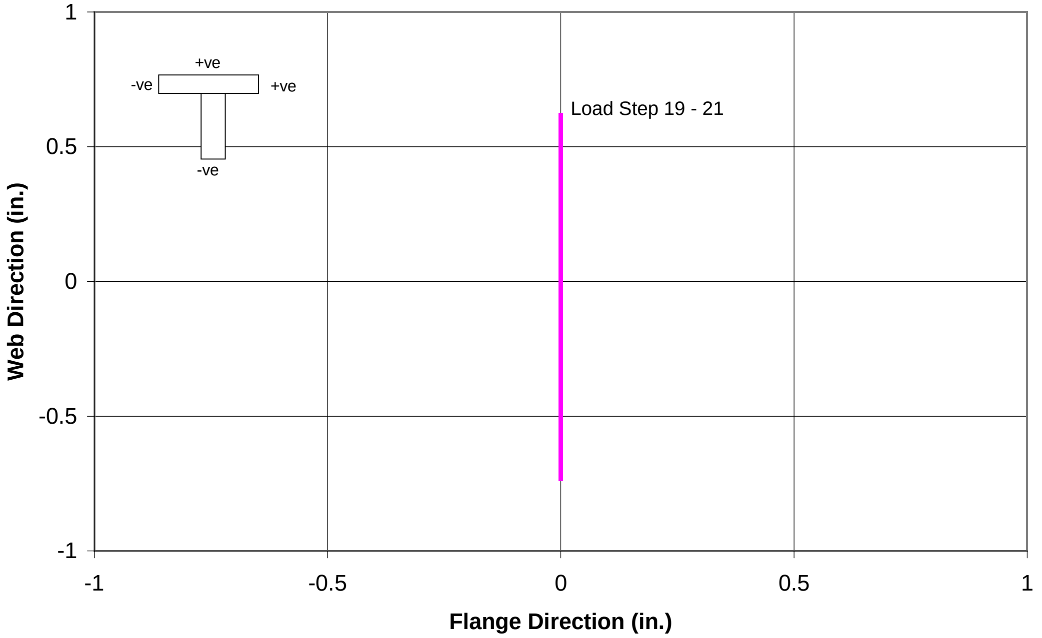

Figure 5-9: Load Steps 19 to 21 to Test NTW2 in the Web Direction at 100% First Yield Displacement

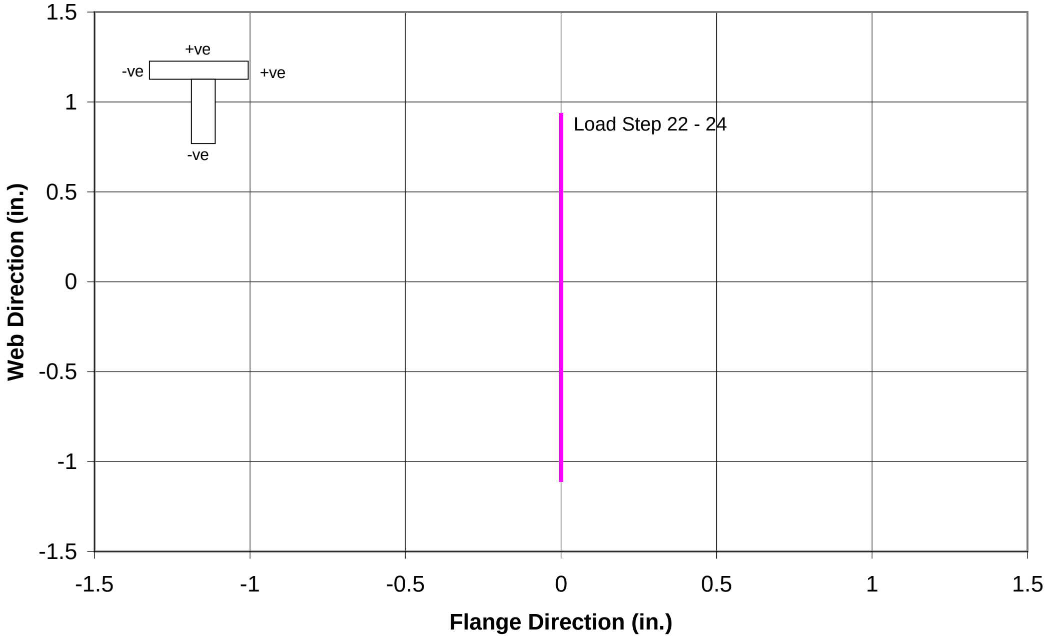

Figure 5-10: Load Steps 22 to 24, to Test NTW2 in the Web Direction of 150% First Yield Displacement

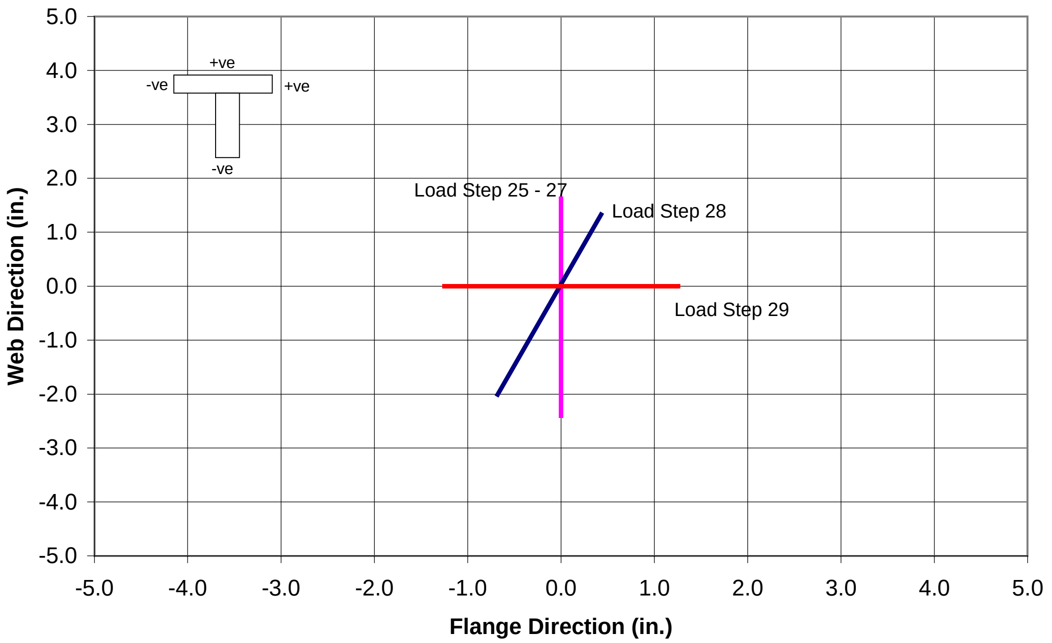

Figure 5-11: Load Steps 25 to 29 to Test NTW2 in Multidirectional Loadings at 1% and 1.5% Drift Levels

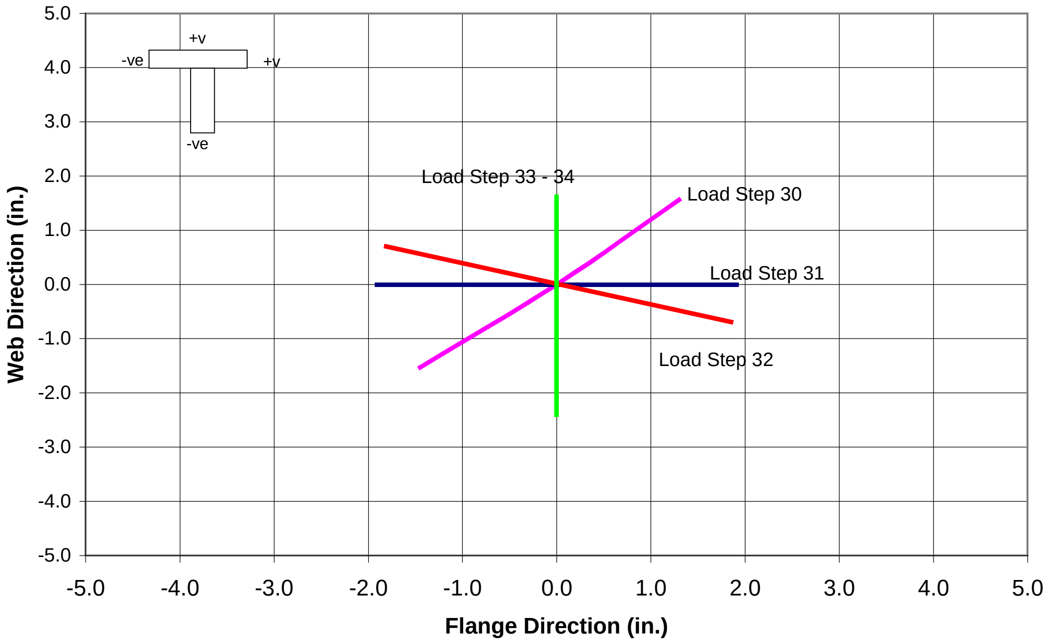

Figure 5-12: Load Steps 30-34 to Test NTW2 in Multidirectional Loadings at 1% and 1.5% Drift Levels

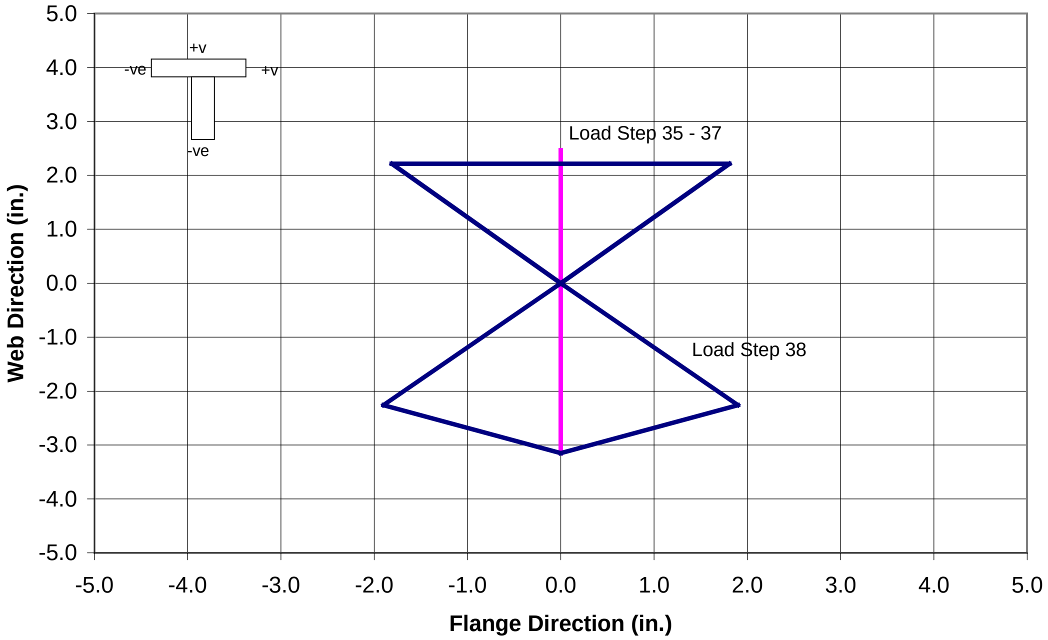

Figure 5-13: Load Steps 35-37, to Test NTW2 at 1.5% and 2.0% Drift in the Web Direction and Load Step 38 to Test 2% "Hourglass" Displacement Path

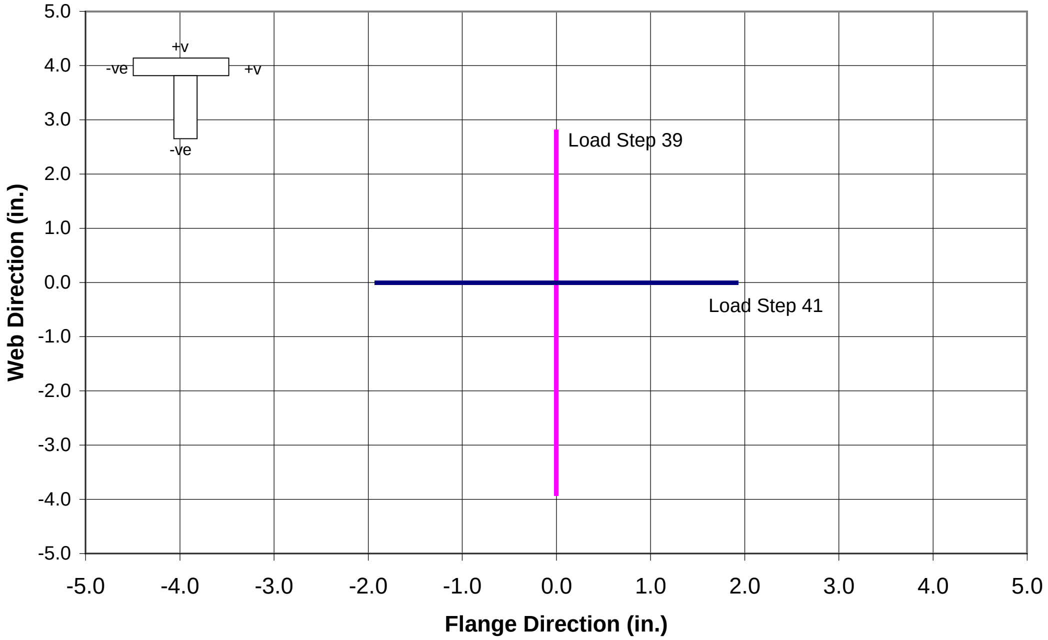

Figure 5-14: Load Steps 39 and 41, to Test NTW2 at 2.0% and 2.5% Drift in the Web Direction and 1.5% Drift in the Flange Direction

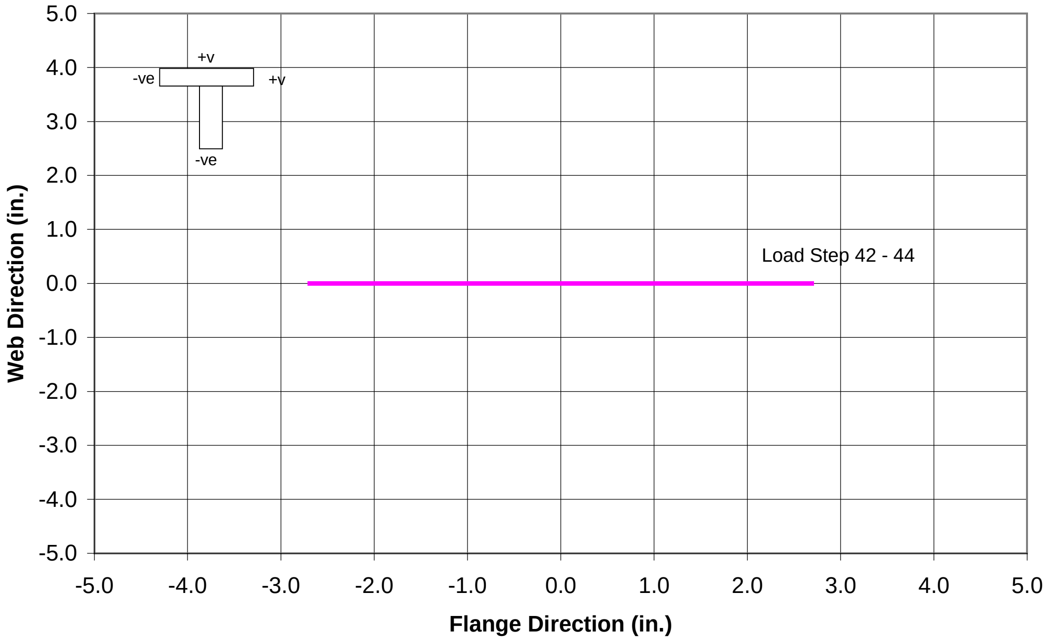

Figure 5-15: Load Steps 42-44 to Test NTW2 at 2.0% Drift in the Flange Direction

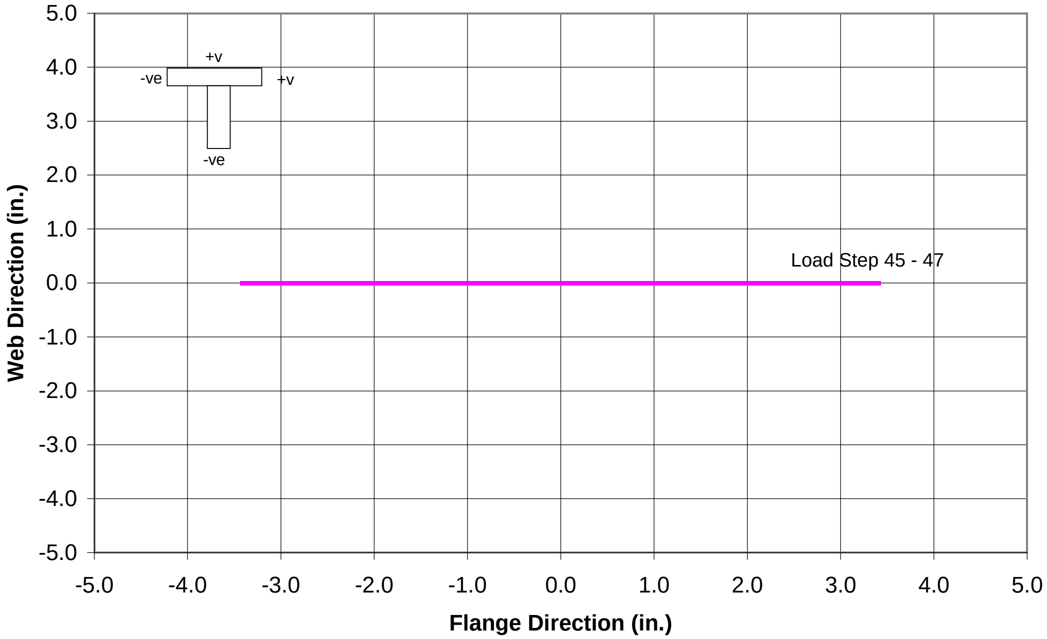

Figure 5-16: Load Steps 45-47 to Test NTW2 at 2.5% Drift in the Flange Direction

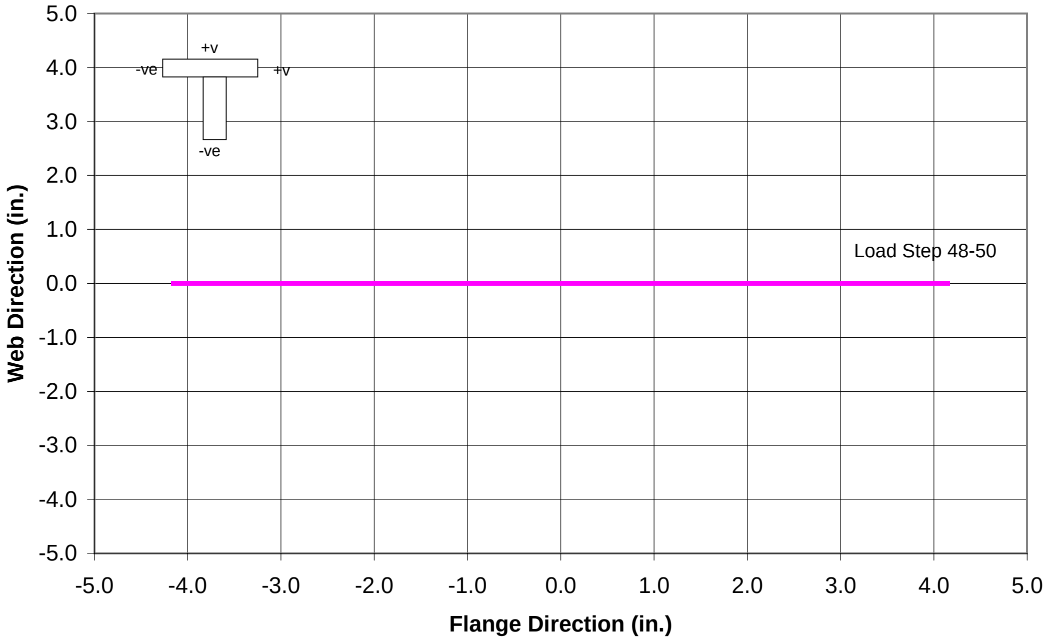

Figure 5-17: Load Steps 48-50 to Test NTW2 at 3.0% Drift in the Flange Direction

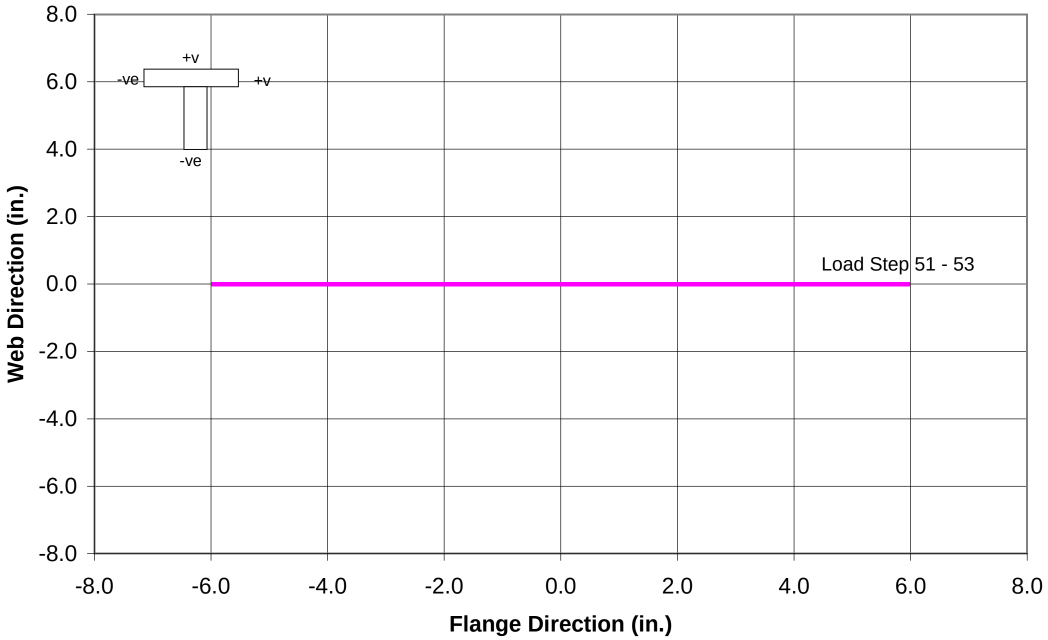

Figure 5-18: Load Steps 51-52 to Test NTW2 at 4.0% Drift in the Flange Direction

The displacements at the control point were applied to the NTW2 analytical model. Figures 5-19 and 5-20 compares the experimental and analytical displacements applied at the second floor of NTW2 as a function of the measurement number in the flange and web directions, respectively. Again, the measurement number refers to the number of times data was recorded during the test, which is also referred to as a "scan number". The second floor displacement of the analytical model was nearly identical to the recorded displacement of the test specimen. The OpenSees displacement was always within 0.07 in. in the flange direction and 0.05 in. in the web direction for the peak values obtained from the recorded potentiometer measurements. Figures 5-21 compares the recorded second floor displacements in the flange and web directions.

Figures 5-21 and 5-22 show the lateral force versus the measurement number for the flange and web directions, respectively. The lateral force could not be plotted as a function of the cumulative displacement because the minor differences in applied displacements quickly accumulate and make any useful comparison as a function of cumulative displacement impossible.

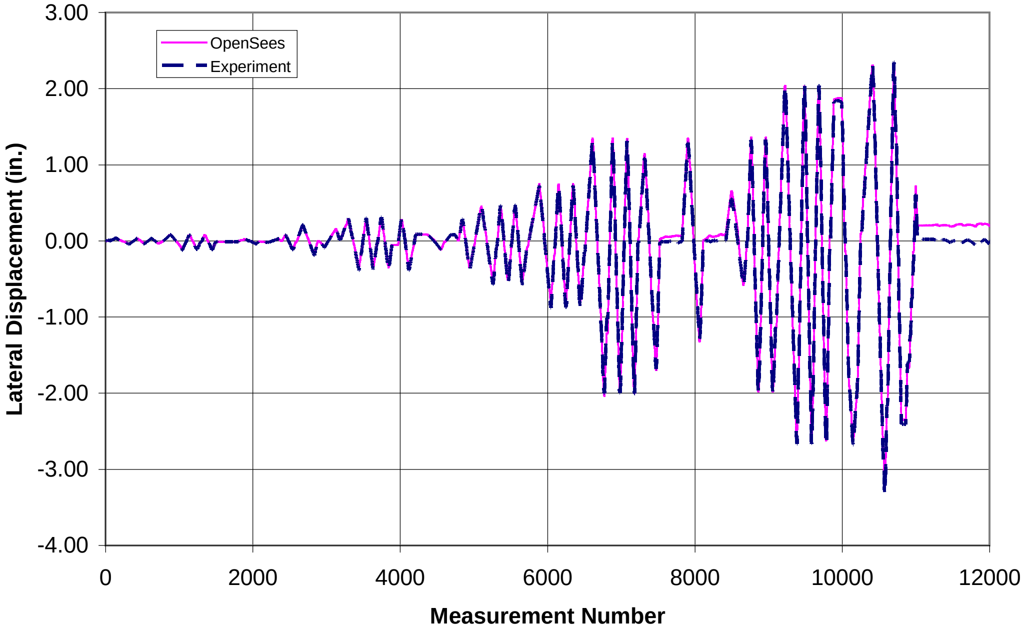

Figure 5-19: Comparison of Second Floor Displacement of NTW2 in the Web Direction as a Function of Measurement Number

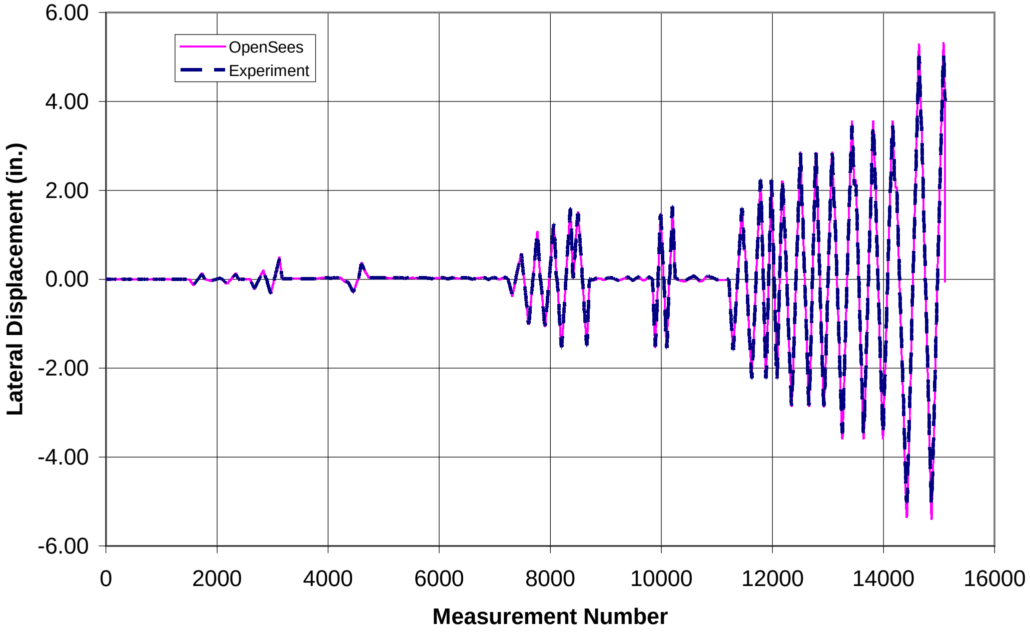

Figure 5-20: Comparison of Second Floor Displacement of NTW2 in the Flange Direction as a Function of Measurement Number

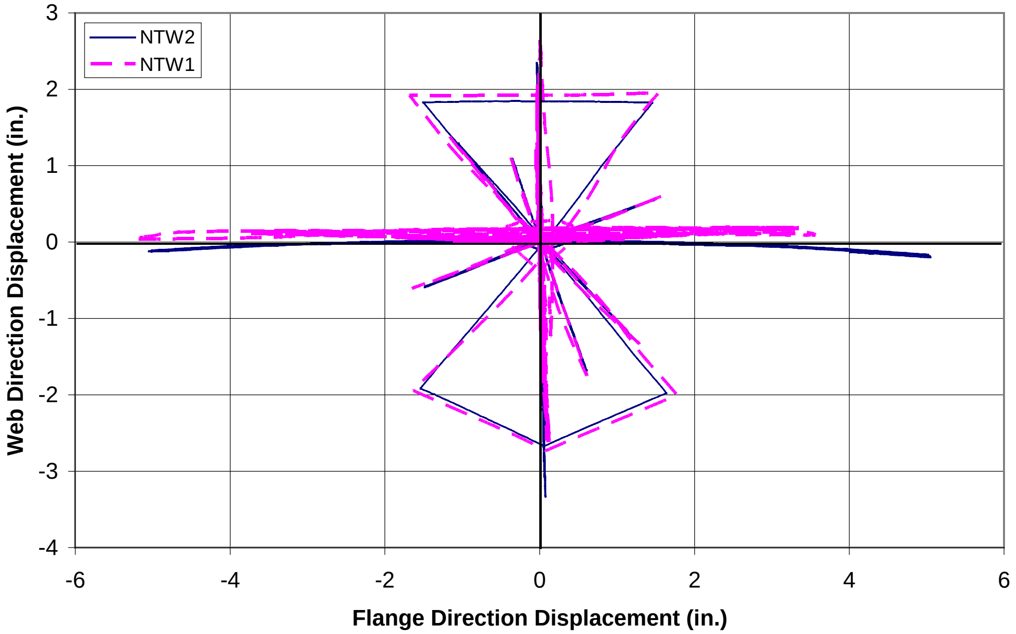

Figure 5-21: Comparison of Second Floor Displacements Recorded for NTW1 and NTW2 in the Flange and Web Directions

5.4 Summary of Response

NTW2 was subjected to to the load path described in Sec. 5.3 beginning on November 29 and was completed on December 6, 2007. As with NTW1 the testing took 7 days to complete. NTW2 showed a significantly different pattern of cracking compared to that observed in NTW1. NTW2 exhibited small, well distributed flexurral cracks in the the flange. Additionally, very few diagonal shear cracks were observed in the flange during testing. Figure 5-22 shows the flange of NTW2 after yielding of the longitudinal reinforcement in the flange. The web of NTW2 exhibited the same crack pattern observed for NTW1. Figure 5-23 shows the large diagonal cracks outside the boundary elements and the fine well distributed cracks in the boundary elements. The increased distributed steel in the flange led to better crack control than in the web where the longitudinal reinforcement was concentrated in the web tip boundary element. As with NTW1, NTW2 exhibited a very stable response with the second and third cycles at a load level exhibiting the negligible degradation in the force resistance.

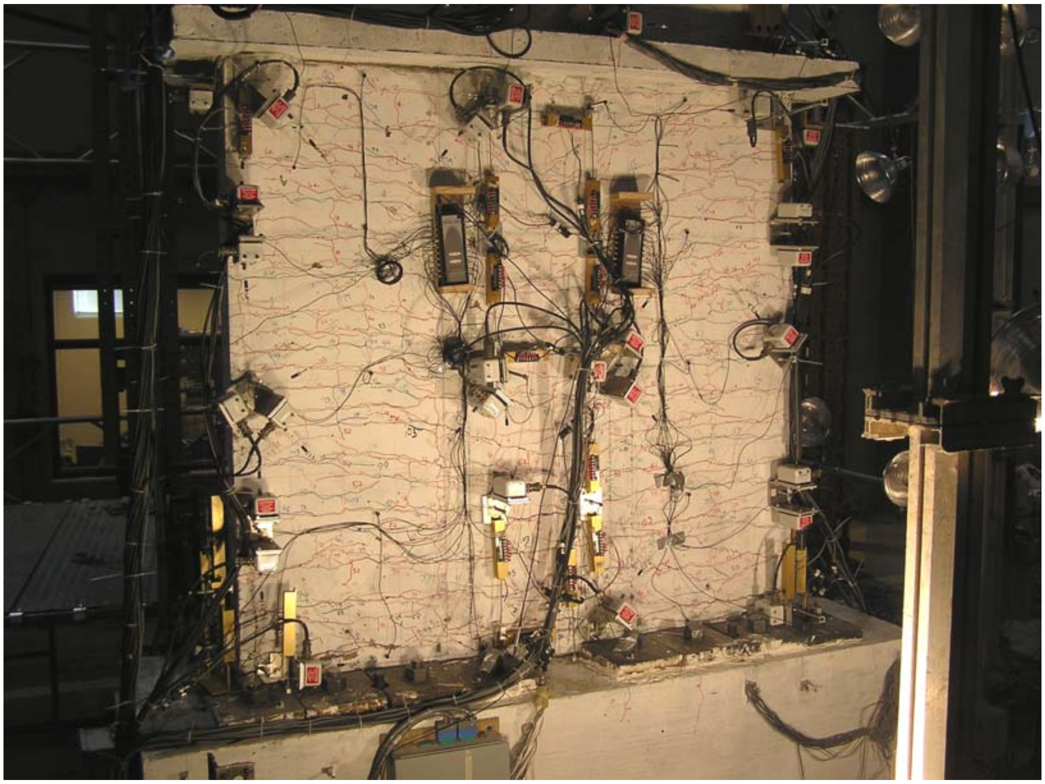

Figure 5-22: Flange of NTW2 after Yielding of the Longitudinal Reinforcement

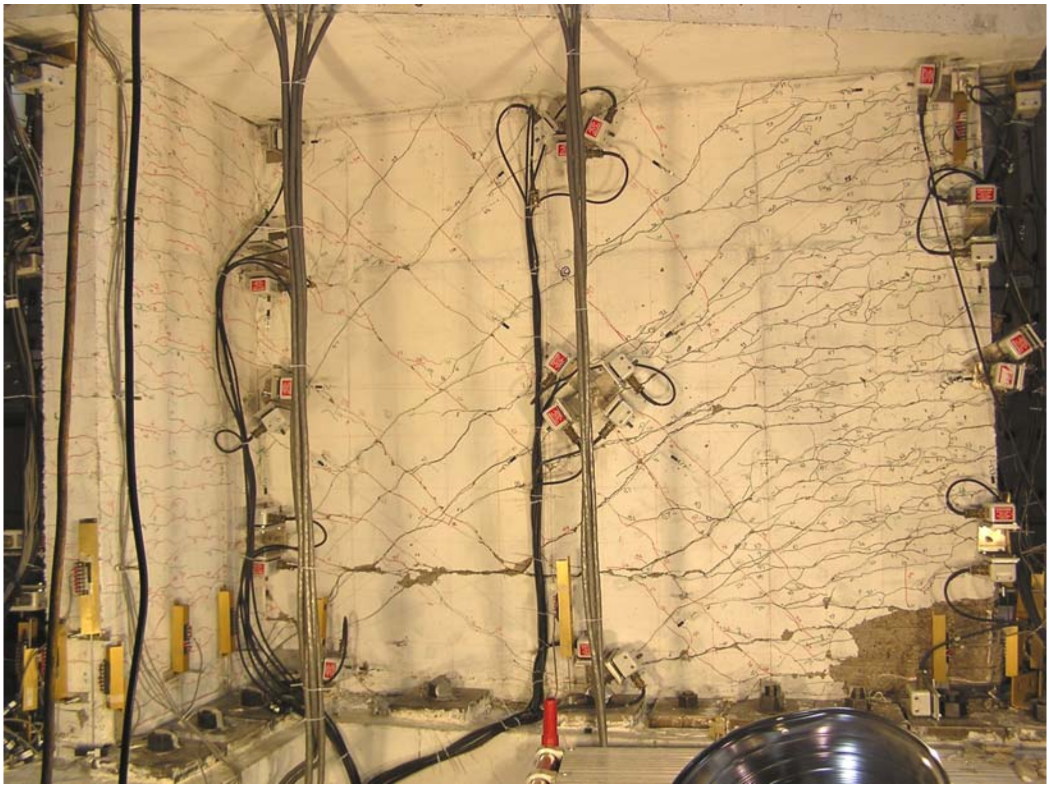

Figure 5-23: Web of NTW2 after Yielding of the Longitudinal Reinforcement

Failure in the web direction was caused by buckling of the longitudinal reinforcement in the web direction. The revised detailing of the web tip boundary element was effective in detailing the buckling of the longitudinal reinforcement until 2.5% lateral drift. Following failure in the web direction, NTW2 was unloaded and returned to approximately zero residual displacement.

NTW2 was then cycled in the flange direction until the longitudinal reinforcement in the flange tip boundary elements buckled at approximately 4% drift. NTW1 experienced bucking of the longitudinal reinforcement in the flange boundary elements at 3% lateral drift, while NTW2 exhibited a stable response on all three cycles at 3% lateral drift.

Overall NTW2 exhibited a very good performance. It was displaced further in both the web and flange direction than NTW1. Additionally, the cracks in the flange were well controlled by the distributed steel in the flange. The splice at the first floor level performed well with no relative movement recorded between the spliced bars. A complete discussion of the experimental response of NTW2 can be found in Brueggen [2009].

5.5 Comparison of Analytical and Experimental Results

This section presents comparison of the experimental and analytical responses at the global and local levels. Since the improvements to the OpenSees capabilities were made the emphasis of the NTW2 analysis was placed in predictability of an OpenSees model using available capabilities. Consequently, no post-test analysis were performed, but appropriate recommendations to further improve the fiber-based analysis of non-rectangular walls are made.

5.5.1 Force-Displacement Responses

The lateral force-displacement responses in the web and flange directions are shown in Figures 5-24 and 5-25, respectively. The experimental response in each direction shows the average of the recorded string potentiometer displacements measured at the flange tips and the force resistance recorded by load cells connected to the actuators during the test. The analytical response was taken from the lateral displacement recorded at the node representing the second floor level of NTW2 while the force resistance was established from the member forces at the bottom end of the beam-column element modeling the wall at the first floor level. As seen in Figure 5-24, the web direction response was generally well captured by the analytical model until strength degradation experienced in NTW2 due to buckling of the longitudinal reinforcement in the web tip boundary element at a lateral displacement of -3.89 inches. A good agreement between the experimental and simulated force-displacement are observed in terms of the force resistance in the flange-in-compression loading direction, the unloading/reloading stiffness, and the residual displacements after unloading from peak lateral displacements.

The force resistance in the flange-in-tension loading direction was underestimated by the analysis by approximately 5%. Figure 5-25 shows the flange direction response was not as well predicted as the web direction response. The peak lateral resistance and the reloading stiffness were significantly overpredicted in the displacement range of 1.8 to 3.5 inches. Similar to NTW!, pinching of the global response was not observed in either the predicted nor measured response. Figures 5-26 and 5-27 compare the measured and simulated lateral force resistance versus the measurement number for the web and flange directions, respectively. In this perspective, the accuracy of the wall response simulation in the web direction is evident. The underestimation of the force in the web direction was likely due not capturing the shear lag in the flange accurately and its corresponding effect on the tensile strain distribution along the flange. The second possible source that could have contributed to this discrepancy was the inaccuracy in the shear deformation of NTW2, which could have affected both directions of loading although larger error should be expected in the flange-in-tension direction due to the increased shear force in that direction.

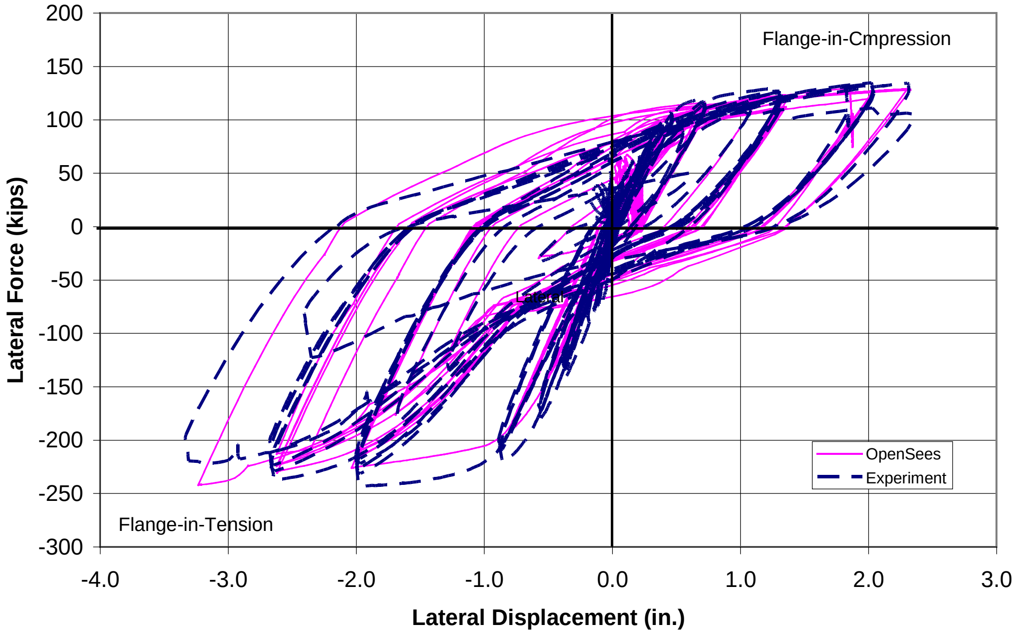

Figure 5-24: Measured and Predicted Force-Displacement Responses of NTW2 in the Web Direction

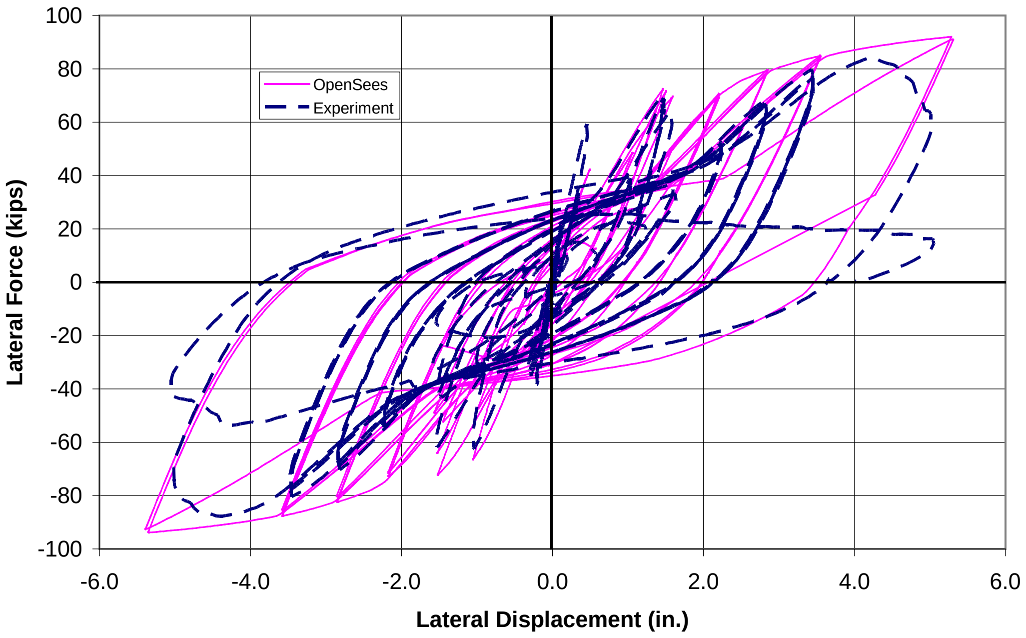

Figure 5-25: Measured and Predicted ed Force-Displacement Responses of NTW2 in the Flange Direction

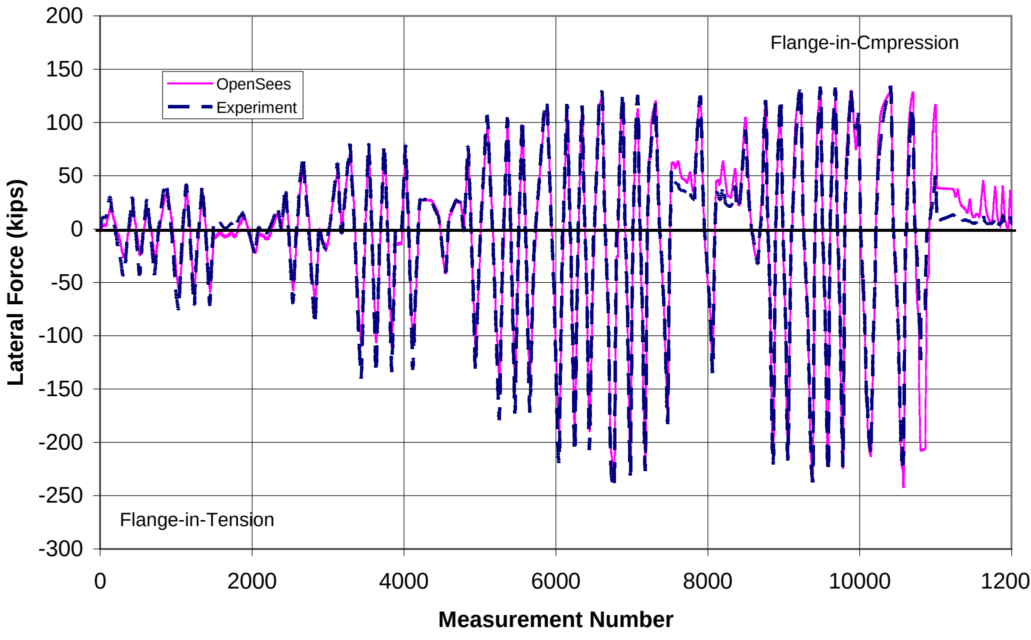

Figure 5-26: Measured and Predicted Force Resistance of NTW2 in the Web Direction as a Function of Measurement Number

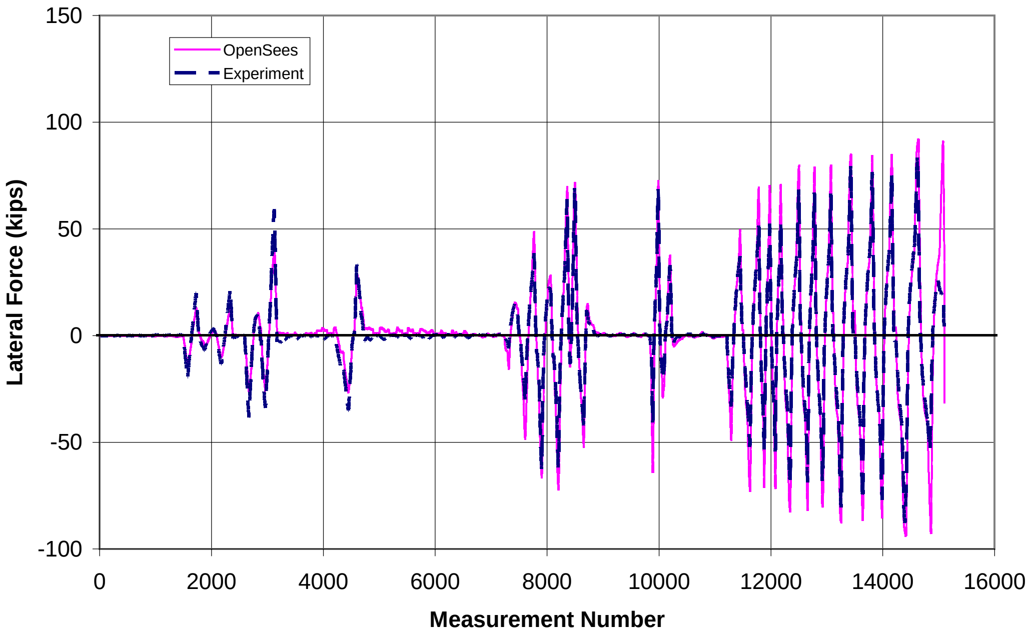

Figure 5-27: Measured and Predicted Force Resistance of NTW2 in the Flange Direction as a Function of Measurement Number

The strain distribution due to shear lag that was used in the section definition of NTW2 was based on the observed strain distribution in NTW1 and TW2 (TW2 was the second T-wall tested by Thomsen and Wallace [1993]). Both of those walls had low amounts of distributed steel between the boundary elements, while NTW2 had a large portion of the longitudinal steel in the flange that was distributed along the flange length. The distribution of the steel can influence the shear stiffness of the unstiffened portion of the flange, referred hereafter as the “free flange overhang”. Increased shear stiffness of the free flange overhang will likely decrease the influence of shear lag, thereby increasing the lateral force resistance. Although this phenomenon was expected, this issue was not addressed due to the lack of information to handle this behavior in the NTW2 model. Figure 5-28 compares the experimental response of NTW2 with simulated response in the web direction that was obtained with the “plane sections remain plane” assumption ignoring the shear lag effects. As expected, the analytical response shows a higher stiffness than that found with the inclusion of shear lag. The higher stiffness observed in the experiment is, therefore, attributed to the decreased influence of shear lag due to the increased shear stiffness of the free flange. Figure 5-29 shows the strain distribution recorded along the length of the flange in NTW2 at 1.5 yield displacement and the predicted strain distribution from the equation used to include the effects of shear lag. The experimental strain was taken from the strain gages located nominally 6 inches about the base block. Although the data is erratic it is seen that the effects of shear lag are noticeably over estimated for NTW2 by the OpenSees analysis.

The shear deformation response of NTW2 was modeled based on that used for the post-test simulation of NTW1. The assumption was made that the shear deformation would not be significantly different in the web between the two walls, because the shear reinforcement in the web was not modified from NTW1. Figure 5-25 shows the comparison between the shear deformation response measured in the web of NTW2 and the shear deformation response of OpenSees model at the first floor level. The difference in the shear deformation behavior would also significantly contribute to alleviating the discrepancy seen in the web direction force-displacement response. The measured response is stiffer than was used in the analysis. The increased stiffness is due to the very high stiffness of the second floor due to the lapped bars in the splice The large amount of steel prevented yielding and cracks opening very far, leading to negligable softening of the shear stiffness. The decreased shear stiffness would decrease the stiffness of the wall model. Since the analysis was conducted in displacement control, this softening would lead to a decreased lateral resistance, and thus increasing the analysis shear stiffness would increase the lateral force resistance and reduce the discrepancy seen in Figure 5-24.

The flange direction response shown in Figure 5-25 and 5-27 exhibit that the OpenSees analysis did not capture the force-displacement response as well as it captured the web direction response. The discrepancies are attributed to a number of different actions: 1) damage due to previous load cycles, 2) error in the residual strains and stresses from the multidirectional loading patterns resulting from inaccurate simulation of shea lag effects, and 3) the shear-distortion response that was taken from the response of NTW1.

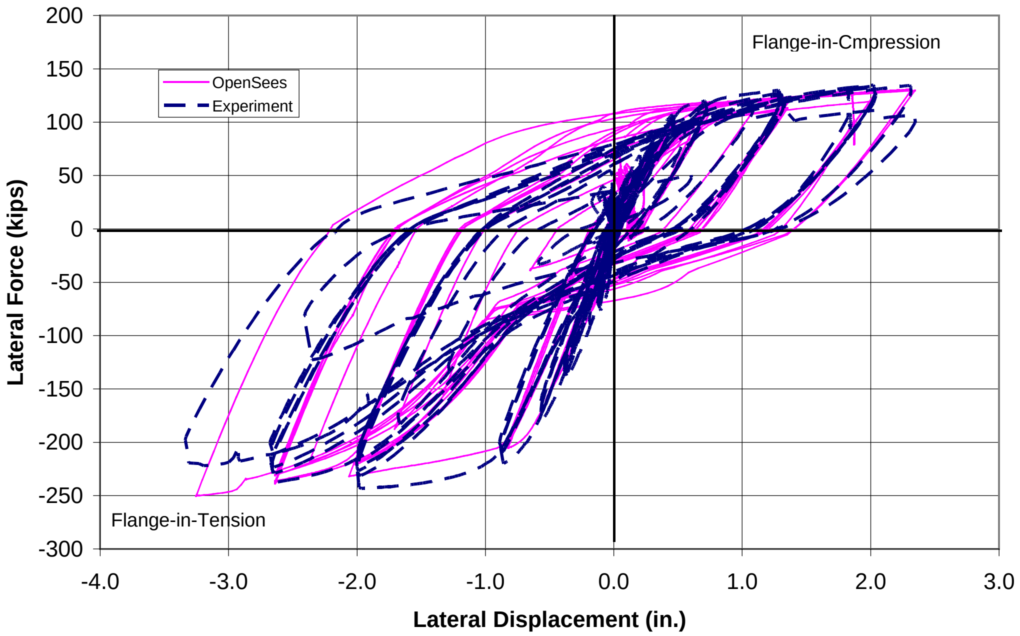

Figure 5-28: Measured and Predicted Force-Displacement Responses of NTW2 in the Web Direction Without Accounting for Shear Lag

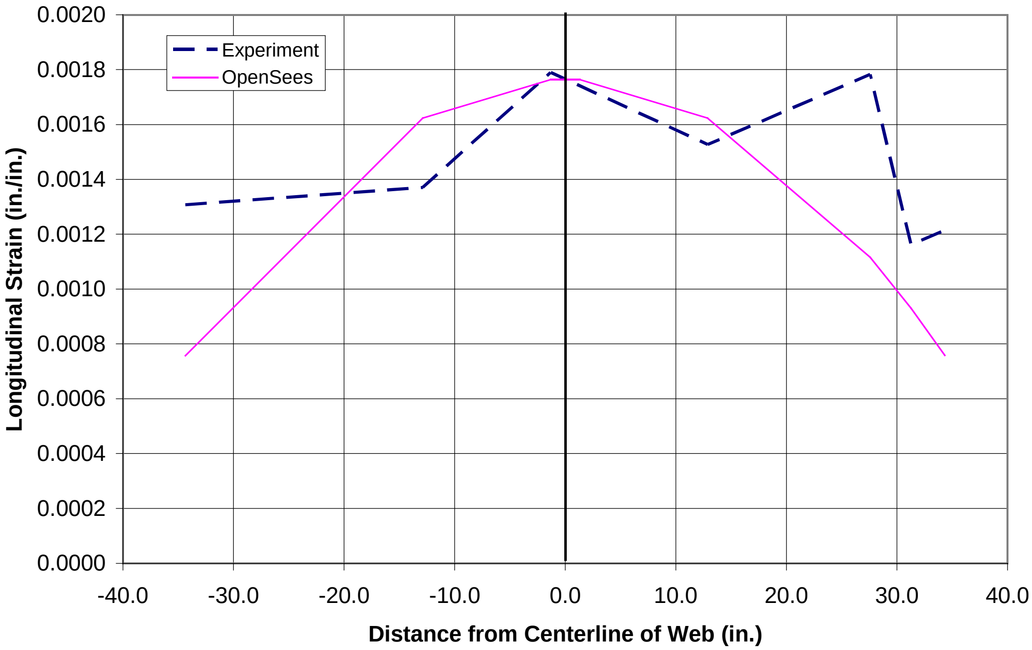

Figure 5-29: Comparison of Measured Strain Distribution in the Flange with that simulated by the OpenSees Model with Shear Lag at 0.75 First Yield Displacement in Web Direction

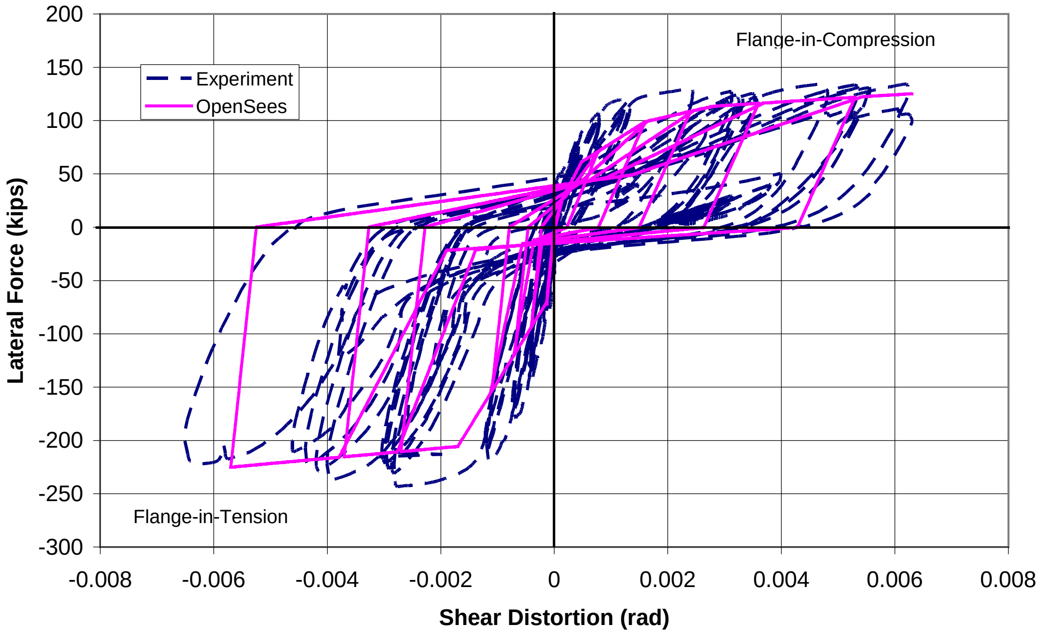

Figure 5-30: Comparison of Measured Shear Response for the First Floor of NTW2 in the Web Direction with the Response of NTW1 OpenSees Material Model

The selected displacement targets typically loaded NTW2 in the parallel to the web direction first at a particular displacement or drift level. This caused moderate to significant damage to the flange of the wall depending on the drift level. For example, the flange was heavily cracked due to the applied loading in the web direction at first yield of the longitudinal reinforcement, see Figure 5-31. If this damage was not fully captured in the simulation as was the cased based on the study reported in Appendix A, it could account for some of the overestimation of the wall resistance in the flange direction. If the shear lag effect was overestimated in the web direction loading, it would be expected that the damage would be underpredicted in the flange tips, as discussed earlier. This would lead to the overprediction of the lateral force resistance seen in the Figure 5-25 and 5-27.

The load path for NTW1 and NTW2 included displacements in the web, flange, and skewed directions with the first load cycles predominately in the web direction. When the flange was placed in tension that caused inelastic strains in the longitudinal reinforcement and then unloaded during web direction loading, the reinforcement fibers were subjected to residual strains. When the wall was then displaced in the flange direction, the strength and stiffness of the wall in this direction were influenced by the residual strains in the longitudinal reinforcement fibers in the flange. Furthermore, the shear lag effects that existed when the flange was in tension during web direction loading lowered the strain at the flange tips. Maintaining accurate estimations of tensile strains in the flange tips is critical for obtaining good force resistance estimation of the wall in the flange direction loading. Thus, overestimation of the effects of shear lag led to an overestimation of both the stiffness and force resistance in the flange direction response. Figure 5-32 shows the the flange direction cyclic behavior of NTW2 for the analysis that was repeated after removing the effects of shear lag. When shear lag was removed, the reloading stiffness was somewhat reduced compared to when shear lag was present in the analysis as shown in Figure 5-25. The reduced stiffness is due to the increased strain and damage in the flange tips. Figure 5-33 shows the comparison of the strain in a longitudinal reinforcement fiber in the flange tip boundary element for the two analysis with and without shear lag effects. As can be seen, the strain in the flange tips was larger when shear lag was not included, leading to a larger residual strain after unloading and thus the reduced lateral stiffness observed in the force displacement response without the effects of shear lag. The overestimation of the stiffness was thus partially influenced by the incorrect simulation of the strain distribution across the flange width during web direction loading.

As stated in the description of the NTW2 model in Section 5.2, the shear stiffness was taken directly from the model used for the analysis of NTW1. The comparison of the shear deformation response of the OpenSees NTW2 model with the measured first floor response is presented in Figure 5-34, which shows that the selected model did not accurately simulate the shear behavior of NTW2 in the flange direction. The decision to distribute the longitudinal steel in the flange would have significantly altered the shear deformation behavior of the flange of NTW2. While it was expected that shear behavior would be altered by the distributed longitudinal steel, information was not available to indicate how the shear model should be modified to account for the change from concentrated to distributed steel. It appears that the shear model significantly overestimated the stiffness of the wall in the positive direction and underestimated the stiffness in the negative direction due to the asymmetric behavior observed for the measured response. The cause for asymmetry response in both the measured data is not clear at this stage, but such an anomaly will influence the cyclic response of NTW2. The applied loading typically started by displacing the flange in the positive displacement or the flange-in-compression directions, which might have had some influence. Pending further investigation of this issue, it is stated that the generally poor simulation of the shear strength and stiffness in the flange direction would contribute to the discrepancies observed in the responses in the flange direction.

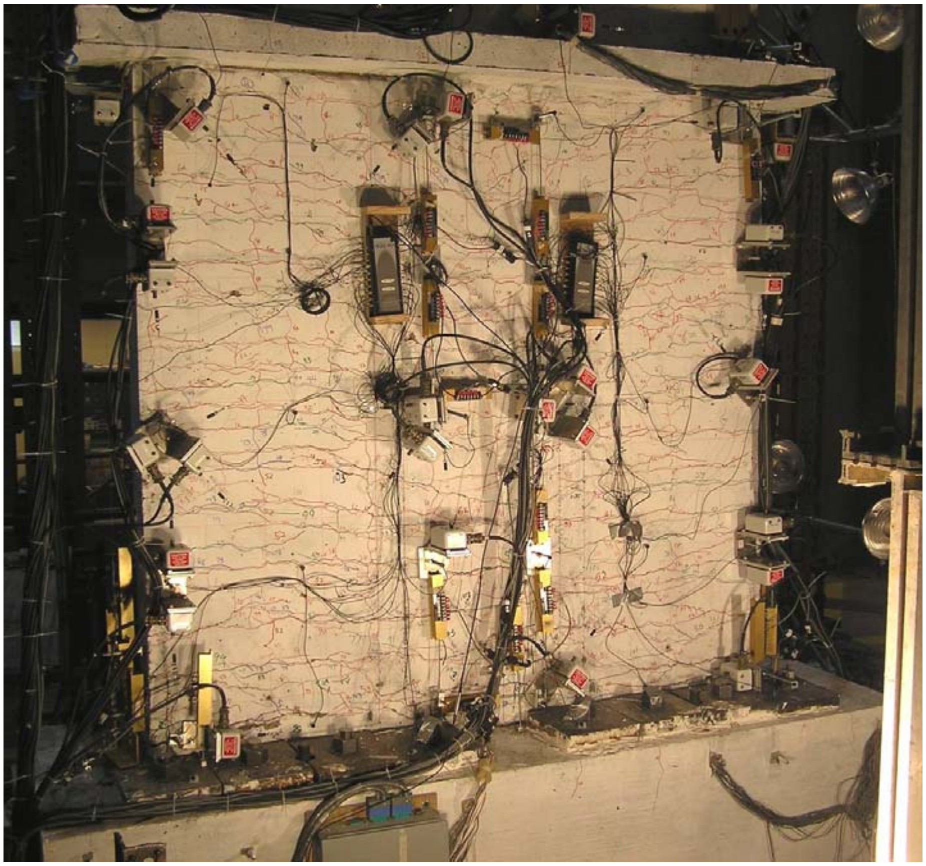

Figure 5-31: Back of Flange of NTW2 following Displacement Beyond First Yield in the Web Direction

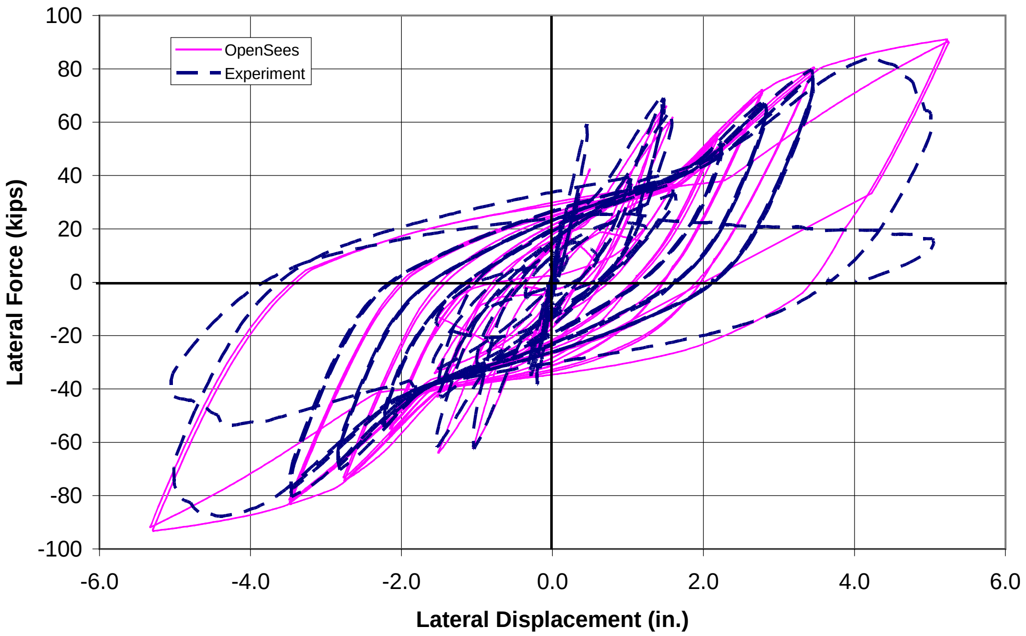

Figure 5-32: Measured and Predicted Force-Displacement Responses of NTW2 in the Flange Direction Without Accounting for Shear Lag in the Web Direction Loading

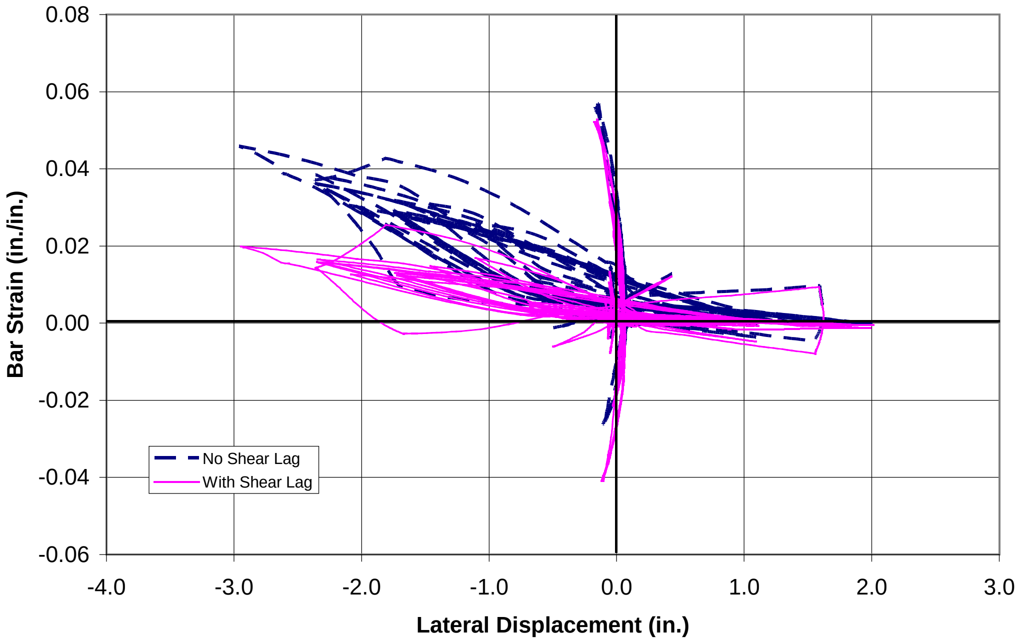

Figure 5-33: Strain in a Longitudinal Reinforcement Fiber in the Flange Boundary Element Located Furthest from Web Centerline and Web Tip With and Without the Effects of Shear Lag

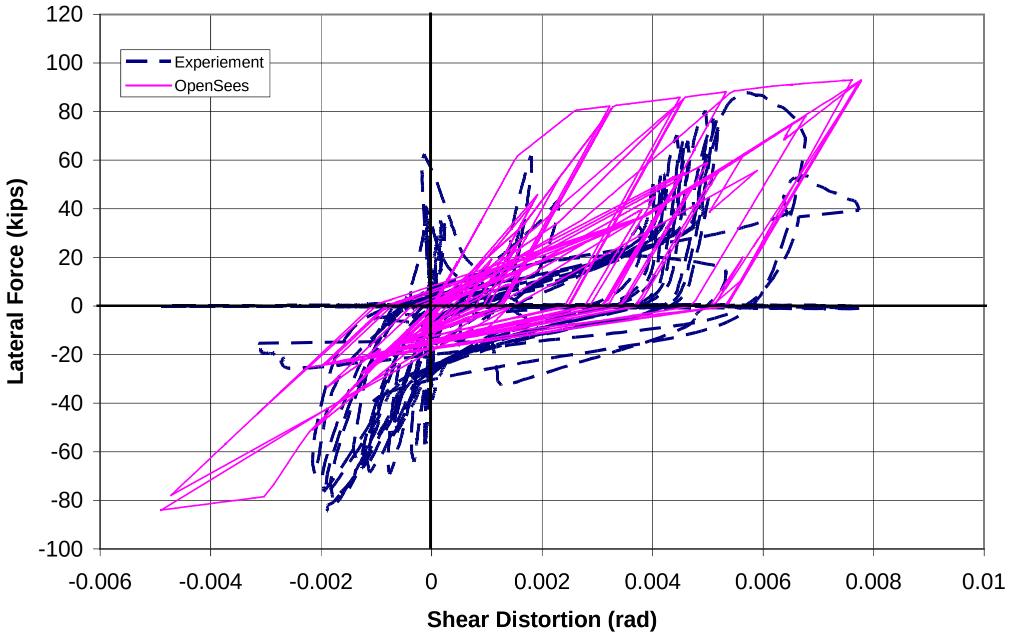

Figure 5-34: Comparison of Measured Shear Response at the First Floor of NTW2 in the Flange Direction with that Predicted by the OpenSees Model

5.5.2 Multidirectional Load Paths

Figure 5-35 compares the second floor displacements for the pentagon-shaped load path applied to NTW2 at 50% of the theoretical first yield. In this figure, the experimental response represents the average of the two string potentiometers attached to the flange tips. It is seen that the OpenSees model was subjected to nearly the same displacement path as the experimental unit NTW2. Figure 5-36 compares the measured and analytical force resistance surfaces corresponding to the load path in Figure 5-35, which shows a good agreement between the predicted and experimental results except at the peak displacements. Furthermore, Figures 5-37 and 5-38 show the force-displacement responses for the pentagon-shaped load path for the web and flange directions, respectively. In the web direction, the peak force was well predicted by the analysis even though the shear was not well simulated. However, the significant discrepancies in the shear response did not develop until after yielding of the longitudinal reinforcement. Though small, NTW2 experienced larger residual displacements than that exhibited by its analytical model. The amounts of residual displacement were somewhat unexpected because this cycle was at 50% of the yield displacement, and that the wall had not been previously displaced beyond the first yield limit state. The most likely source of the residual displacement was progressive cracking and associated damage of concrete during previous load cycles. However, the unloading and reloading stiffnesses of NTW2 were well estimated by the analysis in the web direction. In the flange direction, NTW2 showed slightly stiffer response and increased residual displacements than were recorded by the analysis model, leading to underprediction of the peak forces by as much as 25%. As with the web direction, a slightly larger residual displacement was recorded when unloading from positive peak displacement during testing than observed in the analytical response. The increased residual displacement led to a somewhat larger experimental cyclic loop, and increased energy dissipation than the analytical response.

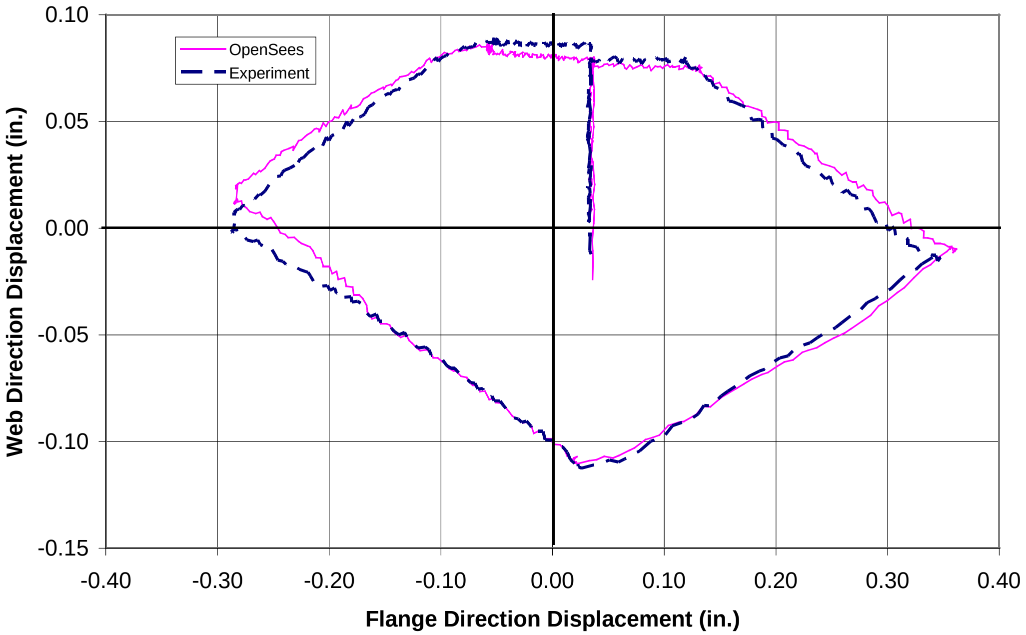

Figure 5-35: Comparison of Displacements at the Top of the Second Floor of NTW2 for the Pentagon Shape Load Path at 50% of the Theoretical First Yield

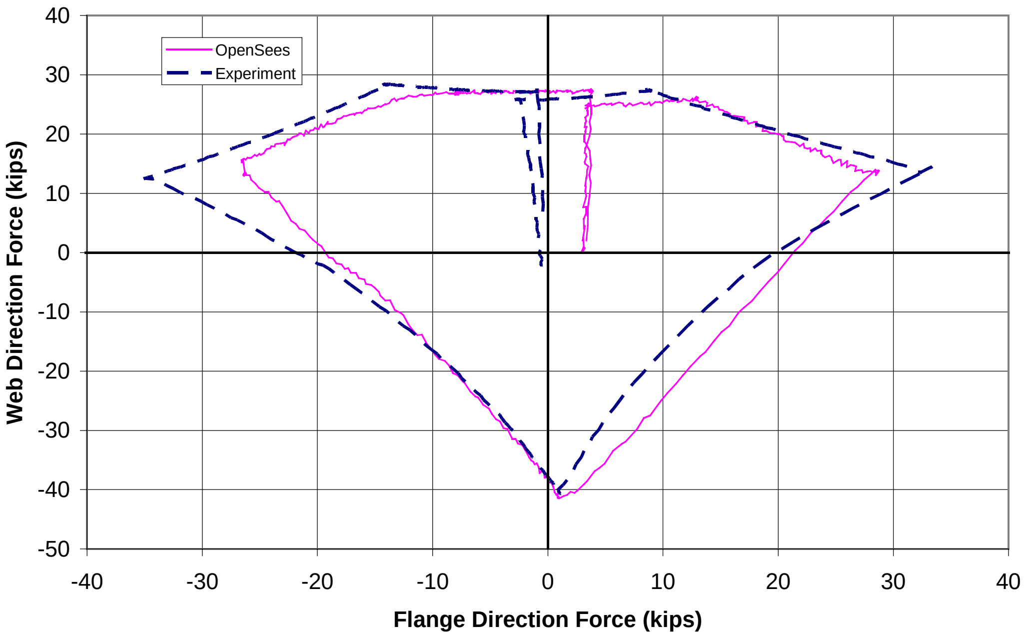

Figure 5-36: Comparison of Forces at the Top of the Second Floor of NTW2 for the Pentagon Shape Load Path at 50% of the Theoretical First Yield

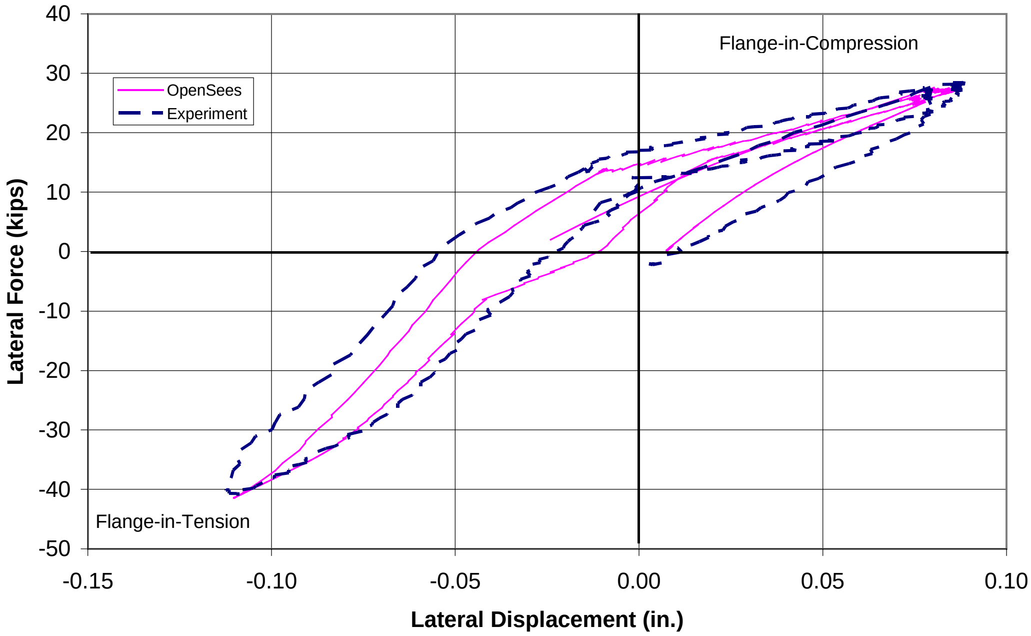

Figure 5-37: Comparison of Force-Displacements Response of NTW2 at the Second Floor for the Pentagon Load Path at 50% of the Theoretical First Yield in the Web Direction

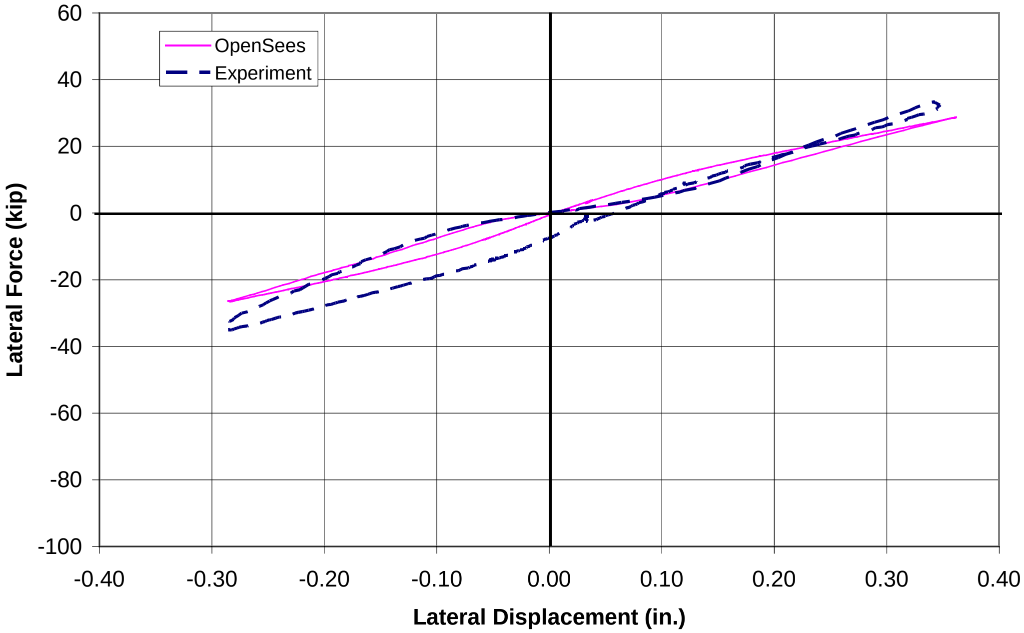

Figure 5-38: Comparison of Force-Displacements Response of NTW2 at the Second Floor for the Pentagon Load Path at 50% of the Theoretical First Yield in the Flange Direction

Figure 5-39 compares the experimental and analytical hourglass load path that subjected NTW2 to 2% lateral drift, which confirms that the test and analytical models were subjected to nearly the same bi-directional lateral displacements. Figure 5-40 shows the lateral force resistance surfaces of the experimental and analytical models for the hourglass shaped load path. It is seen that the peak forces are well simulated by the analysis; however, the force resistance while moving from one peak to the next was not well captured which can be examined more closely by examining the response in the two primary directions. Figures 5-41 and 5-42 show the force-displacement response of NTW2 in the web and flange directions, respectively, for the load path shown in Figure 5-39. The web direction response was almost exactly predicted by the model in both the flange-in-compression and the flange-in-tension directions. The reason this response was well simulated was because the discrepancies in the shear have decreased and the nonlinear strains make the effects of shear lag on the lateral force resistance small. The peak forces were accurately captured, so were the unloading and reloading stiffnesses.

Between the peaks, the force in the flange-in-compression loading direction was underpredicted by approximately 20% at the largest difference being at about -0.5 in. of displacement. In the flange direction, the overall shape and stiffness of the response loops were satisfactorily predicted given the complexity of the load path. The flange direction response was mode accurately predicted in the positive direction; however, in the negative displacement direction, the force was overestimated by as much as 40%. This overestimation was also seen in the simulation of NTW1 for the hourglass shaped load path, in Section 4.4.5. As explained for NTW1 response, the discrepancy was likely caused by not accurately simulating the accumulated damage in the flange direction that was present prior to beginning this specific load path.

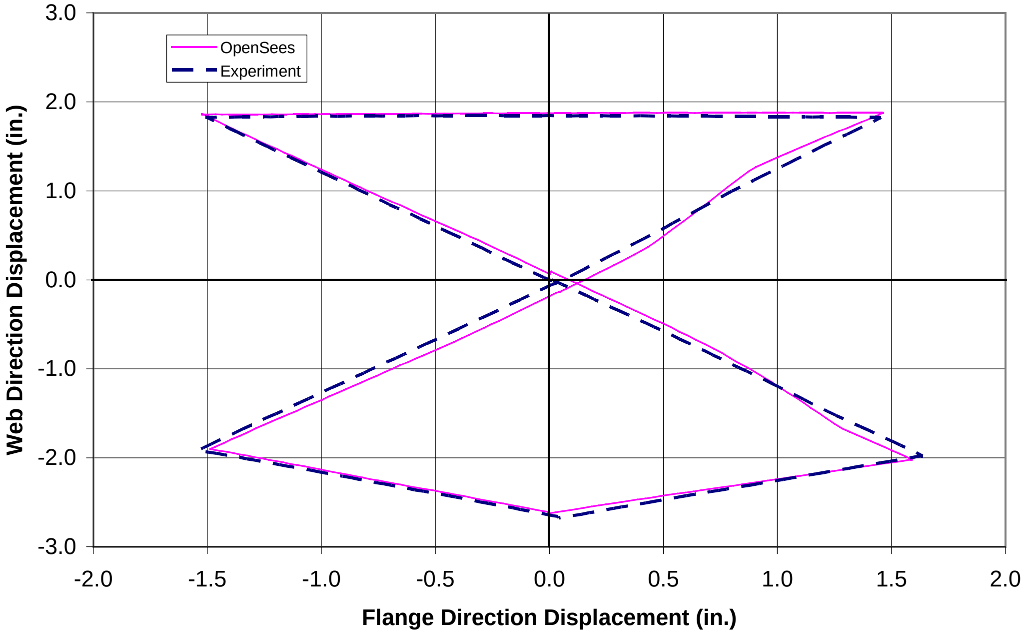

Figure 5-39: Comparison of Displacements at the Top of the Second Floor of NTW2 for the Hourglass Shape Load Path at 2% Lateral Drift

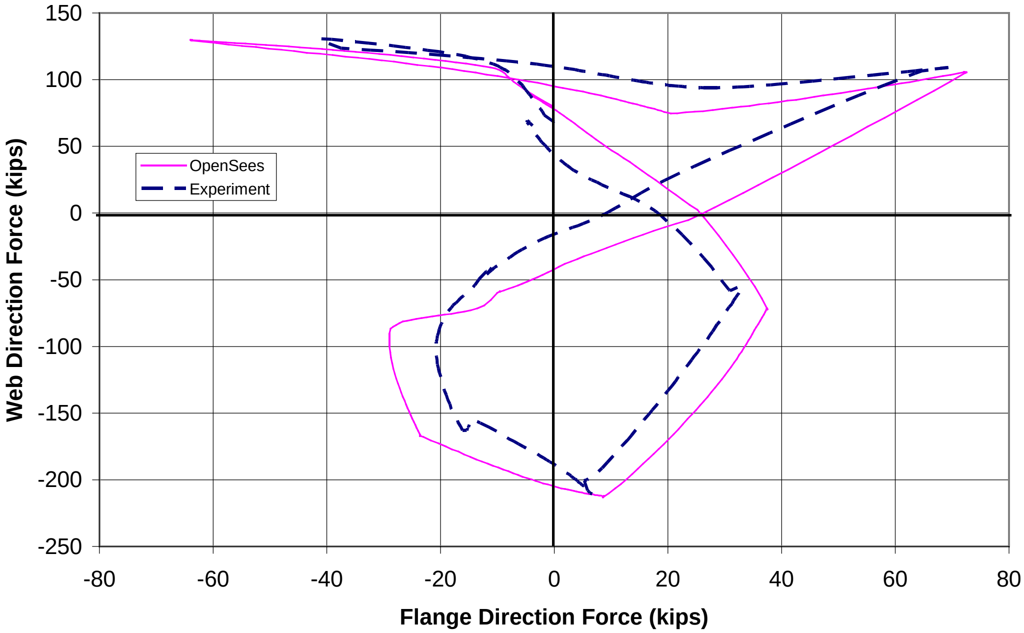

Figure 5-40: Comparison of Forces at the Top of the Second Floor of NTW2 for the Hourglass Shape Load Path at 2% Lateral Drift

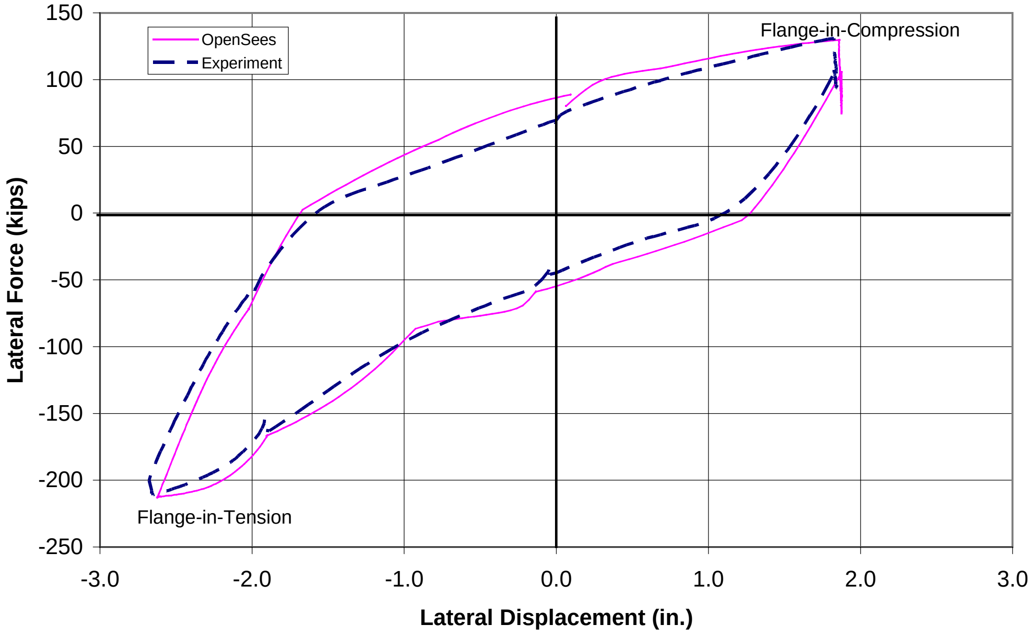

Figure 5-41: Comparison of Force-Displacement Response of NTW2 at the Second Floor Level for the Hourglass Shape Load Path at 2% Lateral Drift in the Web Direction

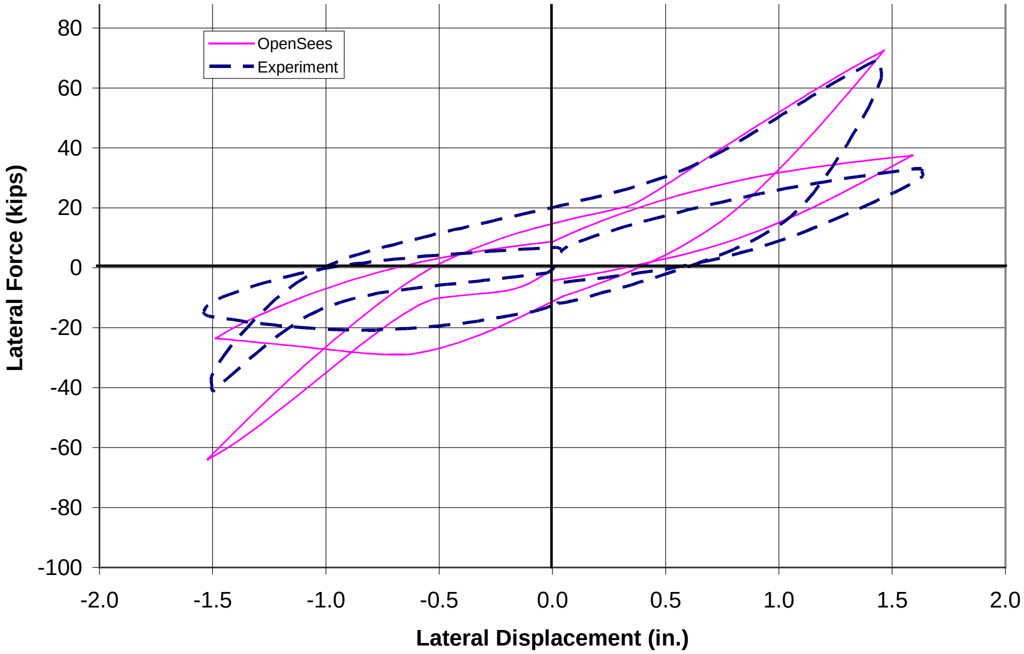

Figure 5-42: Comparison of Force-Displacement Response of NTW2 at the Second Floor Level for the Hourglass Shape Load Path at 2% Lateral Drift in the Flange Direction

5.5.3 First Floor Response

To examine the accuracy of the local responses, the force-displacement responses established at the first floor of NTW2 is shown in Figures 5-43 and 5-44 for the web and flange directions, respectively. The first floor response was not captured as accurately as the second floor response in both directions, which is partly due to the discrepancies between the measured lateral displacements and those imposed to the analytical model. Overall, the web direction response of NTW2 at the first floor level was not well captured by the analysis. Figure 5-24 shows that the elastic stiffness of NTW2 in this loading direction was significantly higher than the OpenSees model. In particular, the flange-in-tension direction had noticeable underestimation of the lateral stiffness of the T-wall by the analysis model. As should be expected, the first floor lateral displacement was heavily influenced by the contribution of the shear distortion of the first floor panel. Figure 5-30 shown earlier indicated that the OpenSees shear material model underpredicted the shear stiffness of the section in the web direction after cracking but before yielding of the longitudinal reinforcement, which is believed to have reduced the stiffness of the analytical model and led to overprediction of the lateral displacement in the elastic range. Additionally, overestimating shear lag effects in the analytical model and the corresponding the difference in the strain distribution in the flange shown in Figure 5-29 would have decreased the stiffness if the analysis model in the flange-in-tension direction. Figure 5-44 shows that in the flange direction of response, the overestimation of the theoretical wall resistance after subjecting NTW2 to the multidirectional loading was similar to that observed for the second floor response (See Figure 5-25). The unloading and reloading stiffness was well captured at the first floor level, but the residual displacements were overpredicted.

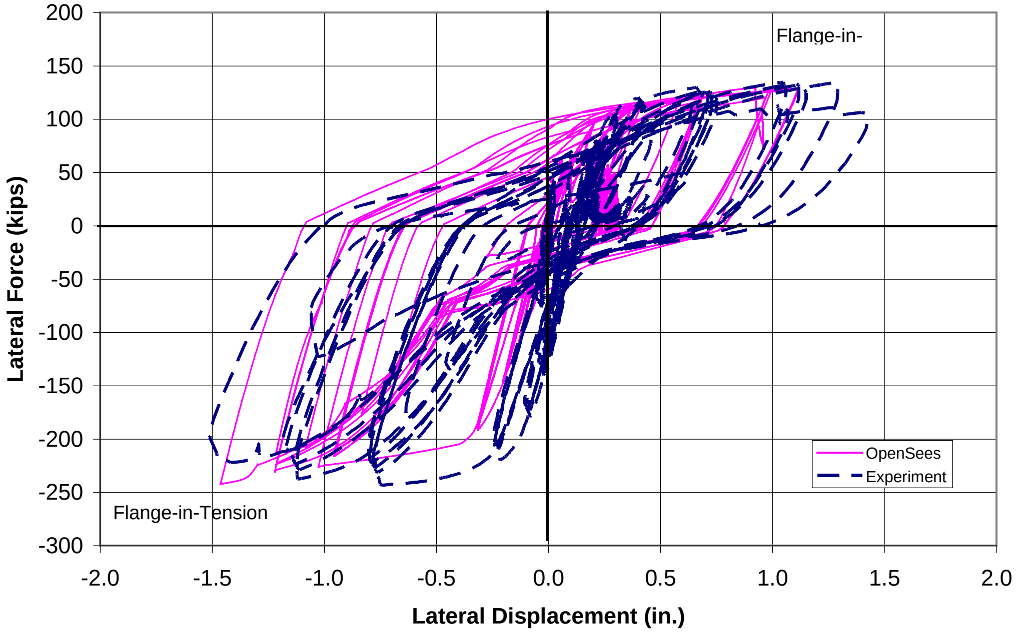

Figure 5-43: Measured and Calculated First Floor Force-Displacement Responses of NTW2 in the Web Direction

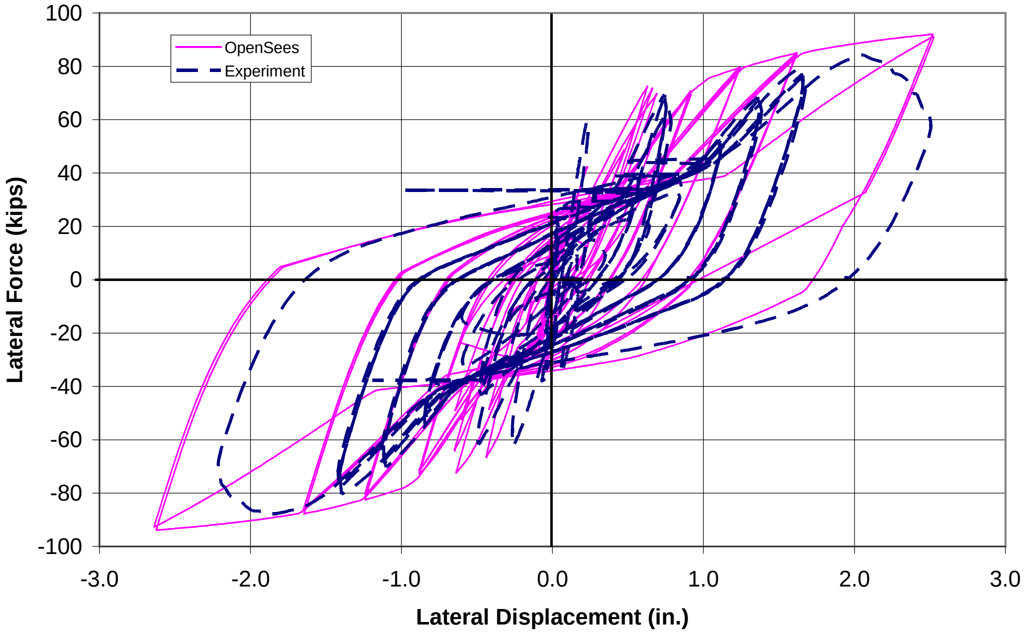

Figure 5-44: Measured and Calculated First Floor Force-Displacement Responses of NTW2 in the Flange Direction

Figure 5-45 and 5-46 compare the measured and analytical first floor lateral displacement of NTW2 as a function of the measurement number in the web and flange directions. It is evident that the OpenSees model was subjected to larger lateral displacements in both directions than was experienced by NTW2 during testing. It is also evident that NTW2 had residual displacements much earlier than was predicted by the OpenSees model. This again suggests that NTW2 experienced larger than predicted flexural actions due to reduced shear stiffness than anticipated based on the analytical response.

Furthermore, the predicted flexural behavior of NTW2 would have been also influenced by by the simple modeling technique used for the spliced regionat the second floor level. In comparison to the modeling technique used for the rectangular wall with a conventional splice (RWS) in Waugh *et al.* [2008], a simpler approach was used to model the splice in NTW2. This is because the prediction of NTW2 response was done prior to completing the analysis of RWS and the splice in RWS was located in the plastic hinge region. To realize the increased flexural contribution in NTW2, Figure 5-47 shows the comparison of the recorded strains in the first floor of NTW1 and NTW2 for a longitudinal rebar located in the web tip at a drift of 1.5%. As can be seen, NTW2 had higher strains in the reinforcement than were recorded for NTW1. This is due to restricting the length of the plastic hinge and placing more rotational demand on the plastic hingeof NTW2. As previously noted, this potential restriction was attempted to be captured by the analysis by increasing the area of the reinforcement fibers in the spliced region. However, the first floor results indicate that the restriction the splice placed on the plastic hinge formation was not fully captured by the OpenSees analysis.

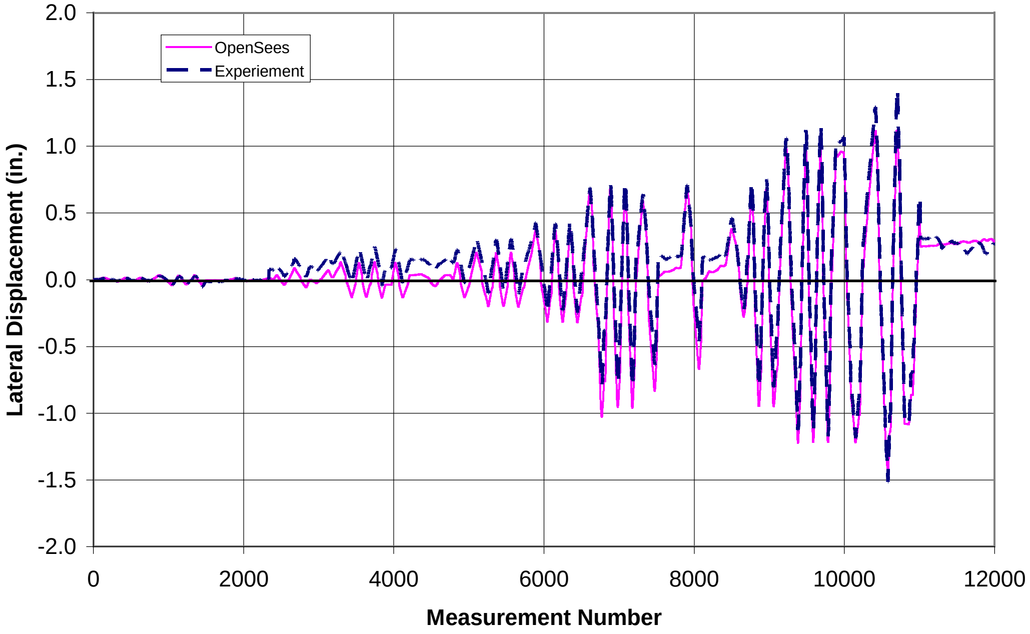

Figure 5-45: Comparison of First Floor Displacement of NTW2 in the Web Direction as a Function of Measurement Number

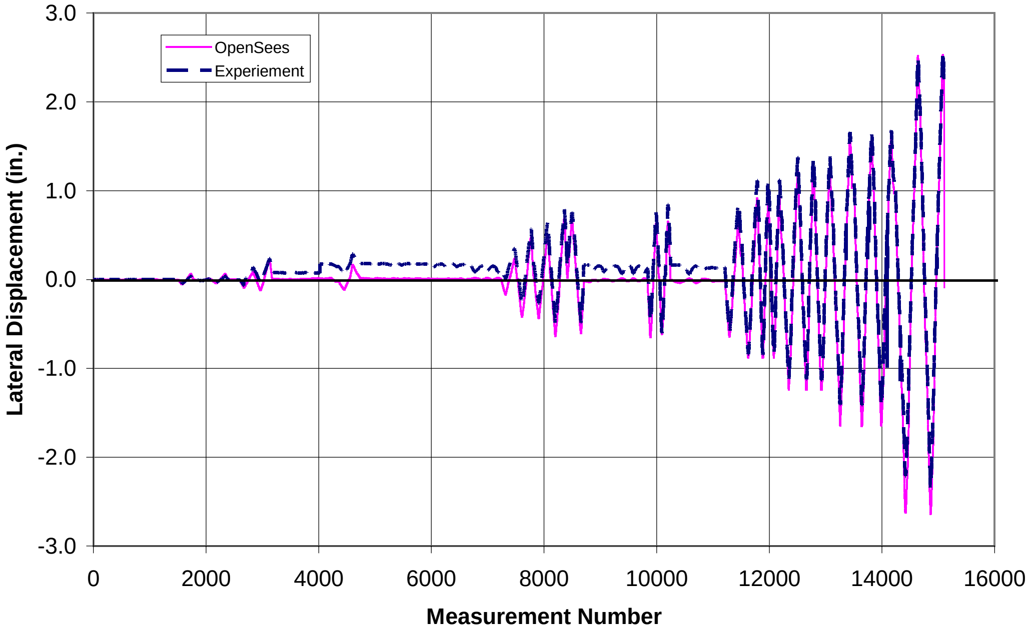

Figure 5-46: Comparison of First Floor Displacement of NTW2 in the Flange Direction as a Function of Measurement Number

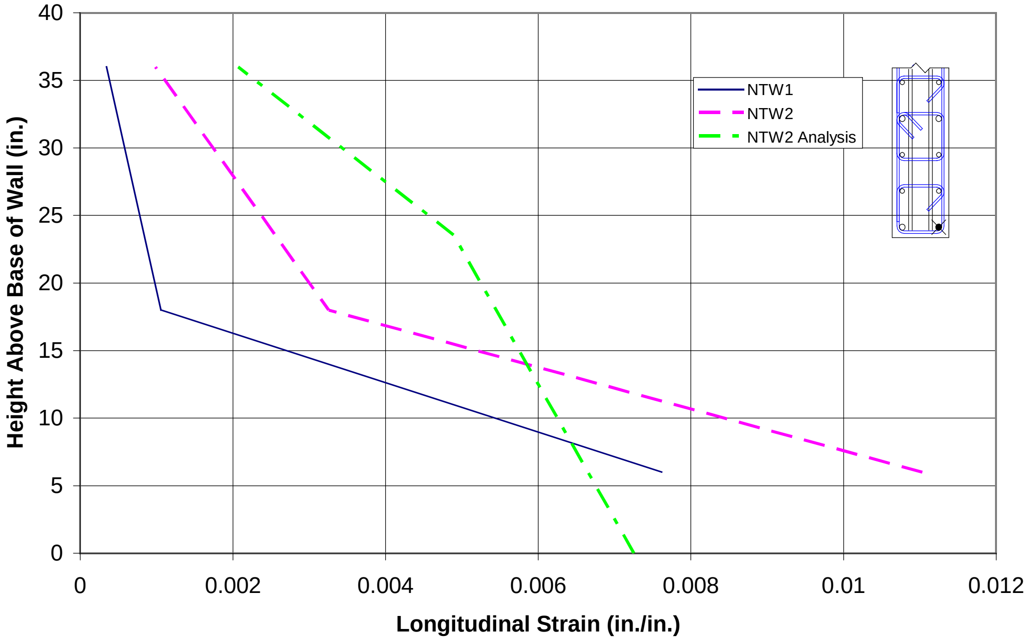

Figure 5-47: Comparison of Longitudinal Strains in the Web Tip of NTW1 and NTW2 at 1.5% Drift in the Web Direction

5.5.4 Local Response

As demonstrated for the first floor response, the accuracy of the local response was reduced due to inadequate simulation of the effects of shear lag and shear distortion in both web and flange directions.

Since the web direction response was the best predicted response by the OpenSees analysis, the local response in this direction was examined in detail. Figure 5-48 and 5-49 show the strain distribution along the web for the flange-in-compression and the flange-in-tension loading directions at different stages . Figure 5-48 shows that for the flange-in-compression direction, the OpenSees analysis accurately predicted the strain distribution, section curvature, and location of the neutral axis. This was expected because the flange-in-compression direction does not have the effects of shear lag, and the global and first floor force-displacement responses were the best simulated by the analysis model.

Figure 5-49 shows that the strain distribution was not accurately simulated for the flange-in-tension direction loading, even though the global force-displacement was reasonably predicted by the analysis. The location of the neutral axis is off by as much as 10 inches. The overestimation of the shear lag effects in the flange-in-tension direction would have made the analysis model more flexible, thus inducing lower tensile strain at a given target displacement.

5.6 Comments on Shear Lag Effects

The analytical and experimental responses of NTW2 in both the flange and web directions implied that the shear lag was not accurately captured in the NTW2 analysis model. As previously noted, the shear lag behavior depends on the shear stiffness of the free flange overhang which is influenced by:

- free flange length to thickness ratio,
- longitudinal reinforcement distribution along the flange,
- amount of longitudinal reinforcement in the flange, and
- spacing and diameter of transverse reinforcement spacing.

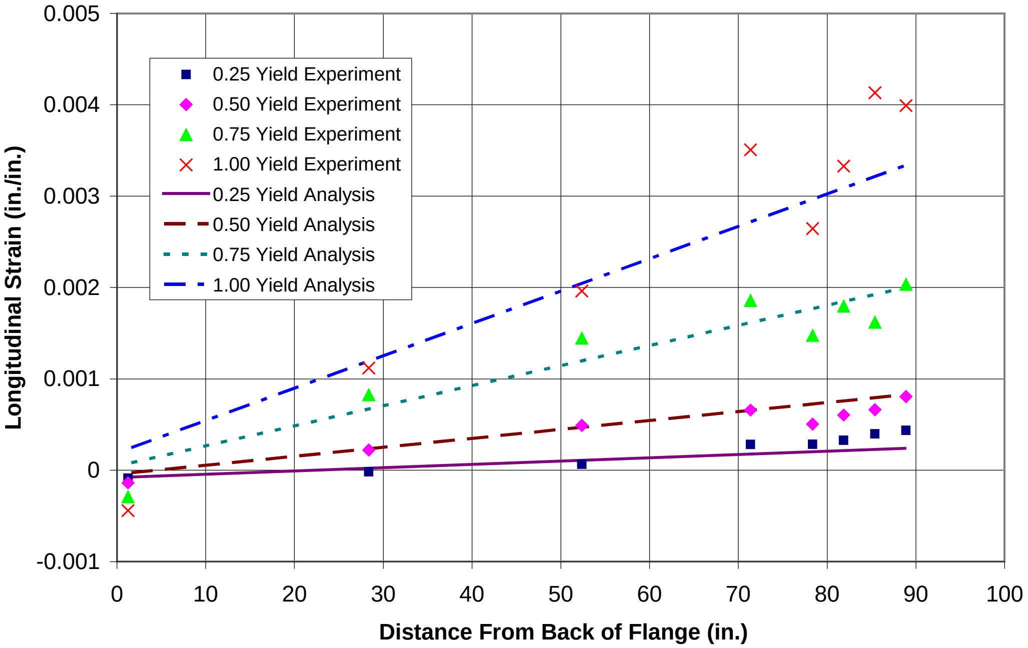

Figure 5-48: Comparison of Strain Profiles for the Flange-in-Compression Direction Response for NTW2

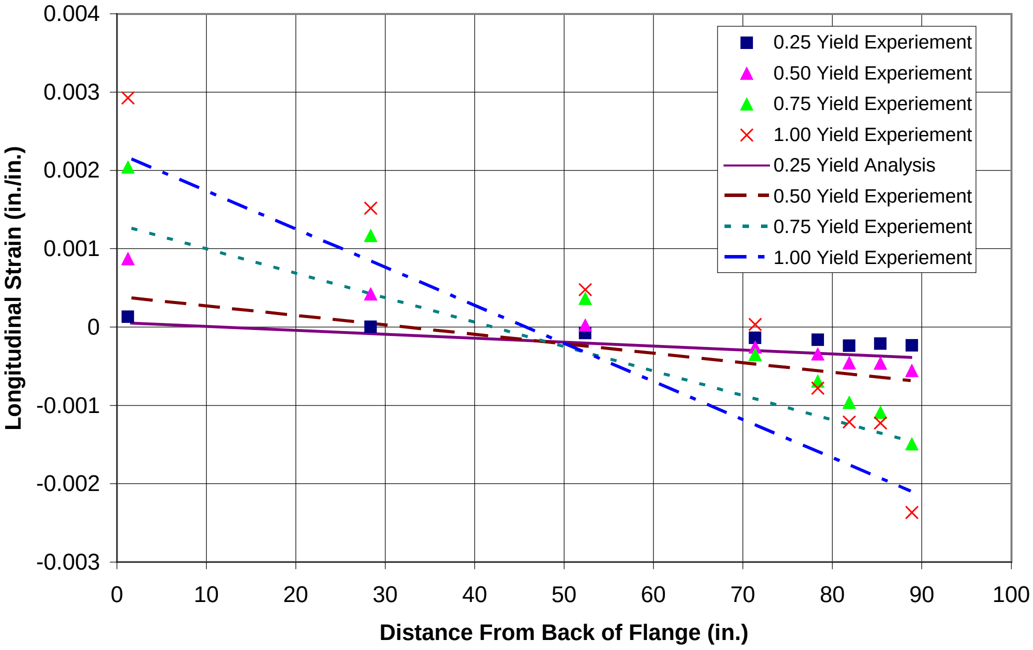

Figure 5-49: Comparison of Strain Profiles for the Flange-in-Tension Direction Response for NTW2

The original shear lag function used in the section definition of the NTW2 model included the strain distribution function using a *B/t* ratio (see Section 4.5.1). However, the other factors were not included in the section. The abstraction built into the design of the OpenSees framework makes it difficult for the section code to determine the size, location, and distribution of the longitudinal reinforcement. A section only knows the location of a fiber and its associated material model. The section is unaware if a particular a particular material model is a concrete or steel material model. Thus it cannot internally determine if the longitudinal steel is concentrated in the flange tips, or distributed along the flange length.

The strain distribution function developed to account for the shear lag effects was from the test data of NTW1 and TW2 (see details in Section 4.5.1), which is reproduced below:

$$\varepsilon = \varepsilon_0 + \Phi_y * z * (-0.1140527 * \left(\frac{B}{t}\right) * \left(\frac{2\mathrm{y}}{B}\right)^2 + 1) + \Phi_z * y \tag{5.1}$$

In both NTW1 and TW2 walls, boundary elements were used and most of the longitudinal reinforcement was grouped at the flange tips. NTW2 had a different longitudinal reinforcement distribution in the flange with a large portion of the longitudinal reinforcement distributed along the flange. Analysis of the strain distribution in the flange of NTW2 indicates that the measured strains in the longitudinal reinforcement of the flange more closely followed Eqn. 5-2:

$$\varepsilon = \varepsilon_0 + \Phi_y * z * (-0.0764606 * \left(\frac{B}{t}\right) * \left(\frac{2\mathrm{y}}{B}\right)^2 + 1) + \Phi_z * y \tag{5.2}$$

Based on the analysis of NTW1 and NTW2, it is obvious that the strain distribution function requires a variable that includes the influence of all aforementioned parameters. Including all the parameters that influence the shear stiffness of the free flange width in one variable would result in a strain distribution function that is of the following form:

$$\varepsilon = \varepsilon_0 + K * \varphi_y * z + \varphi_z * y \tag{5.3}$$

where ε is the strain in the fiber of interest, φ_y is the curvature about the local y-axis, φ_z is the curvature about the local z-axis, K is the shear lag variable including the previously mentioned factors, and y and z are the local coordinates of the fiber of interest. An investigation for determining the variable K is beyond the scope of this study. However, it is noted that not enough data currently exists for such an investigation and that a detailed analytical and experimental study is required to determine the influence of each parameter on the shear lag and strain distribution.

Until such an investigation is conducted, Eq. 5.1 and 5.2 may be used as a guidance to include the shear lag effects based on the longitudinal reinforcement details in the flange of the T-wall under consideration. If the majority of the longitudinal reinforcement is grouped in boundary elements located at the flange tips, then Eq. 5.1 should be used for the analysis to capture the effects of shear lag; however, if the longitudinal reinforcement is distributed then Eq. 5.2 is more suitable. The two cases represented by NTW1 and NTW2 provide an upper and lower bound for the effects of shear lag in the web direction of loading.

5.6.1 Effects of Revised Shear Lag Function

The analysis of NTW2 was reran using Eq. 5.2 to represent the shear lag distribution across the flange. The results are shown in Figure 5-50 and 5-51 for the web and flange directions, respectively. As can be seen, the response was better simulated with the updated shear lag function, particularly in the flange direction. While the simulation was not perfect in capturing the flange direction response, the remaining discrepancy can be attributed to the shear deformation response not being well simulated in this direction. The simulation well captures both the unloading and reloading stiffness of NTW2 accurately, as well as the residual displacement after load has been removed from the specimen. Figure 5-50 and 5-51 support the conclusion that the poor simulation of the shear lag behavior was a significant factor in the poor simulation of the flange direction response.

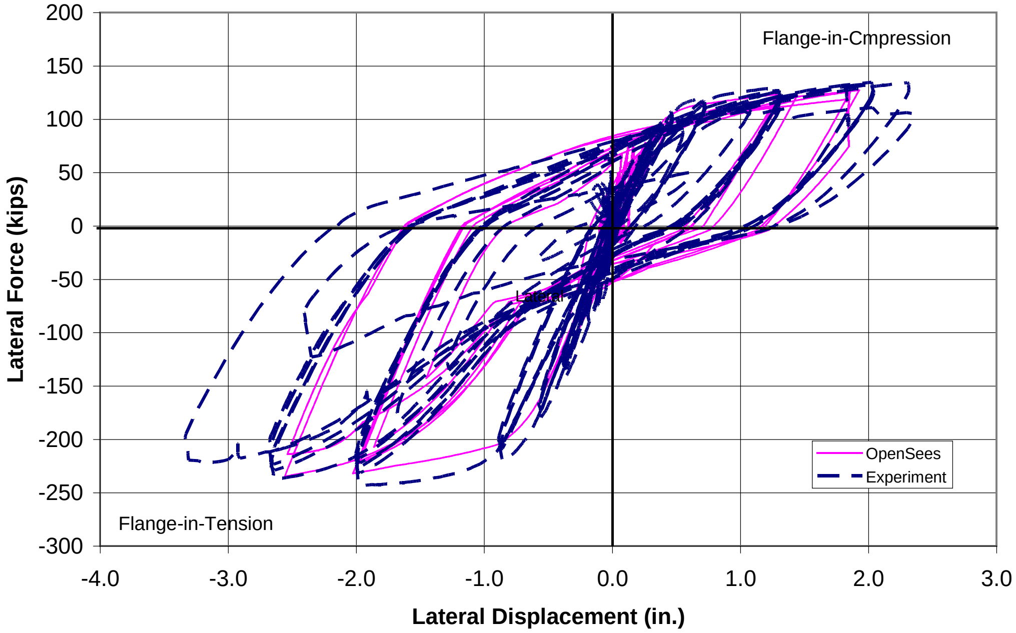

Figure 5-50: Measured and Predicted Force-Displacement Responses of NTW2 in the Web Direction with Revised Shear Lag Function

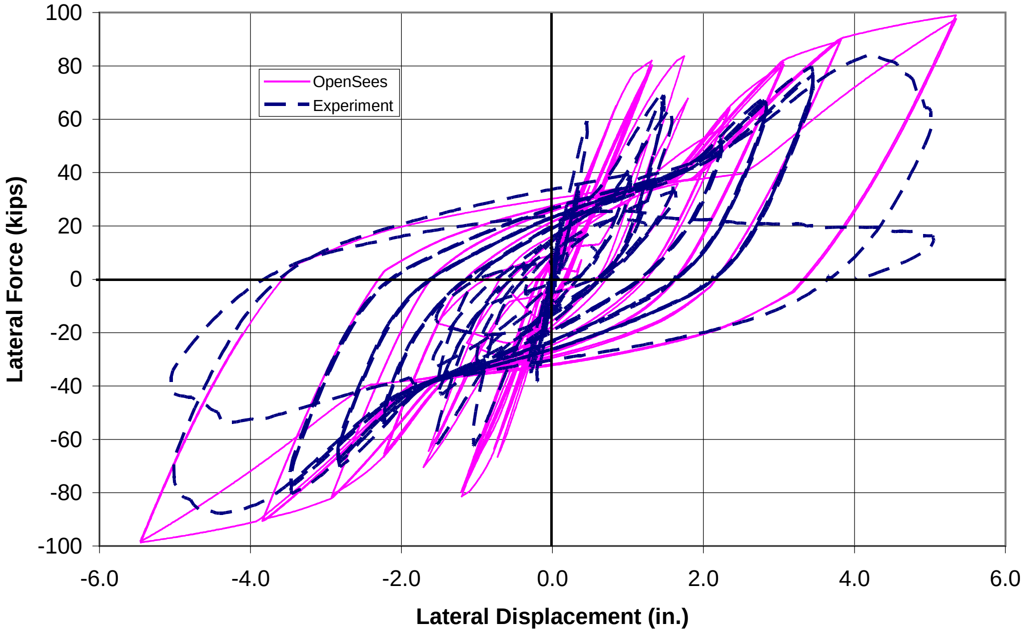

Figure 5-51: Measured and Predicted Force-Displacement Responses of NTW2 in the Flange Direction with Revised Shear Lag Function

Chapter 6: Seismic Analysis of a Pair of T-walls

The T-walls analyzed in Chapters 4 and 5 were single walls subjected to multi-directional quasi-static lateral displacements. However, in the prototype building chosen for the PreNEESR project, pairs of T-walls were used to resist the lateral forces in the transverse direction of the building (see details in Section 4.1). In this direction, one wall in each pair will be subjected to flange-in-tension loading direction, while the other wall will experience flange-in-compression loading direction. The differing stiffness and capacity of the walls in each wall pair connected with the floor diaphragm raises a number of issues for the transverse direction design of the building. Brueggen *et al.* [2007] listed the following issues needing attention:

1) how to estimate relative stiffnesses of T-shaped walls for appropriate distribution of design loads between walls
2) how to accurately determine the critical transverse and longitudinal load combination (i.e., whether or not to consider biaxial loading effects when designing the wall reinforcement)
3) how to detail the wall boundary elements without undue congestion
4) αppropriate estimation of plastic moment and overstrength factor for defining the shear demand in the wall
5) how to distinguish between design philosophies of shear- and flexural-controlled walls, including revisiting of the appropriate R values for each case
6) how to detail the joint between web and flange in order to address potential vertical shear transfer problems associated with engaging reinforcement in flange tips

In an attempt to examine the first design issue listed above, this chapter presents seismic analysis of a slice of a half-scale prototype building shown in Figure 4-1. A half-scale model was preferred because both NTW1 and NTW2 were tested and analyzed at half-scale.

The analytical models of these walls were readily available that included the effects of shear lag and shear distortion. If a full scale model of the building slice were to be used then a new fiber section would have had to be defined; additionally, the shear deformation model would have required modifications. Given the improved performance of NTW2, this wall was used in the OpenSees modeling of the building slice. The building model was subjected to both monotonic pushover and dynamic analyse; the dynamic analysis chosen followed the approach used for the dynamic analysis of the seven-story building slice in Appendix A. The purpose of this analysis was to develop recommendations regarding issue 1. Note that Chapters 4 and 5 have already addressed issues 2 and 4 listed above. Issues 3, 5, and 6 cannot be addressed by the analysis presented herein and reserved for a future investigation.

6.1 Prototype Structure

The prototype structure used in this study was a six-story building located in Los Angeles, CA. Figure 6-1 shows the floor plan of the prototype building, shown previously in Chapter 4. As stated previously, the prototype building had a 22,500 square foot (SF) floor plan with a story height of 12 feet for all floor levels. The gravity and lateral loads of the building were resisted by two separate systems. The gravity load system consisted of a 7 in. cast-in-place (CIP) concrete floor slab spanning between CIP or precast beams. The beams were supported on columns located in a 20 ft by 45 ft grid. The lateral load was resisted by CIP concrete structural walls. T-walls resisted all the lateral force in the transverse directions, while additional rectangular walls were required in the building core to resist seismic force in the longitudinal direction.

The T-walls designed for the prototype structure were shown in Figure 4-2, which was the basis for both NTW1 and NTW2 that were constructed at half scale. The interstory forces and distribution of shear between the two T-walls at each floor level in each pair of walls was a subject of discussion during the design of the prototype building. The method used for distributing the design base shear force influenced the number of walls required in the prototype building. The distribution of the base shear force was eventually performed based on the secant stiffness to the first yield ignoring the effects of concrete confinement. This decision, which was largely influenced by the current code practice (ACI 318-02) led to 5 pairs of T-walls in the prototype building.

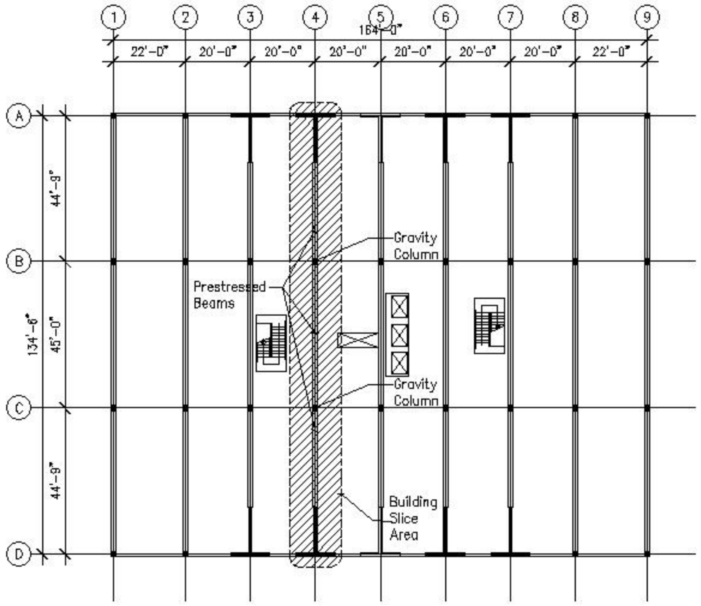

a) Floor Plan

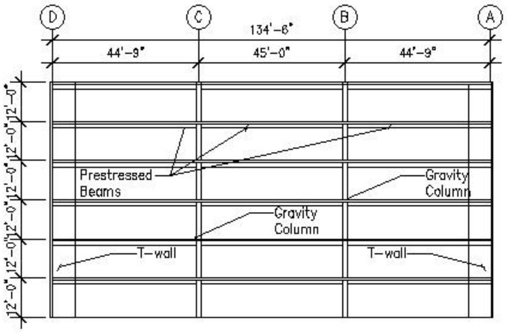

b) Elevation

Figure 6-1: Dimension and Configuration Details of the Prototype Building

The design of the prototype building called for the gravity columns to be unconnected to the floor slab while the prestressed beams were supported on corbels attached to the columns. The corbels allowed gravity loads to be transferred to the columns, but the lack of a connection between the slab and the column allowed the slab to move vertically relative to the column. The details of the floor to column connection would be expected to isolate the gravity column from the lateral force resisting system.

The prestressed beams were made composite with the reinforced concrete floor slabs, by projecting the transverse reinforcement in the prestressed beams into the cast-in-place concrete slab (see Figure 6-2). The prestressed beams had both prestressing strands and mild steel reinforcement, while the floor slab only had mild steel longitudinal reinforcement.

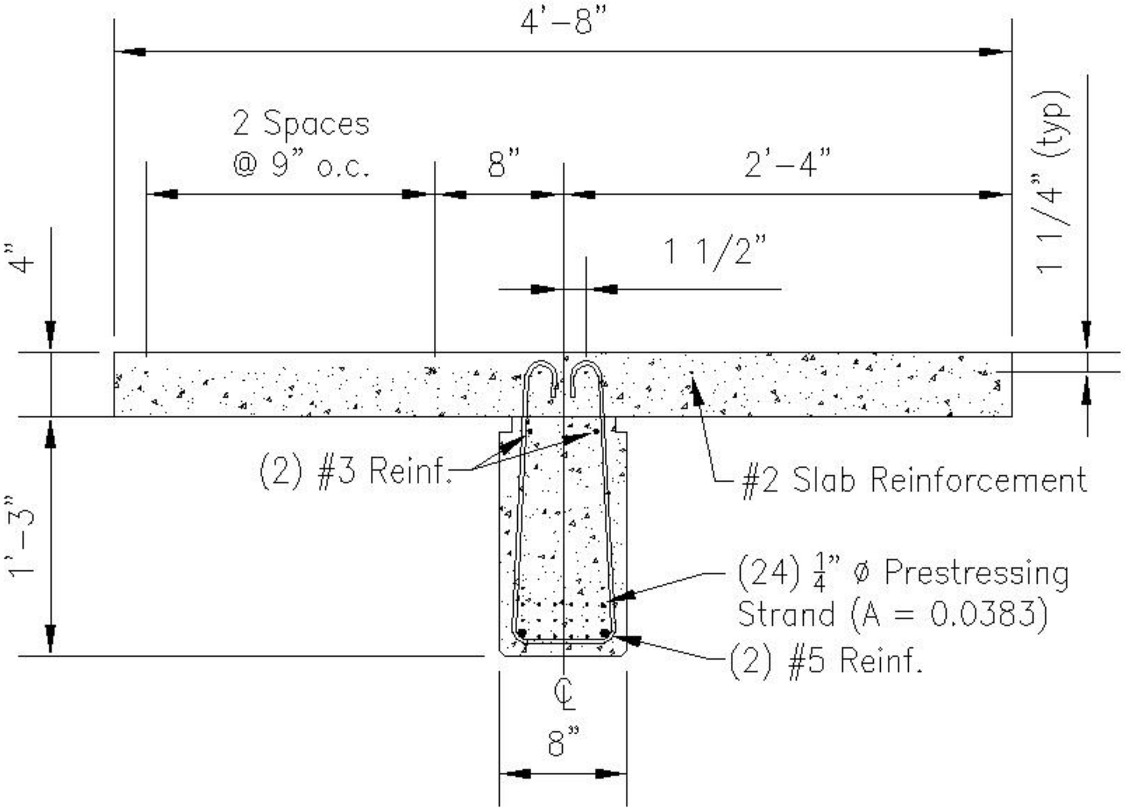

Figure 6-2: Reinforcement Details of the T-beam Representing the Prestressed Beams and Effective Width of the Cast-In-Place Concrete Slab

6.2 Model Description

Although only a slice of the total building was simulated in OpenSees, (Figure 6-1a) shows that the analytical model included all 6 floors in the prototype structure. The structural elements included in the OpenSees model were the two T-walls, two gravity columns located in the interior of the structure, prestressed beams connecting the walls and columns, and the reinforced concrete floor slab. The connection of the columns, prestressed beams, and floor slab was of particular interest in the analysis.

Figure 6-2 shows the centerline model developed for the building slice in OpenSees. The T-walls are primary lateral load resisting elements in this model. These walls were modeled following the approach discussed in Sections 4.7, and 5.2, because this approach has been shown to be satisfactory for a single T-wall under monotonic, cyclic, and dynamic loading, see Chapters 4, 5, and Appendix A.

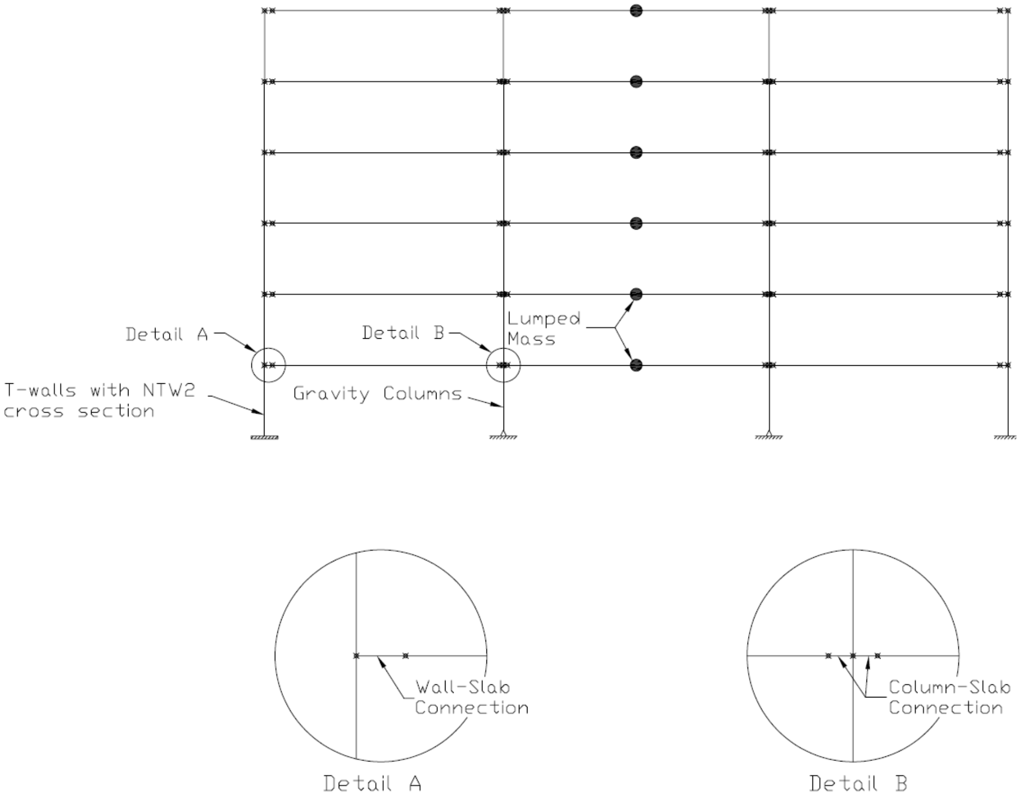

Figure 6-3: Centerline Analysis Model of Building Slice

The two T-walls in the building slice were modeled using one force-based beam-column element to represent each wall at each story level. The reinforcement details of NTW2 were used for the T-walls in this analysis for two reasons: 1) this wall showed good performance during testing; and 2) the single wall model of NTW2 was validated against the experimental data confirming adequate simulation of the force-displacement response of the wall in the web direction. Thus the details of the fiber section used for the T-walls, such as concrete and steel reinforcement material properties, reinforcement arrangement, and fiber size, are not presented here since they were discussed previously in Section 5.2. Additionally, the effects of strain penetration, shear lag, and shear deformation were included in the model as with the analysis of NTW2 presented in Chapter 5. However, the Kent-Park concrete model was used instead of the simplified Chang and Mander concrete model. The concrete model was changed because the input motions were selected so each motion would push the wall into a virgin response region. Thus the robust hysteretic behavior of Chang and Mander is not required, and the Kent-Park model is computationally more efficient.

The influence of gravity columns on the response of a building slice was examined in the analysis of the UCSD shake table test of a 7-story building slice presented in Appendix A. The prototype structure of the T-wall project had two gravity columns located between the two T-walls and the decision to include the gravity columns can have a significant impact on the analysis results. Based on discussions with the design engineer of the prototype structure, the gravity columns were not included in the analysis because these columns were detailed not to restrain the vertical movement of the slab. Thus, the couple formed by the axial load in the gravity columns seen in the analysis of the UCSD seven story building is not expected to develop, see section A.5.2. However, the gravity columns were later added to the analysis model to examine their influence on the response of the building slice (see Section 6.8).

The floor slab in the prototype structure was supported by prestressed beams that span between the T-walls and the gravity columns. These beams were modeled using fiber-based, displacement-based beam-column elements. The displacement-based elements were used because the beams were expected to remain elastic and do not require internal iterations of the element flexibility matrix that the force-based elements can accommodate. A fiber section was used to discretize the prestressed beam cross-sections with a portion of the floor slab based on the recommendation of ACI-318-02 Section 8.10 [2002]. The details of the T-beam formed by the prestressed concrete beam and the composite floor slab is shown in Figure 6-3. The concrete for these elements was modeled using the Kent-Park model to increase the computational efficiency since the improved capabilities of the modified Chang and Mander model from Chapter 3 was not needed for the beam response. The prestressing strands were modeled using an elastic perfectly plastic material model because that was the only available material model that allows an initial strain to be applied to simulate the effects prestressing. The properties for the concrete fibers are shown in Table 6-1 and the reinforcement fiber in Table 6-2. The beams were simply supported between the columns and only the slab was rigidly connected to the wall and thus a six inch long beam-column element with a fiber section representing only the floor slab was used to connect the beam-column elements representing the composite section of the prestressed beams and the cast-in-place floor slab to the beam-column elements representing the T-walls, as shown in Detail A of Figure 6-3. Additionally, an eight-inch long beam-column element with the slab section was used around the column locations, shown as Detail B of Figure 6-3. The prestressed beams were supported on corbels attached to the columns, while the slabs were not connected to the columns. The floor slabs were not connected to the gravity columns until the analysis discussed in Section 6.8.1.

Reinforcement in the slab parallel to the flange of the T-wall was expected to provide dowel action, helping to connect the walls to the floor slab, beyond the contribution of the longitudinal reinforcement in the slab parallel to the web, which is included in the fiber section of the slab. The reinforcement parallel to the flange was modeled using a truss element with a material model simulating the behavior of steel in shear, as indicated in Table 6-2. The yield strength of the reinforcement in shear was taken as 60% of the yield strength in tension, and the elastic modulus was taken as the shear modulus, G. The area of the truss was 1.10 in.^{2}, which was formed by summing the areas of the reinforcement that was parallel to the flange that crossed the web. The truss had a length equal to the distance from the centroid of the T-wall to the web tip. This truss in combination with the fiber section was expected to accurately model the components of the connection between the slab and the wall.

Table 6-1: Analytical Concrete Properties Used for Prestressed Beams in OpenSees Model

f'_c (ksi)	ε_c (in./in.)	f_u (ksi)	ε_u (in./in.)	f_t (ksi)	ε_t (in./in.)
6.00	0.002	0.00	0.000	0.571	0.0002395

Table 6-2: Analytical Reinforcement Properties Used Prestressed Beams in OpenSees Model

Bar Size	Yield Stress (ksi)	Elastic Modulus (ksi)	Strain Hardening Ratio	Initial Strain (in./in.)
#4	72.1*	29000	0.020	N/A
#5	70.7*	29000	0.020	N/A
#6	70.7*	29000	0.020	N/A
Prestressing Stand	270	29000	N/A	0.00174
Steel in Shear	36	11500	0.015	N/A

* Measured properties of reinforcement from NTW2

A node located in the middle of the element representing the beam and slab the two interior columns was used to lump the inertia mass of each floor level. This approach was motivated to simplify the analysis and increase the computational efficiency. The appropriate mass at each floor level was calculated by determining the weight of a half story above and below the floor of the T-walls and the prestressed beams in the building slice and dividing it by gravity. Given the five pairs of T-walls in the building, one fifth of the weight of the floor slab was also added to the total seismic weight. Since the model was a half-scale version of the prototype building, the gravity in the model was taken as twice the gravity for the prototype structure. The weight of the structure was also applied as point loads on the appropriate nodes to account for the gravity effects on T-walls and columns, shown in Table 6-3.

Table 6-3: Applied Mass and Axial Load

Floor Level	Mass (kip*s^2/in.)	Wall Load (kips)	Column Load (kips)
First Floor	0.0735	13.69	9.84
Second Floor	0.0735	13.69	9.84
Third Floor	0.0735	13.69	9.84
Fourth Floor	0.0735	13.69	9.84
Fifth Floor	0.0735	13.69	9.84
Sixth Floor	0.0680	6.85	4.70

Following the recommendations of Priestley and Grant [2004] and the experience of modeling the UCSD structure (see Appendix A), a stiffness proportional damping was used for the dynamic analysis. Very limited viscous damping is representative of a bare structure and well characterized hysteretic behavior is required for energy dissipation, as seen in the analysis of the UCSD structure. The level of viscous damping was chosen as 0.6% of the critical damping on the first mode response and 1.4% on the second mode response. While damping will increase on the higher modes, the 3rd, 4th and 5th modes are not expected to contribute significantly to the overall response. Methods such as mass proportional damping or Rayleigh damping that would limit the damping on the higher modes creates a constant or nearly constant damping matrix regardless of the hysteretic damping that may be occurring. The tangent stiffness was used to form the damping matrix in the analysis. Thus, the viscous damping decreased as damage to the structure accumulated and hysteretic damping increased.

The stiffness matrix was formed using the Krylov-Newton solver, this method was used in the quasi-static analysis of NTW1 and NTW2, as well as the dynamic analysis of the UCSD Seven Story Building Slice in order to increase the computational efficiency of analysis.

6.3 Earthquake Input Motions

The earthquake input motions for conducting the dynamic analysis of the OpenSees model of the T-wall pair were taken from a study conducted by Rahman and Sritharan [2006] on the seismic performance of precast concrete buildings. These input motions were carefully selected to examine the behavior of buildings to various performance levels. One small, two medium, one design-level, and one maximum considered event records were selected for the investigation of the building slice. These events were selected to represent the earthquake intensities of EQ-I, EQ-II, EQ-III, and EQ-IV categories according to the SEAOC Seismology Committee [1999] with IM-a representing an EQ-I level event, IM-b and IM-e represent EQ-III events, and IM-f and IM-h represent EQ-IV events. These input motion records for the different events were established by Rahman and Sritharan by modifying the East-West component of the 1984 Morgan Hill motion record from Gilroy #6 in San Ysido Station (IM-a), the North-South component of the 1989 Loma Prieta record from Saratoga Aloha Avenue (IM-b), the East-West component of the 1995 Kobe-Japan record from station KJM (IM-e), 344 degree component of the 1978 Tabas record from Iran (IM-f), and the North-South component of the 1995 Kobe-Japan record from station KJM (IM-h), respectively. The original ground motions were scaled such that their spectra would be within a dominant period range [Rahman and Sritharan, 2006].

6.4 Pushover Analysis Results

First, a monotonic pushover analysis was conducted on the model representing the prototype building slice at 50% scale. An inverse triangular load was applied to the structure, in order to examine h lateral load performance of the model close to its first mode response. A displacement control integrator was used in order to apply this inverse triangular load for the pushover analysis. Since the building slice was symmetrical in the North-South direction, the pushover was only conducted in one direction and the top of the structure was displaced to 20 in. or 4.6% lateral drift. The loads were applied at the nodes carrying the mass, and then the force would be distributed through the beams. This corresponds to the forces coming from the inertia of the building mass.

Figures 6-4 to 6-9 show the contribution of each wall to the total base shear as well as the story shear force at each floor level established from the pushover analysis. Figure 6-4 shows the contribution of each wall to the total base shear, revealing that the T-wall with the flange-in-tension, (i.e. trailing wall) provided approximately twice as much resistance as the T-wall with the flange-in-compression (i.e. leading wall). This trend is also evident in the responses seen for floors 2 and 3 in Figures 6-5 and 6-6, respectively. The stiffness of the trailing wall is higher than the for the leading wall, the same as observed in the response the first floor as well as the response of NTW1 and NTW2. Figures 6-7 through 6-9 show different trend for the contribution of wall resistance at floors 4, 5, and 6. Unlike that observed at the base, first, and second floors, the leading wall with the flange-in-compression is initially stiffer the trailing with the flange-in-tension, thus providing more resistance for a given lateral displacement. It was found to be due to the reduction in axial load on the T-walls. The stiffness of the wall with the flange-in-compression is less influenced by reduction in axial load than the stiffness of the wall with the flange-in-tension. As the axial load decreases up the height of the wall, the stiffness of the flange-in-tension wall decreases faster than the the stiffness of the flange-in-compression wall, and this trend reverses when the axial load ratios decreases to below $0.008 * f'_c$. In this case, the effective stiffness ratio reverses between the third and fourth floor. This is confirmed by the responses seen in Figures 6-6 through 6-9, which shows that the difference in stiffness increases as the floor height increases.

Additionally, a small but sudden increase in wall resistance occurs at approximately 1.40 in. of displacement at the third, fourth, and fifth floor responses. This sudden increase coincides with flexural yielding at the base of the leading wall. It is believed that this yielding causes an abrupt drop in the stiffness of this wall and thus for a small range of displacements, some reduction in resistance of this wall is seen until the wall resistance increases and flexural yielding occurs at the base of the trailing wall. At this point, the stiffness of both walls returns to the same order of magnitude, then load distribution returns to the expected response. This observation is more pronounced in the upper stories because the magnitude of the sudden change in resistance is larger relative to the total force resisted by the walls. Close examination of the responses in Figures 6-5 and 6-6 confirmed some disturbance in the stiffness at a top displacement of 1.40 in. The axial load on the lower wall increases the stiffness of the flange-in-compression wall which would reduce the magnitude of the stiffness change observed when the base of the wall yields. The disturbance seen at 2.6 in. of displacement corresponds to yielding of material model representing the shear distortion response of T-walls in the trailing wall. The last pair of disturbances in the responses are seen at approximately 4.0 in. of displacement. This corresponds to yielding of the shear material in the leading wall, and returns to the expected response.

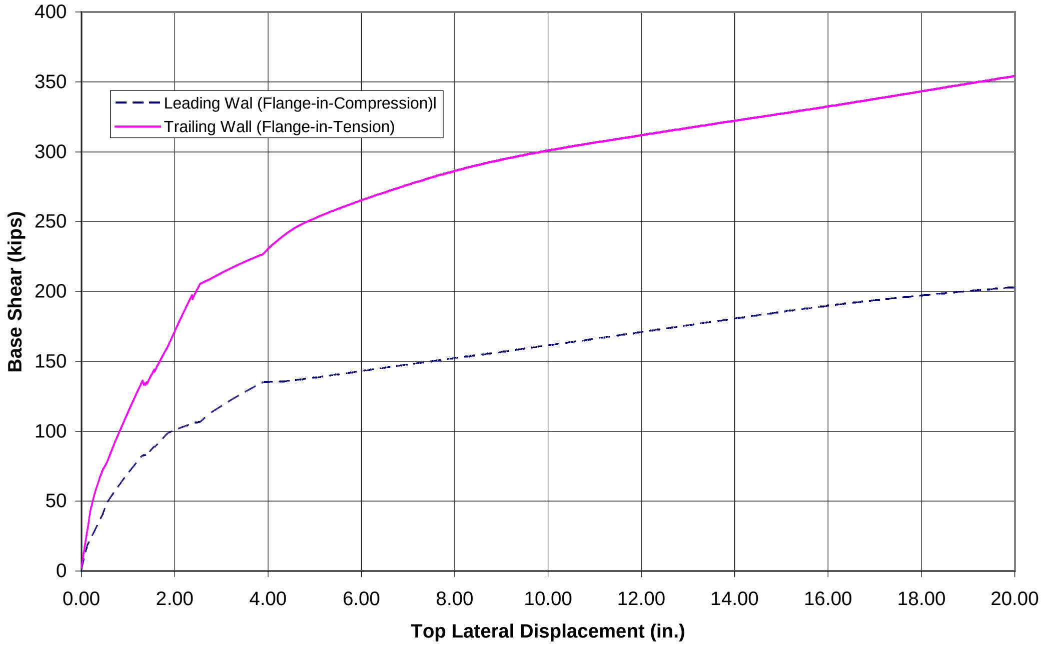

Figure 6-4: The Base Shear Established from a Pushover Analysis for the Pair of T-walls in the Building Slice as a Function of Top Floor Displacement

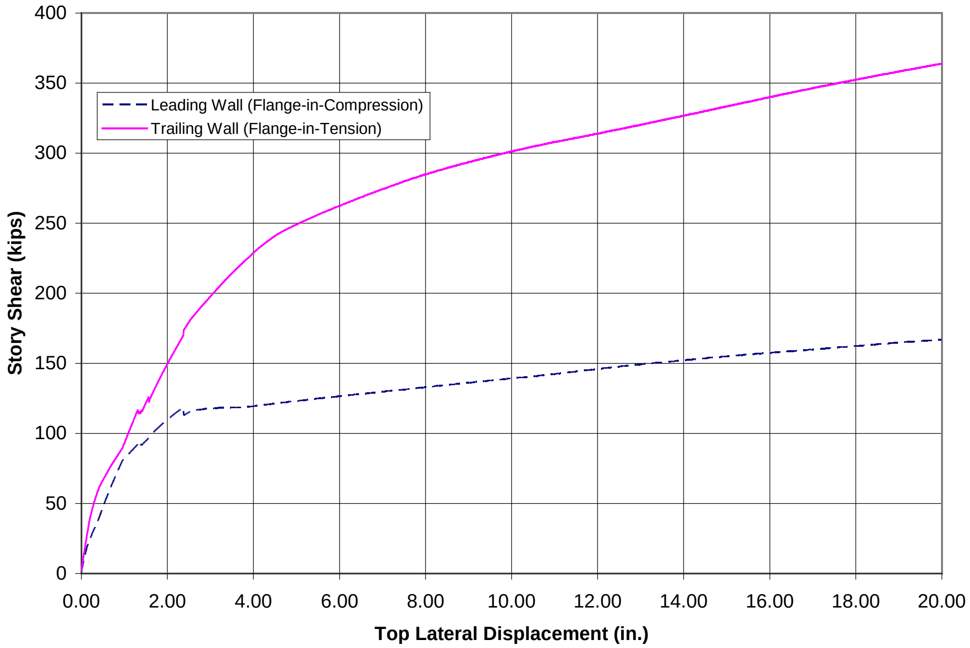

Figure 6-5: Second Floor Story Shear Established from a Pushover Analysis for the Pair of T-walls in the Building Slice as a Function of Top Floor Displacement

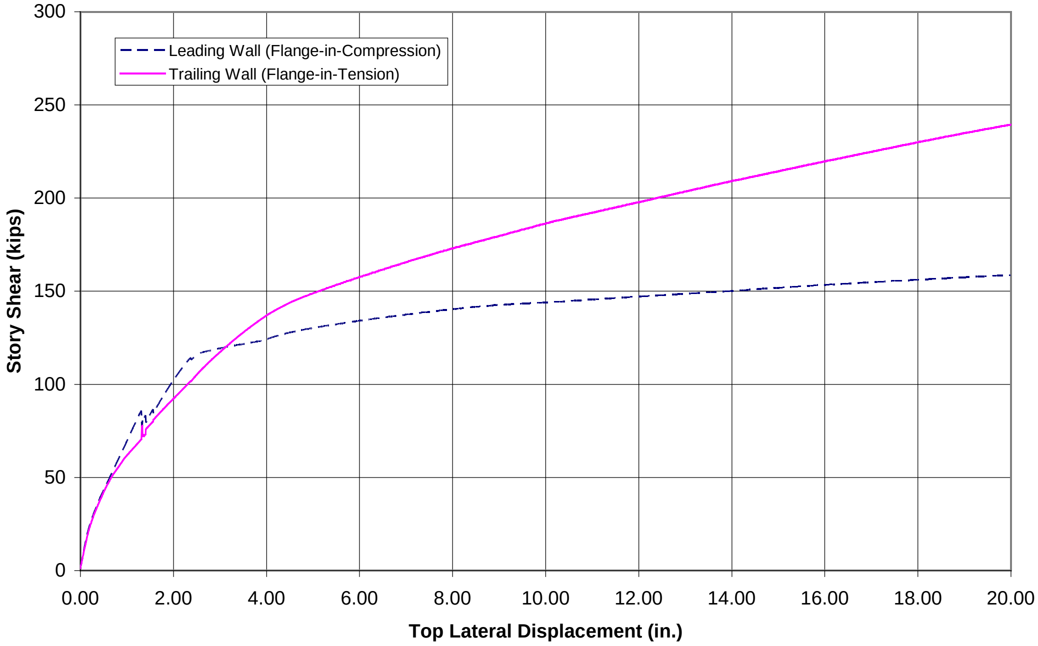

Figure 6-6: Third Floor Story Shear Established from a Pushover Analysis for the Pair of T-walls in the Building Slice as a Function of Top Floor Displacement

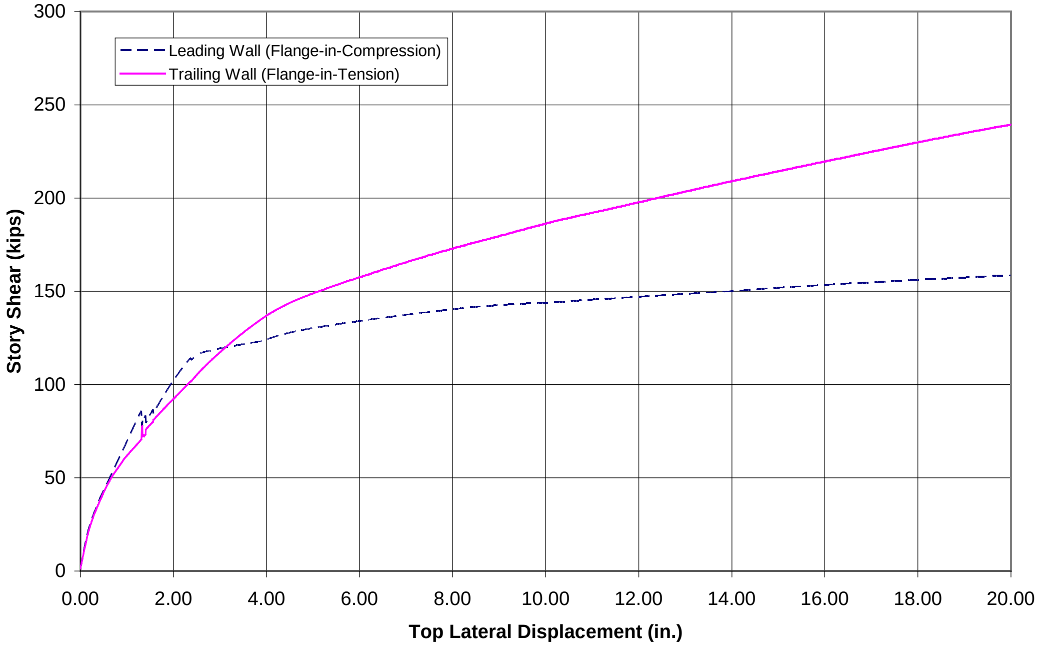

Figure 6-7: Fourth Floor Story Shear Established from a Pushover Analysis for the Pair of T-walls in the Building Slice as a Function of Top Floor Displacement

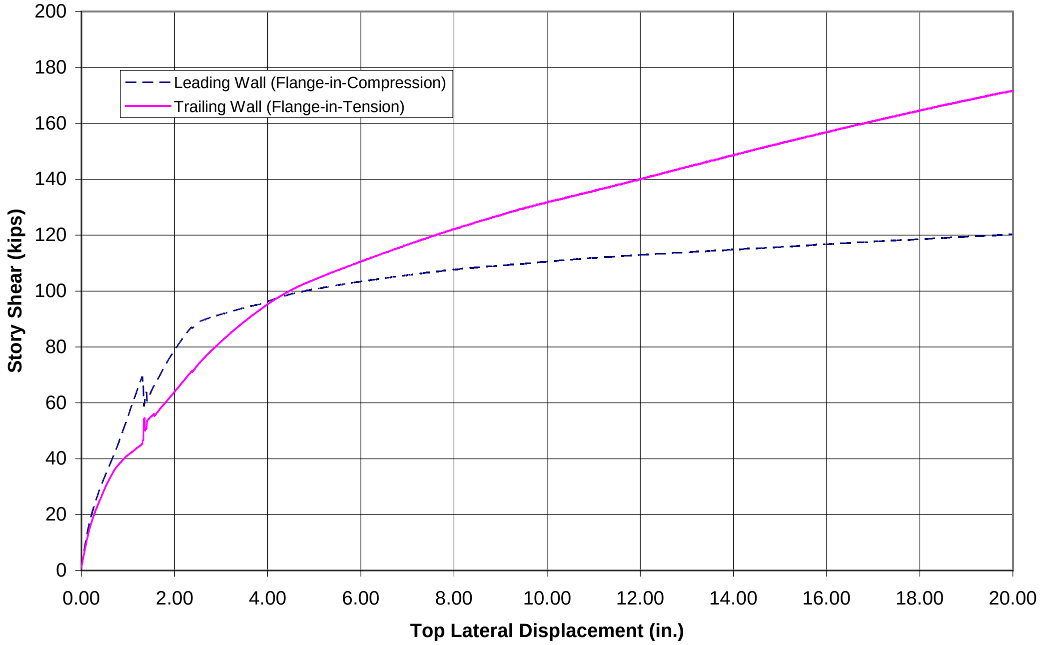

Figure 6-8: Fifth Floor Story Shear Established from a Pushover Analysis for the Pair of T-walls in the Building Slice as a Function of Top Floor Displacement

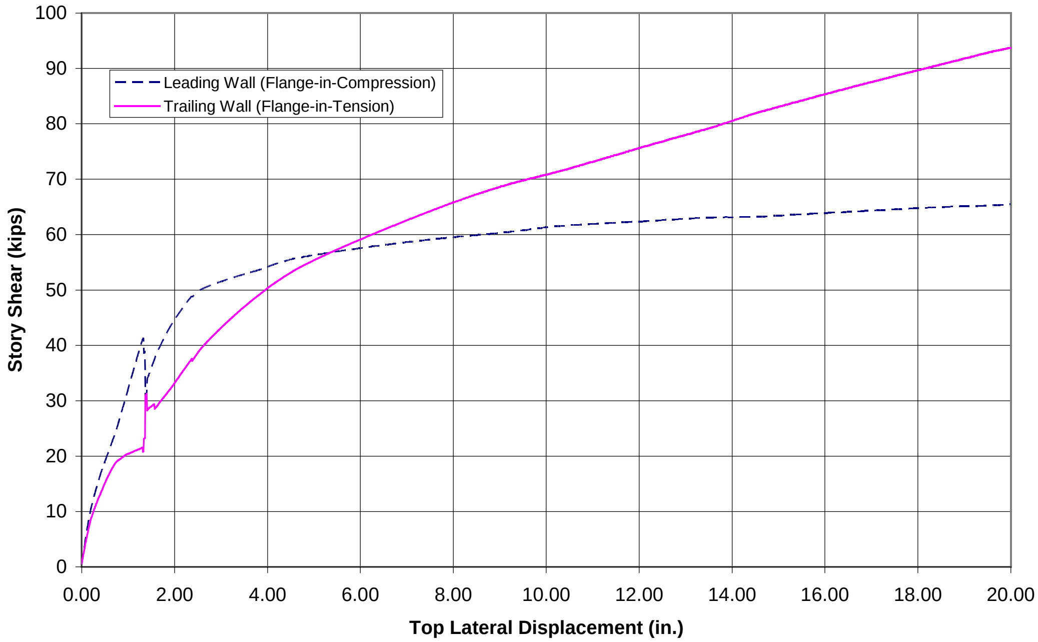

Figure 6-9: Sixth Floor Story Shear Established from a Pushover Analysis for the Pair of T-walls in the Building Slice as a Function of Top Floor Displacement

6.5 Dynamic Analysis

6.5.1 Analysis Objectives

A dynamic analysis was conducted on a pair of T-walls to better understand the distribution of forces to each wall. The monotonic analysis gave a viewpoint on the distribution of base shear to each wall; however, the applied earthquake load is a dynamic load. Dynamic effects, including the influence of higher modes, could potentially change the force distribution and thus how the base shear should be distributed. The peak values from appropriate dynamic analyses are examined to see if they align with the distribution determined from the monotonic response. The Newmark Constant Average Acceleration method was used based on the experience with the UCSD Seven Story Building Slice for the dynamic analysis.

SEAOC [1999] provides limits for the lateral drifts, interstory displacement, and floor level accelerations for the various intensity levels. These limits are meant to ensure acceptable performance of buildings by ensuring specific levels of strength, stiffness, and ductility for different intensities of ground motions. The building slice should meet or not exceed the limits due to the high in-plane stiffness of the T-walls, and historically buildings with structural walls have performed very well during seismic events of various intensities. The OpenSees analysis should be able to produce results that correspond with the expected results for a building designed with wall structures.

The input motions were selected in order to maximize the virgin response of the structure. Thus motions were selected such that the peak ground accelerations were significantly different. The intent of this was to prevent a series events similar to that with EQ3 in the UCSD analysis, see Appendix A. If the intensities of two events are similar, the response is controlled by the unloading and reloading behavior of the material models. Since this was not a goal of this analysis, similar strength events were avoided.

6.4.2 Input Ground Motions

The input motions described in described in Section 6.1 were for a full scale structure, and thus they required modification for use with the 50% scale analysis model. Accordingly, the ground accelerations and the time step were modified using scales of 2 and 0.5, respectively. The scaled input accelerations are shown in Figures 6-10 to 6-14. These events when applied in the order they are presented were intended to subject the building model to progressive damage, maximizing the building response in virgin response territory. In order for the cumulative effects of damage to be accurately captured in the dynamic analysis, the selected events were concatenated in the order of increasing intensity. Six seconds of zero ground accelerations were inserted between the events to allow the structure to come to a complete rest before being subjected to the next base acceleration. The entire duration of applied accelerations was 125 seconds long.

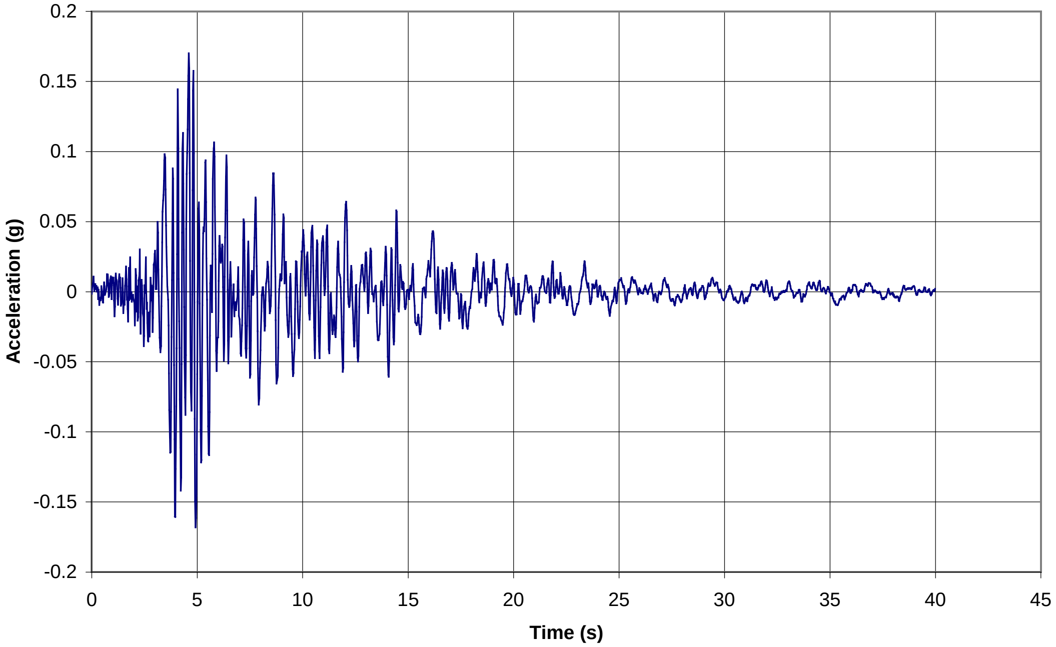

Figure 6-10: Earthquake Input Ground Motion IM-a Representing EQ-I

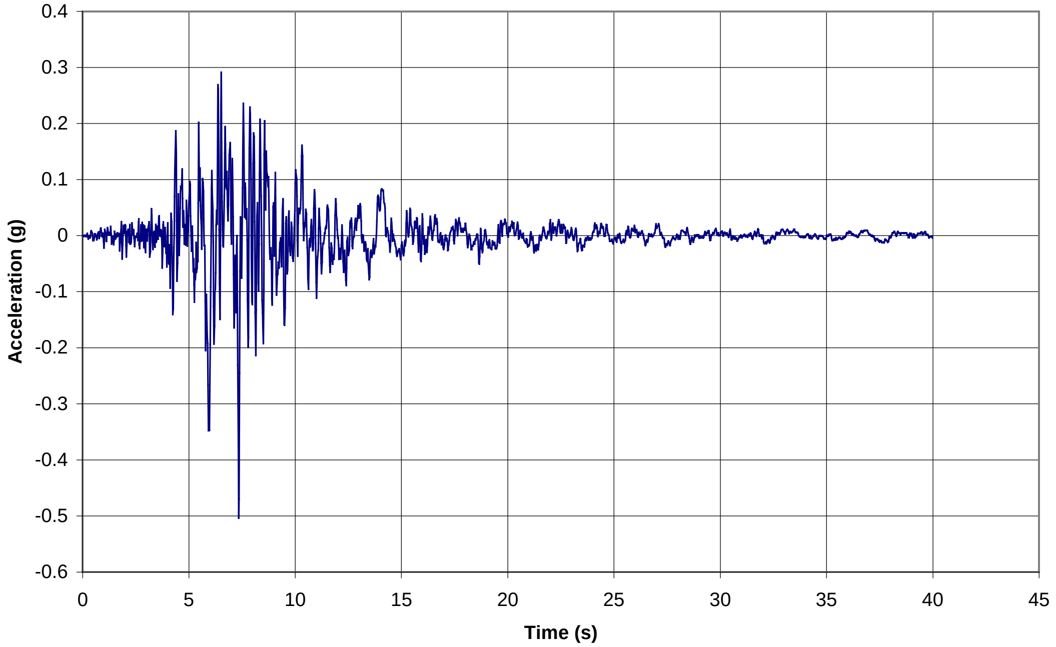

Figure 6-11: Earthquake Input Ground Motion IM-b Representing EQ-III

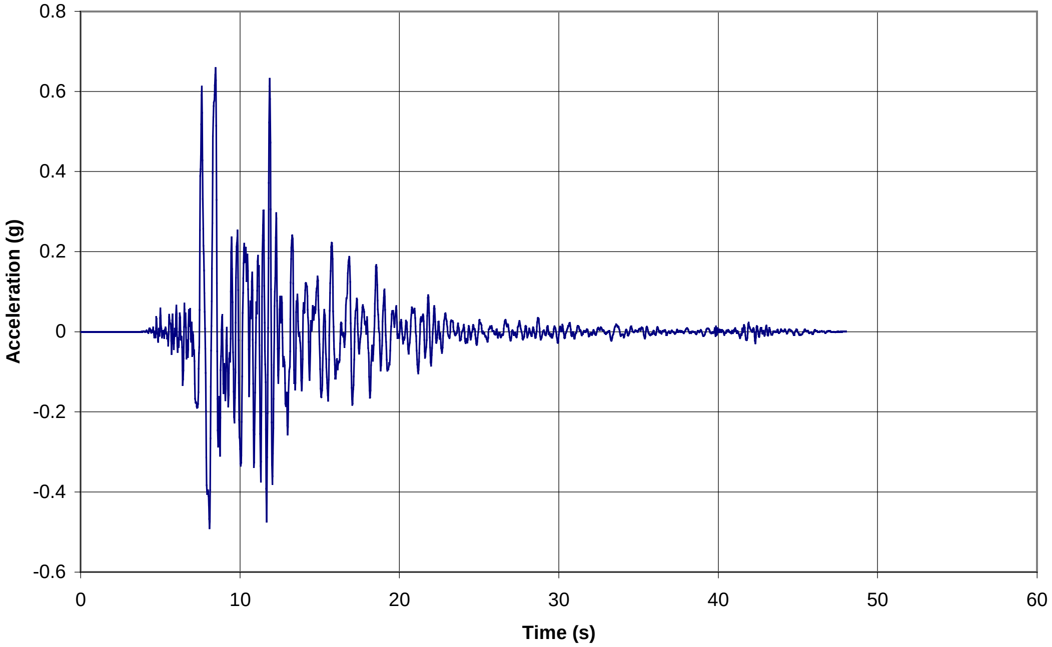

Figure 6-12: Earthquake Input Ground Motion IM-e Representing EQ-III

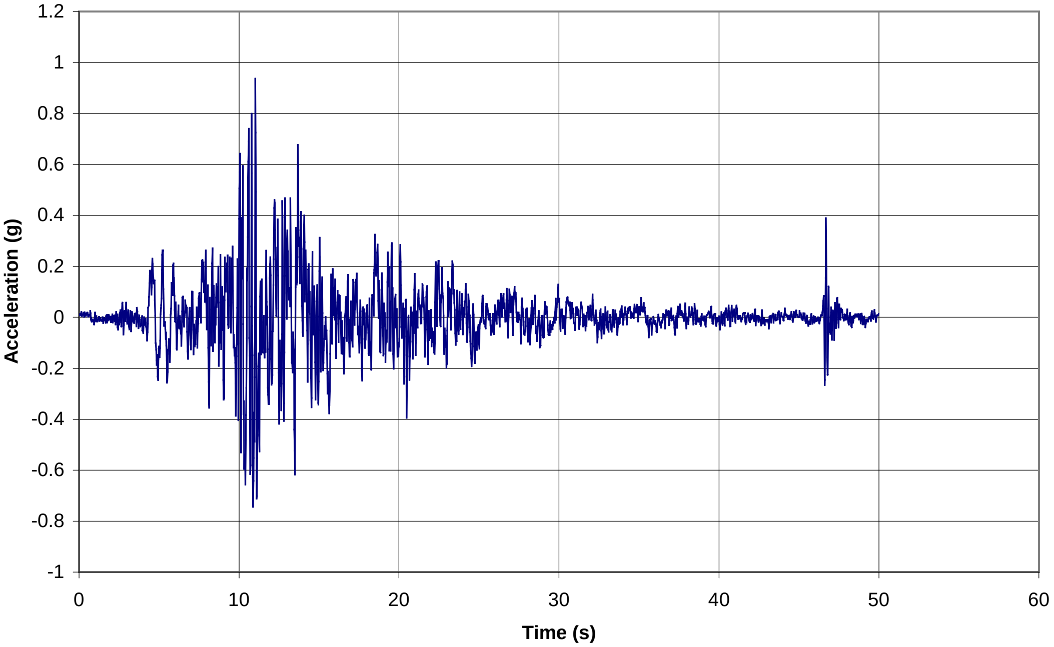

Figure 6-13: Earthquake Input Ground Motion IM-f Representing EQ-IV

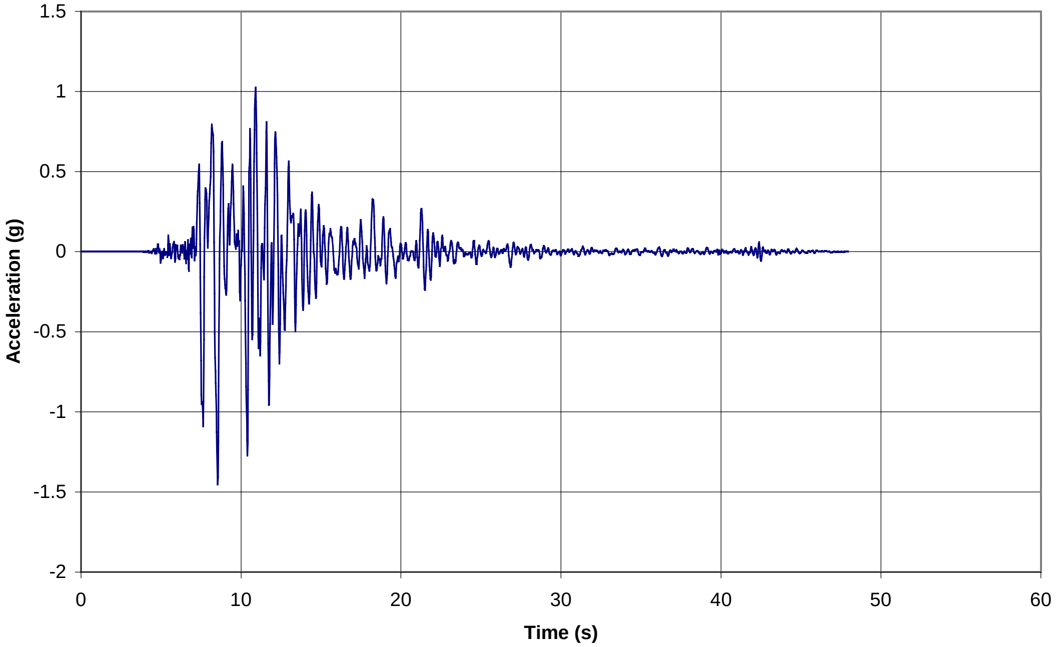

Figure 6-14: Earthquake Input Ground Motion IM-h Representing EQ-IV

6.4.3 Results

The time history responses of the top floor displacement are shown in Figures 6-15 to 6-19, with peak displacements of 0.59 in., 0.95 in., 3.67 in., 3.80 in., and 11.76 in. for IM-a, IM-b, IM-e, IM-f, and IM-h, respectively. These displacements correspond to an average floor drift ratio of 0.14%, 0.22%, 0.85%, 0.88% and 2.7%. Except for the IM-h event, the maximum average floor drifts obtained from the analysis are well below the permissible limits that are considered to define acceptable performance for the various level events according to the SEAOC Seismology Committee [1999]. SEAOC recommended drift limits for a concrete structural wall of 0.4%, 0.9%, 1.4% and 2.1% for EQ-I, EQ-II, EQ-III, and EQ-IV events, respectively. The maximum drift obtained for the IM-h event exceeded the acceptable limit suggested for an EQ-IV event once by 28%; however, IM-h has a very large base excitation, and the structure had already been subjected to IM-f, another EQ-IV event. The max average floor drift ratios obtained for the analysis are about 15-20% larger than those presented by Rahman and Sritharan

[2006] for a building with precast concrete walls that were designed using a force-based approach. Additionally the peak drift is sensitive to choices made about the connection details used between the walls and the prestressed beams, and between the floor slabs and the columns. This sensitivity will be discussed later section in Section 6.8.

The peak floor accelerations are also of interest to the design community. Limits on floor acceleration helps to limit the amount of nonstructural damage during the earthquake event and potentially pose a hazard to occupants of the building during the event. Additionally, similar to deflections due to gravity loads, large accelerations can be very disconcerting to users of the structures and may lead to a perception that the building is unsafe, even if the accelerations pose no danger to the structural elements. Rahman and Sritharan [2006] recommended a limit of 7.08 ft/s^2, 32.18. ft/s^2, 48.29 ft/s^2, for EQ-I, EQ-III, and EQ-IV level events at full scale and correspond to 14.16 ft/s^2, 64.36. ft/s^2, 96.59 ft/s^2 for the half scale model. The peak accelerations from the OpenSees analysis were 41.5 ft/s^2, 68.3 ft/s^2, 96.0 ft/s^2, 177.6 ft/s^2, 146.1 ft/s^2 for IM-a, IM-b, IM-e, IM-f, and IM-h for the top floor. In all cases, the accelerations were well above the acceleration limits.

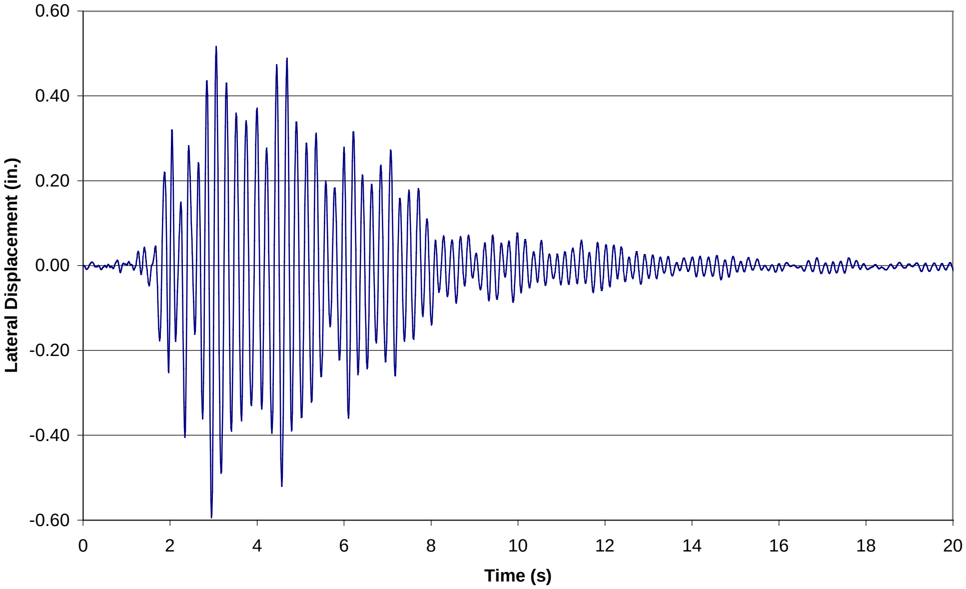

Figure 6-15: Top Floor Lateral Displacement History Obtained for the Half-Scale Model of the Building Slice Subjected to IM-a

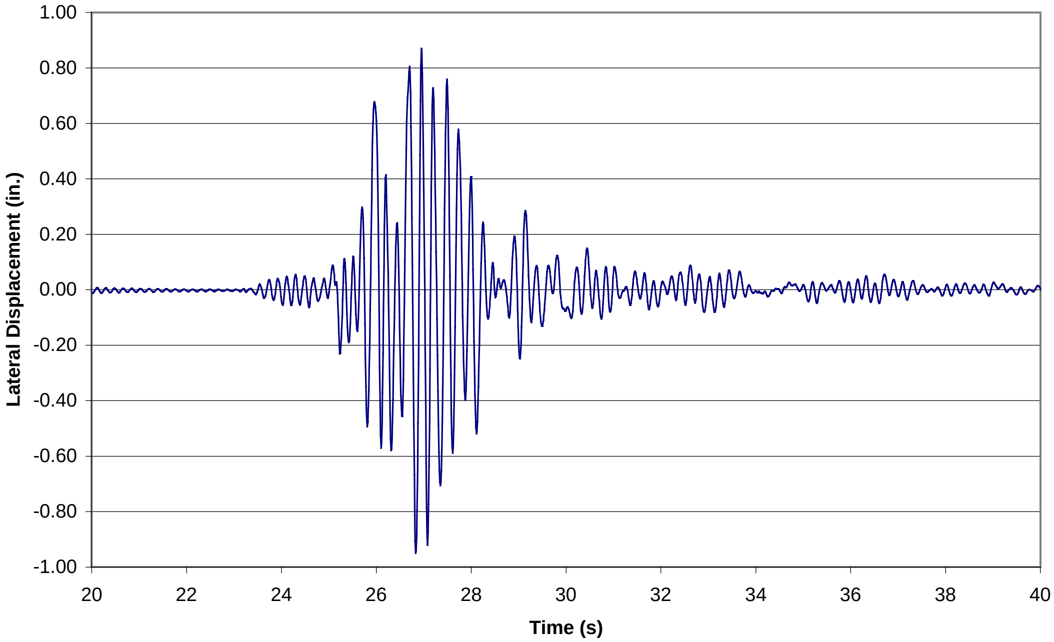

Figure 6-16: Top Floor Lateral Displacement History Obtained for the Half-Scale Model of the Building Slice Subjected to IM-b

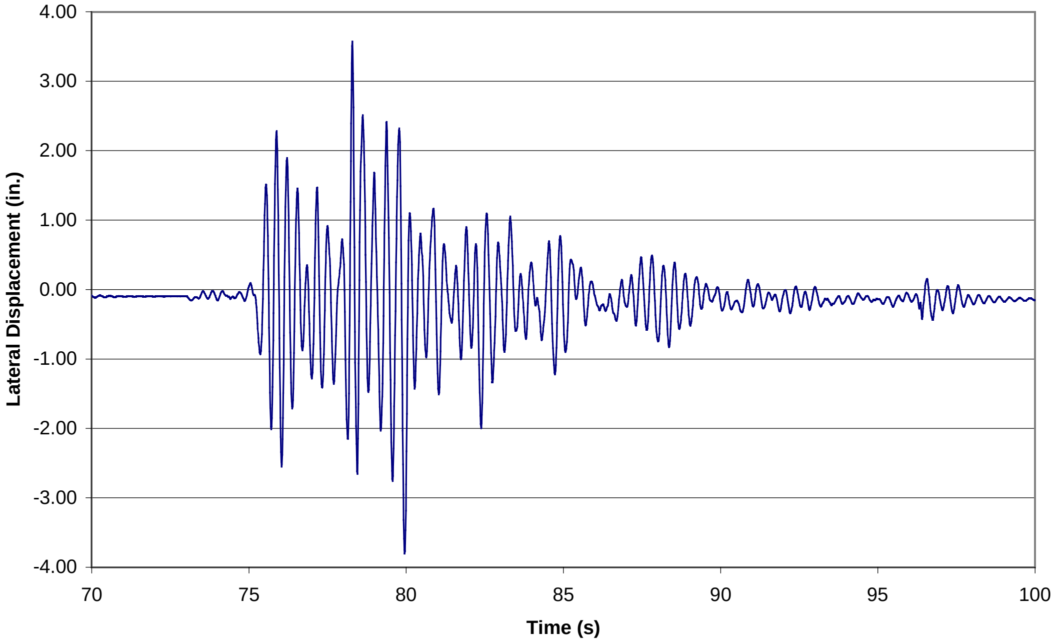

Figure 6-17: Top Floor Lateral Displacement History Obtained for the Half-Scale Model of the Building Slice Subjected to IM-e

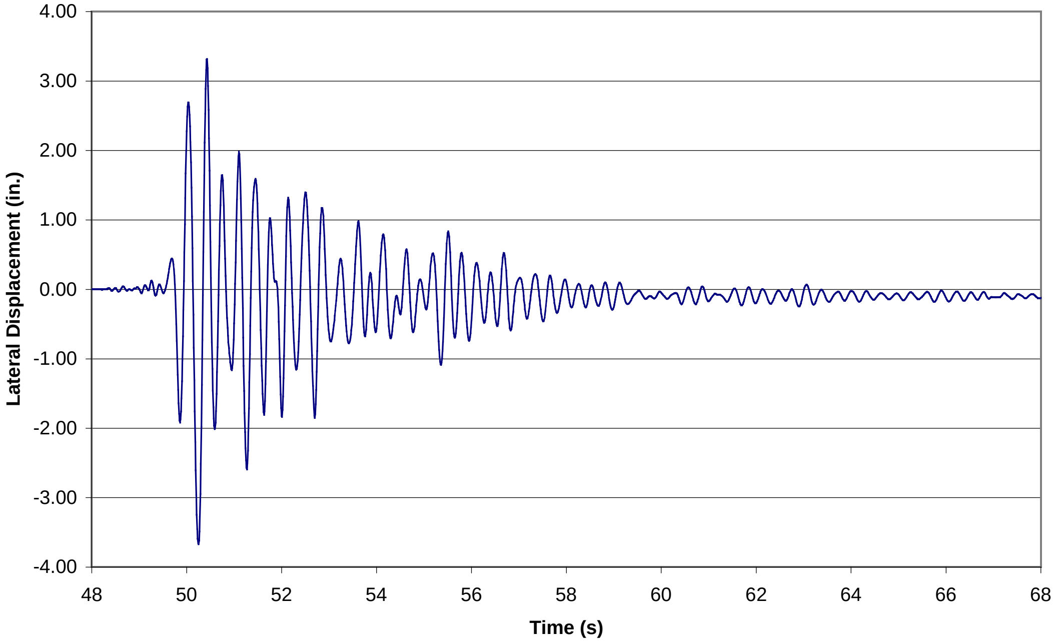

Figure 6-18: Top Floor Lateral Displacement History Obtained for the Half-Scale Model of the Building Slice Subjected to IM-f

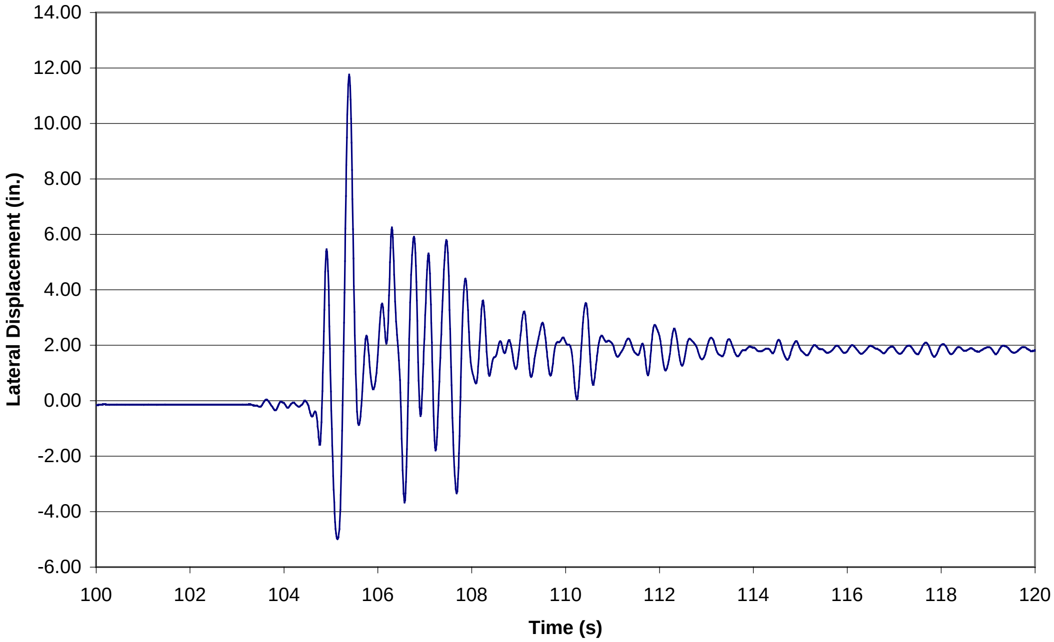

Figure 6-19: Top Floor Lateral Displacement History Obtained for the Half-Scale Model of the Building Slice Subjected to IM-h

6.6 Base Shear Contribution Factor

As stated earlier, the interstory forces and distribution of shear to each T-wall in a pair was a subject of discussion during the design of the prototype building. Figure 6-20 shows the base shear contribution factors calculated from the peak values of the base shear recorded during the dynamic analysis, pushover analysis, and those calculated from a moment-curvature response of a wall cross-section using different approaches. In this context, the base shear of each wall divided by the total base shear defines the "contribution factor". From a design perspective, use of one contribution factor for all levels of response would simplify design calculations. The contribution factor determined from the peak base shear recorded during the dynamic analysis are shown as distinct points in Figure 6-20. With the exception of the points corresponding to the response to IM-h, the contribution factors from the dynamic analysis are closely grouped. Additionally, the pushover analysis shows that the contribution factor stays pretty constant over the various displacement levels as shown in Figure 6-20. Furthermore, a number of approaches that may be used to determine the contribution factors for the flange-in-compression and flange-in-tension loading direction, the following were investigated in this study: 1) secant stiffness defined at the first yield condition ignoring confinement of the concrete, 2) the secant stiffness defined at the first yield condition including confinement of the concrete, 3) ultimate moment capacity include effects of confinement of the concrete and strain hardening of the longitudinal reinforcement, and 4) instantaneous stiffness of the section at each displacement. The approach most consistent with the ACI concrete code would be option 1.

The secant stiffness defined at the first yield condition ignoring confinement of the concrete was the approach used in the design of the prototype building for the NEES walls. This method was used because distributing forces based on relative stiffness is a standard approach that is familiar to designers and is consistent with elastic behavior. Furthermore, ACI-318 does not allow consideration of the effects of confinement of the concrete on the flexural strength of a concrete member. Thus, a moment-curvature analysis of the wall was conducted ignoring the effects of confinement, by using an elastic-perfectly plastic model for the steel behavior. The secant stiffness to first yield of the section can be easily determined from the moment-curvature analysis for both the flange-in-compression and flange-in-tension directions. The contribution factor is plotted in Figure 6-20 at the displacement that corresponds to the first yield in the 6-story wall. However, two problems are apparent in this approach. First, the first yield in each direction occur at different displacements. In the leading wall with the flange-in-compression, the first reinforcement bar yields at 2.06 in., while in the trailing wall with the flange-in-tension first yield doesn't occur until 3.84 in. of displacement. The second problem is the effects of confinement are ignored in the analysis. However, the the effects of confinement of the concrete will influence the behavior of the wall during a earthquake.

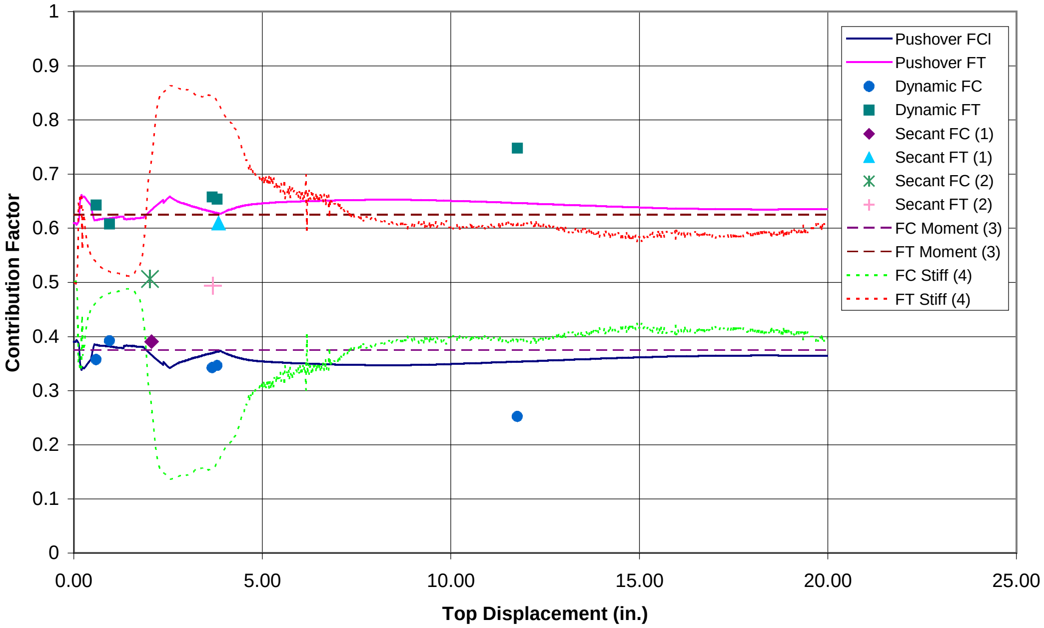

Figure 6-20: Contribution Factor for Base Shear Resistance of a pair of T-walls

The second method is to use the secant stiffness to first yield, but include the effects of confinement of the concrete. This method produced worse results than the previous case that ignored the effects of confinement of the concrete. Figure 6-20 indicates that when the confinement effects are included the base shear is distributed approximately equally to both T-walls, which is inconsistent with the results of both the pushover and dynamic analysis. The secant stiffness for the two directions are nearly identical because the confinement significantly increases the first yield strength of the wall with the flange-in-tension, but has no effect on the yield strength of the wall with the flange-in-compression. Thus the difference in stiffness seen when confinement of the concrete is ignored is significantly reduced. Additionally, the first yield still occurs at two different displacement levels, with first yield occurring at 2.02 in. for the wall with the flange-in-compression, and 3.69 in. for the wall with the flange-in-tension.

A third method that may be used to determine the contribution factors is using the ultimate moment capacity of the section considering confined concrete and the strain hardening behavior of the reinforcement. This method is shown in Figure 6-20 as dotted lines, and well simulates the average contribution factor seen in both the pushover and dynamic analysis, with the exception of IM-h. This approach has two advantages for determining the contribution factors. First, a more realistic model of the section behavior is used by including the effects of confinement of the concrete and the strain hardening behavior of the longitudinal reinforcement. Second, in the nonlinear range, the ultimate moment capacity of the section limits the amount of force that the wall can attract and thus distributing the base shear force based on the ultimate capacity matches the walls behavior in the nonlinear range. In the prototype building, if the base shear had been distributed based on the ultimate moment capacity, only four wall pairs would have been required rather than the five pairs required because the base shear was distributed according to the secant stiffness to first yield when confinement of the concrete is ignored. Reducing the required number of wall pairs would lead to substantial cost savings for the building Rerunning the dynamic analysis and adjusting for only 4 pairs of T-walls did not result in the building slice violating the lateral drift limits on IM-a, IM-b, IM-e, and IM-f. While lateral displacement increased to 0.64 in., 1.14 in., 4.37 in., 6.53 in., and 11.73 in. corresponding to lateral drifts of 0.15%, 0.26%, 1.0%, 1.5%, and 2.7% for IM-a, IM-b, IM-e, IM-f, and IM-h, respectively. The lateral drifts are still below the recommended SEAOC drift limits, for all motions but IM-h. Thus the number of walls could be reduced in the prototype structure while maintaining acceptable performance.

The fourth method is to determine the distribution factors based on the instantaneous stiffness of each wall. However, as seen in the dotted lines in Figure 6-20 this approach produces a highly variable value for the contribution factor. The variability can cause significant under or overestimation of the amount of shear that should be assigned to each T-wall. This is because each wall yields at different displacements, causing the elastic wall to have a much larger stiffness than the wall that has already experienced yielding of the longitudinal reinforcement. The higher stiffness of the elastic wall attracts the majority of the force until it reaches its yield force. Then the contribution factor returns to the range expected from the pushover analysis of the prototype structure.

6.7 Story Shear Envelopes

In the design process, once the base shear is determined, the distribution of the shear up the height of each wall needs to be determined and this issue was also investigated. Typically, an inverse triangular step function is used to distribute the base shear because the first mode typically dominates the dynamic response. The shear envelope for the dynamic analysis results are shown in Figures 6-21 and 6-22 for the flange-in-tension and flange-in-compression walls respectively. The story shear is shown for the peak shear in each direction recorded for each of the events.

The flange-in-tension story shear envelope presented in Figure 6-21 shows the expected triangular step function. However, the flange-in-compression envelope does not show the expected shape. The story shear for the flange-in-compression wall is nearly constant over the bottom two stories for all of the ground motions imposed on the model. For all the ground motions except IM-b, it appears that the wall should be designed to resist the story the base shear up through the fourth floor level. The reason for this is twofold, first the yielding extends over a much longer height in the flange-in-compression direction because the wide compression flange causes a shallow neutral axis depth; second the floor slab forces the walls to move together increasing the demand on the flange-in-compression wall.

During the test of NTW2 at the MAST facility, the wall failed when it reached 250 kips in the flange-in-tension direction. The failure was initiated by buckling of the longitudinal reinforcement in the web; however, prior to failure a long horizontal crack was observed at mid height of the first story running more than half the length the of the web from near the flange-web junction. IM-h places a shear demand greater than 250 kips over the first and second floor levels. If NTW2 had been subject to the demands of IM-h, it would likely have had larger horizontal and diagonal cracks under the influence of shear. The T-walls need to be capable of resisting the story shear of even a very large event such as IM-h without failing to ensure the safety of the occupants.

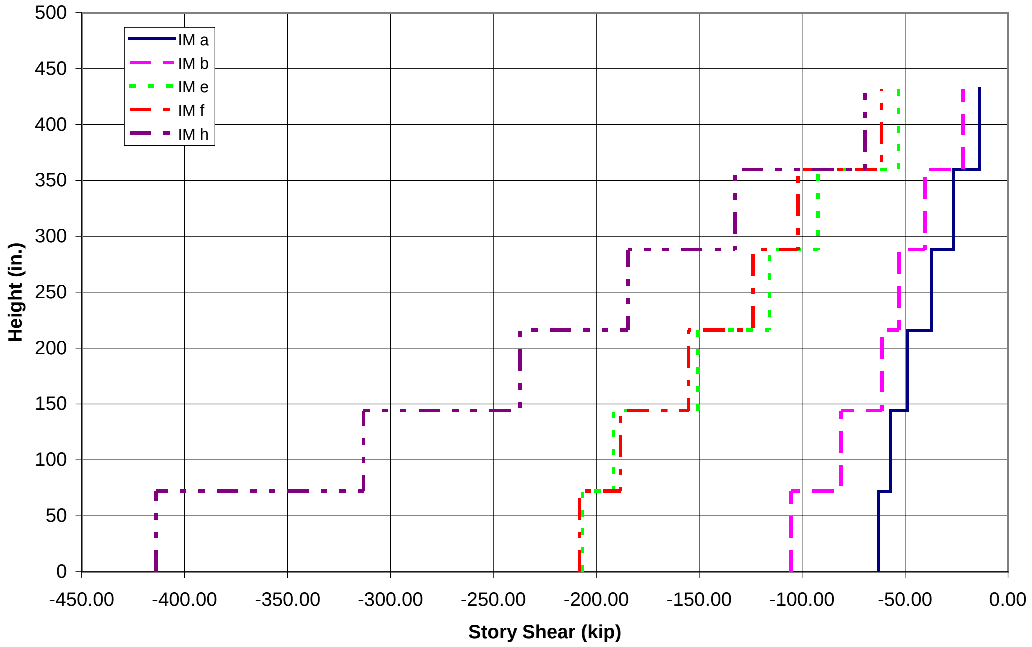

Figure 6-21: Story Shear Envelope Obtained for Trailing Wall with Flange-in-Tension

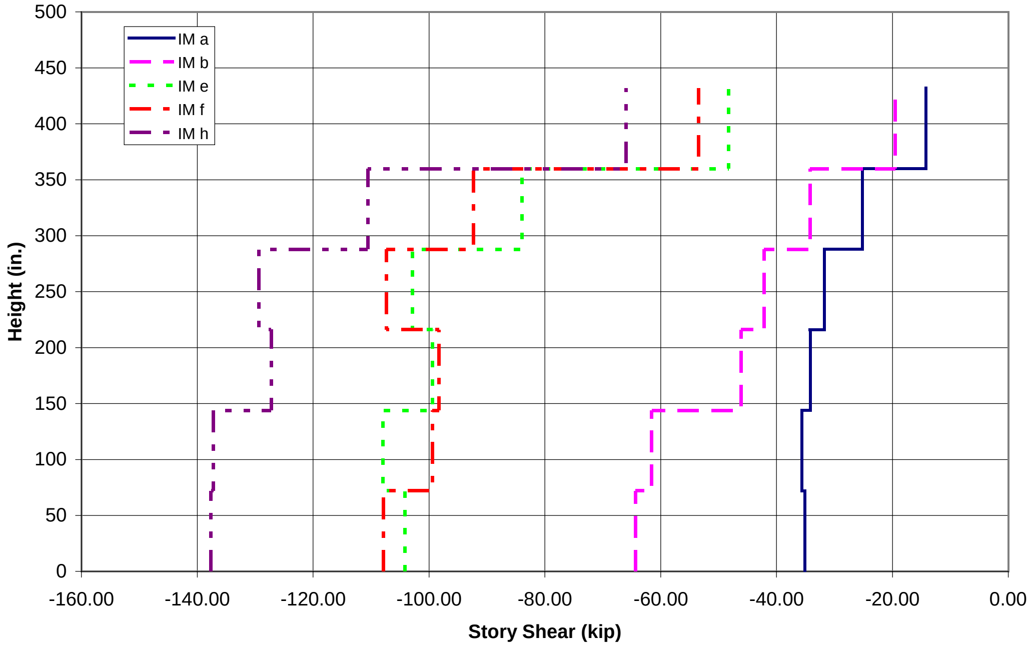

Figure 6-22: Story Shear Envelope Obtained for Leading Wall with Flange-in-Compression

6.8 Effects of Boundary Conditions

The previous sections showed the analysis results for the model that closely followed the idealization for the structure detailed in Section 6.1. However, a number of changes will be made to the structure, and two such changes and their effects on the analysis results were also investigated. First, the impact of rigidly connecting the slab to the gravity columns and allowing moment and force transfer from the slab to the column was studied. Second, instead of simply supporting the prestressed beams, the possibility of rigidly connecting them to the T-walls was examined.

6.8.1 Slab-Column Connection

The slab could be rigidly connected to the gravity columns either as part of new construction or as a retrofit option to improve the performance of the building. Connecting the slab to the column increases the stiffness of the structure in two ways. First, it allows a couple to develop by subjecting the two columns to axial tension and axial compression, thereby helping to resist the inertial forces in the lateral direction. Second, it increases the stiffness of the floor slab by changing the deflected shape of the slab. In a modified model to account for this change, columns were modeled using displacement-based beam-column elements with fiber sections. The columns were six-inch square columns with eight #3 bars distributed around the perimeter. The unconfined concrete and reinforcing steel material models used for the prestressed beams in the original model were used to model the column materials.

Table 6-4 shows the decrease in interstory drift of the new model in comparison to the original model without the columns. Connecting the slabs to the gravity columns did not significantly decrease the lateral drift that the structure experienced. On average, the interstory drift was reduced by 7%. The interstory drift was reduced more in the elastic region than in the inelastic region, particularly IM-b. Additionally, the interstory drift was reduced more in one direction than in the other, but this could be due to asymmetry in the applied ground acceleration. The interstory drift was reduced by approximately 13-16% in one direction for events IM-e and IM-f. The reason for this was that the structure was not displaced as far in that direction as it was in the opposite direction and thus it remained closer to the elastic range. Therefore, the contribution of the columns to the lateral load resistance was a larger percentage of the total lateral resistance and reduced the displacements and corresponding interstory drift more significantly. However, the analysis shows that the longitudinal reinforcement in the column yielded. This would require the column to be designed to experience plastic action, increasing the design and construction time. Additionally, extra transverse reinforcement would be required when compared with the columns designed for only gravity loads. The increased design time, reinforcement, and decreased constructibility make this an undesirable choice from an economic perspective.

Table 6-4: Percent Decrease in Interstory Drift Due to Gravity Columns

	Direction	Floor 1	Floor 2	Floor 3	Floor 4	Floor 5	Floor 6
IM-a	Pos.	3.2%	1.3%	1.2%	0.9%	0.7%	0.4%
	Neg.	5.3%	4.6%	5.4%	5.7%	5.8%	5.6%
IM-b	Pos.	16.8%	19.1%	17.4%	17.5%	17.2%	17.9%
	Neg.	15.2%	9.6%	8.0%	7.3%	7.2%	7.7%
IM-e	Pos.	20.3%	13.5%	13.7%	13.0%	12.7%	11.9%
	Neg.	11.2%	4.4%	4.8%	4.9%	6.0%	9.5%
IM-f	Pos.	20.4%	17.9%	16.1%	15.9%	14.7%	13.8%
	Neg.	8.8%	0.6%	2.6%	2.4%	3.3%	7.9%
IM-h	Pos.	13.4%	8.9%	8.6%	8.1%	7.5%	6.2%
	Neg.	3.3%	5.4%	5.8%	6.6%	6.2%	7.4%

The inclusion of the gravity columns did not alter the contribution of each wall to the base shear resistance. Consequently, it should be expected that the gravity columns would not change the distribution of base shear because it does not change the relative stiffness of each wall, which largely influences that distribution. Thus, the previous discussion of determining the distribution factor is still valid.

6.8.2 Wall-to-Slab Connection

The connection between the wall and the T-beam can be modeled in a number of ways. In Section 6.1, the connection was modeled using the slab alone and a truss element to simulate the dowel action of the slab reinforcement crossing the web. However, the prestressed beam could be rigidly connected to the wall and the amount of the gap between the end of the beam and the wall could be eliminated. If the gap between the wall and the beam is small, then the end of the beam could bear against the wall transferring the compression force while the longitudinal steel in the slab transferred the tension force. If significant moment can be transferred between the prestressed beams and the walls, then a fixed connection would be the proper way to model the connection. A fixed connection between the T-walls and the prestressed beams would significantly stiffen the structure because flexure of the T-wall would induce flexure in the prestressed beams.

Table 6-5 shows that connecting the beams rigidly to the walls has a much larger effect on the interstory drifts when compared to rigidly connecting the columns to the slab. The interstory drift on the top story in IM-h is reduced 48.4%, reducing the displacement to less than 7.0 in. This corresponds to a top story drift of 1.5%, which is less than the SEAOC limit of 2.1%. Decreasing the interstory drift would correspond to decreased damage to both the structural and non-structural elements. The prestressed beams did not yield during the entire dynamic analysis, so they would not need to be replaced or significantly repaired after a large earthquake had occurred, reducing the damage and repair costs.

As with the connection between the gravity columns and floor slab, changing the connection of the prestressed beams to the T-walls does not change the distribution of shear force to each wall. Again this is because the relative stiffness of each wall is not affected.

Table 6-5: Percent Decrease in Interstory Drift Due to Fixed Connection to the Walls

	Floor 1	Floor 2	Floor 3	Floor 4	Floor 5	Floor 6
IM-a	39.4%	49.9%	53.3%	52.7%	53.0%	54.7%
	33.4%	25.5%	37.5%	37.0%	37.3%	38.5%
IM-b	3.1%	17.1%	24.1%	26.8%	28.3%	30.3%
	26.1%	15.4%	25.3%	28.2%	29.9%	31.4%
IM-e	56.6%	47.5%	49.6%	50.3%	51.0%	50.8%
	44.7%	40.9%	46.3%	52.2%	52.7%	56.2%
IM-f	46.2%	22.5%	21.7%	26.9%	27.9%	28.1%
	27.2%	10.1%	0.3%	8.0%	11.4%	16.3%
IM-h	11.8%	3.9%	3.6%	5.0%	4.9%	4.5%
	32.5%	42.8%	43.8%	46.8%	47.1%	48.4%

Chapter 7: Summary, Conclusions, and Recommendations

7.1. Summary of Analysis and Testing

Two T-shaped concrete walls were designed and tested at 1/2-scale at the University of Minnesota's Multi-Axial Testing Facility as part of a PreNEESR project. The two T-wall specimens, referred to as NTW1 and NTW2, had identical cross-sectional dimensions but with different reinforcement details. NTW1 modeled four stories of a six-story prototype wall with the reinforcement details that are typical of the current industry practice. NTW2 modeled only 2 stories with improved reinforced details in the flange and web. The experimental findings of the T-walls are presented in Brueggen (2009), respectively. Both T-wall specimens, were analyzed using a fiber-based analysis approach in order to predict and understand the behavior of T-walls subjected to multidirectional loading. This report has presented the fiber-based analysis of the T-walls investigated as part of this project.

Both T-walls were subjected to the same load protocol that included axial loads and lateral cyclic loads in the parallel to the web direction, parallel to the flange direction, and in inclined directions that subjected the walls to both the web and flange direction displacements. Additionally, the walls were subjected to complex multidirectional load paths in both the elastic and inelastic regions. These load paths were intended to investigate the performance of the walls under multidirectional loading and the ability of the fiber-based models to capture the non-rectangular wall behavior under complex load paths. Complete details of the load paths applied to NTW1 and NTW2 are found in Sections 4.4 and 5.3, respectively.

The analysis of structural walls subjected to multi-directional loading requires that a number of issues be addressed in the development of the analysis model. Those issues are: 1) nonlinear material behavior, including the effects of cracking and confinement of concrete as well as yielding and strain hardening of the mild steel reinforcement; 2) shear deformation of the walls; 3) interaction between the shear and flexural deformations; 4) the effects of shear lag in the flange in nonrectangular walls (e.g., T-walls); and 5) strain penetration effects at the wall-to-foundation interface. The OpenSees models used for the analysis of the T-shaped walls; NTW1 and NTW2 were designed to include the effects of these issues, except for the flexure-shear interaction. Full descriptions of the analytical models used for the specimens were presented in Sections 4.3 and 5.2.

The models used for the analysis in this report used fiber-based beam-column elements that were available in the OpenSees analysis software. A fiber-based approach was selected because the simplification of the material model based on uniaxial behavior enabled more accurate representation of the concrete and steel reinforcement behavior in modeling the wall response. Additionally, the strain distribution induced in the fiber elements of the walls could be modified to include the effects of shear lag. The fiber-based approach also enabled the effects of strain penetration at the wall-to-foundation interface to be included through the use of an interface element and a material model suitable for defining the local slip at the interface as a function of the stress in the longitudinal reinforcing bar, thus capturing the strain penetration effects in a rational manner. However, the fiber-based approach does have two drawbacks. First, the shear distortion is handled at the element level, and thus the analysis requires that the shear deformation of the wall in the flange and web directions be considered separately from the flexural behavior. Second, the separation of the shear and flexure behaviors makes it difficult for the shear-flexure interaction to be handled as directly as desired. However, a careful definition of the shear deformation can allow the nonlinear behavior of shear and flexure to occur simultaneously as other researchers have observed this to be the case due to shear-flexure interaction.

Both pre- and post-test analyses were conducted for NTW1, while only a pre-test analysis was conducted for NTW2. The pre-test analyses of NTW1 showed the importance of using a more realistic concrete cyclic model in analytical simulations of structural walls. The most sophisticated model available in OpenSees was the Kent-Park concrete model, which did not adequately represent the cyclic behavior of concrete. Thus a modified version of a cyclic concrete model proposed by Chang and Mander [1995] was implemented in OpenSees. Additionally, the pre-test analysis of NTW1 ignored the effects of shear deformation because it was assumed that the wall response would be flexure dominated due to their aspect ratios being greater than 2.5. However, the shear deformation contributed significantly to the lateral displacement of these walls, particularly at the first floor level. Finally, the effects of shear lag were ignored in the pre-test analysis of NTW1. While this approach did not significantly affect the global force-displacement response, the accuracy of the local responses such as the strains and location of the neutral axis in the critical region of the walls was compromised. The post-test analysis of NTW1 corrected these deficiencies by incorporating the modified Chang and Mander concrete model, shear behavior in the beam-column element, and strain variation in the flange due to shear lag. These modifications significantly improved the accuracy of the simulation of NTW1 as it was found both the global and local responses of NTW1 were closely compared with experimental results.

The post-test model of NTW1 included four beam-column elements to model the four stories of the test specimen and one interface element for the wall-to-foundation connection. Both the beam-column and interface elements used concrete and steel fibers to discretize the cross-section. The uniaxial material models for the fiber sections were defined using stress-strain relationships for the concrete and longitudinal reinforcement, and stress-slip relationships for the strain penetration material.

The second T-wall, NTW2, provided the opportunity to learn from the post-testing analysis of NTW1 and attempt to predict the response of NTW2 for the proposed multi-directional loading. The response of NTW2 was simulated using four beam-column elements to simulate the two story wall specimen and one interface element to capture the strain penetration effects at the wall-to-foundation connection. The longitudinal reinforcement was spliced at the second floor level in the test specimen, requiring three beam-column elements be used for the second floor in the OpenSees model. Fiber sections were used to represent the cross-section details of the wall while the shear-distortion response was aggregated onto the section using a pinching model. Using the observed shear behavior of NTW1 and a new fiber section that included the shear lag effects, the response of NTW2 was predicted prior to the test. When compared to the experimental results, the force-displacement response was found to be well predicted in the web direction; however, the response was less accurately predicted in the flange direction. The discrepancy in the flange direction response was due to inaccurate simulation of the strain distribution in the flange due to shear lag and the shear deformations. Both of these features in NTW2 were affected by the use of distributed longitudinal steel instead of concentrating them in the boundary elements of the flange as used in NTW1.

Finally, a parametric study on a slice of the prototype building was conducted under real-time earthquake load to understand some issues that arouse during the design of the test specimen. The building slice was subjected to monotonic and dynamic loading. The study provided guidance for distributing the base shear to each T-wall in a wall pair as typically configured in building systems.

7.2 Conclusions on Modeling Reinforced Concrete Structural Walls

7.2.1 Global Response to Multidirectional Loading

The beam-column elements with fiber sections adequately simulated the response of the T-walls subjected to the multi-directional loading. The force-displacement response at the top of the wall was satisfactorily captured by the post-test analysis conducted for NTW1 and by the pre-test analysis of NTW2, both of which are discussed in detail below. In each of these models, an improved concrete hysteretic model and a strain penetration model, which implemented into OpenSees as part of this study, were incorporated. In addition, the models accounted for the shear lag effects and shear deformation as accurately as possible within the current capabilities of OpenSees.

The model of NTW1 yielded a very good simulation of the force-displacement response, giving forces within 5 to 10% of the measured lateral force resistance for a given displacement in both the flange and web directions. The hourglass and pentagon load paths chosen to investigate the wall behavior to complex multi-directional loads were well simulated by the analysis model, in terms of the lateral force resistance and stiffness. The two dimensional force surfaces generated by the analysis model for the elastic and inelastic multidirectional displacement paths were compared to the experimental results, and they were found to be within 5-15% of the measured values.

The lateral displacement response of NTW1 was decomposed into the contributions due to flexural deformation, shear deformation, and strain penetration. The flexural component was particularly well captured by the analysis model; the analysis and experiment both determined the flexural component to contribute 84% of the lateral deformation for the flange-in-compression direction and 85% for the flange-in-tension direction. The strain penetration was captured satisfactorily. However, the analytical model for the slip versus bar stress could be improved, which would lead to an improved simulation of the strain penetration component. The experimental data showed that the strain penetration contribution to the total lateral displacement was 4% in the flange-in-compression direction and 10% in the flange-in-tension direction, while the analysis showed an 8% contribution in both directions. The shear deformation contribution was the least accurately modeled, which requires further improvements as found from the analysis of the rectangular concrete walls. The test data revealed that the contribution of shear deformation to the total lateral displacement was 12% in the flange-in-compression direction and 5% in the flange-in-tension direction. However, the shear contribution in the analysis was found to be about 8% in the flange-in-compression direction and 7% in the flange-in-tension direction at the peak displacements. Additionally, the material model used in this study to capture the shear-distortion behavior is difficult to use and its limited capabilities do not facilitate accurate capturing of the unloading and reloading portions of the shear response. A material model that is specifically designed to model the shear-distortion response of reinforced concrete flexural members would lead to an increased accuracy of the shear and total responses of concrete walls in OpenSees. The total displacement could not be decomposed into different components for the flange direction, because the shear of the flange was not measured above the second floor. Analytically, the contribution of shear to the total displacement was 36% indicating that shear played a larger role in the flange direction response than in the web direction response.

Using the material information available prior to or on day of testing, the analysis model of NTW2 was found to predict the force-displacement response within 15-25% of the measured experimental results. The OpenSees prediction did not capture the stiffness of the wall as accurately as it did for NTW1; however, this was due to NTW2 having a different shear stiffness than NTW1 resulting from minimizing the amount of longitudinal reinforcement in the boundary elements of the flange. Overall, the web direction force-displacement response was predicted within 10% of the experimental response, while the flange direction response was over predicted by as much as 25% at some peak displacements. Similar trends were reflected when the response of the wall to the multidirectional load paths were compared to the experimental results. In the web direction, the analysis predicted the forces within 5 to 10 %, while in the flange direction the analysis over predicted the lateral force resistance by as much as 25%.

Modeling the shear lag effects and shear response of NTW2 based on the observed NTW1 response and the observed difference in the shear stiffness between those of NTW2 and NTW1 affected the results in two ways. First, NTW2 showed a stiffer shear deformation response in the web and flange directions than that used in the OpenSees analysis, leading to under prediction of lateral force resistance in the web direction. Second, the increased shear stiffness of the flange due to the distributed longitudinal reinforcement decreased the effects of shear lag in NTW2, thereby increasing the stiffness of the wall in the flange-in-tension direction loading than that expected from the OpenSees results. The decreased effects of shear lag in NTW2 also led to the over prediction of the flange direction response, due to the under prediction of damage to the flange tips.

7.2.2 Local Response to Multidirectional Loading

Accuracy of the analysis models cannot be sufficiently evaluated based only on the comparison of global responses. Appropriate local response parameters should also be examined. Accurate simulation of the local response is important for two reasons. First, the local response provides a better measure of damage in the structure and in performance-based design methods, which are being more frequently used; design limits are specified using local response parameters. Second, accurate prediction of the local response is a better measure of the capability of the modeling approach. Predicting the local response accurately requires the analytical model to properly model the various components of lateral displacement. Compensation of errors associated with predicting different displacement components may lead to accurate prediction of the global force-displacement of a structure; however, the local response will not be accurate.

The local responses of NTW1 were well captured by the post-test analysis. The calculated neutral axis depth and section curvature at the wall base were satisfactory in both the web and flange directions loading upto the theoretical first yield displacements. The location of the neutral axis was found to be within 0.5 inch of the location determined from the recorded strains for both the web and flange directions, this corresponded to an error of approximately 5%. The strains in the longitudinal reinforcement were simulated within 10 to 20% by the analysis.

In comparison to NTW1, the local responses of NTW2 were not as well predicted. The strain profile and the neutral axis depth were accurately predicted in the flange-in-compression loading direction. The location of the neutral axis was predicted within one-half inch. This direction was the best simulated by the analysis due to not being influenced by the effects of shear lag. In the flange-in-tension direction, the location of the neutral axis was incorrectly predicted, and was off by as much as 10 inches. Such a large error is misleading because it is due to the combination of the discrepancies in the shear deformation and shear lag effects. Improved simulation of these two effects would likely have increased the accuracy of the local response to be similar to that observed for the post-test analysis of NTW1. The inadequate simulation of the shear lag effects and shear deformation primarily led to relatively poor prediction of the local responses in that direction. The post-test analysis of NTW1 and accurate prediction of the flange-in-compression response of NTW2 indicate that, when the shear lag and shear deformation are accurately simulated, the prediction of global and local responses of non-rectangular walls will be greatly improved when the modeling technique used in this study is adopted.

7.2.3 Parametric Study

The codes used in current seismic design practice allow designers to determine the total base shear force that should be resisted by the structure for a design level event. However, little guidance is given on how the forces should be distributed to the different elements in the lateral force resisting system. For buildings with T-walls, this is particularly difficult because T-walls are used in pairs. When the walls are loaded for seismic action in the the web direction, the flange of the leading wall would be in compression and the trailing wall would be subjected to the flange in tension.. The significant difference in the force-displacement response of the two walls in the same loading direction makes the distribution of the force to each wall in the pair unclear. During the design phase of the prototype building, this issue was discussed and depending on the method used to determine the distribution, four or five pairs of walls were required in the prototype building, which clearly has cost implications.

The parametric study conducted as part of this investigation showed that distributing the base shear resistance based on the ultimate bending moment capacity of the two walls was the most appropriate approach and was confirmed by the distribution observed from both a monotonic pushover and dynamic analyses of the building slice. This moment capacity calculation should include the effects of confinement of the concrete, strain hardening of the longitudinal reinforcement, and the effects of shear lag. While moment capacity typically used in design uses assumptions that include plane sections remain plane, neglecting the confinement effects on concrete strength, and the assumption of elastic perfectly plastic steel behavior for the steel reinforcement, the behavior in the inelastic response region will be controlled by the ultimate moment capacity including the effects of strain hardening, concrete confinement and shear lag.. In the case of the prototype building, distributing the base shear based on the ultimate moment capacity would have led to 4 pairs of wall being required, increasing the economy of the lateral fore resisting system, while maintaining the same level of performance as the building with 5 pairs of walls..

7.3 Recommendations for Modeling Structural Walls

Based on the investigation in this report, the following recommendations are made for the simulation of structural walls and wall systems subjected to multidirectional or seismic loading:

- Beam-column elements with fiber sections can accurately simulate the response of structural walls to multidirectional loading and capture the contribution of various lateral deformation components of nonrectangular walls. The beam-column elements offer significant advantages due to their ease of use, computational efficiency, familiarity to engineering community, and ease of model construction.
- The effects of shear deformation and strain penetration should be accurately modeled in nonrectangular walls. In addition, the effects of shear lag should be included in the analysis of nonrectangular walls. Various material models and sections are becoming available in OpenSees that enable these capabilities.
- The material models selected for the analysis dictate the accuracy of hysteretic simulation of the wall behavior. The modified Chang and Mander concrete model introduced in this report is appropriate for use in the simulation of structural walls subjected to multidirectional loads. Similarly the model proposed by Zhao and Sritharan (2007) is appropriate for accounting for the effects of strain penetration.
- The response of the wall will be significantly influenced by the splice details used for the longitudinal reinforcement. Therefore, the splices of the wall

reinforcement should be appropriately modeled to accurately capture the global and local wall responses. Conventional lap splices may be modeled as an equivalent bar with varying cross sectional area along the splice length

7.4 Recommendations for Future Research

The investigation presented in this report has addressed several challenges associated with the analytical simulation of nonrectangular walls subjected to multidirectional loading. A number of issues have become apparent through the course of this investigation, which deserve further investigation as detailed below.

- Shear lag, which is dictated by the shear stiffness of the free flange, has a significant influence on the stiffness of the nonrectangular walls in both the flange-in-tension and flange direction responses. A combination of analytical and experimental investigation on how the shear stiffness of the flange influences the shape of the shear lag function and development of a function that is appropriate for implementation in a fiber section would be appropriate .
- Development of a material model that is appropriate for simulating the shear-distortion of reinforced concrete walls and columns is necessary for OpenSees. It is also important to address the effects of flexure-shear interaction in this model development.
- More data are needed to refine the shape of the bar stress vs. loaded end slip for the bond slip material model. While the indication from this study is that the method used for capturing the strain penetration effects is appropriate, accuracy of the analysis can be improved by improving the stress vs. slip relationship.

References

[1] National Information Service for Earthquake Engineering, University of California, Berkeley. Aug. 2005 <http://nisee.berkeley.edu/images/servlet/EqiisDetail?slide=S3364>

[2] National Information Service for Earthquake Engineering, University of California, Berkeley. Aug. 2005 <http://nisee.berkeley.edu/images/servlet/EqiisDetail?slide=S343>

[3] National Information Service for Earthquake Engineering, University of California, Berkeley. Aug. 2005 <http://nisee.berkeley.edu/images/servlet/EqiisDetail?slide=S3309>

ACI Cpmmittee 318, [2002] "Building Code Requirements for Structural Concrete," American Concrete Institute, Farmington Hills, Michigan, 2002.

Belbari, A. and Hsu, T. [1991] "Constitutive Laws of Concrete in Tension and Reinforcing Bars Stiffened By Concrete," *ACI Structural Journal,* Vol. 94, No. 4, pp. 465-474.

Bolander, J., and Wright, J. [1991] "Finite Element Modeling of Shear Wall Cominate Buildings" *Journal of Structural Engineering,* Vol. 117, No. 6, pp. 1719-1739

Bruggen, B. L. [2009] "Performance of T-shaped reinforced concrete shear walls under multi directional loading", Doctoral dissertation (under preparation), University of Minnesota, MN.

Chang, G.A., and Mander, J.B. [1994] "Seismic Energy Based Fatigue Damage Ananlysis of Bridge Columns: Part 1 – Evaluation of Seismic Capacity," NCEER Technical Report No. NCEER-94-0006, State University of New York, Buffalo, NY.

Chang, s. [2004] "Shear Lag Effect in Simply Supported Prestressed Concrete Box Girders" *Journal of Bridge Engineering,* Vol. 9, No. 2, pp. 178-184.

Coull, A. and Bose, B. [1975] "Simplified analysis of frame-tube structures," *Journal of the Structural Division,* Vol. 117, No. 12, pp. 3623-3644.

Coull, A., and Abu El Magd, S., [1980] "Analysis of wide flanged shearwall structures," *Reinforced Concrete Structures Subjected to Wind and Earthquake Forces,* ACI Special Publication 65, Paper No. SP63-23, pp. 575-607.

Dazio, A. [2006] "Some Aspects of RC Walls Modeling using Fiber Elements," *Proceedings of the NEES/UCSD Workshop Analytical Model of Reinforced Concrete Walls,* San Diego, CA December, 2006.

DeFries-Skene, A. and Scordelis, A. [1964] "Direct stiffness solution for folded plates," *Journal of the Structural Division,* Vol. 90 No. 4, pp. 15-48.

Deshmukh, K., Thiagarajan, G., and Heausler, T. [2006] "Numerical Modeling of Seven Story Reinforced Model Using SAP," *NEES/UCSD Workshop on Analytical Modeling of Reinforced Concrete Walls*, San Deigo, CA December 2006.

Evans, H., and Taherian, A. [1977] "The prediction of shear lag effect in box girders," *Proceedings of the Institution of Civil Engineers*, Part 2, 69, Thomas Telford Services Ltd., London pg. 1065-1075.

Fischinger, M., and Isakovic, T. [2006] "NEES Blind Prediction Testing on RC Wall Building Slice, Multiple-Vertical-Line-Element Model," *Proceedings of the NEES/UCSD Workshop Analytical Model of Reinforced Concrete Walls,* San Diego, CA December, 2006.

Foutch, D. and and Chang, P. [1982] "A shear lag anomaly," *Journal of Structural Engineering,* Vol. 108, No. 7, pp. 1653-1658.

Goodsir, W.J. [1985] "The Design of Coupled Frame-Wall Structures for Seismic Actions," Research Report 85-8, Department of Civil Engineering, University of Canterbury, Christchurch, New Zealand, August 1985.

Grange, S., Mazars, J., and Koronis, P. [2006] "Seven-Story Building Slice Earthquake Blind Prediction Contest: A Simplified Model Using Multifiber Timoshenko Beams" *Proceedings of the NEES/UCSD Workshop Analytical Model of Reinforced Concrete Walls,* San Diego, CA December, 2006.

Hachem, M. [2006] "Earthquake Analysis of Seven-Story Shear Wall Building using ADINA," *NEES/UCSD Workshop on Analytical Modeling of Reinforced Concrete Walls,* San Deigo, CA December 2006.

Haji-Kazemi, H. and Company, M. [2002] "Exact Method of Analysis of Shear Lag in Framed Tube Structures" *The Structural Design of Tall Buildings*, Vol. 11, pp. 375-388.

International Building Code (IBC) [2003] International Code Council, Virgina, USA, 331-377

Johnson, B. [2007] "Longitudinal Reinforcement anchorage Detailing effects on RC shear wall Behavior", Master of Science Thesis, University of Minnesota, 391 pp.

Kelly, T. [2006] "A Blind Prediction Test of Nonlinear Analysis Procedures for Reinforced Concrete Shear Walls," *Bulletin of the New Zealand Society for Earthquake Engineering,* Vol. 40, No. 4. pp. 142-158.

Kelly, T. [2006] "NCEES Blind Prediction Test: Practitioner Entry From Holmes

Consulting Group, New Zealand," *NEES/UCSD Workshop on Analytical Modeling of Reinforced Concrete Walls,* San Deigo, CA December 2006.

Mander, J.B., Priestley, M.J.N., and Park, R., [1988] "Theoretical Stress-Strain Model for Confined Concrete," *Journal of Structural Engineering,* American Society of Civil Engineering, Vol. 114, No. 8.

Martinelli, P., and Fillipou, F. [2006] *"Numerical Simulation of the Shake Table Test of a Full Scale, Seven Story Shear Wall Specimen," Proceedings of the NEES/UCSD Workshop Analytical Model of Reinforced Concrete Walls, San Diego,* CA December, 2006.

Mazzoni, S., McKenna, F., Scott, M.H., Fenves, G.L. [2006] "Open System for Earthquake Engineering Simulation," Pacific Earthquake Engineering Research Center, University of California, Berkeley, California, Ver. 1.7.4.

Moaveni, B., He, X., Conte, J., and Restrepo, J. [2006] "System Identification of a Seven-Story Reinforced Concrete Shear Wall Building Slice Tested on the UCSD-NEES Shake Table," *NEES/UCSD Workshop on Analytical Modeling of Reinforced Concrete Walls,* San Deigo, CA December 2006.

Moffatt, K., and Dowling, P., [1975] "Shear lag in steel box girder bridges," *The Structural Engineer,* Vol. 53, No. 10, pp. 439-448.

Neuenhofer, A., and Filippou, F.C. [1997] "Evaluation of Nonlinear Frame Finite-Element Models," *ASCE Journal of Structural Engineering,* Vol. 123, No. 7, pp. 958-966.

Oesterle, R.G., Aristizabal-Ochoa, J.D., Fiorato, A.E., Russel, H.E., and Corley, W.G., "Earthquake Resistant Structural Walls – Tests of Isolated Walls – Phase II," Report to the National Science Foundation, Construction Technology Laboratories, Portanland Cement Association, Skokie, Illinois, October 1979.

Orakcal, K., and Wallace, J.W. [2006] "Flexural Modeling of Reinforced Concrete Walls – Experimental Verification," *ACI Structural Journal,* Vol. 103, No. 2, pp. 196-205.

Orakcal, K., Wallace, J.W., and Conte, J.P., [2004] "Nonlinear Modeling and Analysis of Slender Reinforced Concrete Walls,*"ACI Structural Journal,* Vol. 101, No. 5, pp. 688-698.

Palermo, D., and Vecchio, F.J. [2004] "Compression Field Modeling of Reinforced Concrete Subjected to Reversed Loading: Verification," *ACI Structural Journal,* Vol. 101, No. 2, pp.155-164.

Pang, X. and Hsu, T. [1992] "Constitutive Laws of Reinforced Concrete in Shear," Research Report UHCEE92-1, Department of Civil Engineering, University of Houstan, TX.

Park, R., and Paulay, T. [1975] “Reinforced Concrete Structures,” New York: John Wiley and Sons.

Priestley, M., Seible, F., and Calvi, G. [1996] “Seismic Design and Retrofit of Bridges,” New York: Wiley-Interscience.

Rahman, A., and Sritharan, S. [2006] “An evaluation of force-based design vs. displacement-based design of jointed precast post-tensioned wall systems,” *Earthquake Engineering and Engineering Vibration*, Vol. 5, No. 2, pp. 285-296.

Seismology Committee [1999] “Recommended Lateral Force Requirements and Commentary (Blue Book),” Structural Engineers Association of California (SEAOC), California, USA.

Sittipunt, C., and Wood, S.L. [1993] “Finite Element Analysis of Reinforced Concrete Shear Walls,” Report to the National Science Foundation, Department of Civil Engineering, University of Illinois at Urbana-Champaign, December 1993.

Song, Q., and Scordelis, A., [1990a] “Formulas for shear lag effect of T-, I-, and box beams,” Journal of Structural Engineering, Vol. 116, No. 5, pp. 1306-1318.

Song, Q., and Scordelis, A., [1990b] “Shear lag analysis of T-, I-, and box beams,” *Journal of Structural Engineering*, Vol. 116, No. 5, pp. 1290-1305.

Taucer, Fabio F, E Spacone, FC Filippou. [1991] “A Fiber Beam-Column Element for Seismic Response Analysis of Reinforced Concrete Structures. Report No. UCB/EERC-91/17,” Earthquake Engineering Research Center, College of Engineering, University of California, Berkeley.

Thomsen, J.H., and Wallace, J.W. [1995] “Displacement-Based Design of RC Structural Walls: An Experimental Investigation of Walls with Rectangular and T-Shaped Cross-Sections,” Report to the National Science Foundation, Department of Civil Engineering, Clarkson University, Potsdam, New York.

Wallace, J.W., and Moehle, J.P. [1989] “BIAX: a computer program for the analysis of reinforced concrete sections, Report No. UCB/SEMM-1989/12,” Earthquake Engineering Research Center, College of Engineering, University of California, Berkeley.

Zhao, J., and Sritharan, S. [2007] “Modeling of Strain Penetration Effects in Fiber-Based Analysis of Reinforced Concrete Structures,” *ACI Structural Journal*, Vol. 104, No. 2, pp. 133-141.

Appendix: UCSD Seven Story Building Slice Analysis

A.1 Background:

The NEES site at the University of California: San Diego (UCSD) is a large scale outdoor shake table. The NEES/LHP Outdoor Shake table is a single degree-of-freedom system, that can be expanded to a six degree-of-freedom system. The shake table is 25 feet (7.6m) wide by 40 feet (12.2m) long, and the current specifications for facility are a ±30 in. (0.75m) stroke, a peak horizontal velocity of 6 ft/s (1.8m/s), horizontal force capacity of 1530 k (6.8MN), overturning moment of 37,000 k-ft (50MN-m) for a 800 k (3.6N) specimen, and a vertical payload capacity of 4500 k (20MN). The frequency range for testing is 0-20 Hz. The facility is the largest shake table outside of Japan and the first outdoor shake table.

In the fall of 2005, a portion of a full-scale seven-story concrete building, which hereafter is referred to as the test building, was constructed and tested under unidirectional earthquake motions using the UCSD shake table. A capacity-based design approach was used to determine the structural details of the building elements, which led to smaller member dimensions and reduced amounts of reinforcing steel than those typically required by a traditional design code approach (Restrepo, 2006). The smaller member sizes and reduced reinforcing steel created a more flexible structure that was both economical and easier to construct, while satisfying criteria to produce ductile response for the building under the selected seismic input motions.

Figures A-1 and A-2 show, respectively, the floor plan and elevation of the test building which consisted of a 16 ft (4.88 m) long cast-in-place (CIP) flange wall, a 12 ft. (3.66 m) long CIP web wall, and a C-shaped precast, segmental pier with unbonded post-tensioning. The web wall primarily provided the lateral force resistance in the earthquake loading direction, while the flange wall and precast pier primarily provided transverse stability and torsional resistance for the test building. In addition, four pin-ended Dywidag prestressing bars, 1.75 in. (44.5 mm) diameter for the first story and 1 in. (25.4 mm) diameter for the second story and above, were used as columns within each story.

The Dywidag bars were grouted inside 4 in. (101.6 mm) diameter, 5/16 in. (8.6 mm) thick steel pipes to prevent them from experiencing buckling. Due to the pin-ended connections, these columns were assumed in design to act as gravity columns and not to contribute to lateral force resistance. The floor at each level was 12 ft (3.66 m) wide, 26 ft 8 in. (8.13 m) long, and 8 in. (203.2 mm) thick reinforced concrete slab, and was supported by the web wall and four steel columns.

Both the flange and web walls had fixed connections to their shake table, while the precast pier connection to the shake table was designed to act as a pin in the loading direction while providing large moment resistance in the orthogonal direction. This was achieved by orienting the post-tensioning tie-downs to the shake table in the direction orthogonal to the direction of the shaking such that it led to insignificant moment resistance in the direction of loading. The flange wall and the precast pier were designed to have pin connections to the floor slab. Figure A-1 shows the link slab connecting the web wall to the flange wall. The link slab incorporated two 152.4 mm deep by 50.8 mm wide slots in the slab near the flange wall to accomplish the pin connection to the main floor slab. The pin connection between the pier and the floor slab was accomplished by using steel angles bolted to the floor slab and precast pier. The bolted connections and the limited moment capacity of the angles prevented the transfer of moment from the main floor slab to the pier. Figure A-3 shows a picture of the 7-story building slice before any testing on the shake table.

The shake table testing of the building included several input motions, which were: one low amplitude white noise, three low intensity earthquakes, and one high intensity earthquake. The low intensity earthquake records chosen were the longitudinal (EQ1) and transverse (EQ2) components from the 1971 San Fernando earthquake recorded at site: *vnuy*, and the longitudinal component from the 1994 Northridge earthquake at site: *whox* (EQ3). The high intensity record was the 360° component taken from *Sylmar Olive View Med* (EQ4) that was recorded in the 1994 Northridge earthquake located near the epicenter of the earthquake [NEES7Story, 2006]. The strongest 30 seconds of ground motions EQ1, EQ2, EQ3, and EQ4 are shown in Figure A-4. The input ground motions for the blind prediction were given at both 50 and 240 Hz; the 50 Hz motions were selected for the dynamic analyses reported in this paper. The low intensity earthquakes were expected to cause limited damage to the test building while the high intensity earthquake was anticipated to cause significant damage to the building. In all cases, the plastic hinge and the associated damage was expected to concentrate in the first floor level of the test building. The structure was tested and the results were kept confidential while the blind prediction competition was conducted. The contest called for a prediction of the maximum values of the story shear forces, overturning moments, inter-story drifts, and story displacements.

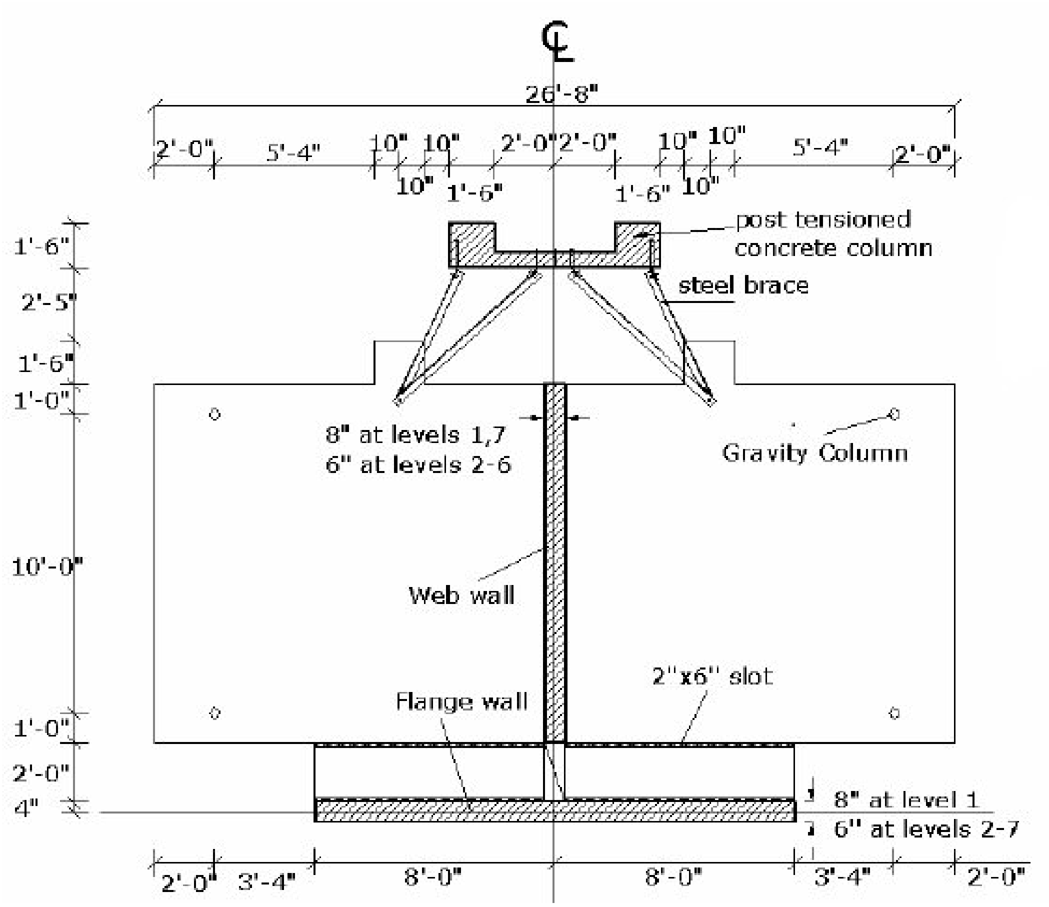

Figure A-1: 7-Story Building Slice Floor plan [Panagiotou et al., 2006]

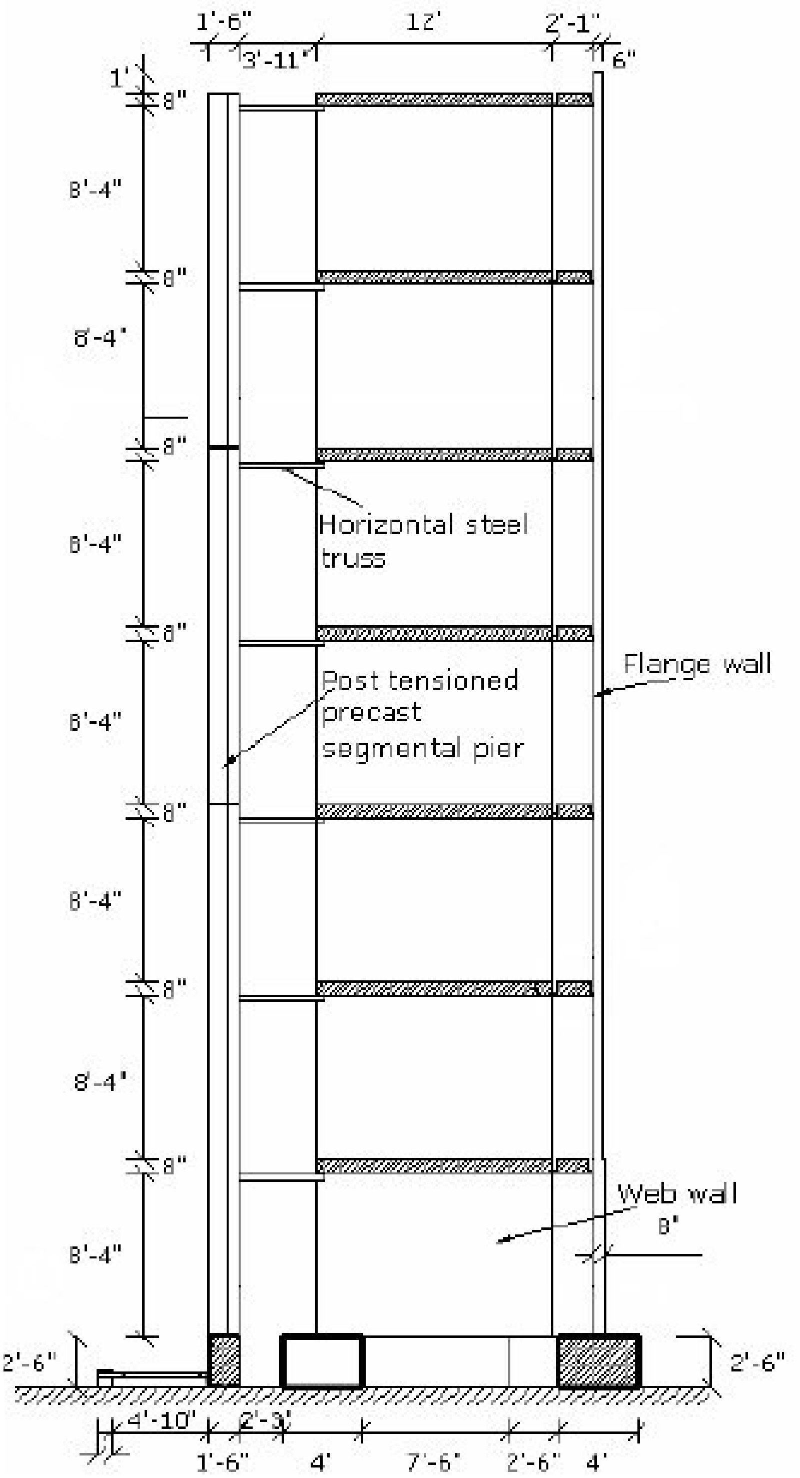

Figure A-2: 7-Story Building Slice Elevation [Panagiotou et al., 2006]

Figure A-3: Constructed Building Slice [2]

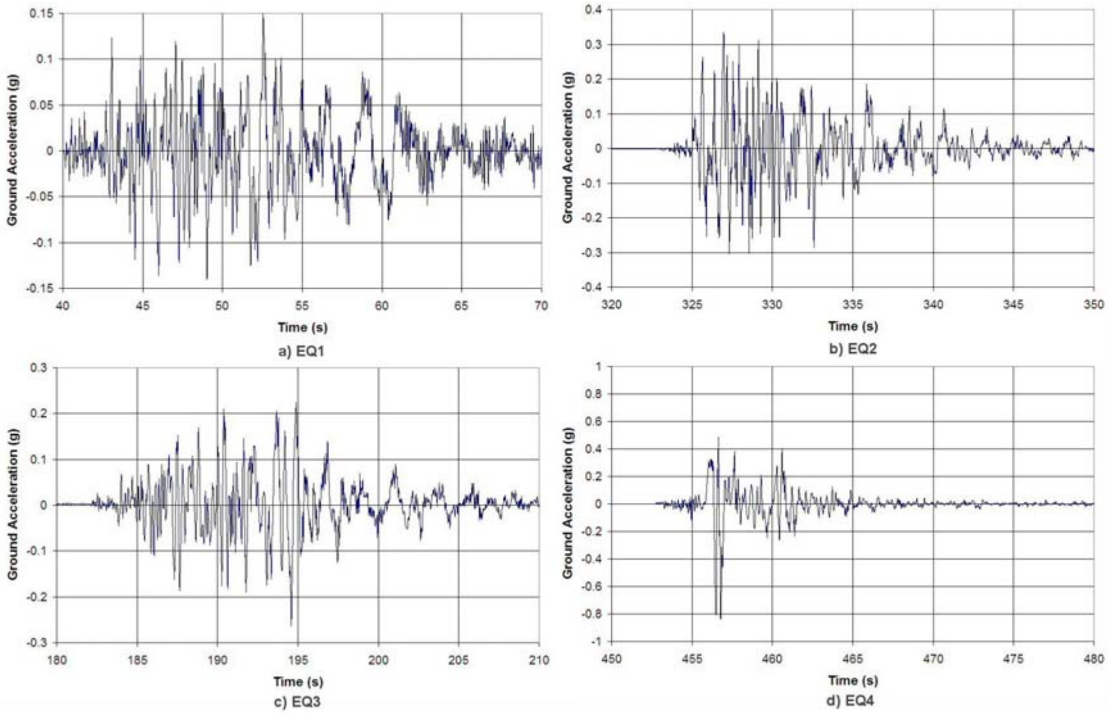

a) EQ1 b) EQ2 c) EQ3 d) EQ4

Figure A-4: Earthquake Input Motions for Shake Table Testing.

A.2 Blind Prediction Contest:

The blind prediction contests required contestants to predict the values of certain forces and drifts of the structure given the input ground motions. The contestants could use any method for generating their prediction, the contestants would be broken into 3 different categories: engineering practitioner, academic and research community, and undergraduate students. A winner would be determined for each category based on the best prediction of the various forces and displacements. The competition required that the contestant submit the absolute maximum for the following values: system overturning moment, system shear force, horizontal floor acceleration, lateral displacement, interstory drift ratio, residual displacements following the testing, and maximum strain in the steel and concrete at 40 in. above the base.

The contestants were given as much information as possible to use in the prediction of the response. A website was made available where contestants could download: the material properties for the concrete and steel used in the construction of the building slice, dynamic properties of the shake table, table of weights of the structure, and the input ground motion used in the testing. Contestants could submit questions and answers would be periodically posted on the website for all contestants. Contestants had approximately 2 months to generate and submit their predictions. The model used for the blind prediction, hereafter referred to as the original model, used OpenSees [Mazzoni *et al.*, 2004] with fiber sections. Other participants used various modeling approaches including: 3D solid elements, plain stress elements, multiple vertical line elements, and elastic beam elements [Restrepo, 2006].

A.3 Description of Original Analytical Model:

The analysis model used for the blind prediction of the behavior of the test building was created in a custom compiled version of OpenSees (Mazzoni et al., 2004) that included the strain penetration model developed by Zhao and Sritharan (2006). The model of the test building was created to balance the need for accuracy in the blind prediction contest with the desire for a relatively simple model that would run quickly and could be built based on the geometry and realistic engineering properties. Based on the previous work done in modeling the response of structural walls to cyclic displacements in an ongoing PreNEESR project (Sritharan et al., 2005), the flange and web walls of the test building were modeled using fiber-based beam-column elements. Because of problems in obtaining compatible forces and deformations for the force-based beam-columns modeling the flange and web walls in the dynamic analysis, displacement-based beam-column elements were chosen instead of the force-based beam-column elements that have been used in the analysis of structural walls in the PreNEESR project. The beam-column elements were assigned fiber sections that discretely model the reinforcement as well as confined and unconfined concrete regions. The fibers representing the longitudinal reinforcement in the various elements were located according to the as-built drawings shown in Figures 4a and 4b, which depict the dimensions and reinforcement details of the flange and web walls at the first floor and for floors two through seven, respectively. The confined concrete properties were calculated using the given transverse reinforcement details and the confined concrete model proposed by Mander *et al.* [1988], and were assigned to the fibers for the appropriate regions of the cross-sections for the first story of the building model. The upper stories had no confinement reinforcement and thus the concrete was modeled using unconfined concrete fibers. Material models "Steel02" and "Concrete03" in OpenSees were used to model the reinforcing steel and concrete behavior. The properties for the unconfined concrete and steel reinforcement material models were chosen to closely match the experimental stress-strain behavior established for these materials. Figures A-7a and A-7b show the measured and modeled monotonic stress-strain curves for the unconfined concrete in the first story walls, and the #4 longitudinal bars used in the flange and web walls, respectively. It can be seen that the chosen concrete model adequately captures the unconfined concrete behavior. The behavior of the reinforcing steel was accurately modeled up to a strain of about 0.06 and significant discrepancies between measured and modeled behaviors expected at larger strains. To account for the low cycle fatigue behavior, the fracture strain for the longitudinal reinforcement was taken as 0.06 and thus the steel reinforcement strains were limited to 0.06 during the analysis. The tension capacity of concrete was modeled using a peak tensile strength of $7.5\sqrt{f'_c}$ with nonlinear post-peak softening following the University of Houston model presented by Hsu [1993], where f'_c is in psi. Figure A-7c and A-7d show the cyclic response characteristics of the steel and concrete material models, while the parameters used for the concrete and reinforcement material models in the analysis are given in Tables A-1 and A-2, respectively.

The base blocks of the test building were rigidly connected to the shake table and therefore the analysis model assumed no relative movement between the base block and shake table. Furthermore, the table was assumed to remain rigid without undergoing any deformations. Consequently, fully fixed boundary conditions were applied at the base of the walls in the analysis model.

The strain penetration effects resulting from anchoring the wall longitudinal reinforcing bars into the base block were included in the model using a zero-length section element with the same cross-section as the wall elements above it. However, the steel material model in this element was replaced with the strain penetration model developed by Zhao and Sritharan [2007] which describes the total bar slip due to strain penetration as a function of stress in the bar. This accounted for the additional flexibility resulting from the wall end rotation due to penetration of strain along the longitudinal reinforcement into the foundation block. The bottom node on the interface element was fixed for all degrees-of-freedom while the top node was only restrained against lateral translation. The bottom ends of the beam-column elements modeling the first story flange and web walls of the building were connected to the top nodes of the interface elements.

The unbonded post-tensioned pier was also modeled using displacement beam-column elements. Fiber sections were used to represent the cross-section of the pier, shown in Figure A-7, for the concrete and mild steel reinforcement that was discontinued above the base block. Anticipating primarily to respond in elastic manner, the post-tensioning rods were modeled using a truss element that was given an elastic perfectly plastic material model and an initial strain to simulate the effect of prestress. The truss element shared the node at the top and bottom of the beam-column element modeling precast piers. One problem with this approach is the post-tensioning rod did not bend with the pier along the height. The boundary condition at the base of the pier was assumed to be pinned and was free to rock at the connection between the pier and the base block during the excitation of the structure.

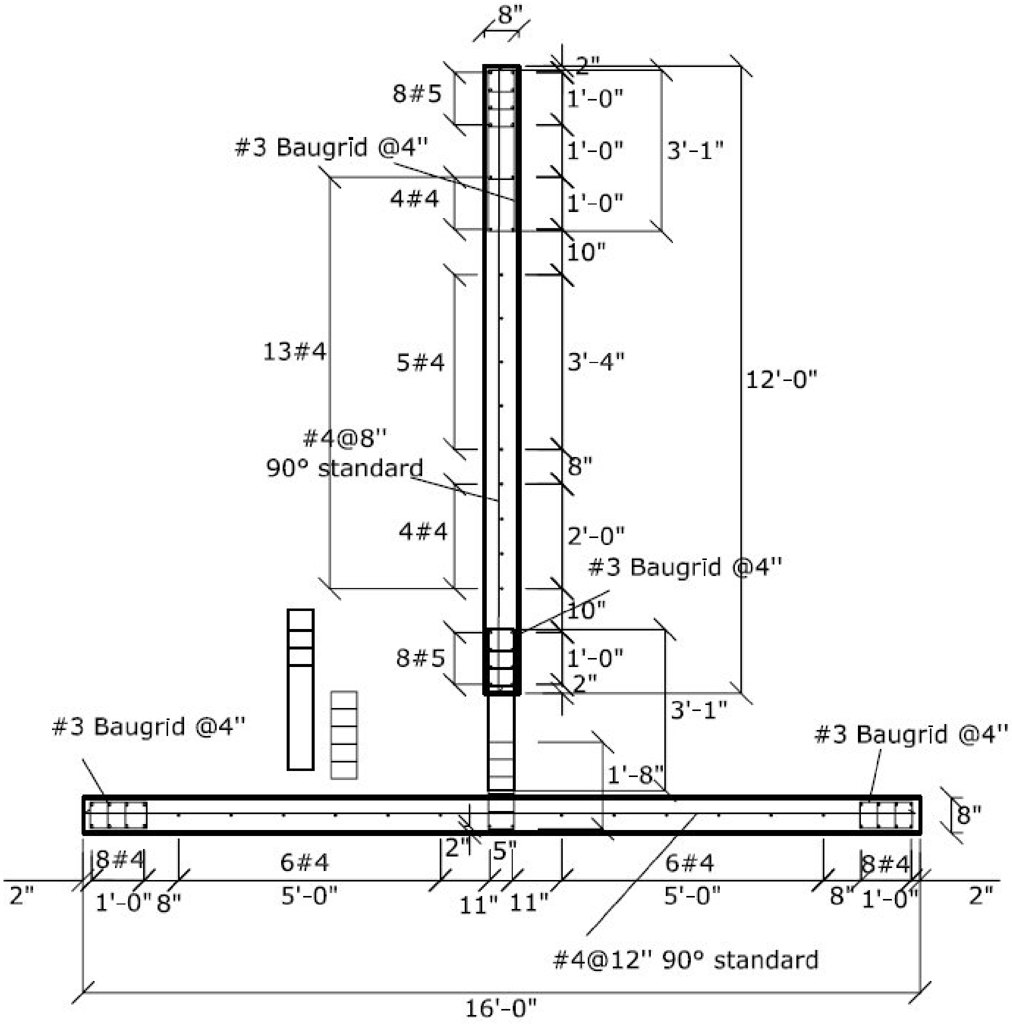

Figure A-5: Level 1 Wall Reinforcement Details [1]

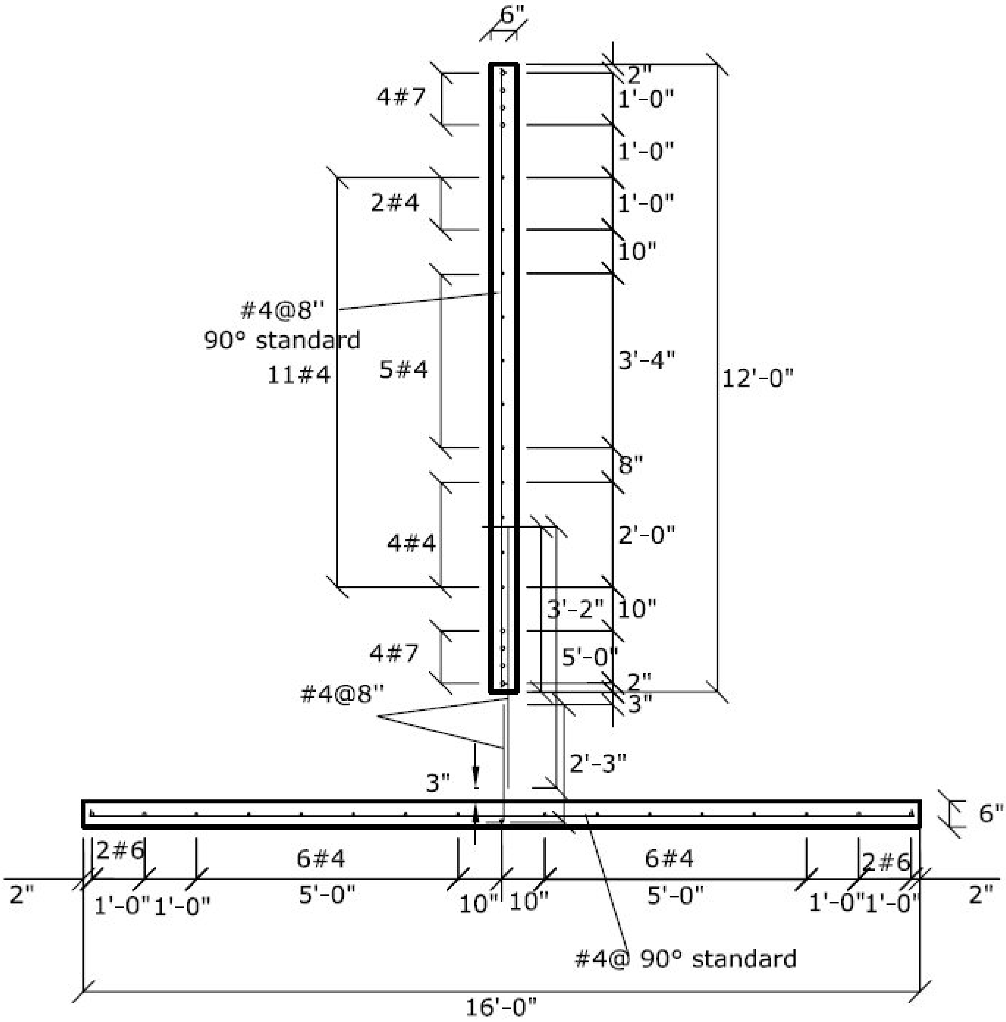

Figure A-6: Level 2-6 Wall Reinforcement Details [1]

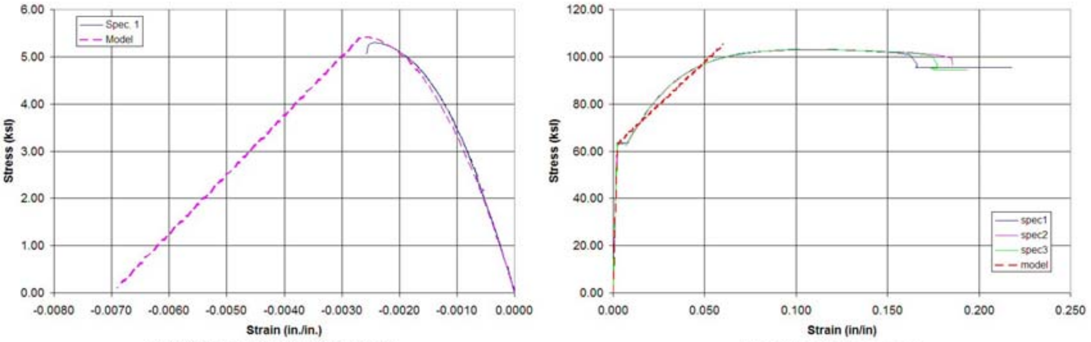

a) First Floor Unconfined Concrete

b) Wall #4 Reinforcement

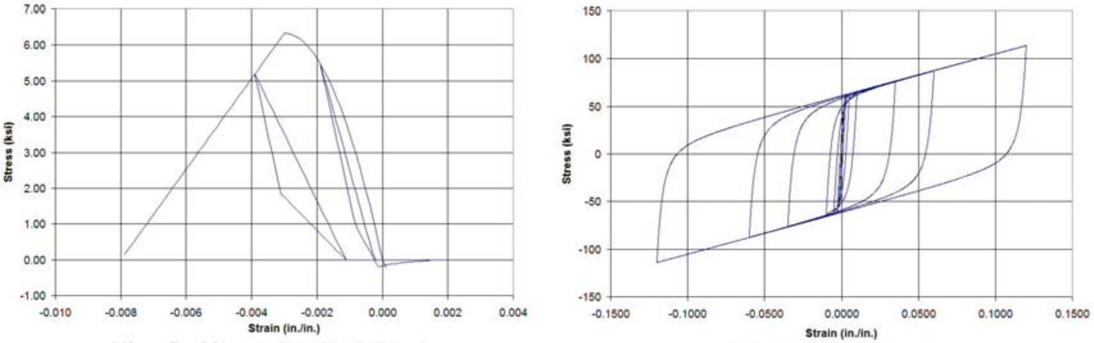

c) Unconfined Concrete Model Cyclic Behavior

d) Steel Model Cyclic Behavior

Figure A-7: Material Model Comparison

Table A-1: Nodal Gravity Forces and Masses

Location	Nodal Forces (kip)	Mass (kip*s^2/ft)
1st Floor Web Wall	10.4	0.323
1st Floor Flange Wall	13.87	0.431
2nd-6th Floor Web Wall	23.8	0.739
2nd-6th Floor Flange Wall	13.6	0.422
7th Floor Web Wall	16.0	0.497
7th Floor Flange Wall	4.8	0.149
1st-7th Floor Pier	8.125	0.252

Table A-2: Concrete Material Properties as defined in OpenSees

Location	Peak Compressive Stress (ksi)	Peak Compressive Strain (in/in)	Ultimate Compressive Stress (ksi)	Ultimate Compressive Strain (in/in)	Peak Tension Stress (ksi)	Peak Tension Strain (in/in)
First Floor Walls	5.427*	0.002664	0.0	0.007	0.626	0.000135
Second-Sixth Level Walls	5.697	0.002307	0.0	0.007	0.626	0.000144
Precast Segmental Pier	5.621	0.002375	0.0	0.007	0.626	0.000119
Slab Beams & Link Slab	5.427	0.002664	0.0	0.007	0.626	0.000136

* Based on the average response of tested concrete cylinders

Table A-3: Steel Material

Size & Location	Yield Stress (ksi)	Young's Modulus (ksi)	Strain Hardening Ratio
#4 – Flange and Web Walls	63.0*	29000	0.025
#5 – Flange and Web Walls	65.0*	29000	0.0225
#6 – Flange and Web Walls	69.0*	29000	0.025
#7 – Flange and Web Walls	67.0*	29000	0.025
#4- Precast Pier	67.0*	29000	0.025
#5 – Precast Pier	71.0*	29000	0.025
Prestressing	127.5*	29000	0.01
Gravity Columns	36.0*	29000	0.01

* Based in the average response of tested reinforcement bars

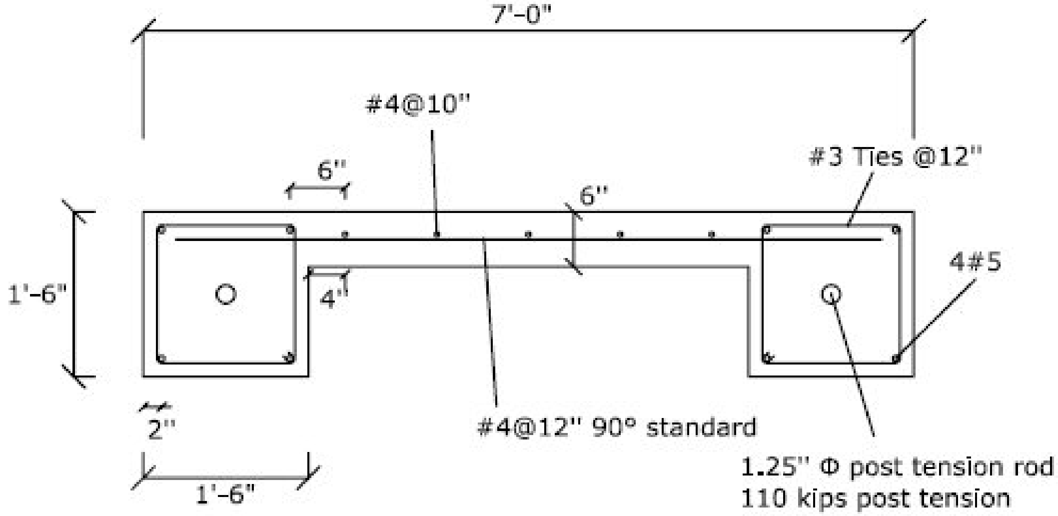

Figure A-8: Post-Tensioned Segmental Pier Cross Section [1]

The floor slab was assumed to act as an infinitely rigid diaphragm, which was achieved in the model by constraining the translational nodes of the flange wall, web wall, and the post-tensioned pier to have no relative lateral displacements. Because of the slots in the slab and the bracing struts, causing the flange wall and pier to be pin connected to the floor slab, a similar constraint was not imposed on the rotational degrees of freedom.

The seismic mass of the structure was lumped at the floor levels to simplify the model and speed up the analysis. The mass corresponding to each floor was calculated by determining the weight of the floor slab and one half story height of the flange wall, web wall, and pier above and below the floor, and concentrated at the floor level nodes. The weight of the structure was also applied as point loads on the nodes at each floor level to account for the gravity effects. The masses and point loads applied to the structure are shown in Table A-3.

In the analysis model, Rayleigh damping was used to capture effects of the viscous damping in the system. Two damping coefficients, α and β, are required in OpenSees to define the Rayliegh damping, with a number of options to define stiffness coefficient. The coefficient α is applied to the mass matrix for the system, while β is applied to the stiffness matrix to determine the damping. In a nonlinear system, the stiffness matrix used for calculating the damping matrix can have a significant impact on the results of the analysis. OpenSees provides three different options for the stiffness matrix to use in calculating the damping: the initial stiffness matrix, the stiffness matrix of the current time step, and the stiffness matrix for the last converged time step. OpenSees provides options to input coefficients for all three of the matrices; however, any of the coefficients can be zero. The α and β coefficients for the damping were selected so that damping stayed near 5% for periods in the range of 0.5 to 2.5 seconds, and the they were applied to the mass matrix and the initial stiffness matrix, respectively. This approach was to prevent the damping from becoming too large when the section cracks and reinforcement yields. Unaware that OpenSees will accept zero for a coefficient, a value of 0.001 was selected for the coefficient on the stiffness matrix for the current time step and the stiffness matrix for the last converged time step.

The input accelerations shown in Figure A-4 were applied to the base of the building model in the direction parallel to the web wall. Using the Newmark's constant average acceleration method for the integrator, the analysis was conducted at a time increment of 0.02 seconds to limit the amount of output that must be post-processed. However, when the analysis failed to converge 10 substeps were carried out at 0.002 seconds to find a solution, and then the time step was increased back to 0.02 seconds.

In order to account for the effects of accumulated structural damage on the response of the test building, all input motions were concatenated. Six seconds of zero ground acceleration was added between the earthquake records to allow the structure to come to rest prior to being subjected to the next base input motion. The low accelerations at the end of the ground motions combined with the six seconds of padding were adequate for the structure to return to rest. The total applied ground motion record to the test building was slightly more than 522 seconds long from start to finish.

A diagram delineating the original OpenSees model is shown in Figure A-8. The nodes used in the model are numbered from 1 through 26; the double nodes at the base of the wall are where the zero-length interface element was located to include the strain penetration into the base block.

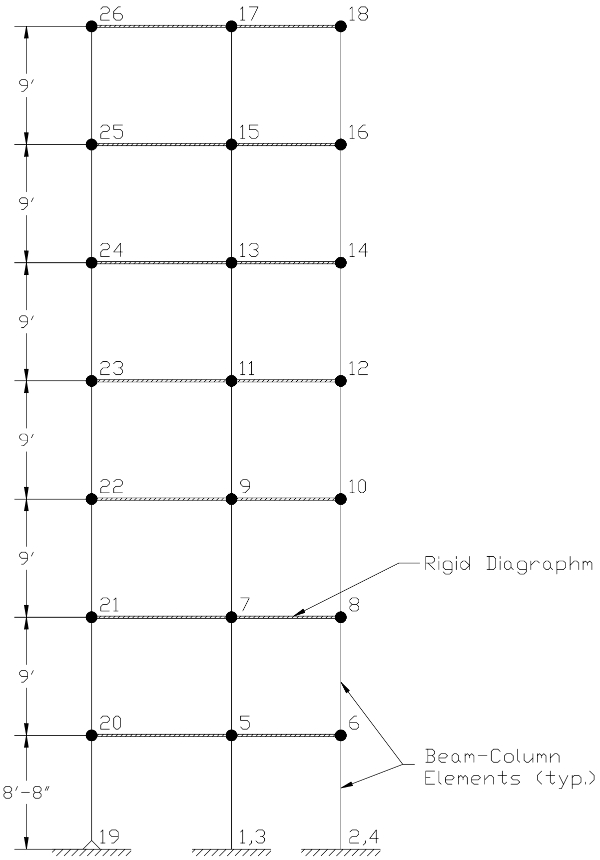

Figure A-8: OpenSees Model Diagram

A.4 Results of Original Analytical Model:

Key results from the original OpenSees model are compared with the measured results provided in NEES7Story (2006) in Figures A-9 – A-12. Overall, the predicted results are lower than the experimental results. Figure A-9 compares the envelopes of the overturning moments while Figure A-10 compares the envelopes of the story shear forces. The original model underpredicts the moments by 30 – 40%, while the story shear envelope is underpredicted by 20 – 40% for the four earthquake input motions. The story displacements are shown in Figure A-11, and show better comparisons with the measured data than those seen for the prediction of forces induced in the structure. A satisfactory prediction of the displacement envelope occurs for EQ1 and EQ3; while the model showed a stiffer response than the one recorded during the shake table testing for EQ2 and EQ4. In general the floor accelerations, shown in Figure A-12, are the best predicted. For events EQ1, EQ2, and EQ3, the analysis model gives values within 20% of the floor accelerations recorded for the test building. For EQ4, the floor accelerations were overpredicted by 20 – 35%.

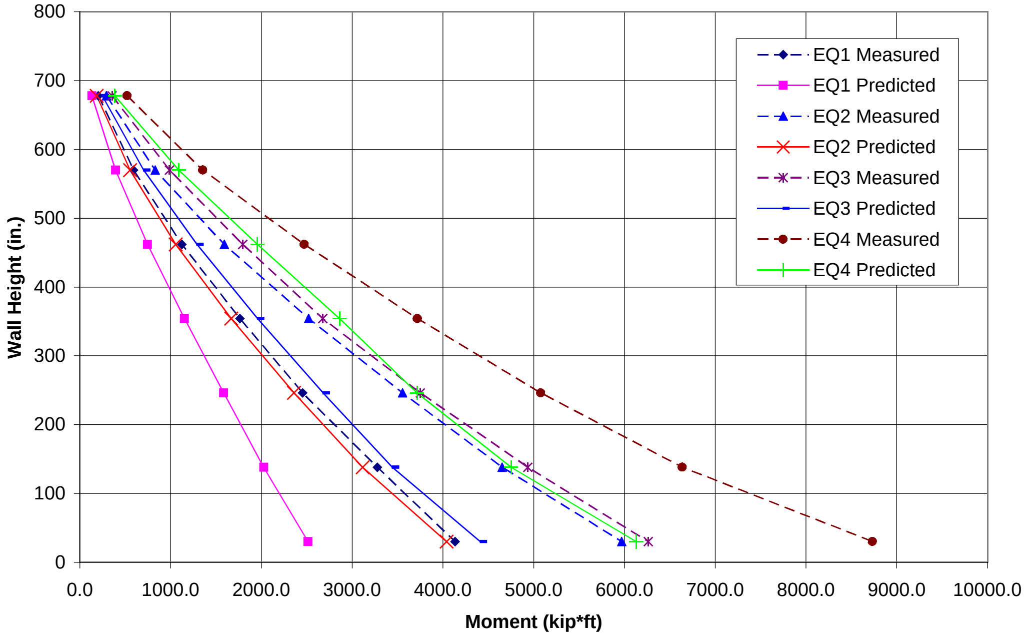

Figure A-9: Comparison of the Predicted and Measured Values of the Overturning Moments

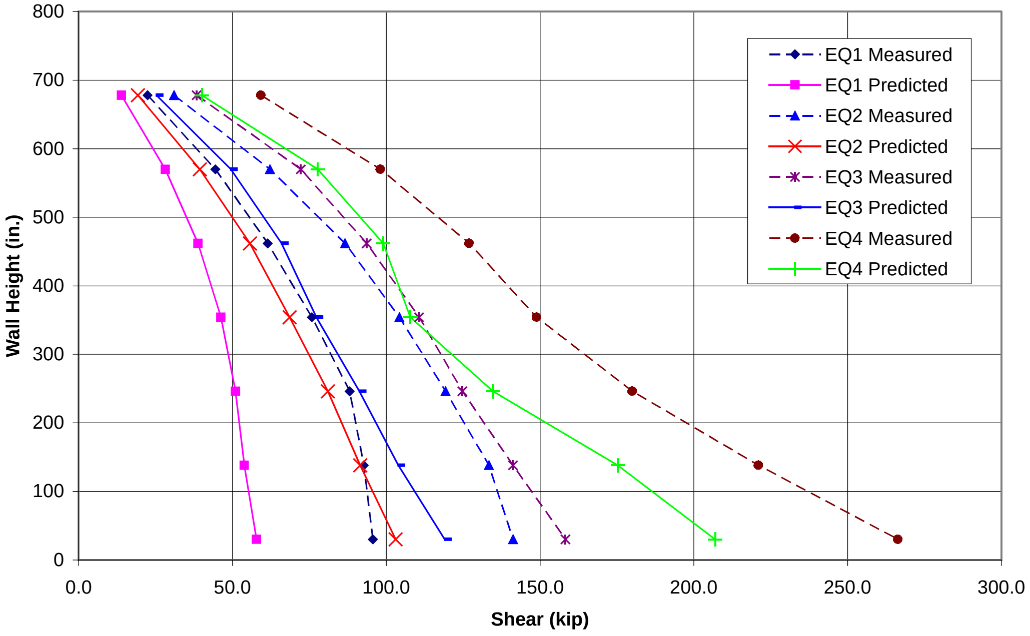

Figure A-10: Comparison of the Predicted and Measured Values of the Story Shear Force

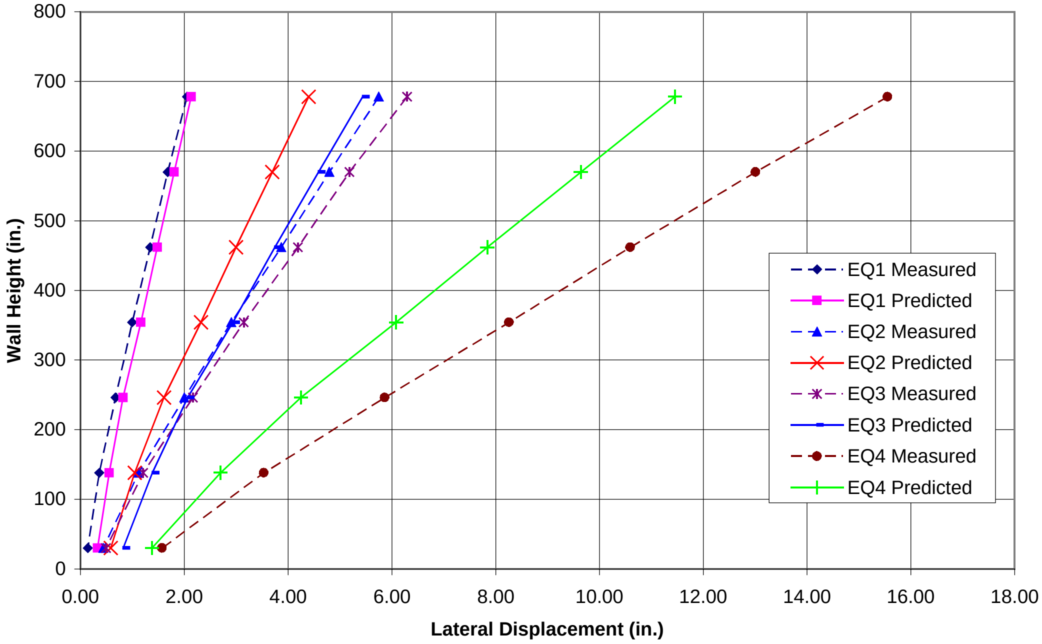

Figure A-11: Comparison of Predicted and Measured Values of Story Displacements

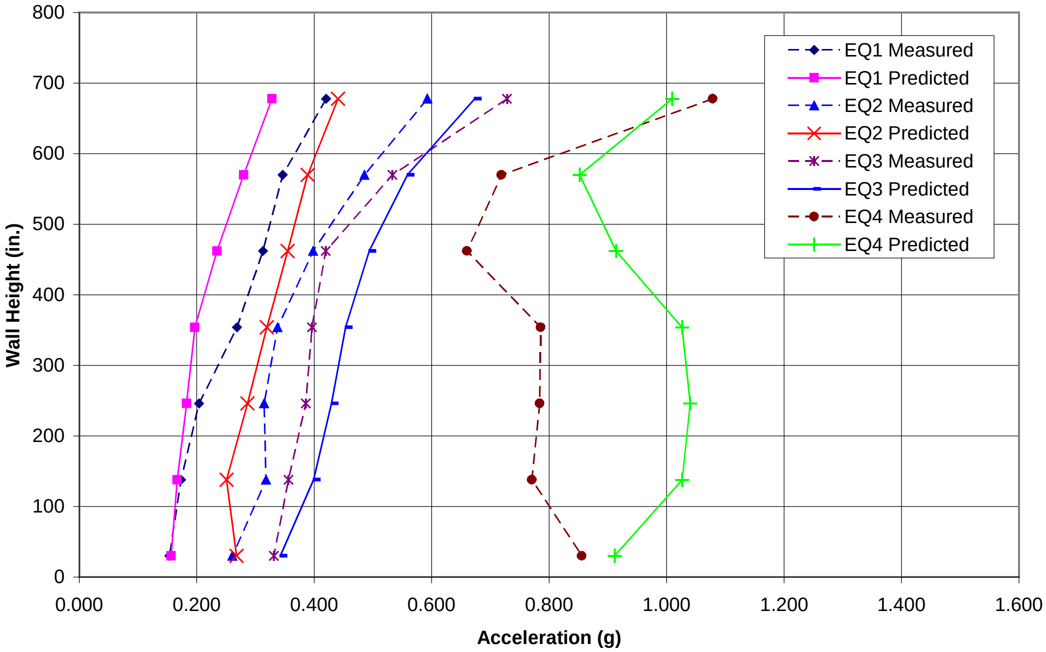

Figure A-12: Comparison of Predicted and Measured Values of Floor Acceleration

A.5 Post Prediction Analytical Model:

Because the OpenSees model did not capture the building's response adequately, the model was revised to determine how to improve the simulation of the building. A workshop was held at UCSD on the simulation of reinforced concrete wall structures. Based on the discussions at the workshop and a review of the decisions in building the OpenSees model, an improved analytical model was developed. The 2D centerline model approach was maintained along with lumping the masses at the floor level nodes.

The number of elements and nodes in the improved analytical model maintains the simplicity and efficiency of the original model. A diagram delineating the improved OpenSees model is shown in Figure A-13, which had a total of 83 nodes and 81 elements including 56 beam-column elements, 22 truss elements, and three zero-length interface elements.

A.5.1 Lateral Force Resistance System

The web and flange walls were modeled in the improved model were simulated the same as in the original model. However, the first floor walls were modeled using force-based beam column elements rather than the displacement based beam column elements used in the original model, because force-based beam column element are considered to be a better choice for modeling the plastic hinge regions [Neuenhofer and Filippou, 1997]. The number of fibers in each fiber section was reduced to increase the computational efficiency. The first floor web wall section was discretized using 100 confined concrete fibers and 302 unconfined concrete fibers, while the first floor flange wall section was discretized with 20 confined concrete and 456 unconfined concrete fibers. The sections for the upper level flange wall used 60 unconfined concrete fibers to discretize the wall, while the upper level web wall section used 72 unconfined concrete fibers. A single beam-column element with five integration points along the element length was used to represent each wall within each story

The other elements in the original model were not modified in the improved model. The post-tensioned segmental pier were modeled the same as in the original model using beam-column elements and a truss element to model the unbonded post-tensioning rods. Additionally, the strain penetration at the wall-foundation interface was again modeled with the zero-length element using the strain penetraion material. Since both of these elements were deemed acceptable in the original model they were not modified for the improved analytical model.

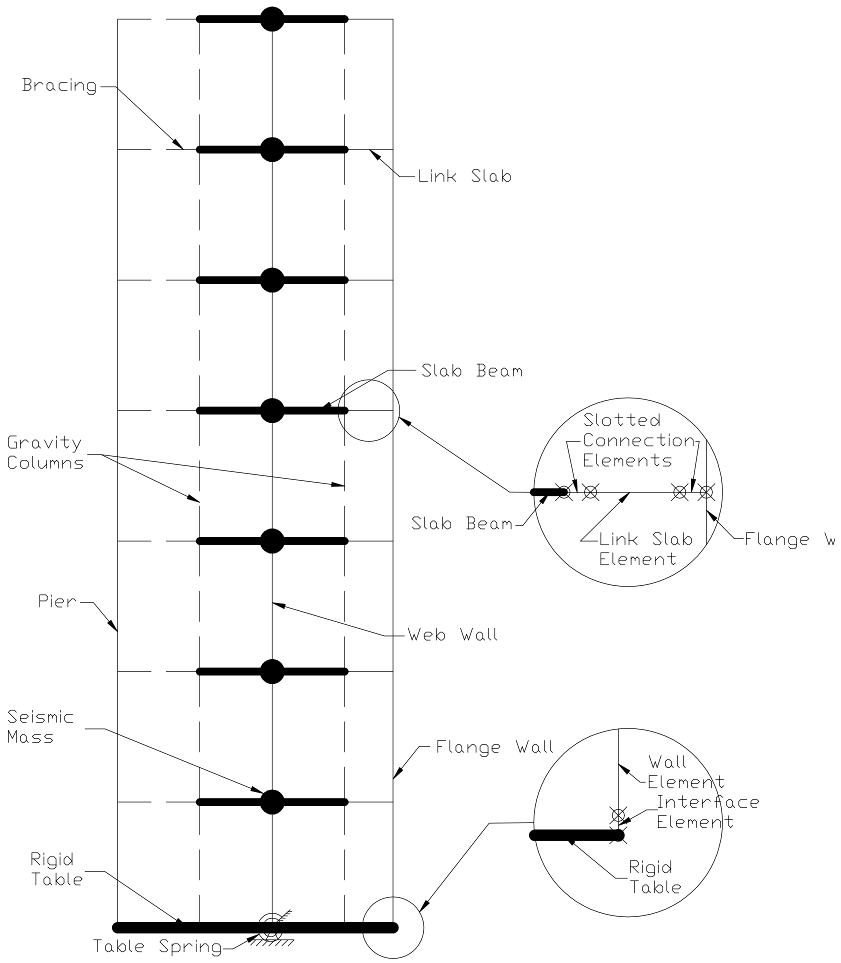

Figure A-13: Improved OpenSees Model Diagram of Test Building

A.5.2 Floor Slabs and Gravity Columns

One element overlooked in the original model was the effects of the gravity columns and floor slabs in the building slice. The gravity columns played and important role in the overall structural behavior but was ignored in the original model. Consistent with the design assumptions, most participants in the blind prediction did not model the floor slab and columns because the specially detailed pinned connections at the column ends were intended to remove them from providing the lateral load resistance. However, the influence of the gravity columns and floor slab on the overall force-displacement response of the test building was evident during testing, and was confirmed by Panagioutou and Restrepo [2006] using a pushover analysis of the building. The primary reason for this influence was that the columns developed significant axial strains during testing due to their interactions with the floor slab. Consequently, the columns closer to the compression side of the web wall were subjected to compression forces and those near the tension side of the web wall were subjected to tensile forces. This enabled a large moment couple to be developed due to the distance of 10 ft (3.05 m) between the compression and tension columns and effectively contributing up to 24% to the lateral force resistance of the test building. The interaction between the floor slabs and gravity columns were dictated by the flexural stiffness of the floors, fixed connection between the slab and walls, and axial constraints imposed to the floor slabs by the gravity columns. Therefore, it was expected that the extent of the flexural cracking of the concrete floor slab occurring perpendicular to the direction from the compression region of the web wall to the tension columns and tension region of the web wall to the compression columns to have influenced the amount of force developed in the gravity columns. Figure A-14 shows a part of the ANSYS [Swanson Analysis Systems, 1992] model created to understand the interaction between the floor slab and gravity columns. The ANSYS model included the web wall, floor slab, and four gravity columns per floor for the seven floors in the building slice. The floor slab and web wall were modeled using the concrete element Solid65, but the flange wall was not modeled. This element is an eight node brick element that incorporated tension cracking and compression crushing of the concrete material, but the latter capability of the model was turned off because crushing of concrete can prematurely occur in an ANSYS analysis as reported by Barbosa and Ribeiro [1998]. The effect of the confined concrete was modeled by modifying the uniaxial behavior defined for the material in the boundary elements of the web wall using the confined concrete model of Mander *et al.* [1988]. The longitudinal and transverse reinforcement in the Solid65 element is smeared across the element area and defined with orientation relative to the global coordinate system and a uniaxial material model describing its stress-strain characteristics. The nodes along the top of the wall in the model were constrained to displace equally parallel to the length of the web wall. The behavior of this 3D model was studied by imposing monotonic displacement that followed the first mode response of the test building.

The 3D slab effect was introduced into the 2D OpenSees model using a beam-column element at each floor level. A bilinear moment-curvature envelope was selected to define the section behavior of this element. The initial slope of the moment-curvature relation is based on the uncracked slab properties with the flexural stiffness of 10,000,000 and 30,000,000 k-in-rad (1130 and 3390 MN-m-rad) for positive and negative moments, respectively. The two different stiffness values are due to the different reinforcement mats in the top and bottom of the slab. The moment at the transition between the two linear portions was defined by the flexural cracking moment occurring over an effective width of the width of the slab. This moment was estimated to be 1350 k-in. (152.5 kN-m), based on an effective slab width of 11.5 times the slab thickness (or 7.64 ft) that was determined from the ANSYS analysis results (see Fig. A-14b). A post cracking stiffness ratio of 20% determined using the nominal strength and the corresponding curvature of the slab section over the effective width defined the second slope. This approach for modeling the 3D effects of slab-gravity column interaction in the 2D OpenSees model was validated by comparing the axial force induced in the columns vs. interstory displacement with that obtained from the ANSYS model. Figure A-15a showing this relationship at the first story level confirms that the 3D effects of the slab-column interaction in the 2D model was satisfactory, while A-15b shows the origin centered hysteretic model used for the moment-curvature behavior of the section of the beam-column element

The columns were modeled using truss elements with the appropriate cross sectional area to simulate the axial constraints provided by the Dywidag bars. Since the OpenSees model was only 2D, the area of the two columns on each end of the web wall were modeled with a single truss element with twice the area of a single column. Small rigid links were used to model the thickness of the floor slab to accurately simulate the clear length of the gravity columns.

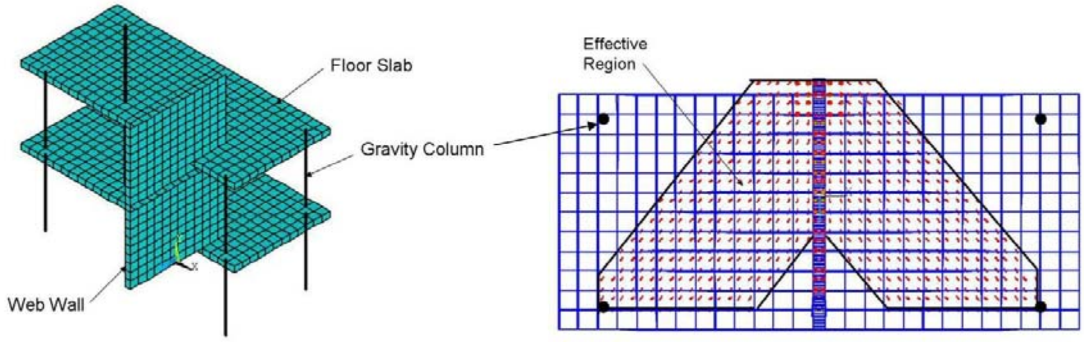

a) Bottom two stories of the ANSYS model of the test building

b) Fully cracked floor slab

Figure A-14: Ansys Model used to understand the 3D Effects of the Floor Slab

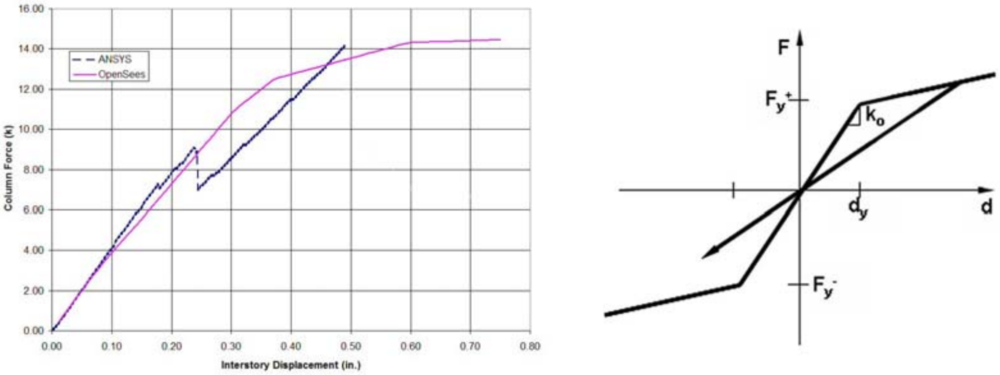

a) Column Force Comparison

b) Origin Centered Hysteretic Model

Figure A-15: Calibration of Axial Force Induced in Columns vs. Interstory Displacement and the Model chosen for the Cyclic Behavior

A.5.3 Link Slab Connection

Similar to the gravity columns, the effects of the link slabs were typically overlooked by the participants in the blind prediction contest. The link slab, shown in Figure A-1, refers to where notches were cut in the portion of floor slab connecting the flange and web walls. The intent of the detail was to minimize the moment resistance at the flange wall-to-slab interface while allowing the transfer of in-plane inertia forces. Despite minimizing the moment, a significant shear along the length of the notch was possible, which, in turn, increased the axial load in the web wall. Panagioutou and Restrepo [2006] observed this stiffening effect in their pushover model and showed that it almost doubled the axial load on the web wall when yielding of the horizontal notch reinforcement occurred as observed in the test.

In the original model, the effect of the notches was included by constraining the lateral displacements of the flange and web wall, while the rotational DOFs for the flange and web wall nodes were not constrained. Other participants in the contest used similar approaches by using either constraint equations or truss elements to model the effect of the link slab; however, neither approach captures the axial stiffening of the web wall and associated increase in the lateral force resistance. In the improved model, the link slab was modeled using three beam-column elements with fiber sections. Two beam-column elements were used to model each of the reduced sections of the slot, and the third beam-column element modeled the slab between the slots. The cross-sections for both the slab and slot sections were modeled using fibers representing the unconfined concrete and longitudinal reinforcement. This approach allowed yielding of the slab reinforcement along the notch, imposing the appropriate amount of additional axial load on the web wall. The additional axial load increases the resistance of the web wall by approximately 16%.

A.5.4 Shake Table Flexibility

The connection between the test building and the shake table was modeled in the boundary conditions for the wall and pier elements. However, the shake table and foundation as a whole experienced some rotation and the building's response was influenced by the rotational stiffness of the table. The table flexibility was neglected in the original model. As shown in Figure A-13, a zero-length elastic rotational spring was used to account for this additional flexibility in the improved model; rigid beams were used to link the rotational spring to the bases of the web and flange walls, gravity columns, and precast pier. Table A-4 lists the rotational stiffness of the table and foundation measured in each direction by the UCSD researchers for each of the ground motions. As indicated in the table, the average rotational stiffness obtained from the stiffness reported for the two directions during testing of EQ2, EQ3, and EQ4 was used in the improved analytical model. The rotational stiffness reported for EQ1 was relatively high compared to the values for the other events and thus was not included when finding the average value. This approximation was used since the effects of all earthquakes were examined in one analysis and the expected error in displacement due to underestimating the table stiffness for EQ1 was expected to be less than 5%. With this average value representing the rotational stiffness, one node of the rotational spring was fully fixed against deformation while the other node was allowed to rotate parallel to the web wall.

Table A-4: Base Spring Rotational Stiffness

Rotational Spring stiffness due to combined flexibility of table and foundation (kips-ft/rad)*10^7	EQ1	EQ2	EQ3	EQ4	Model
Direction 1	1.326	0.883	0.711	0.711	0.7904
Direction 2	1.378	0.888	0.684	0.746	0.7904

A.5.5 Influence of Shear Deformation

Experimental research has shown that shear deformation can contribute significantly to the lateral displacement, especially at the lower floor levels, even in slender, flexure dominated walls [e.g., Thomsen & Wallace, 1995]. The effects of shear deformation need to be included to better simulate the lateral displacement, especially at the lower floor levels. The fiber sections used for the wall in the original model did not include any shear effects in the section formulation, requiring the shear response to be handled separately.

Some of the other participants did not have to separately handle the shear deformation because the modeling approach they used included the effects of shear within their chosen elements. However, OpenSees does not have an option for including shear in the element definition and the fiber sections used in the analysis sums the uniaxial response of the fibers to determine the axial and moment resistance of the section. Because the fibers have zero resistance to transverse loads, the shear deformation cannot be determined by the section. In the original model an estimate of the additional lateral displacement due to shear deformation was added during post-processing of the results. The method selected to incorporate shear deformation in the improved model was to aggregate a shear force-deformation response onto the fiber sections used to model the web walls. Because the small lateral force resisted by the flange wall and the short dimension parallel the shear force, the shear deformation of the flange wall was neglected. Aggregating the shear response does not cause the axial strains seen by the fibers due to curvature of the wall to change, neglecting the possible flexure-shear interaction.

The lateral force versus shear deformation hysteretic response of the web wall was modeled using a uniaxial material model. Figure A-16 shows the "pinching4" material model available in OpenSees that was used for this purpose at the first floor level. A minimum of three points with an optional fourth point are needed to define the response envelope of this model. Because the measured shear deformation of the web wall was not available, only three points were defined for the pinching model as follows: 1) point 1 was defined using the lateral force corresponding to the first flexural cracking of the web wall (25 k) and the uncracked shear stiffness, 2) point 2 was defined using the lateral force that was expected to cause flexural yielding of the longitudinal reinforcement (70 k) and effective shear stiffness, and 3) point 3 was defined using the ultimate lateral force resistance (105 k) and post-yield shear stiffness. The uncracked shear stiffness was obtained according to Park and Paulay [1975] for an uncracked rectangular beam. The effective shear stiffness to the uncracked shear stiffness was taken as the same ratio as the flexural stiffness at yield to the gross flexural stiffness; this ratio was determined to be 20% of the uncracked stiffness. Furthermore, research by Massone and Wallace [2004] has shown that when inelastic flexural action occurs, inelastic shear action also begins because of coupling of the two responses. In order to simulate this coupling, the lateral force at yield was used to define the point when the tangent stiffness changes from the effective shear stiffness to the post-yield shear stiffness. The post-yield stiffness was defined based on the observed shear force versus deformation responses of NTW1 and RWN from the PreNEESR wall tests [Brueggen *et al.*, 2007] and RW2 and TW2 tested by Thomsen and Wallace [1995]. Based on those data sets, the post-yield shear stiffness should be approximately 1.0% of the effective shear stiffness. Shear stiffness for the second floor and above was modeled using an elastic material model with stiffness equal to 35% of the uncracked shear stiffness to reflect the cracking of the wall.

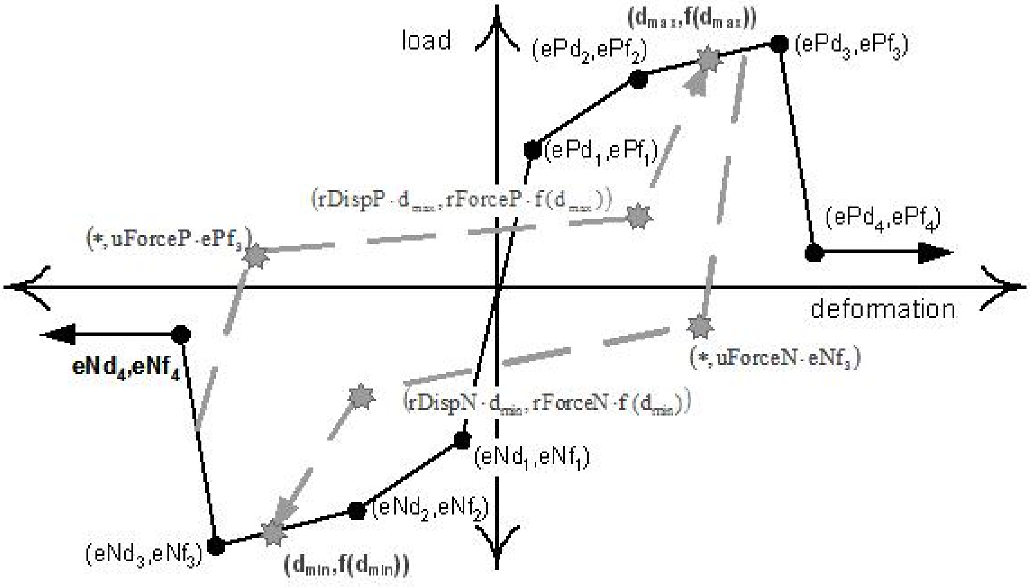

Figure A-16: Pinching4 Material Model used to account for the Shear Deformation Contribution [Mazzoni et al., 2004]

A.5.6 Viscous Damping

In a nonlinear system, the stiffness matrix used for calculating the damping matrix can have a significant impact on the results of the analysis. As stated in section 6.3 in the original model, Rayleigh damping was used in conjunction with the current stiffness matrix, allowing damping to decay as damage accumulated. The coefficients needed to define the Rayleigh damping were obtained assuming five percent viscous damping for the first and third modes that were found from cracked section properties.

Priestley and Grant [2004] recommended that stiffness proportional damping be used for nonlinear analysis because Rayleigh damping heavily weights the mass matrix, leading to an almost constant damping matrix during a nonlinear response of the structure regardless of the degradation that occurred to the stiffness of the structure. Furthermore, test observations by Moaveni, *et al.* [2006] indicated approximately three percent damping on the first longitudinal mode when testing to white noise. However, Panagioutou and Restrepo [2006] used only 0.3 percent damping for the first longitudinal mode for accurate simulation of the test building's response to earthquake input motions. Such low damping may have been due to excluding the nonstructural elements in the test structure and flexural cracking over a lower height due to the reduced longitudinal reinforcement in the test building. Consequently, in the improved model the stiffness proportional viscous damping corresponded to 0.5% damping on the uncracked first mode period and 0.8% damping on the uncracked third mode period. This corresponded to 0.02% and 0.5% viscous damping, respectively, on the cracked first and third mode responses of the building.

A.6. Results of the Improved Model

The capabilities of the improved model can be seen best by comparing key time history responses with the measured data provided for the test building [NEES7Story 2006]. For this purpose, top floor displacement, base moment, and top floor acceleration are used. This is followed by comparison of envelope responses for variables that are of interest from a design viewpoint.

A.6.1 Time History Response

Top Floor Displacement

The top floor displacement time history is shown in Figure A-17 - A-20 representing, respectively, the response during the most intense 30 seconds of EQ1, EQ2, EQ3, and EQ4. The figures show that the period of the test building was well captured by the analysis model for all earthquake intensities, except around 12-15 seconds into the EQ4 motion. Additionally, all the significant peak displacements recorded during EQ1, EQ2, and EQ4 were generally well simulated, and were within 5% of the measured values. The peaks on EQ3 were under predicted by as much as 25%.

The cause of the discrepancy for the EQ3 event was extensively studied, because similar discrepancies were observed in the predictions by other participants (e.g., Kelly, 2007]. The fact that EQ2 and EQ3 were comparable in earthquake intensity was the primary cause for large discrepancies in the response of EQ3 and the unloading and reloading behaviors of the material models rather than their envelopes had a large influence on the analytical response of EQ3. Typically, the envelope response of materials are more accurately characterized than their reloading and unloading action. This hypothesis was confirmed by scaling the accelerations of EQ2 by 0.6 without altering the other events and rerunning the analysis. Figure A-21 shows this modification significantly improved the EQ3 response of the test building. The concrete material model used for the analysis here had very simple unloading and reloading behavior as shown in Figure A-7c. The poor simulation of EQ3 would be improved by using a concrete material model that has a hysteretic behavior which better simulates the unloading and reloading behavior of the concrete. Furthermore, the pinching4 model may not be adequately simulating the shear deformation of the web wall; however, without the measured data for the shear deformation, the accuracy of the shear behavior cannot be evaluated. The simple unloading and reloading behavior of the “pinching4” model was also expected to have influenced the response of the test building to EQ3.

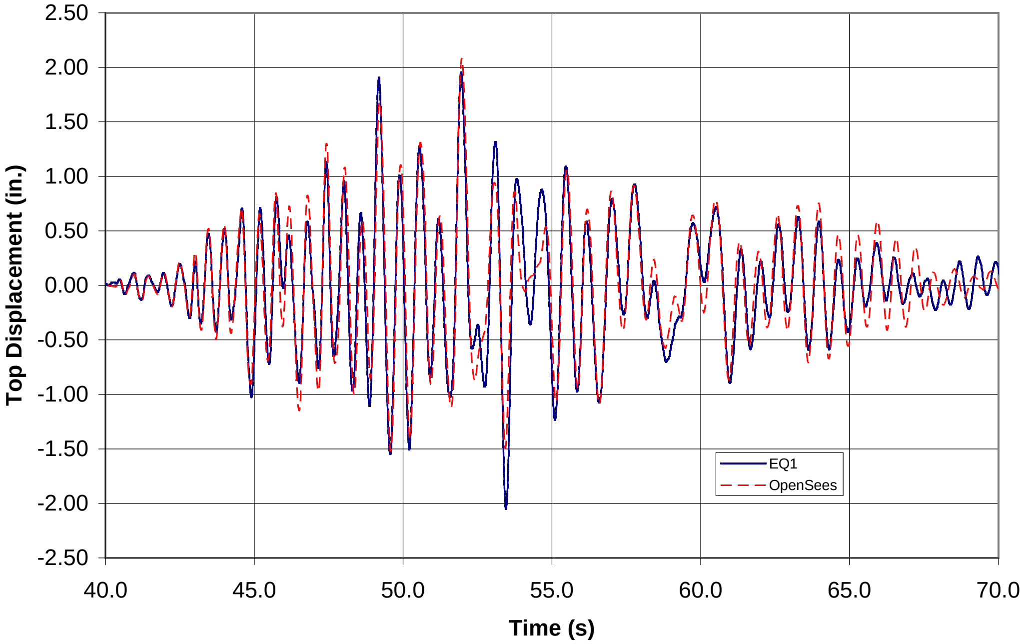

Figure A-17: EQ1 Top Floor Lateral Displacement Comparison

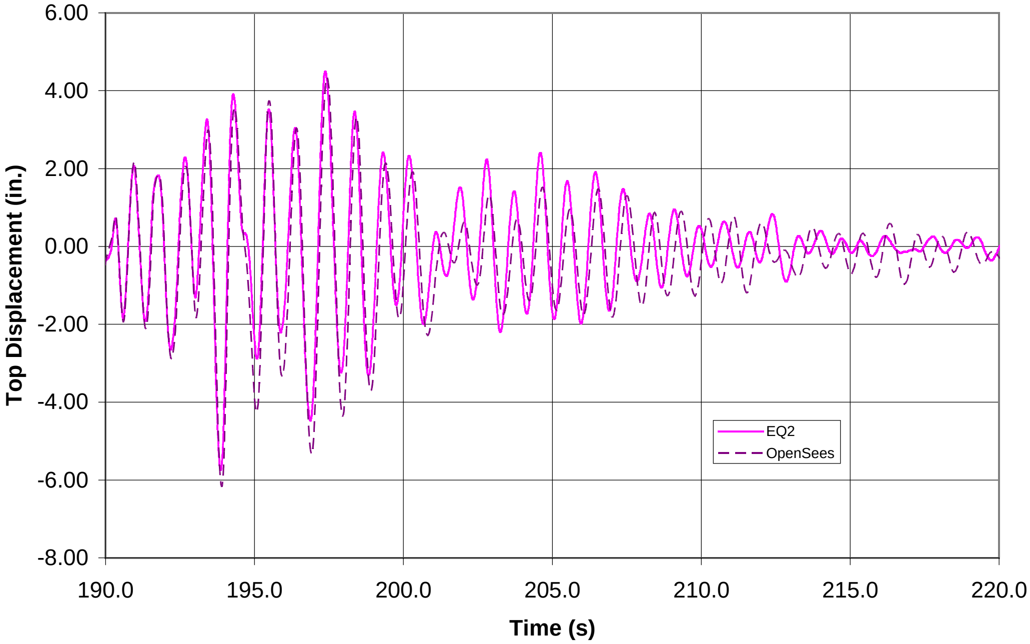

Figure A-18: EQ2 Top Floor Lateral Displacement Comparison

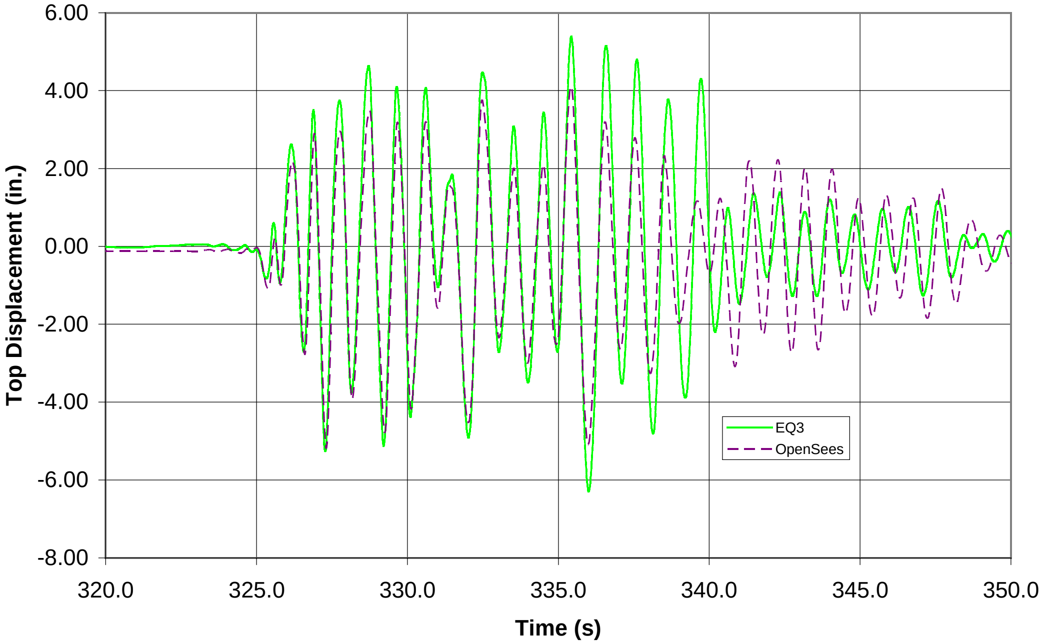

Figure A-19: EQ3 Top Floor Lateral Displacement Comparison

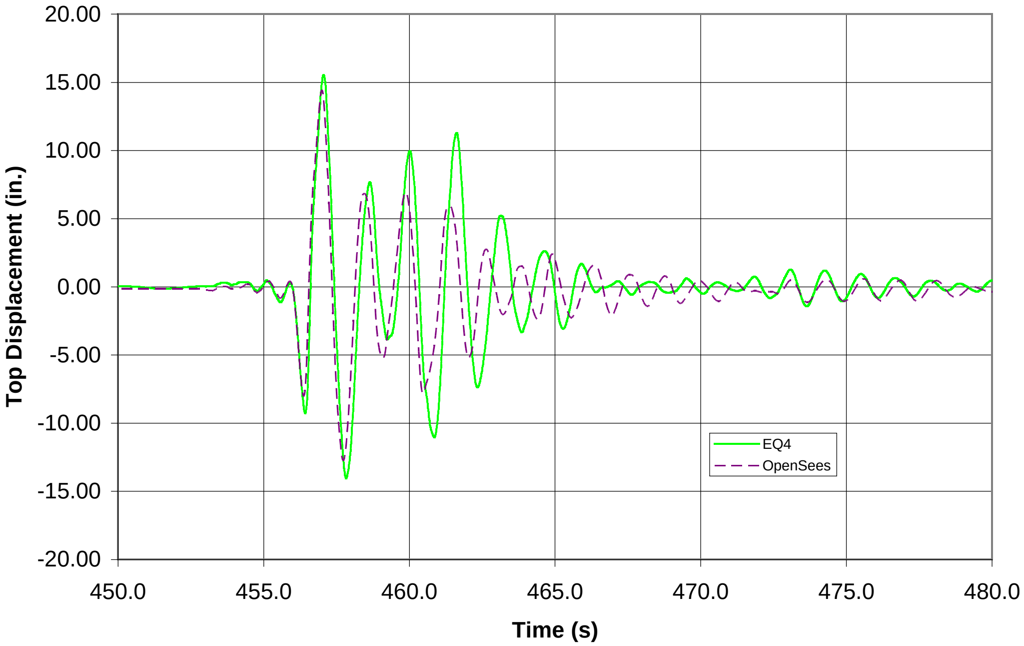

Figure A-20: EQ4 Top Floor Lateral Displacement Comparison

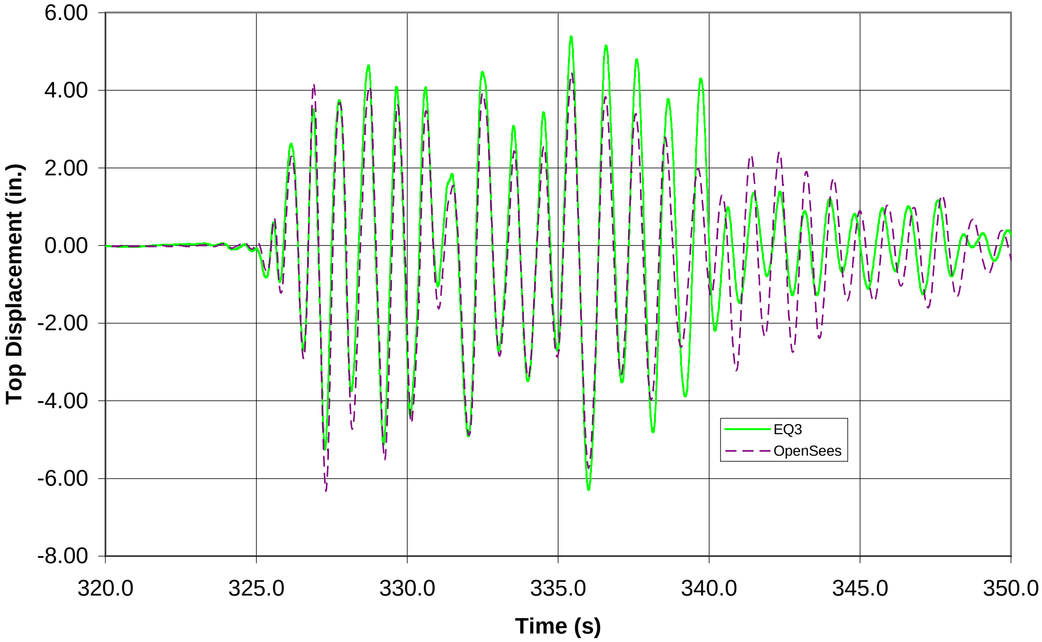

Figure A-21: EQ3 Lateral Displacement Comparison with Rescaled EQ2

Base Overturning Moment

The base moment was determined by summing the moments at the base of the web and flange walls, and the couple generated by the gravity columns that had about 10 to 24% contribution to the base overturning moment. Time history comparison for the base moment is shown in Figure A-22 - A-25, in which many of the characteristics observed for the top floor displacement time history are also seen in the base moment plot comparison. The period of the structure was well captured, showing that the analysis adequately captured the damage and subsequent softening of the structural stiffness. The peak values were generally well captured and are within 10-15% of the measured values for EQ1, EQ2, and EQ4. As previously noted, the response of EQ3 is poorly simulated giving results within 25% of the measured values for the aforementioned reasons.

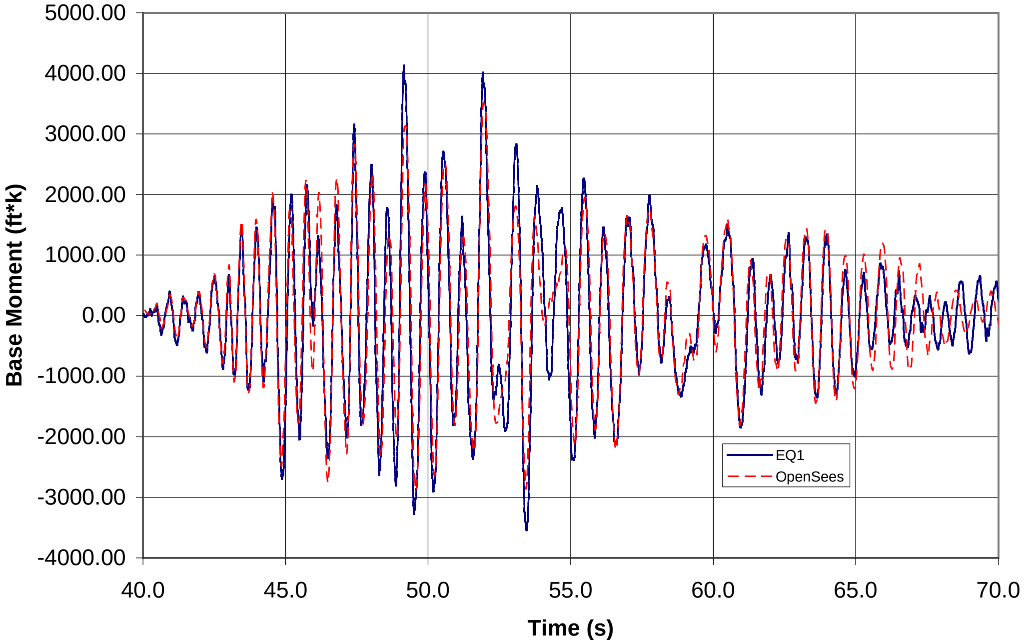

Figure A-22: EQ1 Base Moment Comparison

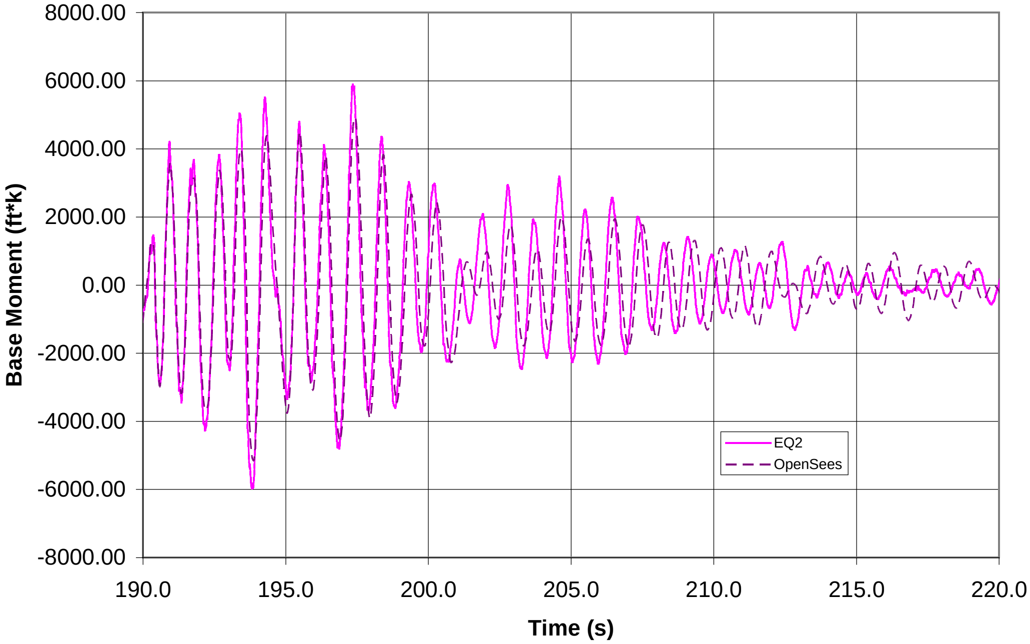

Figure A-23: EQ2 Base Moment Comparison

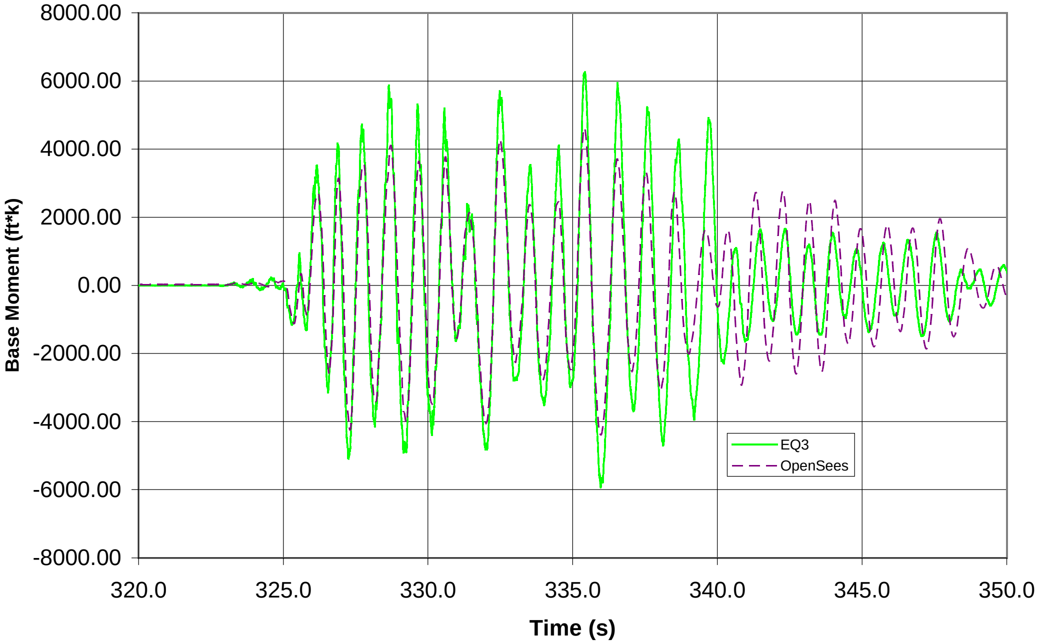

Figure A-24: EQ3 Base Moment Comparison

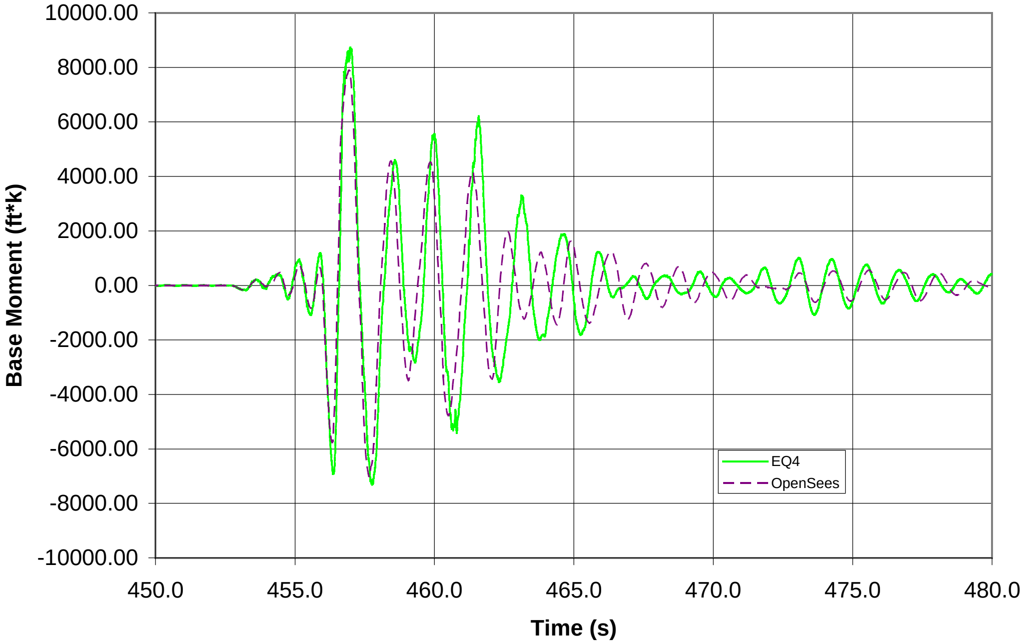

Figure A-25: EQ4 Base Moment Comparison

Base Shear Force

The base shear force was determined similar to the base overturning moment, summing the base shear in the flange and web walls, and post-tensioned pier. The time history comparison is shown in Figure A-26 – A-29. The trends seen in the overturning moment time history is seen in the base shear response. The peak values and period were captured with similar accuracy to the base overturning moment response. However, the shear force tends to be slightly over predicted the base shear but is within 5-10% of the experimental peak values. EQ3 base shear response is under predicted by approximately 25%. The poor simulation of EQ3 is due to the reasons discussed previously. The gravity columns did not have a significant influence on the shear demand of the structure. Unlike in the overturning moment, the gravity columns did not contribute significantly to the base shear resistance.

Top Floor Acceleration

The top floor acceleration time histories for all ground motions are shown in Figure A-26 through A-29. The acceleration time history shows the expected response considering the under prediction of the lateral displacement. The period of the structure was again well captured by the analysis; however, the peak values are typically over predicted by the analysis by approximately 10-20% when compared with the responses measured during the test.

The simulation of the top floor acceleration was generally considered satisfactory given the large time step used for the input excitations used for the analysis and analysis time step. Simulation of the accelerations in a dynamic analysis can be sensitive to the time step used in the analysis and it typically requires a small time step to obtain accurate acceleration responses. The large time step used in the analysis allows a good simulation of the floor level accelerations without requiring an extensive amount of computational time needed to use a small time step and post-process the corresponding analysis output

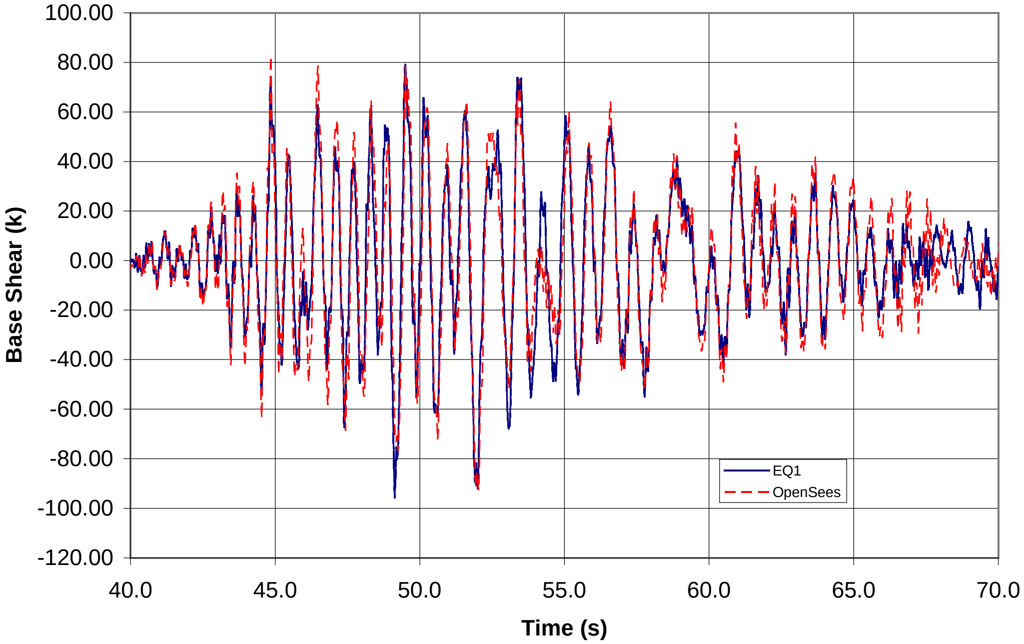

Figure A-26: EQ1 Base Shear Time History

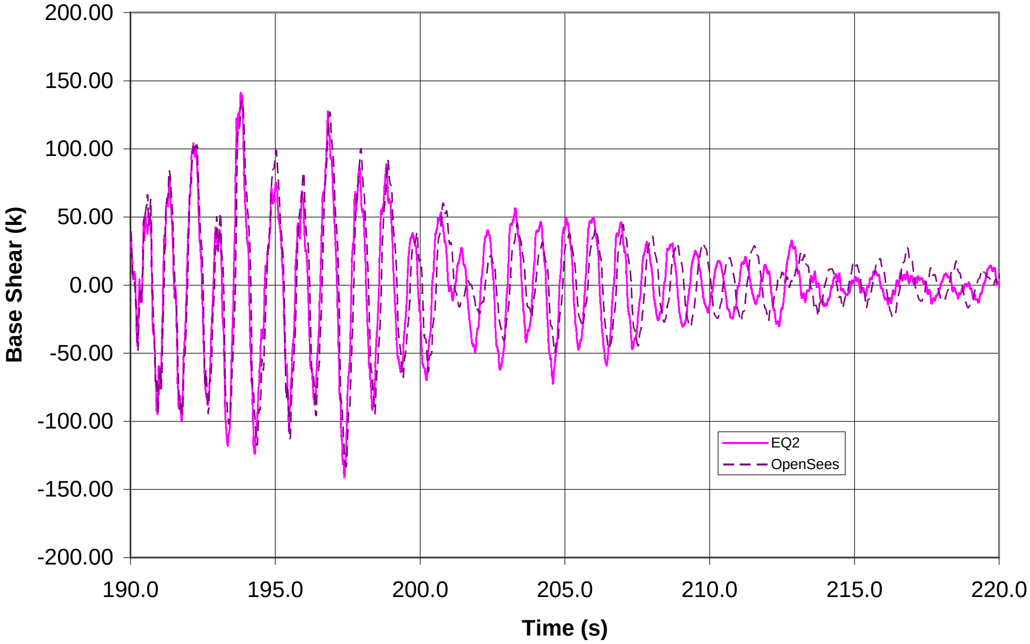

Figure A-27: EQ2 Base Shear Time History

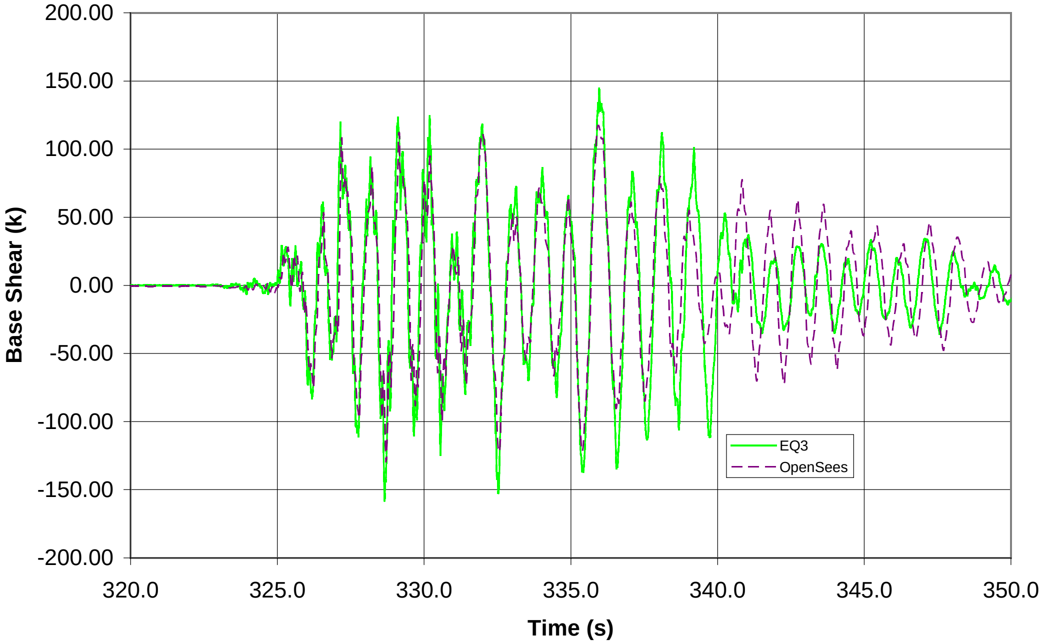

Figure A-28: EQ3 Base Shear Time History

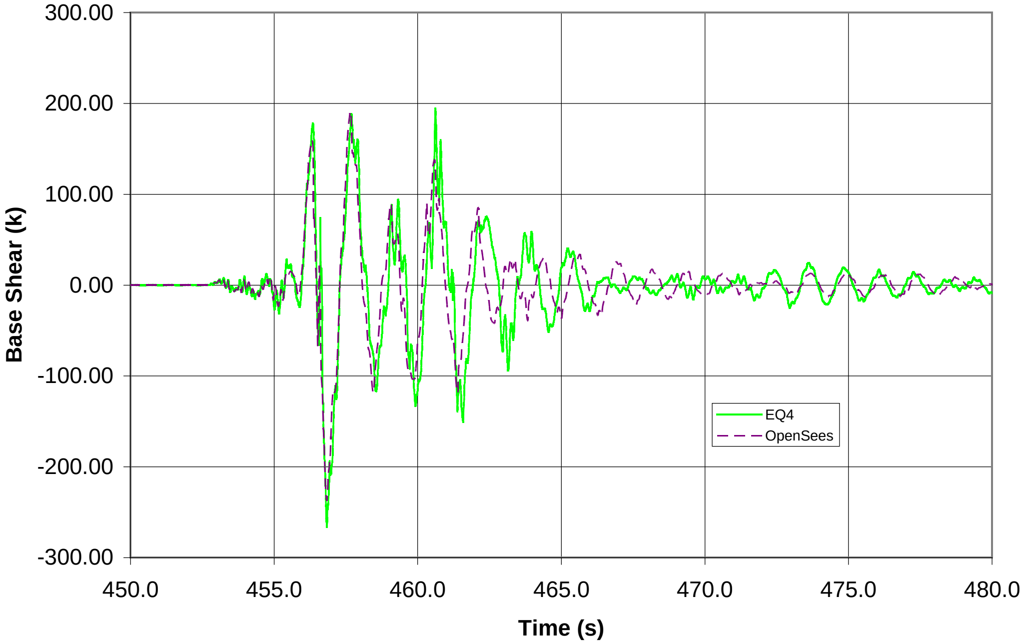

Figure A-29: EQ4 Base Shear Time History

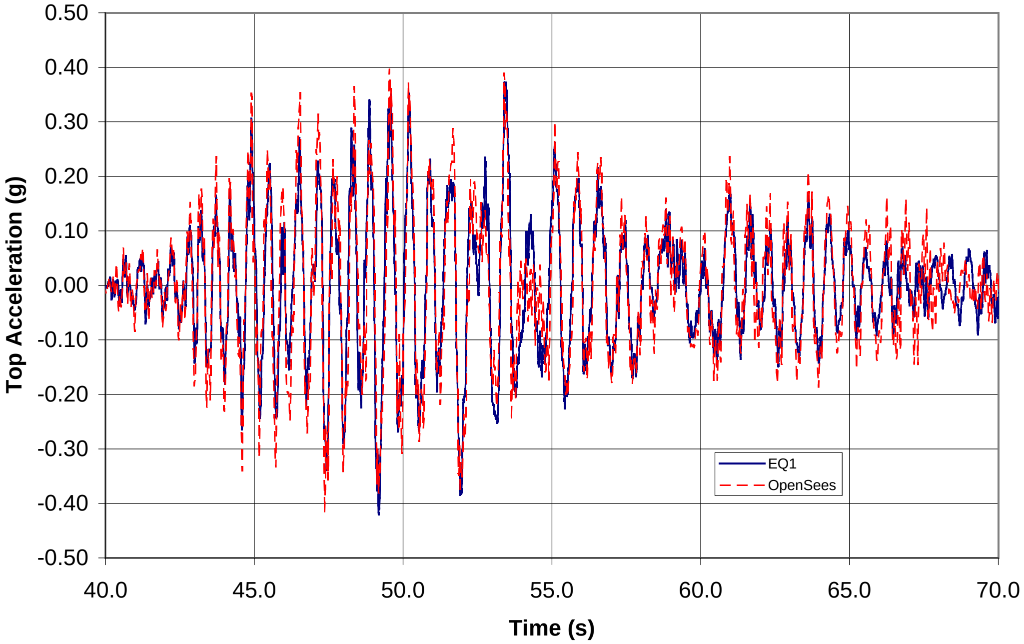

Figure A-30: EQ1 Top Floor Acceleration Time History

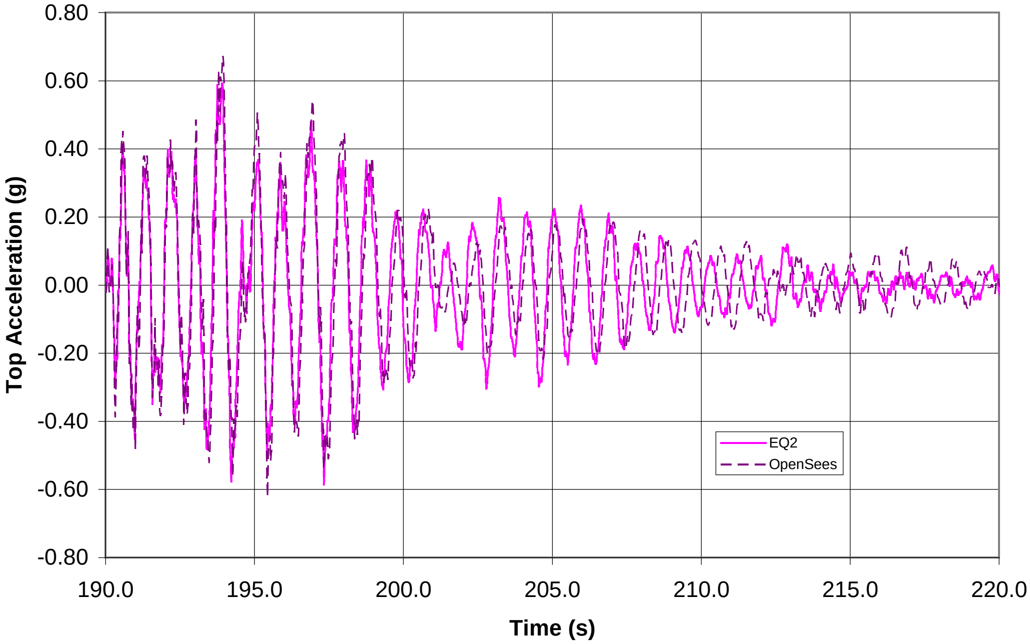

Figure A-31: EQ2 Top Floor Acceleration Time History

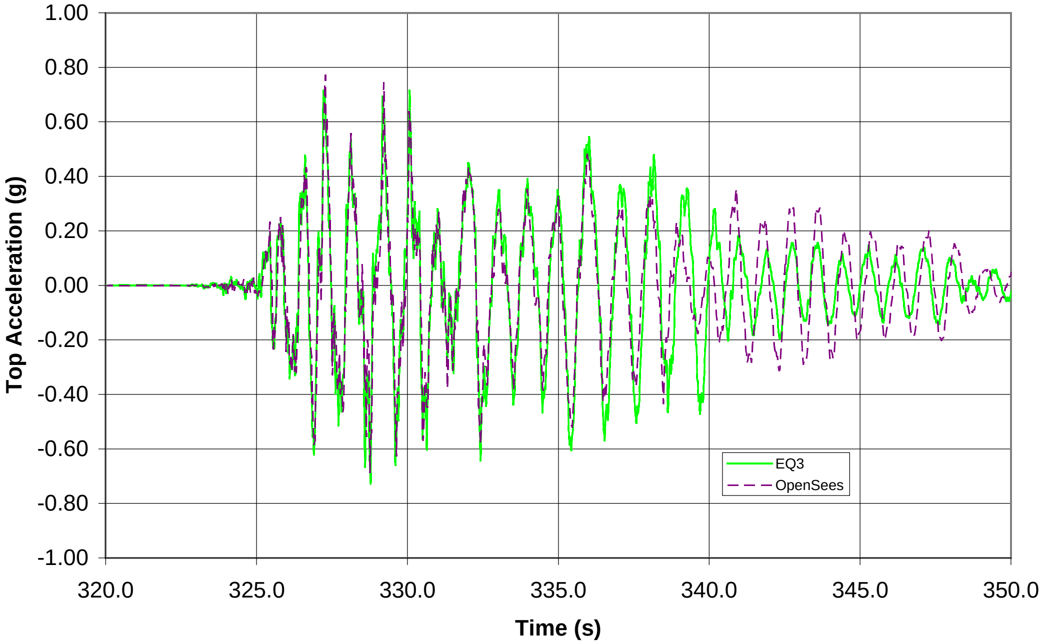

Figure A-32: EQ3 Top Floor Acceleration Time History

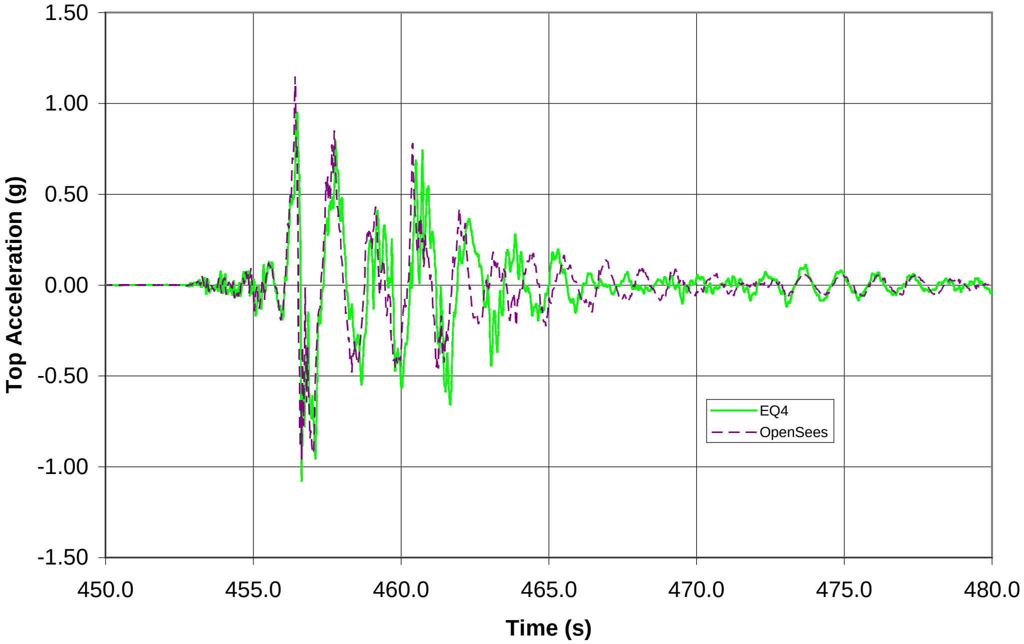

Figure A-33: EQ4 Top Floor Acceleration Time History

A.6.2 Envelope Responses

The envelope responses of the test building model along with their experimental values are shown in Figure A-34, A-35, A-36, and A-37 representing the lateral displacement, interstory drift, overturning moment, and story shear, respectively. The comparison of the envelopes are discussed below in recognition of their influence on design.

Lateral Displacement

The floor level lateral displacements shown in Figure A-34 are generally well simulated, with the exception of EQ3. The displacements of EQ3 were under predicted by about 17%. For the rest of the ground motions, the predicted lateral floor displacements were within 10% of the recorded values during the shake table tests. The top floor displacements were generally better captured than the first floor displacements. This could be due to the influence of the shear deformation, since shear deformation has a larger impact on the lower floor level displacements.

The peak average interstory drift obtained from the top floor displacement divided by the height of the building is used in the design of the structure. Despite designing the building as a flexible structure, the test building did not experience excessive lateral drifts. The maximum average drift ratios were 0.27% for EQ1, 0.81% for EQ2, and 1.88% for EQ4, and the corresponding measured values were 0.27%, 0.76%, and 2.06%, respectively. As expected, a poor comparison was expected for EQ3 response and the calculated and measured peak average drifts for this event were 0.69% and 0.83%, respectively.

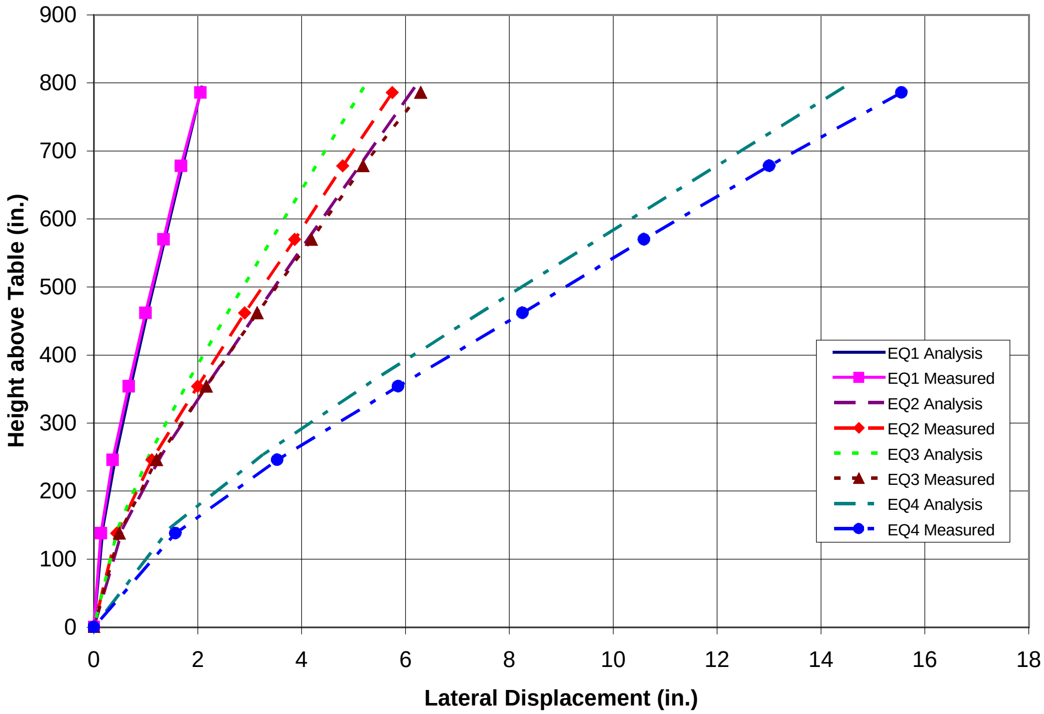

Figure A-34: Lateral Displacement Envelope

Interstory Drift Ratio

An accurate simulation of the interstory drift is important to predict the damage to structural as well as nonstructural elements. The interstory drift ratios, shown in Figure A-35, were well simulated by the analysis were within 10% of the experimental values for EQ1, EQ2, and EQ4. The EQ3 interstory drift was poorly simulated with results being within 20% of the measured values for the reasons previously discussed.

Overturning Moment Envelope

The overturning moments, shown in Figure A-36, were generally under predicted by the analysis compared to the envelopes established from the measured data. If the results for EQ3 are ignored, then the analytical results were within 5-15% of the recorded values. The results for EQ3 were within 25% of the measured values except for the top two floors, where they were under predicted by 30-40%. The moment generated by the gravity columns contributed approximately 20% of the overturning moment resistance for EQ2, EQ3, and EQ4, while approximately 10% for EQ1.

The difference between the measured and calculated overturning moments is believed to be due to the influence of the higher mode effects, which might not have been as well captured as the first mode response. However, it is noted that the time history shown in Figures A-22 - A-25 for the base moment was generally well simulated as a function of time.

Story Shear Forces

The story shear forces, depicted in Figure A-37, show a similar trend to that observed for the overturning moments. The analysis under predicted the measured responses by approximately 5-15% for EQ1, EQ2, and EQ4; however, EQ3 was under predicted by approximately 25%. As stated before, the analytical response of the test building during EQ3 was controlled by the unloading and reloading behavior of the material models and improvements to the cyclic behavior of the material models would improve the analytical response of the building to EQ3. Overall, the story shear forces were adequately captured, and an accurate prediction of the shear demand would help ensure that shear failure of the walls would not control the seismic behavior of the building.

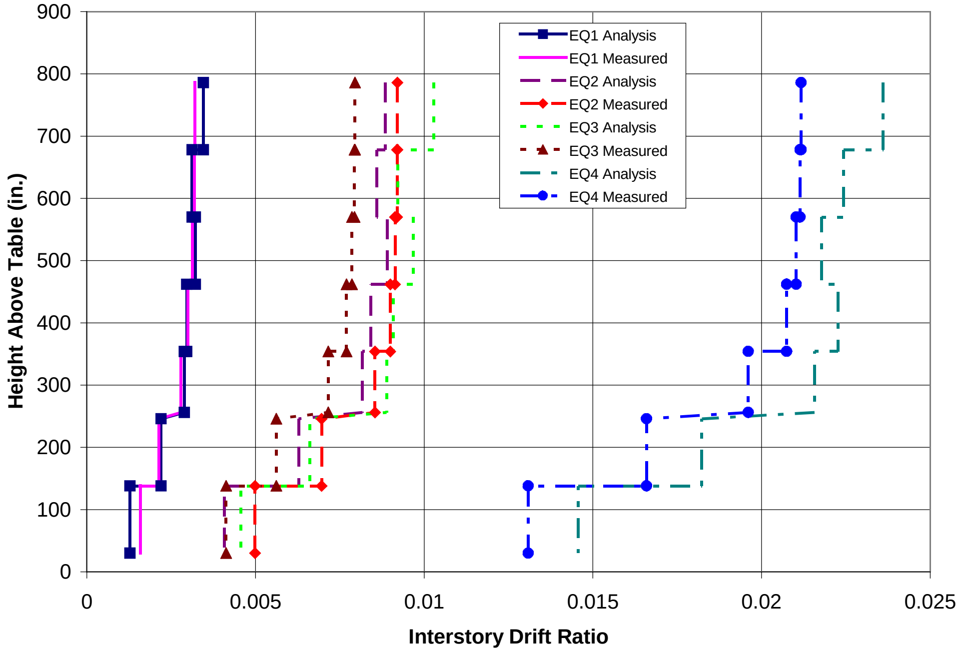

Figure A-35: Interstory Drift Envelope

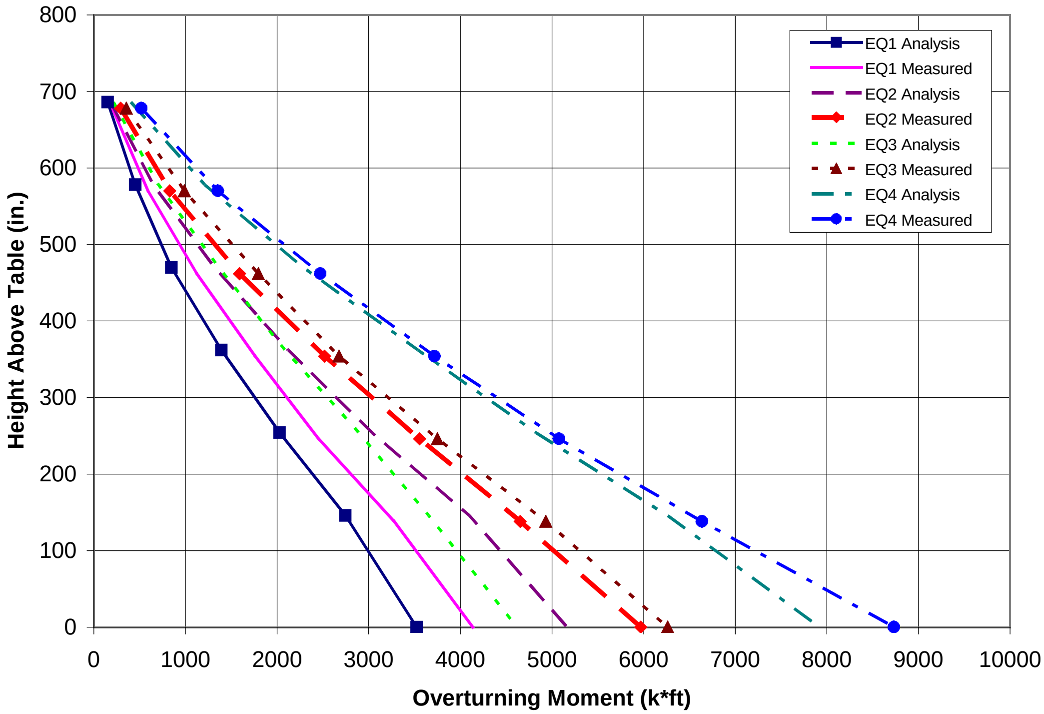

Figure A-36: Overturning Moment Envelope

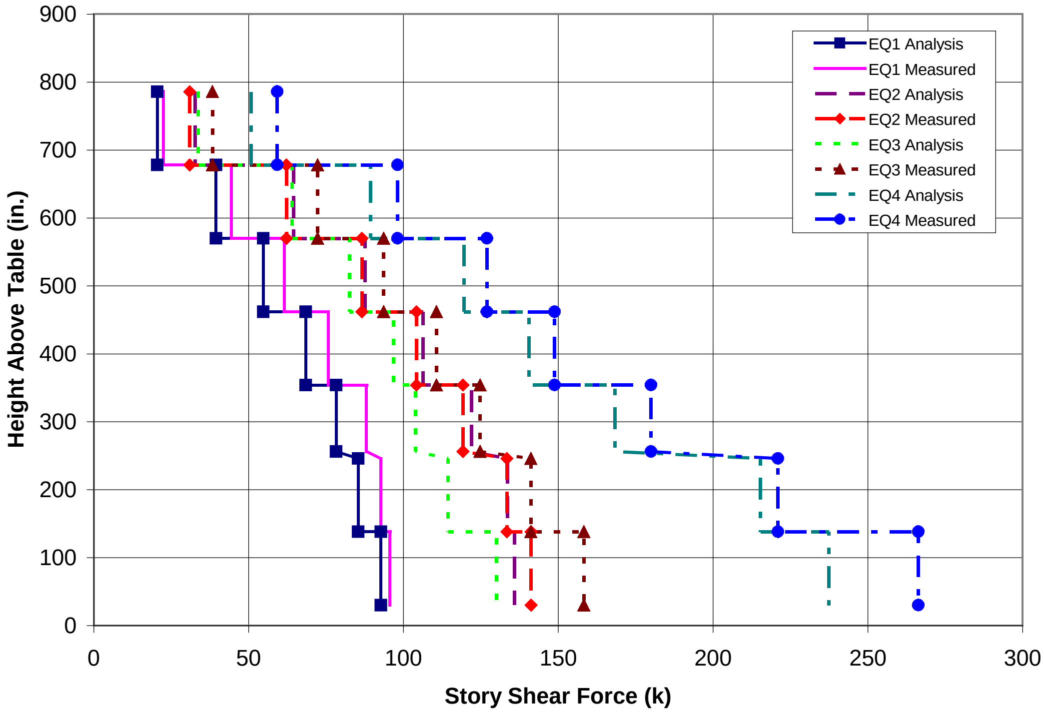

Figure A-37: Story Shear Force Envelope

A.7 Summary Conclusions, and Lessons Learned

A 2D centerline model was created in OpenSees for a full-scale portion of a building that was designed and subjected to shake table tests at UCSD. This model emphasized simplicity and ease of creation based on the geometry and material properties. The original model used beam-column elements to model the flange and web walls, and the post-tensioned pier that was used primarily to provide stability to the test building. The improved model added elements ignored in the original model such as the link slab, gravity columns, and a rotational spring to simulate the flexibility of the shake table, all of which led to significant improvements to the analytical model. The link slab and notches were modeled with beam-column elements, providing the stiffening of the web wall observed in the test. The gravity columns contributed to the lateral resistance by developing axial tension and compression in the columns located at opposite ends of the web wall, thereby creating a moment couple. The axial loads in the columns were controlled by the 3D deformation of the floor slabs. A 3D ANSYS analysis was conducted to determine an effective slab width of 11.5 times the slab thickness, which was used to define the behavior of a beam-column element at each floor level to capture the corresponding effect in the 2D OpenSees model. The improved model remains simple and easy to construct, while giving accurate simulation of the structural response.

The conclusions drawn from the analysis of a large system such as the test building studied herein are:

- Simple, computationally efficient 2D models with fiber sections that satisfactorily account for any 3D effect are sufficient to predict the response of concrete wall buildings subjected to unidirectional earthquake motions. In this study, the effect that the floor slabs had on the axial load in the gravity columns was investigated using a 3D ANSYS model and such an effort will not be needed if an effective floor slab width needed to include in the 2D model is known.

- Inclusion of the gravity columns, link slab, and table flexibility were required to accurately capture the response of the structure to the earthquake input motions.

Neglecting these components in the original model significantly affected the ability of the model to predict the dynamic response of the building.

- The gravity columns contributed significantly to the overturning moment in the structure. The couple generated by the axial load in the columns contributed 10-24% to the overturning moment. The contribution of the gravity columns generally increased as the intensity of the earthquake motions increased.
- The time history responses for the top floor displacement, base overturning moment, and top floor acceleration were well predicted by the improved 2D model for EQ1, EQ2, and EQ4 motions. The analysis gave results within 5% of the measured values for displacement while the base overturning moments and top floor acceleration peak values were within 10-15%.
- When subjected to input motions EQ1, EQ2, and EQ4, the improved 2D model gave results that were within 5-15% of the envelope for displacement, interstory drift, overturning moment, and story shear forces.
- Under input motion EQ3, the discrepancies between the analytical responses and the measured values were as large as 25%. This was due to EQ3 having a similar peak intensity to EQ2, which made response of the test building to EQ3 to be dependent heavily on the unloading and reloading behavior of the material models used in the analysis.
- Despite the building being designed as a flexible structure, the earthquake analysis of the test building did not produce excessive floor displacements or unacceptably large interstory drift ratios, which is encouraging and consistent with the test observations.

The participation in the blind prediction and follow up analysis of the 7-story building provided a number of lessons about simulating the response of a complex system. These lessons are:

- Although gravity load resisting systems are frequently ignored in the seismic design and analysis of structures, they can significantly contribute to the lateral load resistance of a building. This situation may be expected if gravity columns are subjected to axial forces resulting from their interaction wit the floor slabs during lateral movement of the building, enabling moment couples to be generated. Since the distance between gravity columns is typically large, the resulting couple will be significant and should not be ignored.

- In dynamic analysis of concrete buildings, a 5% viscous damping is routinely assumed. At very low intensity of shaking, it was reported that the test building exhibited a damping ratio in the range of 2 – 6%. However, it appears that for a concrete building with almost no nonstructural elements and flexural cracking occurring within lower stories of the building, a significantly lower viscous damping ratio in the range of 0.3-1.0% should be expected.
- Stiffness proportional damping is preferred over Rayleigh damping for dynamic analysis of concrete buildings designed to respond nonlinearly. This is because it allows the viscous damping to decline as hysteretic damping increases. This follows the recommendation of Priestley and Grant [2004] regarding viscous damping in concrete structures.
- Accurate representation of the material response envelopes likely leads to satisfactory peak response of the structure subjected to earthquake loads that push the structure to respond in a virgin territory. However, accurate representation of the unloading and reloading paths of the models used for the material and shear behavior are critical when assessing the performance of a structure subjected to earthquake motions of intensities that do not dominate the structural response in a virgin territory. This should be expected when a structure is subjected to earthquakes of similar or lower intensities than those of the previously used input motions.

A.8 References

Barbosa, A. F., and Ribeiro, G. O. [1998] "Analysis of Reinforced Concrete Structures Using ANSYS Nonlinear Concrete Model," In: Idelsohn, S., Onat, E., and Dvorkin, E., (Eds.), *Computational Mechanics: New Trends and Applications,* pp. 1-7.

Brueggen, B., Waugh, J., Aaleti, S., Johnson, B., French, C., Sritharan, S., Nakaki, S. [2007] "Tests of Structural Walls to Determine Deformation Contributions of Interest for

Performance Based Design," *Proceedings of the 2007 Structures Congress*, American Society of Civil Engineers, Reston, VA.

Dazio, A. [2000] "Entwurf und Bemessung von Tragwandgebäuden under Erdbebeneinwirkung," dissertation IBK Bericht—254, ETH, Zurich, Switzerland.

Hines, E.M., Restrepo, J. I., and Seible, F. [2004] "Force-Displacement Characterization of Well-Confined Bridge Piers," *ACI Structural Journal*, Vol 101, No. 4.

Hsu, T.C. [1993] Unified Theory of Reinforced Concrete. Boca Raton, FL, CRC Press.

Kelly, T. [2007] "A Blind Prediction Test of Nonlinear Analysis Procedures for Reinforced Concrete Shear Walls," *New Zealand Society for Earthquake Engineering Bulletin,* Vol. 40, No. 3, pp. 142-159.

Mander, J.B., Priestley, M.J.N., and Park, R. [1988] "Theoretical Stress-Strain Model for Confined Concrete," *Journal of Structural Engineering*, Vol. 114, No. 8, pp. 1804-1826.

Massone, L.M., and Wallace, J.W. [2004] "Load Deformation Response of Slender Reinforced Concrete Walls," *ACI Structural Journal*, Vol. 101, No. 1, pp. 103-113.

Mazzoni, S., McKenna, F., Scott, M.H., Fenves, G.L. [2004] "Open System for Earthquake Engineering Simulation," *Pacific Earthquake Engineering Research Center*, University of California, Berkeley California, Ver. 1.6.0.

Moaveni, B., He, X., Conte, J.P., and Restrepo, J.I. [2006] "System Identification of a Seven-Story Reinforced Concrete Shear Wall Building Slice Tested on the UCSD-NEES Shake Table," *NEES-UCSD Workshop on the Analytical Model of Reinforced Concrete Walls*, San Diego, CA.

NEES7Story [2006] NEES @ UCSD Seven Story Building-Slice Earthquake Blind Prediction Contest. http://nees.ucsd.edu/7story.html, accessed June 13, 2007.

Neuenhofer, A., and Filippou, F.C. [1997] "Evaluation of Nonlinear Frame Finite-Element Models," *ASCE Journal of Structural Engineering*, Vol. 123, No. 7, pp. 958-966.

Panagiotou, M., and Restrepo, J. [2006] "Model Calibration for the UCSD 7-Story Building Slice", *NEES-UCSD Workshop on the Analytical Model of Reinforced Concrete Walls,* San Diego, CA.

Park, R. and Paulay, T. [1975] "Reinforced Concrete Structures", New York, Wiley pp. 769.

Restrepo, J. [2006] "Proceedings of the NEES/UCSD Workshop Analytical Model of

Reinforced Concrete Walls", *NEES-UCSD Workshop on the Analytical Model of Reinforced Concrete Walls,* San Diego, CA.

Sritharan, S., Zhao. J., Waugh, J., and Govindarasu, M. [2005] "Nonrectangular Concrete Walls under Multi-directional Loads – Analytical simulation and remote participation in experimental research," *Proceeding of the First US-Portugal International Workshop on Grand Challenges in Earthquake Engineering*, Lamego, Portugal.

Swanson Analysis System [1992] "Ansys User's Manual (for Ansys Revision 5.0) Part IV: Theory" *Swanson Analysis Systems*.

Thomsen, J.H., and Wallace, J.W. [1995] "Displacement Based Design of RC Structural Walls: An Experimental Investigation of Walls with Rectangular and T-Shaped Cross-Sections," *Report to the National Science Foundation*, Department of Civil Engineering, Clarkson University, Potsdam, New York.

Waugh, J. and Sritharan, S. [2006] "Description of Analysis Model Used for Predicting Behavior of 7-Story Test Building," *NEES-UCSD Workshop on the Analytical Model of Reinforced Concrete Walls*, San Diego, CA.

Zhao, J. and Sritharan, S. [2007] "Modeling of Strain Penetration Effects in Fiber-Based Analysis of Reinforced Concrete Structures," *ACI Structural Journal,* 104(2), pp. 133-141.